

Magazine of Civil Engineering

125th

ISSN
2712-8172



124(8), 2023



Magazine of Civil Engineering

ISSN 2712-8172

Online peer-reviewed open-access scientific journal in the field of Civil and Construction Engineering

Founder and Publisher: Peter the Great St. Petersburg Polytechnic University

This journal is registered by the Federal Service for Supervision of Communications, Information Technology, and Mass Media (ROSKOMNADZOR) in 2020. Certificate EI No. FS77-77906 issued February 19, 2020.

Periodicity: 8 issues per year

Publication in the journal is open and free for all authors and readers.

Indexing: Scopus, Web of Science (ESCI, RSCI), DOAJ, Compendex, Google Academia, Index Copernicus, ProQuest, Ulrich's Serials Analysis System, CNKI

Corresponding address: 29 Polytechnicheskaya st., Saint Petersburg, 195251, Russia

Chief science editor: associate member of RAS, D.S. in Engineering, Vitaly V. Sergeev

Deputy chief science editors:

D.S. in Engineering, Galina L. Kozinets

D.S. in Engineering, Sergey V. Korniyenko

Executive editor: Ekaterina A. Linnik

Translator, editor: Darya Yu. Alekseeva

DT publishing specialist:

Anastasiya A. Kononova

Contacts:

E-mail: mce@spbstu.ru

Web: <http://www.engstroy.spbstu.ru>

Date of issue: 23.12.2023

© Peter the Great St. Petersburg Polytechnic University. All rights reserved.

© Coverpicture – Ilya Smagin

Editorial board:

T. Awwad, PhD, professor, Damascus University, Syrian Arab Republic

M.I. Balzannikov, D.Sc., professor, Samara State University of Economics, Russia

A.I. Belostotsky, D.Sc., professor, StaDyO Research & Engineering Centre, Russia

A.I. Borovkov, PhD, professor, Peter the Great St. Petersburg Polytechnic University, Russia

A. Borodinecs, Dr.Sc.Ing., professor, Riga Technical University, Latvia

M. Veljkovic, PhD, professor, Delft University of Technology, The Netherlands

R.D. Garg, PhD, professor, Indian Institute of Technology Roorkee (IIT Roorkee), India

M. Garifullin, PhD, postdoctoral researcher, Tampere University, Finland

T. Gries, Dr.-Ing., professor, RWTH Aachen University, Germany

T.A. Datsyuk, D.Sc., professor, Saint-Petersburg State University of Architecture and Civil Engineering, Russia

V.V. Elistratov, D.Sc., professor, Peter the Great St. Petersburg Polytechnic University, Russia

T. Kärki, Dr.-Ing., professor, Lappeenranta University of Technology, Russia

G.L. Kozinets, D.Sc., professor, Peter the Great St. Petersburg Polytechnic University, Russia

D.V. Kozlov, D.Sc., professor, National Research Moscow State Civil Engineering University, Russia

S.V. Korniyenko, D.Sc., professor, Volgograd State Technical University, Russia

Yu.G. Lazarev, D.Sc., professor, Peter the Great St. Petersburg Polytechnic University, Russia

M.M. Muhammadiev, D.Sc., professor, Tashkent State Technical University, Republic of Uzbekistan

H. Pasternak, Dr.-Ing.habil., professor, Brandenburgische Technische Universität, Germany

F. Rögner, Dr.-Ing., professor, Technology Arts Science TH Köln, Germany

V.V. Sergeev, D.Sc., professor, Peter the Great St. Petersburg Polytechnic University, Russia

T.Z. Sultanov, D.Sc., professor, Tashkent Institute of Irrigation and Agricultural Mechanization Engineers, Republic of Uzbekistan

M.G. Tyagunov, D.Sc., professor, National Research University "Moscow Power Engineering Institute", Russia

M.P. Fedorov, D.Sc., professor, Peter the Great St. Petersburg Polytechnic University, Russia

D. Heck, Dr.-Ing., professor, Graz University of Technology, Austria

A.G. Shashkin, D.Sc., PI Georekonstruktsiya, LLC, Russia

V.B. Shtilman, D.Sc., JSC B.E. Vedeneev VNIIG, Russia

Contents

Sabri, M.M., Ihson, J., Fahad, A., Hasib, R. Stabilization of expansive soil with lime and brick dust	12401
Sainov, M.P. Concrete face rockfill dam located on deformed foundation: stress-strain state	12402
Denisov, A.V. Radiation changes in hardened Portland cement paste under the influence of gamma radiation	12403
Kharnoob, M.M. Planting steel reinforcement for concrete columns: In case of small distance at missing places in concrete columns	12404
Usanova, K., Barabanshchikov, Yu.G., Dixit, S. Cementless binder based on high-calcium fly ash with calcium nitrate additive	12405
Jawad, S.I., Karkush, M.O. Shear strength and chemical properties of soft clayey soil treated with magnetized water	12406
Zlateva, P., Petkova-Slipets, R., Yordanov, K. Properties of grey marl bricks with additions of rice husks	12407
Mushchanov, V.F., Mushchanov, A.M., Orzhehivskiy, A.N., Tcepliaev, M.N. Optimum space frames with rectangular plans	12408
Ivanov, E.N., Semenov, K.S., Barabanshchikov, Yu.G., Akimov, S.V., Kuleshin, A.S., Titov, N.T. Concrete heat liberation in thermal stressed state analysis	12409
Kokaya, D.V., Zaborova, D.D., Koriakovtseva, T.A. Environmental analysis of residential exterior wall construction in temperate climate	12410
Zotov, D.K., Kozinets, G.L., Kozinets, P.V., Chernov, V., Badenko, V.L. Digital models for retrospective analysis of the structure of currents in the Neva Bay	12411
Sergeev, V.V., Kotov, E.V., Horobrov, S.V., Sabri, M.M., Nemova, D. Hydrodynamic analysis of an unsteady pressureless filtration flow in earth cofferdams	12412
Bulanov, P.E., Vdovin, E.A., Stroganov, V.F. Increasing the level of aging stability of bitumes modified by kaolinite	12413



Research article

UDC 624

DOI: 10.34910/MCE.124.1



Stabilization of expansive soil with lime and brick dust

M.M. Sabri¹ , J. Ihson², A. Fahad², R. Hasib²

¹ Peter the Great St. Petersburg Polytechnic University, St. Petersburg, Russian Federation

² Department of Civil Engineering, COMSATS University Islamabad, Abbottabad, Pakistan

✉ mohanad.m.sabri@gmail.com

Keywords: expansive soils, lime, brick dust, stabilization, compressive strength, plasticity, swell index, SEM analysis, construction, sustainable.

Abstract. Expansive soils in construction pose significant challenges due to their low strength, high compressibility, and potential for swelling. The article is dedicated to assessing the effectiveness of using lime and brick dust as additives to enhance the properties of highly plastic soils. Various tests were performed on soil samples treated with different lime and brick dust concentrations, including moisture content, maximum dry density, unconfined compressive strength, yield strength, plasticity, and swelling index. The results indicate that the addition of 5 % lime improved the soil's strength properties, resulting in a significant increase in its compressive strength. With increased lime concentration, a decrease in plasticity was observed, indicating that the soil became less plastic. Scanning electron microscopy analysis revealed changes in the surfaces and pores of the treated soil samples, suggesting structural changes induced by the lime and brick dust treatment. Furthermore, adding lime significantly reduced the plasticity index of the soil, and brick dust reduced the soil's swell index, with the lowest index of 8 % observed in the sample treated with 5 % lime and 30 % brick dust. The study's findings suggest that lime and brick dust can improve the stability of expansive soils, rendering them more suitable for construction purposes.

Funding: This research was supported by a grant from the Russian Science Foundation No. 22-79-10021, <https://rscf.ru/project/22-79-10021/>

Citation: Sabri, M.M., Ihson, J., Fahad, A., Hasib, R. Stabilization of expansive soil with lime and brick dust. Magazine of Civil Engineering. 2023. 124(8). Article no. 12401. DOI: 10.34910/MCE.124.1

1. Introduction

Soil stabilization is a crucial process in civil engineering involving additives to enhance soil properties, such as compressive strength, shear strength, and settlement problems. Soil stabilization is essential to enhance the problematic geotechnical properties of soil. Various soil stabilization techniques exist worldwide. Each method has its advantages and limitations [1-7]. The effect of nano-silica fume on gypseous collapsibility and shear strength was studied by [8,9]. The additives used for soil stabilization include Portland cement, lime, rice husk ash, asphalt, and rubber, among others. Some additives are combined with others to create substances with superior and well-controlled properties. Proper procedures are followed to replace the natural soil content with these additives, which are often less expensive, pozzolanic, and environmentally friendly.

Expansive soils are a common geological hazard that causes severe damage to structures, roads, and other infrastructure [10,11]. Lime stabilization is a popular and effective method to reduce the swelling potential of expansive soils [12,13]. In addition, adding brick dust to the soil-lime mixture can further enhance its stabilizing properties [14,15].

Previous research has shown that lime and brick dust can improve expansive soil's mechanical and geotechnical properties, including increased strength and reduced swelling potential [16,17]. Furthermore, researchers have also investigated the optimal mixture proportions of lime, brick dust, and expansive soil to achieve the best results [6,18,19].

Various techniques have been used to evaluate the effectiveness of the soil stabilization methods, including laboratory tests such as unconfined compressive strength, California Bearing Ratio, and Atterberg Limits, as well as field tests such as plate load tests and pavement performance evaluations [20]. However, it is essential to consider the stabilized soil's long-term performance; therefore, long-term monitoring and evaluation are also crucial.

Research in this field has explored various combinations of additives for soil stabilization. For instance, Kamon and Nontananandh [21] combined lime and industrial waste to stabilize soil, while Atom and Al-Sharif [22] evaluated burned olive waste as a soil stabilizer. Before initiating the stabilization process, it is essential to accurately assess the soil's characteristics [23], as locally available soil may differ from soil tested elsewhere. Climatic factors and soil types also require different technical stabilization techniques [24]. The rate of curing, for example, can be affected by temperature, while a wet climate may affect the stabilization process.

Agricultural nations face challenges related to agricultural waste, which contains minerals and silicates that plants ingest as they grow. Some plants, such as rice, wheat, sunflowers, and tobacco, contain higher concentrations of silicates in their bodies, while inorganic materials are present in plants in the form of free salts and particles that combine cationic and anionic groups from fibers [25]. In light of these issues, this study aims to investigate the effects of lime and industrial waste, specifically brick dust, on natural soil's strength, consistency, and density.

2. Materials and Methods

2.1. Materials

2.1.1. Soil Collection

This study aimed to investigate the effectiveness of soil stabilization techniques using lime and brick dust on a representative soil sample found in various locations. A soil sample weighing 60 kg was collected for this study. The sample was obtained at a depth of 1.5 to 2 meters, as shown in Fig. 1. The studied physical and chemical properties of the investigated soil are summarized in Tables 1 and 2.



Figure 1. Collection of Undisturbed Soil Sample at 2-meter depth.

2.1.2. Brick Dust

In recent years, various additives have been used to improve the properties of expansive soils. However, many of these additives have adverse environmental effects. Brick dust, for example, can increase soil salinity, which affects plant growth. Researchers have suggested using this waste product to address this issue to create stable soil for construction foundations and road subbases. For this study, 10 kg of class B brick dust was collected from the kiln industry.

2.1.3. Lime

In this research, lime was employed as an optimizing agent to minimize the maximum amount of brick dust required while enhancing the strength of the soil. For this purpose, a quantity of 5 kg of lime was prepared.

2.2. Methods

Mixing lime and brick dust for soil stabilization in the laboratory was carried out in several key steps. Soil samples were obtained from the site, and their properties, including plasticity, density, and moisture content, were tested to determine the appropriate amount of lime and brick dust to be added to the soil. The additives were weighed and thoroughly mixed to ensure a homogenous mixture, with the percentage of lime and brick dust calculated based on the soil properties. The resulting mixture was gradually added to the soil while being constantly mixed.

The optimum levels of lime are prepared for soil samples at 2 %, 4 %, 5 %, and 6 %. According to test results, the hydration reaction for high plastic clay is almost finished at 5 % lime. Therefore, 5 % is chosen as the optimized value. Further, Brick dusts were added at 5 %, 15 %, 20 %, and 30 % to the optimized lime.

After the preparation process, the stabilized soil was tested to determine its properties. The properties of the stabilized soil were compared to those of the original soil to evaluate the effectiveness of the stabilization process, with the percentage of lime and brick dust used is a critical factor in determining the results.

The investigation involved testing the prepared soil reference and treated samples using various methods, including sieve analysis, liquid Limit, plastic Limit, shrinkage limit, standard Proctor test, and unconfined compression strength test. The particle size distribution of the soil samples was determined through a wet sieve analysis in accordance with the ASTM D 7928-16 standard, with soils that passed through a #200 sieve classified as clayey. The liquid limit and plastic limit of the samples were determined using ASTM D422-63 and ASTM D4318-00 standards, respectively. The shrinkage limit was determined following the guidelines outlined in ASTM-D4943 standard. The samples' maximum dry density and optimum moisture content were determined through the standard Proctor test as per ASTM D698. Finally, the unconfined compression strength test was performed as per ASTM D2166 to evaluate the strength of the treated samples.

Unsoaked curing of samples was performed at different lime and binder dosage levels (2, 4, 5, and 6 percent) to optimize the lime treatment process for seven days. Both lime and BD were used as binders in the curing process. Unsoaked curing was reported up to 28 days at intervals of (2, 4, 7, 14, and 28 days).

Furthermore, SEM (Scanning Electron Microscope) analysis was conducted on reference and treated soil samples to evaluate their physical and chemical properties at a microscopic level.

Table 1. Summary of properties of the reference soil samples.

SAMPLE №.	PROPERTIES	VALUE
1	Liquid Limit (%)	55.3
2	Plastic Limit (%)	28.02
3	Plasticity Index	25.78
4	Shrinkage Limit (%)	22.82
5	% age Passing #200	95
6	Soil Type (USCS)	CH
7	Soil Type (AASHTO)	A-6-7
8	MDD (g/cm ³)	1.58
9	OMC (%)	20.49
10	Unsoaked UCS (MPa)	0.5
11	Swell Index (%)	29.63

Table 2. Summary of chemical properties of the reference soil samples.

SAMPLE №.	PROPERTIES	VALUE
1.	pH value	>7(Alkaline)
2.	Organic content	0.4 to 204 %
3.	CaCO ₃	5 to 15 %
4.	SiO ₂	50 to 55 %
5.	SiO ₂ , Al ₂ O ₃	3 to 5 %
6.	Montmorillonite mineral	30 to 50 %

3. Results and Discussion

3.1. Sieve Analysis

The fine particle gradation of the reference soil is given in Fig. 2.

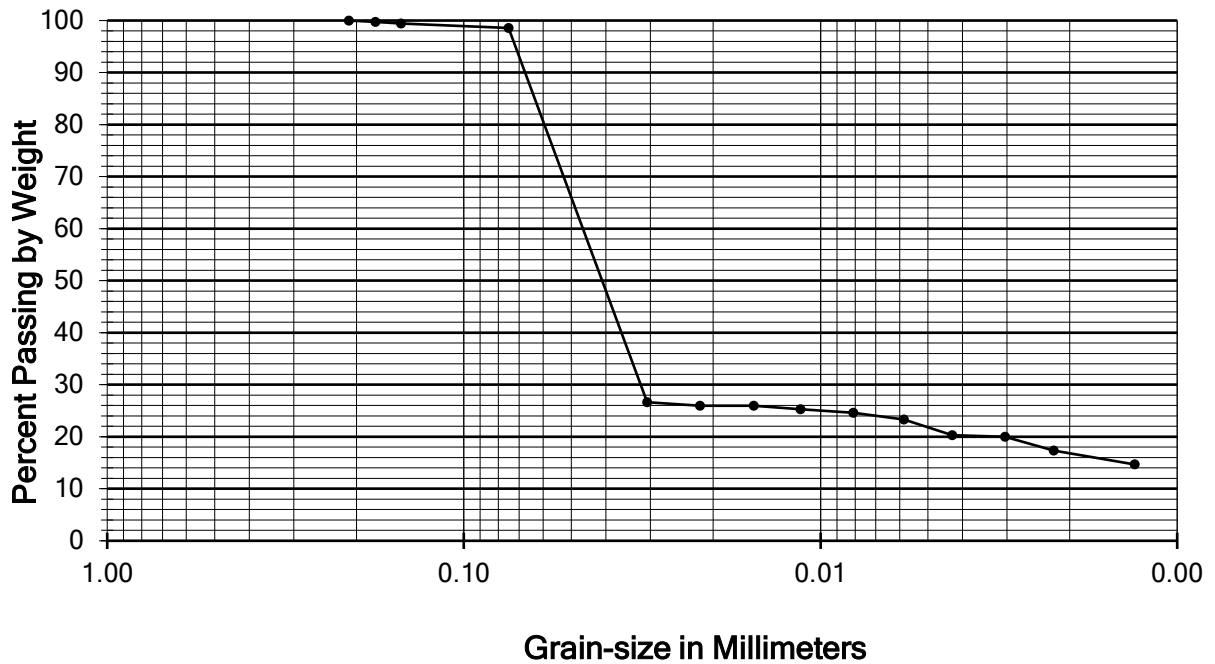


Figure 2. Fine Particle Gradation of the reference soil.

3.2. The moisture content and maximum dry density for Different Lime Content

Four tests were carried out by adding 2, 4, 5, and 6 % lime by the weight of the soil. A standard Proctor test was conducted on all soil-lime samples at the given 2, 4, 5, and 6 % of the soil to determine the moisture content and maximum dry density for each sample.

The maximum dry density and moisture content relationship of the reference and treated samples were determined and presented in Fig. 3. This figure illustrates the effect of the added lime content on the soil's maximum dry density and moisture content.

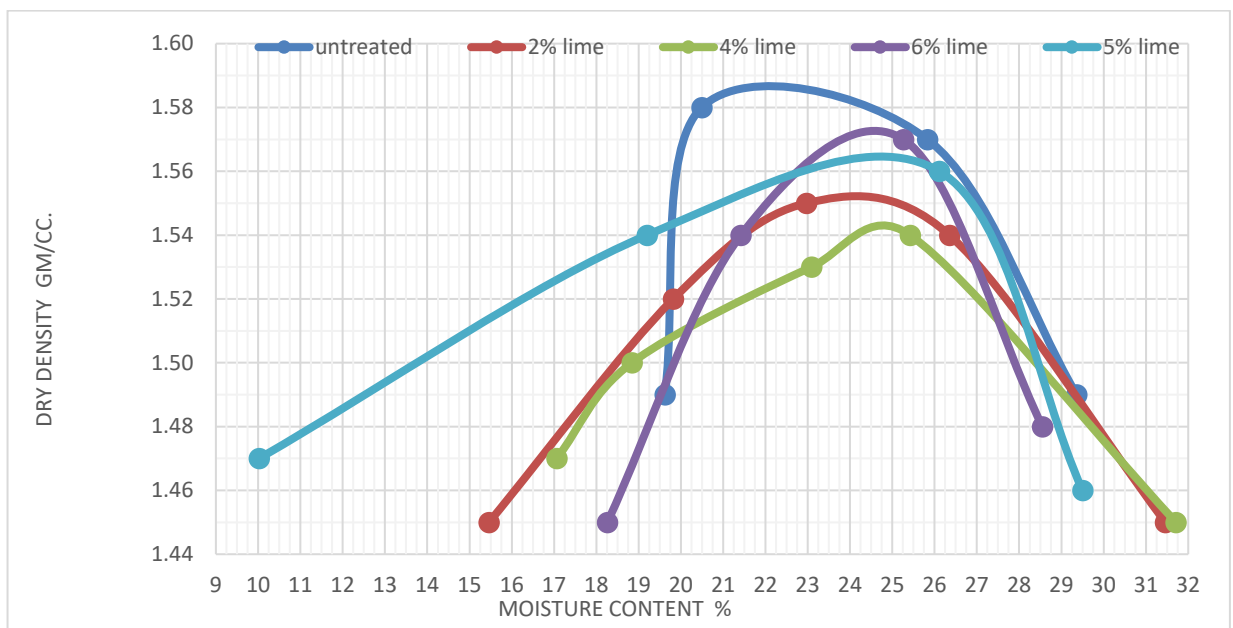


Figure 3. The maximum dry density and moisture content at different Lime contents.

3.3. Optimization of lime using unconfined compression test UCS

Unconfined compression tests were conducted in this study to determine the strength properties of the investigated high plastic soils. The soil samples were treated with different levels of lime, namely 2 %, 4 %, 5 %, and 6 % by weight of the soil, to improve their strength characteristics. Based on the gained results, it was observed that the hydration reaction of the high plastic clay was almost complete at 5 % lime concentration, which resulted in the maximum strength improvement. Consequently, 5 % was chosen as the optimal lime content for the soil samples.

A comparison of the compressive strength results of the reference (untreated) and the soil samples treated with 5 % lime showed a significant improvement in the strength of the treated soil samples (Fig. 4). The data showed that the soil samples stabilized with 5 % lime had a compressive strength of 3.335 MPa, which was considerably higher than the strength of the reference samples (0.488 MPa).

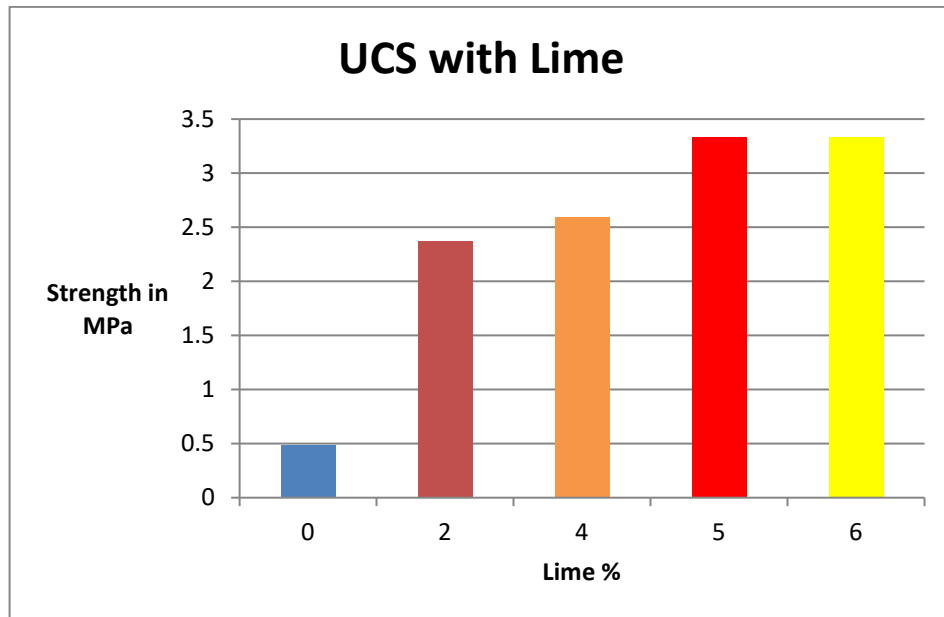


Figure 4. The average strength of the reference and treated samples at the given lime percentage.

3.4. 'Atterberg's Limits of Soil Treated with Lime and Brick Dust

In this study, testing was carried out on optimized lime, i.e., 5 % and 15 %, 20 % and 30 % BD, to observe how the liquid Limit and plasticity of high plastic soil changed while shrinkage limits increased. The liquid Limit of soil was measured using the Casagrande apparatus. The Atterberg's Limits Test was run on optimized lime and various BD percentages in this phase. The liquid Limit of the treated soil is given in Fig. 5-8. Table 3 summarizes 'Atterberg's limits of reference and treated soil. The results indicate the change in the liquid Limit of the treated soil with increasing BD and lime concentration. The addition of lime had a significant effect on the plasticity of the soil. The plasticity index decreased as the lime concentration increased, indicating that the soil became less plastic. The study also showed that adding lime significantly affected the plasticity of the soil—the plasticity index decreased, indicating that the soil became less plastic. The plasticity index was found to be 26 % for the reference sample, while it decreased to 22 %, 21 %, 19 %, and 16 % at 5 % lime and 15 %, 20 %, 25 %, and 30 % brick dust, respectively.

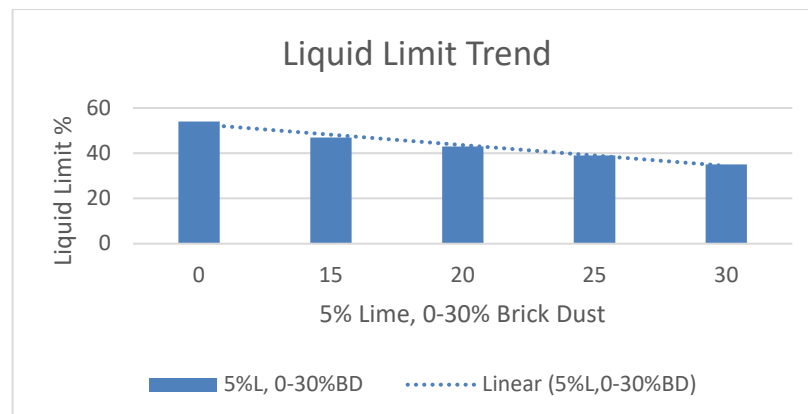


Figure 5. Liquid limits of treated soil.

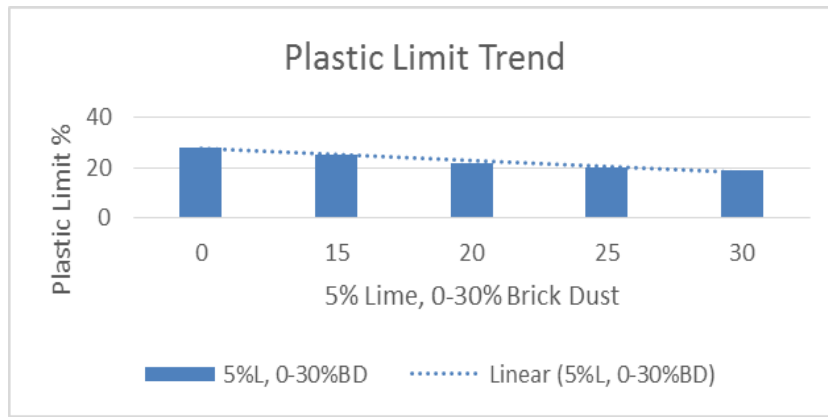


Figure 6. Plastic limits of treated soil.

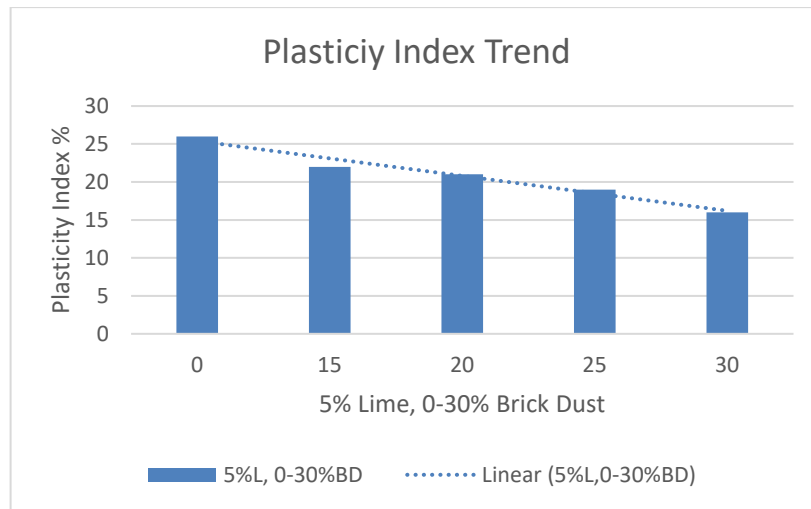


Figure 7. Plasticity index of treated soil.

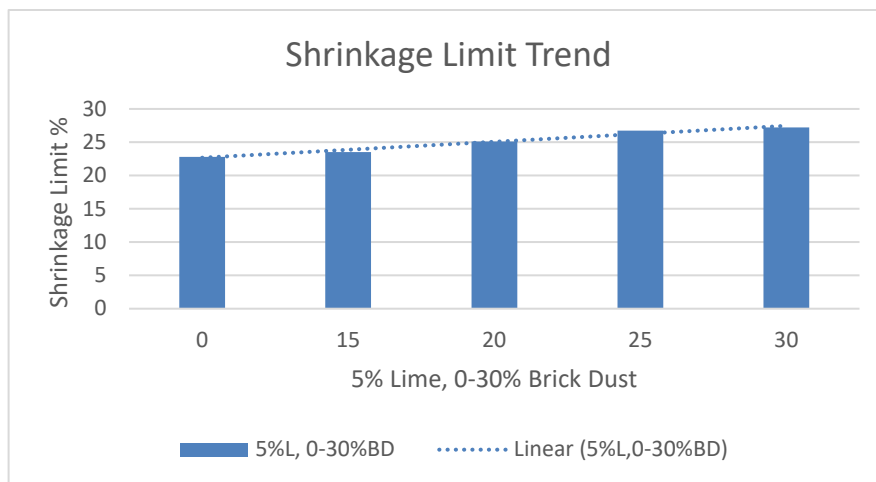


Figure 8 Shrinkage limits of treated soil.

Table 3. Summary of the 'Atterberg's limits of untreated and treated soil.

'ATTERBERG'S LIMIT	UNTREATED SOIL	5%LIME, 15%BD	5%LIME, 20%BD	5%LIME, 25%BD	5% LIME, 30%BD
LIQUID LIMIT	54%	47%	43%	39%	35%
PLASTIC LIMIT	28%	25%	22%	20%	19%
PLASTICITY INDEX	26%	22%	21%	19%	16%
SHRINKAGE LIMIT	22.82%	23.5%	25.1%	26.72%	27.2%

3.5. Free Swell Index

Fig. 9 represents the relationship between the percentage of lime and brick dust and the swell index of the soil. The results clearly show that the swell index decreases as the percentage of lime and brick dust increases. As shown in Table 4, the untreated soil had a swell index of 29 %, which is significantly higher than the treated soil samples. Adding 5 % optimized lime and increasing amounts of brick dust reduced the swell index, with the lowest swell index of 8 % observed for the sample treated with 5 % lime and 30 % brick dust.

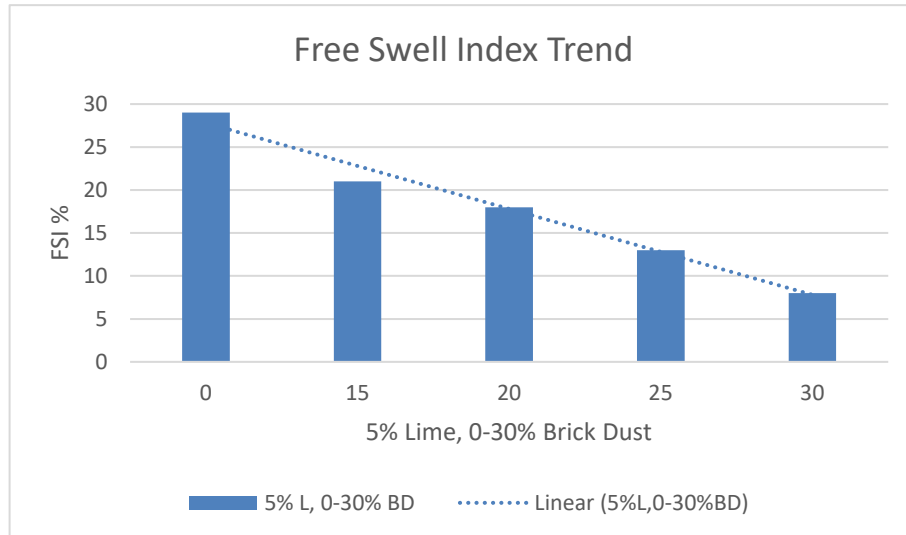


Figure 9 Swell potential of treated soil.

Table 4. Summary of Free Swell Index (FSI).

FSI %	UNTREATED SOIL	5%LIME, 15%BD	5%LIME, 20%BD	5%LIME, 25%BD	5%LIME, 30%BD
SWELL%	29	21	18	13	8

3.6. SEM Analysis

Various SEM tests were carried out on the reference and treated samples. The SEM analysis results are shown in Fig. 10–13. Fig. 13 displays the SEM images of the treated sample, which was cured for 28 days with 5 % lime and 25 % BD. Comparing the images at scales of 10, 20, and 100 micrometers reveals various variations in faces (shape, size, homogeneity), and holes (size, open or closed).



Figure 10 Untreated Sample (10 micrometer).

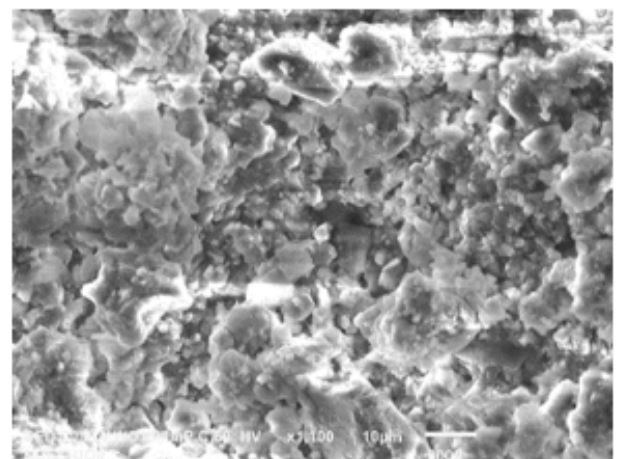


Figure 11 Treated Sample (10 micrometer).

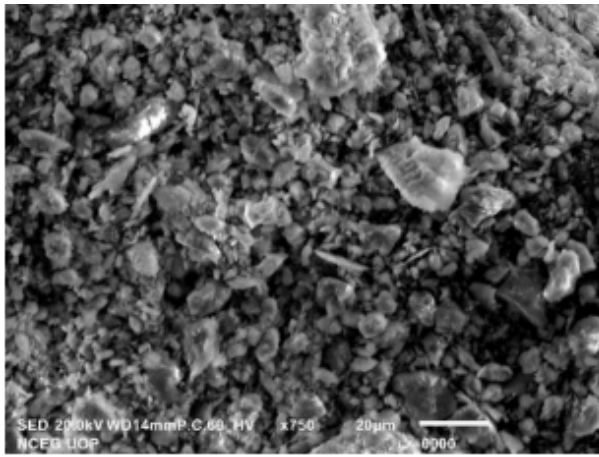


Figure 12 Untreated sample (20 micrometer).

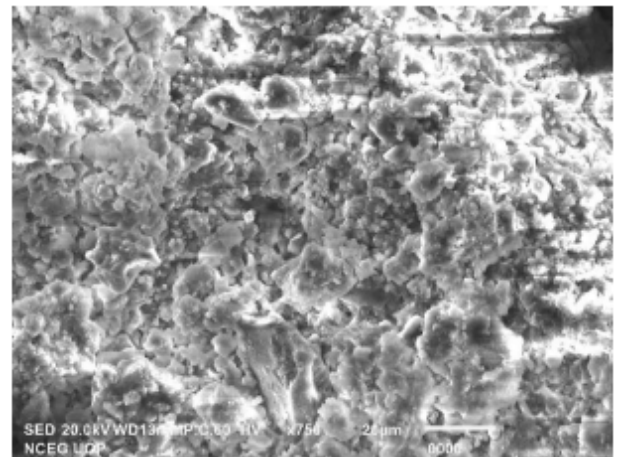


Figure 13 Treated sample (20 micrometer).

4. Conclusion

The study investigated the effects of lime and brick dust additives on the shear strength and limits of expansive soils at an optimized percentage. The main findings are:

1. The addition of 5 % lime concentration improved the maximum shear strength for the soil samples.
2. Adding lime significantly reduced the plasticity index of the soil, with a decrease observed as the lime concentration increased. The plasticity index decreased from 26 % for the reference sample to 22 %, 21 %, 19 %, and 16 % at 5 % lime and 15 %, 20 %, 25 %, and 30 % brick dust, respectively.
3. Adding lime and brick dust reduced the swell index of the soil, with the lowest swell index of 8 % observed for the sample treated with 5 % lime and 30 % brick dust.
4. The SEM analysis revealed variations in the faces and holes of the treated sample, indicating the effectiveness of lime and brick dust as stabilizers.
5. The study suggests that the optimized 5 % lime by the soil weight is the optimum percentage for stabilizing the investigated soil type. This percentage significantly improves the soil's shear strength and physical properties, enhancing stability and reducing plasticity.

5. Future Recommendations

1. BD used in this research was taken from only one source and one class, i.e Class B only. As composition and properties of BD varies with class and region so efforts should be made to compare the effect of brick dust taken from various sources and classes of all over the country.
2. To determine the swell potential of soil, this research focused on determining one dimensional swell potential. The overall free swell potential of soil should also be determined.
3. In this research, only lab testing was taken into consideration, field investigations should be done to implement the suitability of BD and lime as a stabilizing agent for high plastic clays.
4. Stabilization projects should be planned at ideal temperature conditions for trials in the field. The temperature is around 30 °C.
5. Compaction effort should commence as soon as possible after mixing.
6. Soil should be cured for at least 28 days at ambient temperature before subsequent construction.

References

1. Wang, G., Chen, S., Xia, M., Zhong, W., Han, X., Luo, B., Sabri, M.M.S., Huang, J. Experimental Study on Durability Degradation of Geopolymer-Stabilized Soil under Sulfate Erosion. *Materials*. 2022. 15. DOI: 10.3390/ma15155114
2. Fan, J., Wang, D., Qian, D. Soil-cement mixture properties and design considerations for reinforced excavation. *Journal of Rock Mechanics and Geotechnical Engineering*. 2018. 10. Pp. 791–797. DOI: 10.1016/j.jrmge.2018.03.004
3. Li, Z., Zhang, L., Sun, D., Zhang, Q., Wang, D., Wang, L. Quantitative Design Method for Grouting in Sand Layers: Practice in Qingdao Metro Line 2. *Processes*. 2022. 10. DOI: 10.3390/pr10050840
4. Sharafutdinov, R.F. Clay soil stiffness under consolidated isotropic drained triaxial tests. *Magazine of Civil Engineering*. 2023. 121(5). Article no. 12106. DOI: 10.34910/MCE.121.6

5. Alhokabi, A., Hasan, M., Amran, M., Fediuk, R., Vatin, N.I., Alshaeer, H. The Effect of POFA-Gypsum Binary Mixture Replacement on the Performance of Mechanical and Microstructural Properties Enhancements of Clays. *Materials (Basel)*. 2022. 15. DOI: 10.3390/ma15041532
6. Karkush, M.O., Almurshedi, A.D., Karim, H.H. Investigation of the Impacts of Nanomaterials on the Micromechanical Properties of Gypseous Soils. *Arabian Journal for Science and Engineering*. 2022. 48. Pp. 665–675. DOI: 10.1007/s13369-022-07058-z
7. Al-Murshedi, A.D., Karkush, M.O., Karim, H.H. Collapsibility and Shear Strength of Gypseous Soil Improved by Nano Silica Fume (NSF). *Key Engineering Materials*. 2020. 857. Pp. 292–301, DOI: 10.4028/www.scientific.net/KEM.857.292
8. Hunter, D. Lime-induced heave in sulfate-bearing clay soils. *Journal of Geotechnical Engineering*. 1988. 114. Pp. 150–167. DOI: 10.1061/(ASCE)0733-9410(1988)114:2(150)
9. Çokça, E. Use of class C fly ashes for the stabilization of an expansive soil. *Journal of Geotechnical and Geoenvironmental Engineering*. 2001. 127. 568–573. DOI: 10.1061/(ASCE)1090-0241(2001)127:7(568)
10. Al-Rawas, A.A., Hago, A.W., Al-Sarmi, H. Effect of lime, cement and Sarooj (artificial pozzolan) on the swelling potential of an expansive soil from Oman. *Building and Environment*. 2005. 40. Pp. 681–687. DOI: 10.1016/j.buildenv.2004.08.028
11. Karkush, M.O., Al-Murshedi, A.D., Karim, H.H. Investigation of the impacts of nano-clay on the collapse potential and geotechnical properties of Gypseous soils. *Jordan Journal of Civil Engineering*. 2020. 14. Pp. 537–547.
12. Dash, S.K., Hussain, M. Lime Stabilization of Soils: Reappraisal. *Journal of Materials in Civil Engineering*. 2012. 24. Pp. 707–714. DOI: 10.1061/(ASCE)MT.1943-5533.0000431
13. Al-Mukhtar, M., Khattab, S., Alcover, J.F. Microstructure and geotechnical properties of lime-treated expansive clayey soil. *Engineering Geology*. 2012. 139–140. Pp. 17–27. DOI: 10.1016/j.enggeo.2012.04.004
14. Bell, F.G. Lime stabilization of clay minerals and soils. *Engineering Geology*. 1996. 42. Pp. 223–237. DOI: 10.1016/0013-7952(96)00028-2
15. Karkush, M.O., Al-Taher, T.A.A. Geotechnical Evaluation of Clayey Soil Contaminated with Industrial Wastewater. *Archives of Civil Engineering*. 2017. 63. Pp. 47–62. DOI: 10.1515/ace-2017-0004
16. Karkush, M.O., Resol, D.A. Geotechnical properties of sandy soil contaminated with industrial wastewater. *Journal of Engineering Science and Technology*. 2017. 12. Pp. 3136–3147.
17. Karkush, M.O., Ali, H.A., Ahmed, B.A. Improvement of unconfined compressive strength of soft clay by grouting gel and silica fume. *Proceedings of China-Europe Conference on Geotechnical Engineering*. 2018. Pp. 546–550. DOI: 10.1007/978-3-319-97112-4_122
18. Sabri, M.M.S., Vatin, N.I., Ponomarev, A.B., Nurmukhametov, R.R., Kostyukov, I.I. Settlement of Soil Reinforced with Vertical Fiberglass Micro-Piles. *Materials*. 2022. 15. 15144744. DOI: 10.3390/ma15144744
19. Maichin, P., Jitsangiam, P., Nongnuang, T., Boonserm, K., Nusit, K., Pra-ai, S., Binaree, T., Aryupong, C. Stabilized High Clay Content Lateritic Soil Using Cement-FGD Gypsum Mixtures for Road Subbase Applications. *Materials*. 2021. 14. 1858. DOI: 10.3390/ma14081858
20. Mohamadi, M., Choobasti, A.J. Stabilization of sandy soil using microfine cement and nanosilica grout. *Arabian Journal of Geosciences*. 2021. 14. DOI:10.1007/s12517-021-07844-3
21. Kamon, M., Nontananandh, S. Combining industrial wastes with lime for soil stabilization. *Journal of Geotechnical Engineering*. 1991. 117. Pp. 1–17.
22. Attom, M.F., Al-Sharif, M.M. Soil stabilization with burned olive waste. *Applied Clay Science*. 1998. 13. Pp. 219–230.
23. Ali, F.H. Stabilization of a residual soil. *Soils and Foundations*. 1992. 32. Pp. 178–185.
24. Dumbleton, M.J. Investigations to assess the potentialities of lime for soil stabilization in the United Kingdom. HM Stationery Office, 1962.
25. Basha, E., Hashim, R., Mahmud, H., Muntohar, A. Stabilization of residual soil with rice husk ash and cement. *Construction and Building Materials*. 2005. 19. Pp. 448–453.

Information about authors:

Mohanad Sabri, PhD

ORCID: <https://orcid.org/0000-0003-3154-8207>

E-mail: mohanad.m.sabri@gmail.com

Jehangir Ihson,

E-mail: ihson.j@gmail.com

Amin Fahad,

E-mail: fahadamin77@gmail.com

Rehman Hasib,

E-mail: haseeb.rehman914@gmail.com

Received 07.04.2023. Approved after reviewing 18.04.2023. Accepted 21.10.2023.



Research article

UDC 69.01

DOI: 10.34910/MCE.124.2



Concrete face rockfill dam located on deformed foundation: stress-strain state

M.P. Sainov *Moscow State University of Civil Engineering (National Research University), Moscow, Russian Federation*✉ mp_sainov@mail.ru**Keywords:** dams, concrete face rockfill dam (CFRD), cutoff wall, stress-strain state, finite element method, soil foundation, numerical modelling

Abstract. Concrete face rockfill dam (CFRD) located on soil foundation has a composite structure of the seepage control facility. It includes three elements: the dam concrete face, the seepage control cutoff wall (CW) in the foundation and the concrete apron connecting them. There is an urgent task to study workability and stress-strain state (SSS) of the seepage control facility as a whole structure as well as each element separately. Method. The SSS analysis of an abstract dam with the aid of numerical modeling was conducted to solve this task. A 100 m high CFRD located on a 100 m thick foundation layer was considered. Analyses were conducted for several alternatives of foundation soils with deformation modulus from 40 to 5000 MPa. Results. The analyses showed that the SSS of the dam on the soil foundation drastically differs from the SSS of the dam on the rock foundation. The concrete face and the cutoff wall are subject to considerable compressive longitudinal forces. Due to bending deformations in CW and the concrete apron, considerable tensile stresses may occur. Conclusions. A number of recommendations was formulated for providing strength of the elements of the composite seepage control facility of the dam on soil foundation. To provide strength of the concrete face it is necessary that the deformability of the dam soil be close to the foundation soil. To provide CW with strength, it is recommended use the material with rigidity of no more than by 2–3 times greater than the foundation soil rigidity. The most vulnerable element of the structure of the composite seepage control facility is the concrete apron. To avoid cracking in it, it should be cut by transversal joints to form separate slabs.

Citation: Sainov, M.P. Concrete face rockfill dam located on deformed foundation: stress-strain state. Magazine of Civil Engineering. 2023. Article no. 12402. DOI: 10.34910/MCE.124.2

1. Introduction

Concrete face rockfill dam (CFRD) is one of the embankment dam types, which may be used practically in any conditions, where stone is available for the dam body.

The classic structure of CFRD used from the end of the 20th century is built on rock foundation. It includes 2 elements: a concrete face and a concrete apron. A concrete face (CF) covering the upstream face is made thin-walled and is uncut vertically. A short concrete apron is located on the foundation surface from where the grout curtain in rock foundation is fulfilled. CF and the apron are separated from each other by a perimeter joint. It has a movable connection; it is made in a way of providing potential deflections and other displacements of the face relative to the apron.

If a CFRD is located on soil (deformed) foundation, its structural design is similar to the classic one, however, it has its specific features. The main difference is the presence of the cutoff wall (CW) in the foundation to prevent seepage. CW joins the upstream face of the apron forming a unified seepage control

contour (Fig. 1). Thus, a CFRD on soil foundation has a seepage control facility (SCF) of a composite structure. It includes not two but already three elements.

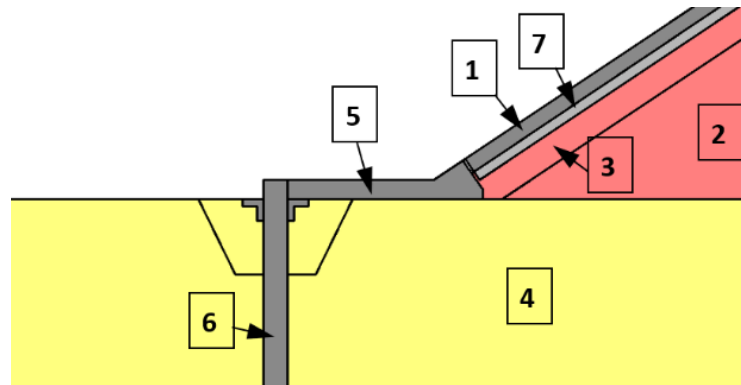


Figure 1. Diagram of the interface of the seepage control facility elements: 1 – reinforced concrete face; 2 – rockfill dam shell; 3 – supporting zone; 4 – foundation layer; 5 – concrete apron; 6 – cutoff wall in the foundation; 7 – lean concrete layer.

CFRDs located on a foundation deformed layer are rather popular. Parameters of such dam structural designs are listed in [1–6]. Alto Anchicaya dam 154 m high built on soil foundation may be considered the first ultra-high CFRD of modern structural design. This dam was constructed in 1983 in Columbia on a 34 m thick layer of sand and gravel.

In the 21st century, a number of CFRDs were constructed on soil foundation. At their listing we will indicate their height H and thickness of soil deposits layer T . The list contains the following dams: Dhauliganga (2006, India, $H = 56$ m, $T = 70$ m), Aertash (Turkey, $H = 164.8$ m, $T = 94$ m) [1], Limon (Chili, $H = 82$ m, $T = 46$ m) [7], Nalan (2005, China, $H = 109$ m, $T = 24$ m) [8], Jiudianxia (2008, China, $H = 136.5$ m, $T = 56$ m) [9], Chahanwusu (2009, China, $H = 107.6$ m, $T = 47$ m) [10], Miaojiaba (2011, China, $H = 111$ m, $T = 48$ m) [2, 11].

The highest CFRD on soil foundation is Aertash dam in Turkey; it was constructed on a layer of alluvial soils [1]. Its CF is from 0.4 to 1 m thick, with the 1.2 m thick CW. The CW is made of reinforced concrete.

In 2014, a dam received a CW providing water tightness not only of the foundation but also of the lower part of the dam for the first time [12, 13]. It is the 140 m high Arkun dam constructed in Turkey. Such a structure may be considered as a perspective type of CFRD refinement.

However, in order to use the structural designs of the dams with composite seepage control elements it is necessary to be assured in their safety and tightness of the elements interface. At that, it is necessary to take into account that the composite seepage control facility works in other conditions as compared to the classic structure of CFRDs located on the rock foundation.

A number of foreign publications are dedicated to stress-strain state (SSS) analyses of CFRDs located on deformed foundation. Some publications [8–10, 14] are dedicated to determination of the dam and foundation deformations, while neglecting the strength of the seepage control facility elements in them.

A large scope of investigations was carried out by Chinese specialists [2, 3, 12]. With the aid of 3D numerical modeling of SSS and field observations over deformations and stresses at constructed Miaojiaba dam they studied SSS of CW integrated in the composite SCF. However, CF strength was not estimated. Besides, these investigations were conducted only on the example of one particular structure.

In order to study workability of composite SCF of the dam on deformed foundation we carried out methodical investigation of the foundation properties' effect on SSS. Some preliminary results have been published earlier in [15].

Assessment of workability of seepage control facility of CFRDs located on soil (deformed) foundation is an urgent issue. For this purpose, it is necessary to carry out SSS analyses of such dams.

These analyses should solve the following issues:

Issue No. 1. Workability of the elements of traditional CFRD structure at its location on the deformed foundation. How does the foundation deformation affect SSS and strength of the concrete face and the concrete apron?

Issue No. 2. Workability of the CW interface with the concrete apron. Is the interface between CW and the concrete aprons still tight?

2. Materials and Methods

In the study, we considered an abstract 100 m high rockfill dam located on a 100 m thick layer of the deformed foundation (Fig. 2).

The structure of the dam is as follows. The dam slopes are 1:1.7. On the upstream slope of the dam there is a concrete face (CF) of variable thickness (from 0.3 m on the top to 0.8 m at the toe). The face is placed on the lean concrete supporting zone [16, 17], which is called “extruded curb” or “extrusion-sidewall” (SW). Deformation modulus of lean concrete is approximately 5000 MPa [18]. A thin layer of mastic is placed between the face and the supporting zone, which is intended for decreasing friction in compliance with the bond-breaking concept used for structures of modern CFRDs [19].

The wall in the foundation is 1.2 m thick. It is connected with the face by an apron 10 m long and 1 m thick.

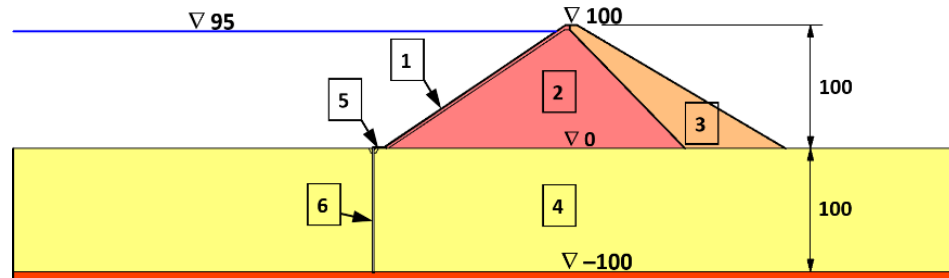


Figure 2. Diagram of concrete face rockfill dam located on deformed foundation layer:
1 – reinforced concrete face; 2 and 3 – upstream and downstream parts of the shell of the rockfill dam; 4 – foundation layer; 5 – concrete apron; 6 – seepage control wall in the foundation.

SSS analyses of the structure were carried out by the finite element method with the aid of the author’s computer program NDS_N. Analyses were conducted in 2D formulation.

The dam and the foundation were divided into 1220 solid finite elements and 76 contact finite elements (Fig. 3). The contact elements modeled had non-linear character of the interface between soils and rigid constructions. In order to simulate a complicated character of SSS of rigid thin-walled constructions we used finite elements with cubic power of displacements approximation. The total number of freedom degrees of the finite element model amounted to 11852.

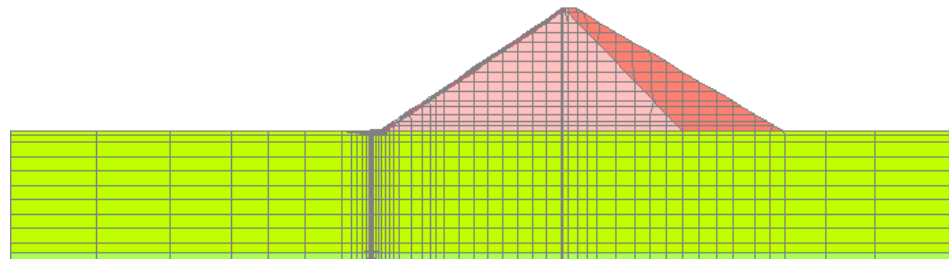


Figure 3. Diagram of finite element discretization of the structure.

The study was conducted for several combinations of the dam and foundation soil deformation properties.

We considered two alternatives of the dam body rockfill (rock mass). In the first alternative (alternative A) the rockfill modulus of linear deformation E_{dl} of the dam upstream was assumed to be equal to 120 MPa, and in the second (alternative B) it was 480 MPa. The modulus of linear deformation of rockfill in the downstream part of the shell was taken 2 times less than that of the upstream part.

In addition, we considered four alternatives of foundation soil types and, accordingly, characteristics of foundation deformation. Alternatives “a” and “b” correspond to soils of gravel-pebble, alternatives “c” and “d” to rocks. Alternative “a” approximately corresponds to foundation soils of Aertash dam [1], and alternative “d” corresponds to soils of Karkhe dam [20].

Mechanical properties of foundation soils are presented in Table 1. The table also indicates the strength indices of foundation soils by Mohr-Coulomb model. For rockfill, the angle of internal friction was taken equal to 47° .

The cutoff wall material was assigned depending on deformability of foundation soils. It was assumed that deformation modulus of the wall material should not exceed the deformation modulus of the foundation soil by more than 5 times (Table 1). We chose cast clay-cement concrete for alternative “a”; plastic concrete

for alternatives “b” and “c”; concrete for alternative “d”. The CW measurements data for Karkheh dam show plastic concrete has deformation modulus of approximately 500–2000 MPa and compressive strength of 2–3.5 MPa [20, 21]. The CW measurements data for Kureika dam suggest the cast clay-cement concrete has deformation modulus 30–200 MPa, and its uniaxial compressive strength comprises 1–2 MPa [22].

In total, we considered eight design alternatives with various combinations of the dam and foundation material (Table 1). Alternatives “A.d” and “B.d” correspond to the case of using the traditional structural design of CFRD on rock foundation.

Table 1. Mechanical properties of materials in design alternatives.

Alternative No.	Dam				Foundation			CW	
	E_{d1} [MPa]	E_{d2} [MPa]	ν_n	E_o [MPa]	ν_o	φ_o	c_o [kPa]	E_c [MPa]	ν_c
A.a	120	60	0.2	40	0.33	38	0	200	0.33
A.b	120	60	0.2	200	0.33	40	0	1000	0.30
A.c	120	60	0.2	1000	0.33	30	30	5000	0.25
A.d	120	60	0.2	5000	0.25	33	50	29000	0.20
B.a	480	240	0.2	40	0.33	38	0	200	0.33
B.b	480	240	0.2	200	0.33	40	0	1000	0.30
B.c	480	240	0.2	1000	0.33	30	30	5000	0.25
B.d	480	240	0.2	5000	0.25	33	50	29000	0.20

Designations: E_{d1} , E_{d2} are rockfill modulus of linear deformation in the upstream and downstream parts of the dam respectively; E_o , E_c are module of linear deformation of the foundation soil and the wall material respectively; ν_n , ν_o , ν_c are Poisson’s ratios of rockfill, foundation soil and the wall material respectively; φ_o , c_o are the angle of internal friction and specific cohesion of foundation soil respectively.

For the face concrete, the modulus of linear deformation was taken equal to 29000 MPa, Poisson’s ratio was 0.2.

Computation was conducted for loads of dead weight and hydrostatic pressure acting on the upstream faces of seepage control facilities. It was assumed that SCF fully cuts through the impervious foundation layer and reaches headwater. Therefore, SCF is subject to total hydrostatic pressure from the upstream and downstream sides.

SSS analyses were carried out with consideration of the dam construction and the reservoir impoundment sequence. The following staged diagram was assumed. At the first stage, we modeled the formation of the foundation SSS, then arrangement of SCF in it. During the following 15 stages, we modeled layered dam filling by horizontal layers. Only after that the face was “placed” for the full height. Then gradual reservoir impoundment was modeled with growth of hydrostatic pressure on the upstream part of the face, the apron and the wall.

3. Results and Discussion

The dam SSS analysis for all the considered alternatives was fulfilled until the level of the reservoir impoundment reached the elevation of 95 m. The analysis was conducted for the following parameters: displacement of the dam and the foundation, displacements of the upstream part of the face and CSF, stresses in the dam body and the foundation, stresses on the upstream and downstream faces of CF. The distribution of displacements and stresses is shown in Fig. 4–14, and their maximum values are in Table 2.

Table 2. Parameters of the dam SSS for design alternatives.

Alternative No.	Dam	Foundation	Dam SSS		Concrete face SSS			Wall SSS		
	E_{d1} [MPa]	E_o [MPa]	U_x [cm]	U_y [cm]	U_n [cm]	max σ_n [MPa]	min σ_n [MPa]	U_x [cm]	min σ_y [MPa]	max σ_y [MPa]
A.a	120	40	179	311	186.8	–	-9.6	161	-6.1	0.3
A.b	120	200	50	72	47.3	–	-7.6	35	-4.7	-0.2
A.c	120	1000	23.8	41	24.8	–	-3.1	9.6	-4.8	0.6
A.d	120	5000	18.2	37	20.7	0.3	-2.0	3.1	-4.3	–
B.a	480	40	185	307	172.8	2.1	-10.7	117	-6.4	0.4
B.b	480	200	36	61	36.2	–	-7.2	28	-4.9	-0.2
B.c	480	1000	11.1	15.8	10.5	–	-4.2	8.2	-4.9	-0.3
B.d	480	5000	5.7	10.2	6.2	–	-2.0	3.0	-4.5	0.2

3.1. Analysis of the dam and foundation displacements

Displacements of the computational domain over the construction period for different alternatives are shown in Fig. 4 (settlements U_y) and Fig. 5 (horizontal displacements U_x). Displacements of the foundation from its dead weight are not taken into account.

The analysis shows that the considered alternatives of the foundation and the dam properties greatly differ by value and character of the dam displacements' distribution.

In case of rigid rock foundation ($E_o = 5000$ MPa) the zone of maximum settlements U_y is located in the center of the dam body (Fig. 4, c, d), and in case of soil foundation ($E_o = 40$ MPa) it is located at the dam toe (Fig. 4, a, b). Maximum values of the structure settlements during construction in these alternatives differ approximately by an order of magnitude.

Maximum horizontal displacements U_x in most of the alternatives are observed on the dam upstream face (Fig. 5). Only in case of deformed foundation (in alternatives of series "a") the zone of high horizontal displacements is also located on the boundary between the dam and the foundation (Fig. 5, a, b). In this case the maximum dam displacement is approximately 30 times greater than that of rock foundation.

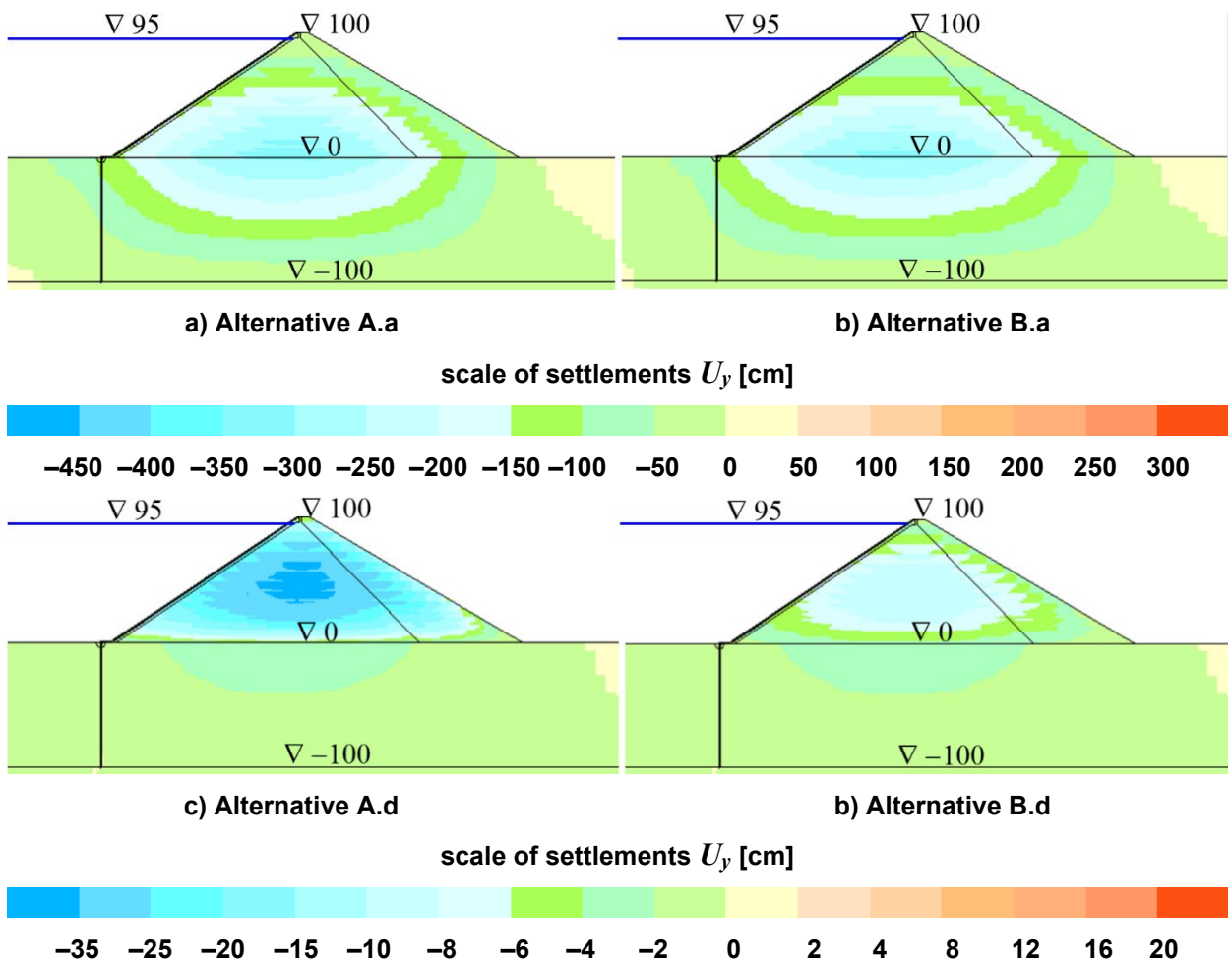


Figure 4. Distribution of the structure settlements in different alternatives: a, b – at $E_o = 40$ MPa; c, d – at $E_o = 5000$ MPa; a, c – at $E_{dI} = 120$ MPa; b, d – at $E_{dI} = 480$ MPa.

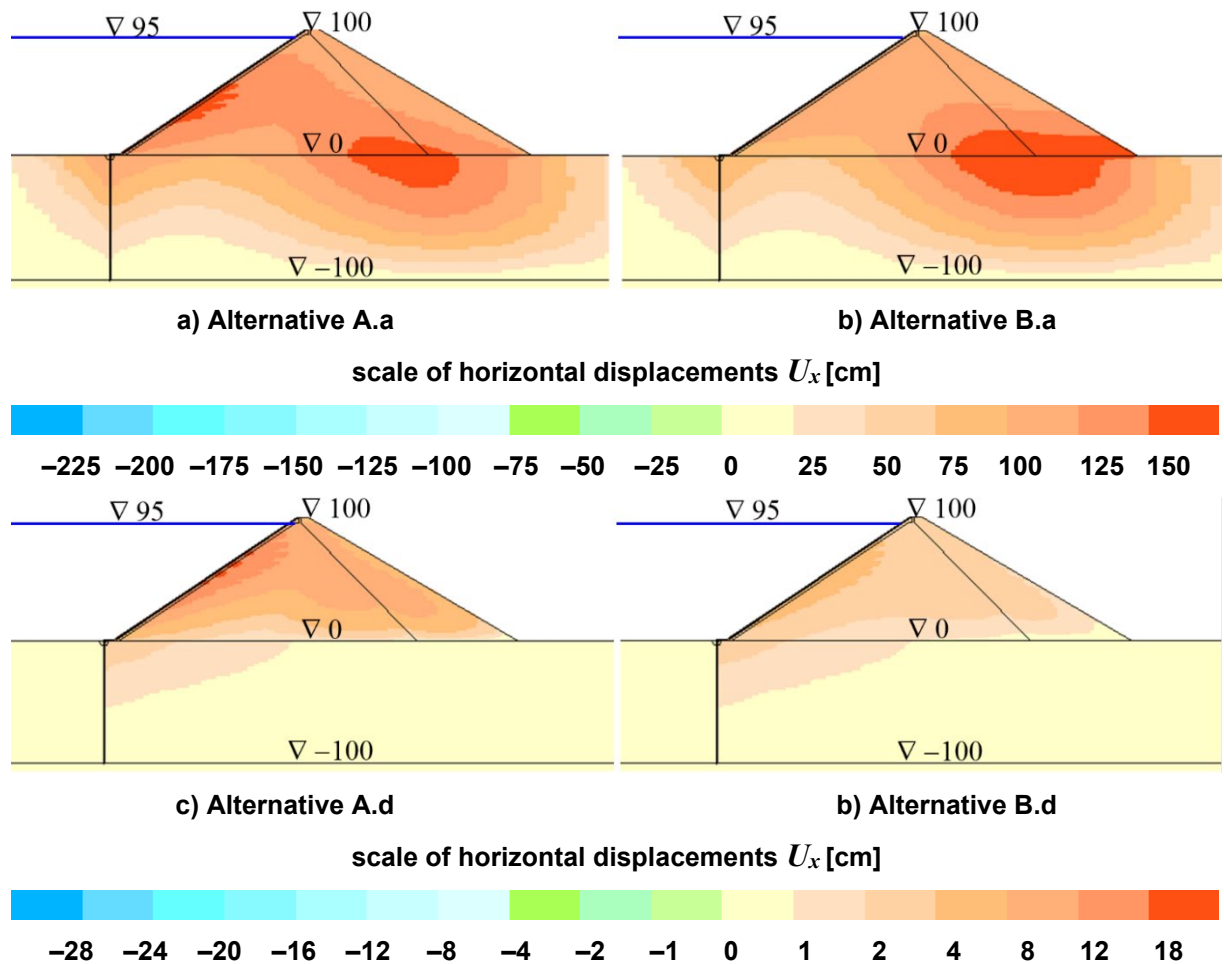


Figure 5. Distribution of the structure horizontal displacements in different alternatives: a, b – at $E_o = 40$ MPa; c, d – at $E_o = 5000$ MPa; a, c – at $E_{dl} = 120$ MPa; b, d – at $E_{dl} = 480$ MPa.

3.2. Analysis of stresses in the dam and foundation

Distribution of axial normal stresses σ_y and σ_x is shown in Fig. 6 and 7 respectively. The stresses presented in the figures do not take into account the stresses from the foundation dead weight.

The value and the character of distribution of vertical stresses σ_y slightly depend on the foundation deformation (Fig. 6). Stresses in the dam uniformly increase from the crest to the toe. In the upper part of the dam, the stresses σ_y are somewhat higher than in the downstream due to hydrostatic pressure on the face. In the foundation the compressive stresses actually do not vary depth wise.

In the zone of SCF arrangement, the stresses σ_y are relatively not high. In the downstream part from the wall the compression level slightly increases and in upstream part the stresses σ_y actually drop to 0 (Fig. 6).

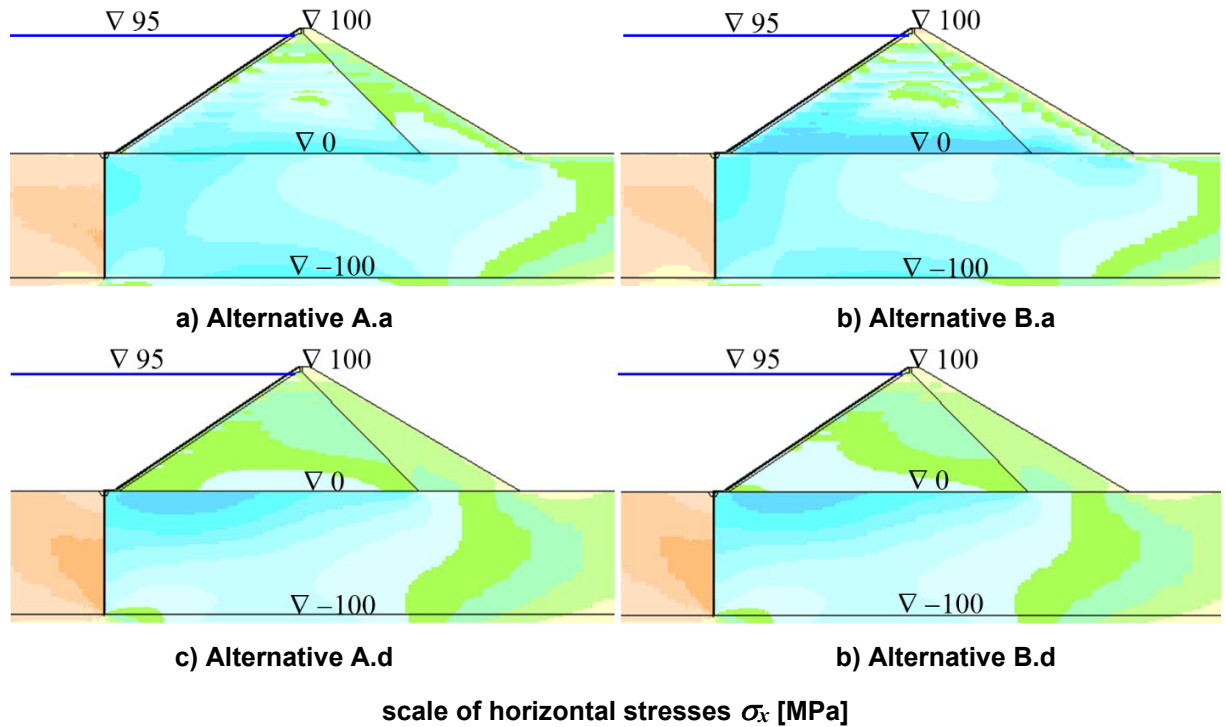
With respect to stresses σ_x , the soil from the upstream side of the wall has deficit of compressive stresses and from the downstream part, there is additional compression due to hydrostatic pressure on the wall (Fig. 7).

The value and the character of distribution of horizontal stresses σ_x are greatly dependent on the ratio between deformation properties of the foundation and the dam body. The alternatives, where deformation moduli of the foundation and the dam considerably differ from each other, are characterized by considerable differences in the values of stresses σ_x between the dam body and the foundation.

At $E_o \gg E_{dl}$ (rigid rock foundation), a characteristic concentration zone of compressive stresses σ_x forms in the upper part of the foundation (Fig. 7,c,d); thus, the dam body soil has deficit of compressive stresses.

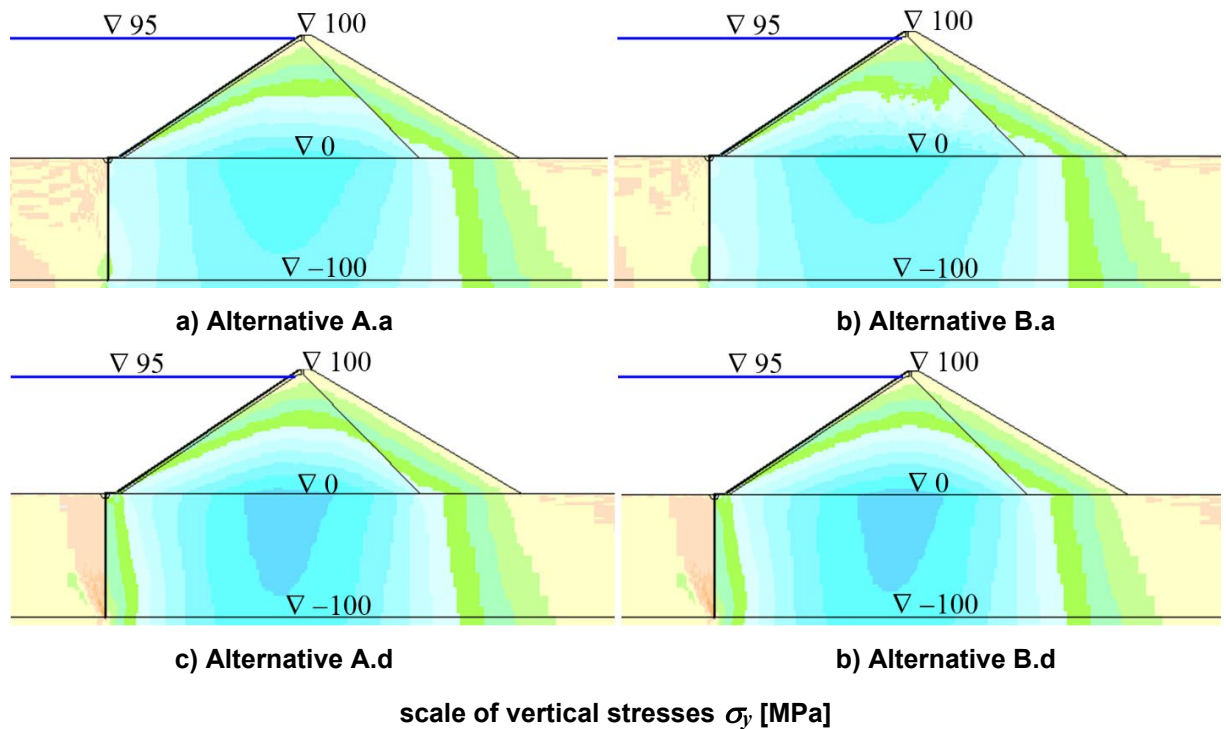
At $E_o < E_{dl}$ (deformed soil foundation), a characteristic zone of soil shear strength loss forms in the lower part of the dam (Fig. 7,a,b). If during the analysis the soil is considered to be elastic, the tensile

stresses σ_x appear in this zone. As our calculations allowed for the fact that the soils had tensile strength, the tensile stresses would not occur and the soil is subject to loosening deformations. Tensile deformations result in additional settlements and displacements of the structure.



-1.0 -0.9 -0.8 -0.7 -0.6 -0.5 -0.4 -0.3 -0.2 -0.1 0 0.1 0.2 0.3 0.4 0.5

Figure 6. Distribution of horizontal stresses σ_x in different alternatives: a, b – at $E_o = 40$ MPa; c, d – at $E_o = 5000$ MPa; a, c – at $E_{dI} = 120$ MPa; b, d – at $E_{dI} = 480$ MPa.



-2.0 -1.8 -1.6 -1.4 -1.2 -1.0 -0.8 -0.6 -0.4 -0.2 0 0.2 0.4 0.6 0.8 1.0

Figure 7. Distribution of horizontal stresses σ_y in different alternatives: a, b – at $E_o = 40$ MPa; c, d – at $E_o = 5000$ MPa; a, c – at $E_{dI} = 120$ MPa; b, d – at $E_{dI} = 480$ MPa.

3.3. Displacements of cutoff wall (CW)

In the same way as the displacements of the whole structure, displacements U_x of the wall are directed toward the downstream side. They have nearly uniform distribution heightwise and reach maximum at the wall head (Fig. 8). The displacements cause bending deformations at certain parts of the wall. Wall bending occurs at the section of thrust into the rigid apron and at conjugation with the rock foundation.

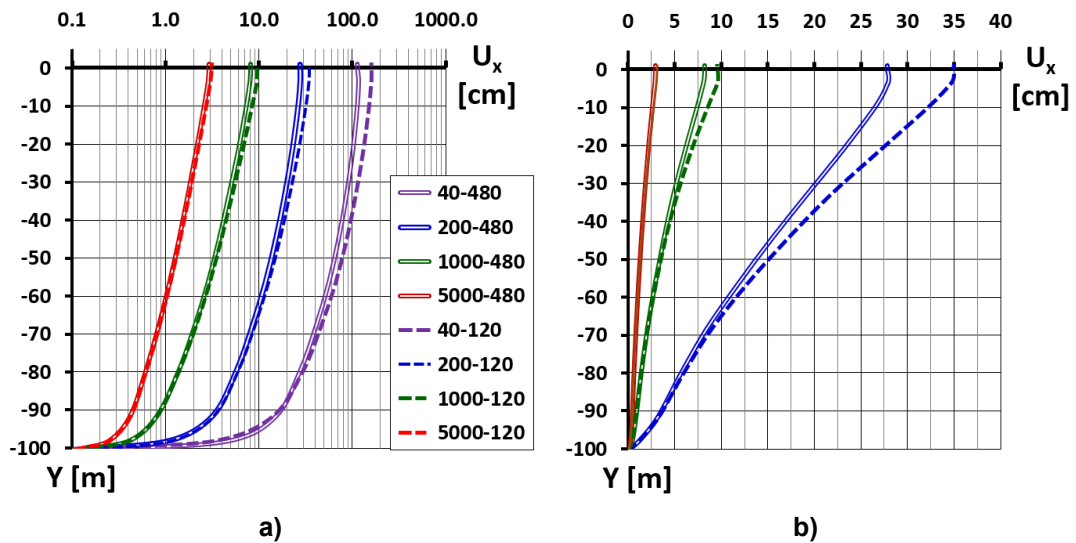


Figure 8 Displacements of the wall made in the foundation of variable rigidity. In the designation of the alternatives the first number indicates deformation modulus of foundation soil (MPa), the second number is deformation modulus of the dam soil (MPa): a – in logarithmic scale, b – in natural scale.

3.4. Analysis of concrete face displacements

Displacements of CF are shown in Fig. 9 in the form of its deflections, i.e. displacements in the direction perpendicular to the upstream face.

For the rigid foundation (alternatives of series “d”) the non-uniform distribution of the face deflections height wise is typical (Fig. 9). It provides evidence of deformations of the face transverse bending. Actually, height wise the face deflects toward the downstream side except for the top most part. At rigid foundation the maximum of value displacements and settlements are observed approximately at $\nabla 45$ m.

The higher the foundation deformation, the greater the face deflections. Deflections increase face height wise, but they are more intense near the dam toe (Fig. 9). In case of the soil foundation the face maximum deflections are observed specifically near the dam toe.

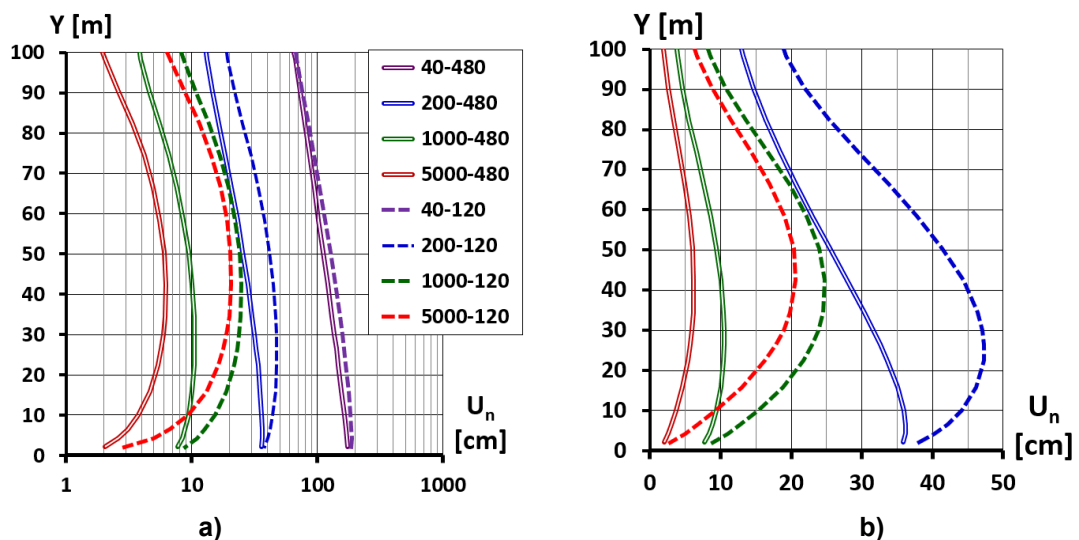


Figure 10. Height wise distribution of face deflections. In the designation of the alternatives the first number indicates deformation modulus of foundation E_o (MPa), the second number is deformation modulus of rockfill E_{dl} (MPa): a – in logarithmic scale, b – in natural scale.

Analysis of maximum values of the face deflections $U_{n,max}$ (Table 2) permits making the following conclusions:

- At rigid (rock) foundation ($E_o > 1000$ MPa) the maximum value of deflection slightly depends on deformation modulus of the foundation E_o and is mainly determined by deformation modulus of rockfill E_d .
- At soil foundation ($E_o < 200$ MPa) the maximum value of deflection actually does not depend on the dam rockfill deformation and mainly depends on deformation modulus of foundation E_o .
- At most deformed soil foundation (alternatives of series “a”) CF deflections amount to more than 1 % of the dam height.

3.5. Concrete face stress state

As it is known from the results of numerical modeling, CF stress state is formed not only due to deformations of transverse bending, but also due to longitudinal deformations [23, 24]. Analyses show that the lower part of the dam face on rock foundation may be subject to tensile longitudinal force.

Similar results were obtained for the alternatives of series “d” ($E_o = 5000$ MPa). Figs. 11, 12 show CF heightwise distribution of stresses σ_E , directed along the slope, i.e. longitudinal stresses. Fig. 11 shows stresses on the upstream and downstream parts of the face, and Fig. 12 shows average values of stresses (axial stresses).

As on the most part of the face length the bending is represented weakly, the stresses on its parts are close to each other. Only in the zone of conjugation with the apron, there is additional compression due to bending on the face upstream part, and on the downstream part, the compression decreases.

The value and the character of stresses’ distribution in CF depend on deformation of the foundation and the dam soils. The more the difference in deformation between the foundation and the dam is, the more the value of both average longitudinal stresses and irregularity of their distribution is.

In the alternatives of the dam on the rigid foundation (alternatives of series “d”), tensile stresses σ_E occur in the lower part of the face (Fig. 11, 12).

In the alternatives of the dam on the soil foundation (alternatives of series’ “a”, “b”), high compressive longitudinal stresses in the face are typical. Average compressive stresses reach approximately 9 MPa (Fig. 12). Maximum compression is observed at the height of 30 m. Compressive strength of the face concrete is provided if concrete of grade B30 is applied.

However, in case of soil foundation in the face beside compressive there may also occur tensile longitudinal stresses. Such effect was obtained in alternative B.a, where the dam deformation modulus was 12 times greater than the foundation deformation modulus. This alternative indicates considerable tensile stresses (Fig. 11, b), which exceed the tensile strength of B30 concrete (1.1–1.75 MPa).

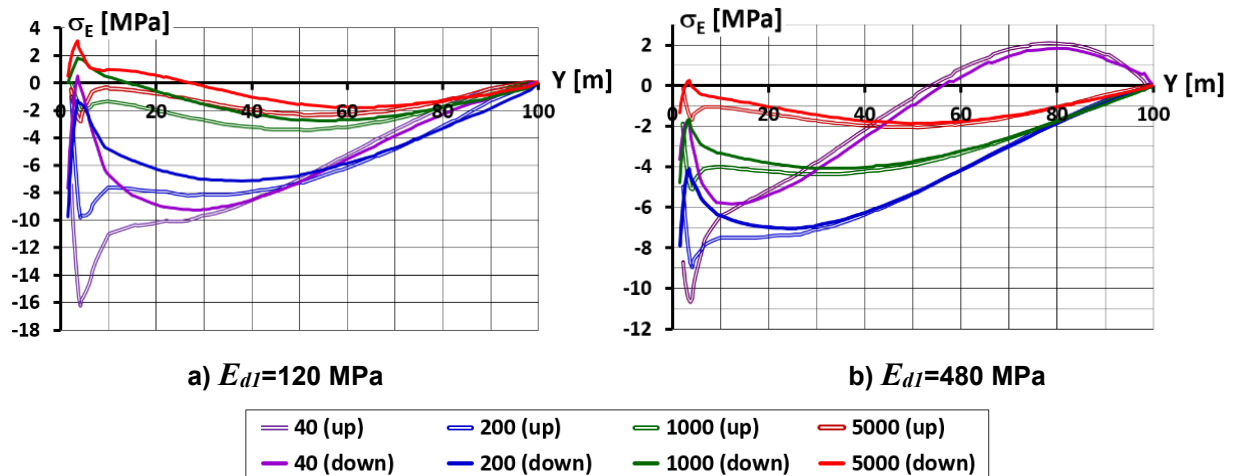


Figure 11. Face height wise distribution of longitudinal stresses on the upstream and downstream sides. Designations indicate the value of deformation modulus of the foundation (MPa) and the face side.

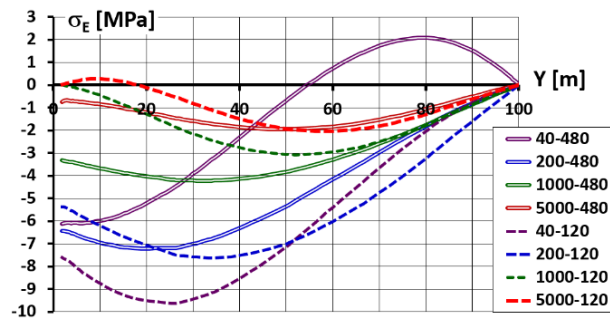


Figure 12. Face height wise distribution of average longitudinal stresses.

In alternative A.a, where the dam deformation modulus is only 3 times greater than the foundation deformation modulus, this effect is not observed. Thus, in CFRD on soil foundation there is a danger of strength loss of the face concrete.

3.6. Wall stress state

Fig. 13 shows average by the wall thickness vertical stresses σ_y for all the alternatives. For all the alternatives it is typical that the wall is subject to over compression in vertical direction. This effect is known from the results of field measurements and numerical modeling of CW SSS in foundations of high embankment dams [5, 15].

Excess of compressive stresses is related to the fact that the wall material is more rigid than the foundation soil. It occurs due to friction of soil settling relative to the wall. Compression stresses increase depth wise.

At most of the wall sections the stresses on the upstream and downstream faces of the wall are approximately similar. At the sections of conjugation of the wall with the rock foundation and with the apron, bending deformations cause the zones of concentration of compressive stresses and sometimes of tensile stresses (Fig. 13).

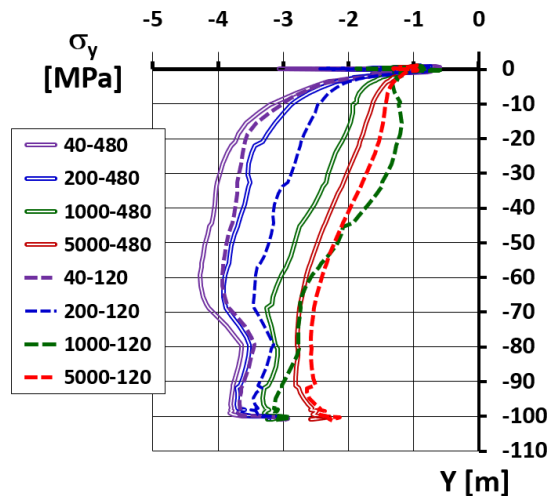


Figure 13. Wall height wise distribution of average vertical stresses.

From the point of view of providing compressive strength to the wall material, the unfavorable situation develops in the alternatives with the most deformed foundation (alternatives of series «a»). In this case, the compressive stresses reach approximately 4 MPa (Fig. 13), i.e. they exceed uniaxial compression strength of cast clay-cement concrete (approximately 2 MPa). However, from the experiments of a number of authors [25, 26] it is known that the strength of clay-cement increases significantly in the presence of lateral compression. Taking into account the influence of lateral compression effect, the strength of the CW can be ensured.

Evidently, a great risk for the wall workability is presented by tensile stresses in the bending zones. Tensile stresses at the section of CW conjugation with the rigid concrete apron are typical for the alternatives with soil foundation (alternative of series' «a», «b»). In these alternatives, the upper part of the joint between CW and the apron opens, thus, putting the seepage control contour at risk of tightness loss.

3.7. Stress state of the apron

Bending deformations are typical for SSS of the concrete apron. It is evident in Fig. 14 showing all the alternatives the distribution of horizontal stresses along the upstream and downstream parts of the face. Stresses are non-uniformly distributed along the thickness of the face.

The left and the right parts of the apron bend in different ways. The left part of the apron (approximately 4 m long) bends in upward direction, which is related to interaction with the wall (Fig. 14). The right part of the face bends downward.

The wall transfers compressive longitudinal (horizontal) force with intensity of approximately 1 MPa to the apron. However, bending deformations cause tensile stresses on the apron faces. Their value varies depending on the foundation rigidity.

At rigid (rock) foundation the stresses in the apron are small; its strength is provided with large safety factor. At deformed (soil) foundation, the tensile stresses are so great (Fig. 14), that they exceed concrete tensile strength. Moreover, in alternative "A.a", compressive stresses exceed compressive strength of B30 grade concrete.

Thus, the concrete apron is the most vulnerable element of the composite seepage control facility of the dam on the deformed foundation. Besides, its high rigidity creates the unfavorable stress state in the head part of the wall.

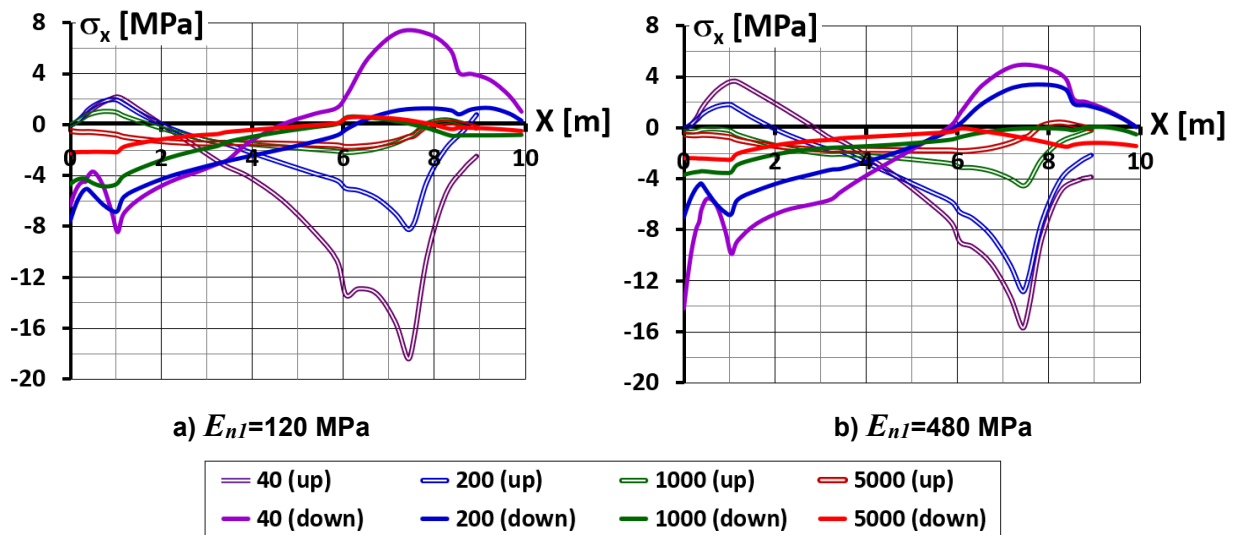


Figure 14. Distribution of average horizontal stresses lengthwise the apron on the upstream and downstream faces. In the designation there shown the value of deformation modulus of foundation (MPa) and the face.

4. Conclusion

Stress-strain state of CFRD, located on the deformed soil foundation drastically differs from SSS of the dam on the rigid rock foundation. Increase of the foundation deformation not only creates unfavorable SSS for the dam rockfill, but threatens the strength of the seepage control facility elements as well as tightness of their connections.

The degree of the foundation effect on the dam SSS depends on the thickness and deformation of the foundation soils as well as the width of the rock canyon. Nevertheless, one can distinguish several threats for the composite seepage control facility of CFRD, located on the deformed soil foundation:

1. The concrete face of the dam on soil foundation is subject to considerable compressive longitudinal forces. Taking into account the occurrence of possible stresses in the face from other factors (for example, from temperature effects), there is a risk of concrete compressive strength loss. Besides, if the foundation is by an order of magnitude more deformed than the rockfill, considerable tensile forces may also occur in the face leading to a probable loss of concrete tensile strength.
2. In spite of the fact that the seepage control wall is beyond the dam profile, it is subject to increased compressive stresses in vertical direction. Therefore, the wall material is at risk of compressive strength loss. In order to provide strength, it is recommended to choose the wall material with rigidity not more than 2–3 times greater than that the foundation soil.

3. Due to the wall thrust into the rigid concrete apron, there are two probable unfavorable effects for the tightness of the dam seepage control contour. First of all, it is formation of cracks in the wall head, secondly, it is opening of the joint between the apron and the wall. Wall connection to the apron should be designed as tight to prevent large displacements.
4. Concrete apron is the most vulnerable element of the composite seepage control facility. Due to great tensile stresses at bending there is a risk of crack formation in the apron. Designing the composite seepage control facility should include the measures for preserving the apron water tightness.

The problem of providing workability to the apron may be solved using several methods.

The first method is cutting the apron by transversal joints into 2–3 slabs. For example, the 10 m long apron of Aertash dam was cut into 3 slabs. The joints are located at a distance of 3 m and 6 m from the wall. This method provides effective decrease of tensile stresses. However, Fig. 14 shows that the joints are located not in the most dangerous sections, therefore, preventing of crack formation in the apron is not guaranteed.

The design of 92 m high dam Khao Laem (or Vajiralongkorn, Thailand) provided a concrete gallery above the apron, which permits grouting of the foundation and checking the condition of the apron.

The other method is possible. The author considered the alternative of the dam structural design, where the apron is made of asphalt concrete. It was shown that a decrease of the apron rigidity was favorable for the face SSS; strength of all the elements was provided. However, this method was tested only by the way of numerical modeling for one particular case.

References

1. Fu, Z., Chen, S., Ji, E. Practices in constructing high rockfill dams on thick overburden layers. *Dam Engineering*. 2019. Pp. 1–21. DOI: 10.5772/intechopen.78547
2. Wen, L., Qin, Y., Chai, J., Li, Y., Wang, X., Xu, Z. Behaviour of concrete-face rockfill dam on sand and gravel foundation. *Proceedings of the Institution of Civil Engineers: Geotechnical Engineering*. 2015. 168 (5). Pp. 439–456. DOI: 10.1680/jgeeng.14.00103
3. Wen, L., Chai, J., Xu, Z., Qin, Y., Li, Y. Deformation and stress behaviours of concrete-face rockfill dam built on sand and gravel foundation. *Shuilì Fadian Xuebao/Journal of Hydroelectric Engineering*. 2016. 35 (9). Pp. 63–77. DOI: 10.11660/sfidxb.20160908
4. Wen L., Chai J., Xu Z., Qin Y., Li Y. A statistical review of the behaviour of concrete-face rockfill dams based on case histories. *Géotechnique*. 2017. 68 (9). Pp. 749–771. DOI: 10.1680/jgeot.17.p.095
5. Wen L., Chai J., Xu Z., Qin Y., Li Y. A statistical analysis on concrete cut-off wall behaviour. *Proceedings of the Institution of Civil Engineers — Geotechnical Engineering*. 2018. 171 (2). Pp. 160–173. DOI: 10.1680/jgeen.17.00142
6. Sainov, M., Soroka, V., Gunasekaran, M. Combination of rockfill dam reinforced concrete face and seepage control wall in the foundation: stress-strain state. *Construction of Unique Buildings and Structures*. 2022. 99. 9902. DOI: 10.4123/CUBS.99.2
7. Lyapichev, Yu.P. Static and dynamic analyses of the heightening of concrete face gravel dam Limon. (Peru). *Structural Mechanics of Engineering Constructions and Buildings*. 2019. 15 (2). Pp. 158–168.
8. Shen, T., Li, G.Y., Li, Y., Li, J., Feng, Y.L. Numerical analysis of joint types between toe slab and foundation of CFRD in alluvial deposit layer. *Chinese Journal of Rock Mechanics and Engineering*. 2005. 24. Pp. 2588–2592. DOI: 10.3321/j.issn:1000-6915.2005.14.030
9. Gan, L., Shen, Z.Z., Xu, L.Q. Long-term deformation analysis of the Jiudianxia concrete-faced rockfill dam. *Arabian Journal for Science and Engineering*. 2012. 39 (3). Pp. 1589–1598. DOI: 10.1007/s13369-013-0788-6
10. Sun, D.W., Wang, K.P., Yao, H.Q. 3D Finite Element Analysis on ChaHanWuSu CFRD Built on Thick Alluvium Deposits. *Advanced Materials Research*. 2011. 243–249. Pp. 4482–4487. DOI: 10.4028/www.scientific.net/AMR.243-249.4482
11. Wen, L., Chai, J., Xu, Z., Qin, Y., Li, Y. Monitoring and numerical analysis of behaviour of Miaojiaba concrete-face rockfill dam built on river gravel foundation in China. *Computers and Geotechnics*. 2017. 85. Pp. 230–248. DOI: 10.1016/j.compgeo.2016.12.018
12. Haselsteiner, R., Balat, V., Ersoy, B. The Optimization of the Design of a Concrete Faced Rockfill Dam by the Application of Sand-Gravel Fill Zones. *Bundesanstalt für Wasserbau*. 2011. Pp. 669–676.
13. Haselsteiner, R., Kaytan, E., Pamuk, R., Ceri, V. Seepage control design of the Arkun Dam in Turkey. *International Journal on Hydropower and Dams*. 2012. 19 (1). Pp. 90–95.
14. Sun, D., Deng, H., Tian, B., Li, N. Deformation and stress analysis of Dahe CFRD built on thick alluvium deposits. *Chinese Journal of Geotechnical Engineering*. 2008. 30 (3). Pp. 434–439.
15. Sainov, M.P., Soroka, V.B. Enhancement of a seepage control facility of an earth-filled dam that has a concrete face and a cutoff wall. *Stroitel'stvo: nauka i obrazovanie [Construction: Science and Education]*. 2022. 12(1). 2. DOI: 10.22227/2305-5502.2022.1.2
16. Materon, B., Resende, F. Construction Innovations for the Itapebi CFRD. *International Journal on Hydropower & Dams*. 2001. 8(5). Pp. 66–70.
17. Zhang, G., Zhang, J.-M. Modeling of low-cement extruded curb of concrete-faced rockfill dam. *Canadian Geotechnical Journal*. 2011. 48 (1). Pp. 89–97.
18. Cheng, P., De-fa, G.U.O., Qing, W. Application of extrusion-sidewall technology to the project of rock fill dam with face slab. 2008. Pp. 201–203.
19. Pinto, N.L.D.S. Questions to ponder on designing very high CFRDs. *International Journal on Hydropower and Dams*. 2001. 8 (5). Pp. 61–65.

20. Mirghasemi, A.A., Pakzad, M., Shadravan, B. The world's largest cutoff wall at Karkheh dam. *International Journal on Hydropower and Dams*. 2005. 12 (2). Pp. 2–6.
21. Faridmehr, I., Yazdanipour, M.R., Jokar, M.J., Ozbakkaloglu, T. Construction and Monitoring of Cement/Bentonite Cutoff Walls: Case Study of Karkheh Dam, Iran. *Studia Geotechnica et Mechanica*. 2019. (July). Pp. 1–16. DOI: 10.2478/sgem-2019-0019
22. Grishin, V.A., Deryugin, L.M. Experience in the use of bentonite-cement concrete for repairing the core of the earthfill dam of Kureiskaya HPP. *Power Technology and Engineering*. 2006. 40 (2). Pp. 90–95.
23. Arici, Y. Investigation of the cracking of CFRD. face plates. *Computers and Geotechnics*. 2011. 38 (7). Pp. 905–916. DOI: 10.1016/j.compgeo.2011.06.004
24. Sainov, M.P. Strength of ultra-high rockfill dam concrete face. *Magazine of Civil Engineering*. 2021. 101 (1). 10113. DOI: 10.18720/MCE.101.13
25. Rasskazov, L.N., Radzinskii, A.V., Sainov, M.P. Strength and Deformability of Clay-Cement Concrete in a Complex Stress State. *Power Technology and Engineering*. 2015. 48(5) Pp. 361-365. DOI: 10.1007/s10749-015-0534-1
26. Razavi S.-K., Hajjalilue-Bonab M., Pak A. Design of a Plastic Concrete Cutoff Wall as a Remediation Plan for an Earth-Fill Dam Subjected to an Internal Erosion. *International Journal of Geomechanics*. 2021. 21(5): 04021061. DOI: 10.1061/(ASCE)GM.1943-5622.000199

Information about authors

Mikhail Sainov, Doctor of Technical Sciences

ORCID: <https://orcid.org/0000-0003-1139-3164>

E-mail: mp_sainov@mail.ru

Received 13.02.2023. Approved after reviewing 01.12.2023. Accepted 11.12.2023.



Research article

UDC 691.3:691.542:621.039.538:620.1

DOI: 10.34910/MCE.124.3



Radiation changes in hardened Portland cement paste under the influence of gamma radiation

A.V. Denisov 

Moscow State University of Civil Engineering (National Research University), Moscow, Russian Federation

 den-al-v@inbox.ru

Keywords: Portland cement, hardened cement paste, gamma radiation, influence of heating, radiation changes, radiation damage, thermal changes, linear dimensions, strength, forecasting

Abstract. The possibility of using materials in radiation protection shields when designing new and extending the service life of existing nuclear energy facilities requires knowledge or the ability to predict their radiation changes. The studies were carried out due to the lack of data sufficient to predict radiation changes in hardened Portland cement paste (HPCP) and concrete under the influence of gamma radiation when used as radiation shield materials for nuclear energy facilities. The research is based on published data on the effect of gamma radiation on concrete at irradiation temperatures of 20–30 °C and on HPCP at 70–375 °C. The author carried out computational and analytical studies to assess and establish the possibility of predicting radiation changes in HPCP under the influence of gamma radiation. The studies were conducted using the previously developed and tested method of analytical determination of radiation changes in concretes according to data on changes in their components. The formulas used in this method made it possible to determine (restore) the radiation changes of the HPCP from experimental data on radiation changes in concretes and aggregates. According to the available results of concrete irradiation, changes in linear dimensions and strength during compression of HPCP under the action of only gamma radiation were calculated (restored). The dependences of radiation changes in HPCP on the magnitude of the absorbed dose in the range from $3.8 \cdot 10^4$ to $4.7 \cdot 10^8$ Gy after irradiation at 20–30 °C were established. According to the available data on the irradiation of HPCP with gamma radiation at temperatures from 70 °C to 375 °C, the effect of the irradiation temperature on radiation changes in the HPCP was revealed. Mathematical expressions that approximate the established dependencies are selected. On the basis of the obtained mathematical expressions, radiation changes in the linear dimensions and strength of HPCP for compression, caused only by the action of gamma radiation, after irradiation to the values of absorbed doses from $3 \cdot 10^4$ Gy to $1 \cdot 10^{10}$ Gy were calculated. The calculations of radiation-thermal changes in the linear dimensions and strength of HPCP under the action of gamma radiation and heating after irradiation to the values of absorbed doses from $3 \cdot 10^4$ Gy to $1 \cdot 10^{10}$ Gy and the accompanying heating at temperatures from 20 °C to 500 °C were estimated.

Citation: Denisov, A.V. Radiation changes in hardened Portland cement paste under the influence of gamma radiation. Magazine of Civil Engineering. 2023. 124(8). Article no. 12403. DOI: 10.34910/MCE.124.3

1. Introduction

Facilities with various nuclear installations provide sources of ionizing radiation that can cause radiation changes in concrete building structures and radiation protection. The most important are radiation deformations (changes in linear dimensions (or dimensions) and volume) and strength.

The most significant radiation changes in concretes are caused by neutron radiation, so the effect of neutrons on concretes and their components is the most studied and described in the most detail in the

research works [1–12]. There are methods of analytical determination (calculation) of radiation and thermal changes in concretes and their components described in the research works [9, 13–15]:

- concretes according to data on radiation and thermal changes in their components (aggregates and hardened cement paste);
- aggregates according to data on radiation and thermal changes in crystals of their constituent minerals;
- minerals under the action of neutrons according to data on fluence and neutron spectrum, irradiation temperature;
- hardened Portland cement paste (HPCP) under the action of neutrons according to data on fluence and neutron spectrum, irradiation temperature.

The available methods of analytical determination are based on a number of simplifications considering that microstructural stresses due to cracking in concretes completely relax, and in aggregates are reset to the value of tensile strength, therefore they have a fairly simple, convenient for analysis and use type. However, despite the simplifications, the possibility of practical use of these methods is shown experimentally.

Work is also being carried out on numerical modeling of the processes of radiation changes, crack formation, creep and plasticity of concretes and their components, described, for example, in the research works [16–22]. Numerical methods more strictly take into account the processes occurring in concretes and their components, but are associated with the use of a large number of parameters, not all of which can be determined accurately enough. In this regard, these methods do not give more accurate results than the methods described in the research work [9, 13–15].

The effect of gamma radiation on concretes and their components is not studied well, though the volumes of concrete exposed to gamma radiation are more significant than the volumes exposed to neutrons. Only a few data are available on specific concretes and mortars [1, 2, 7, 10–12, 23–38] indicating the presence of radiation changes after exposure to gamma radiation. Moreover, some authors (for example, [35, 36] associate changes in concrete after exposure to gamma radiation by the effect of heating in the process of irradiation. Although there is evidence, for example, [1, 2, 25], indicating a change in the linear dimensions and properties of concretes after irradiation at temperatures of 20–30 °C.

Radiation changes in concretes under the influence of gamma radiation can be determined by the mentioned above method of analytical determination of radiation and thermal changes in concretes from data on radiation and thermal changes in their components (aggregates and hardened cement paste). The use of this method is permissible, since the cause of the changes does not matter, since the method has been tested both when exposed to neutrons and when exposed to heating. However, this requires data on radiation changes in aggregates and HPCP. To do this, it must be possible to predict radiation changes in aggregates and HPCP under the influence of gamma radiation.

Evaluation and substantiation of forecasting radiation changes in concrete aggregates under the influence of gamma radiation at different absorbed doses and irradiation temperatures were performed in the research work [39].

For HPCP, it is not possible to predict its radiation changes. There are limited data [27, 29, 31–36, 38] on the change in linear dimensions, structure, mass, strength after irradiation with small doses of gamma radiation (up to $5 \cdot 10^7$ Gy mainly at elevated temperatures (from 70 to 375 °C). Moreover, changes in HPCP after irradiation with gamma radiation, as well as concretes, are associated mainly with the effect of heating accompanying irradiation. However, taking into account the results of the study of concrete after irradiation at 20–30 °C, gamma radiation causes a decrease in the dimensions (shrinkage) of HPCP, as there is a decrease in the dimensions of concrete. In this regard, further research is needed.

In general, the available experimental data do not allow to predict radiation deformations and changes in strength under the influence of gamma radiation for concretes of any composition and at higher absorbed doses. In this regard, the purpose of this research work is to establish, on the basis of existing experimental data, radiation changes in HPCP under the influence of gamma radiation and to establish the possibility of predicting them in a wide range of absorbed doses and temperatures of irradiation. Achieving this goal will make it possible to analytically determine the radiation changes in concretes under the influence of gamma radiation.

To achieve this goal, the following tasks were solved:

- Development of methods of computational and analytical studies;

- Selection and analysis of available published data on radiation changes in concretes and their components under the influence of gamma radiation, which can be used to perform computational studies;
- Establishment on the basis of available experimental data obtained on the basis of computational and analytical studies of radiation changes in HPCP under the influence of gamma radiation and their dependencies on the absorbed dose, temperature and possible other factors. Selection of mathematical expressions that approximate established dependencies.

2. Methods

The introduction showed that the available publications provided limited data on radiative changes in the linear dimensions and strength of HPCP under the influence of gamma radiation and mainly at elevated temperatures. However, there are data on radiation changes in concrete after irradiation with gamma radiation at 20–30 °C in a relatively wide range of absorbed doses. In this regard, the values of radiation changes in HPCP under the influence of gamma radiation alone and their dependence on the absorbed dose were determined by calculation from the available experimental data on the effect of gamma radiation on concretes at 20–30 °C. To do this, the method of analytical determination of radiation changes in concretes was used according to data on changes in their components. The formulas used in this method make it possible to reconstruct the radiation changes of the HPCP from the data on radiation changes in concretes and aggregates.

When calculating radiation changes in linear dimensions (deformations), the following formulas of the method of analytical determination of radiation deformations of concretes based on data on radiation deformations of their components (HPCP, fine aggregate, coarse aggregate), described in the research works [9, 13, 15], were used, given with a slight error in a more convenient form:

$$\frac{\Delta V_{CM}}{V_{CM}} = \frac{\Delta V_{FA}}{V_{FA}} \left(C_{com}^{FA} \right)^{\frac{1}{3}} + \left[1 - \left(C_{com}^{FA} \right)^{\frac{1}{3}} \right] \frac{\Delta V_{CP}}{V_{CP}}, \quad (1)$$

$$\frac{\Delta V_C}{V_C} = \frac{\Delta V_{CA}}{V_{CA}} \left(C_{com}^{CA} \right)^{\frac{1}{3}} + \left[1 - \left(C_{com}^{CA} \right)^{\frac{1}{3}} \right] \frac{\Delta V_{CM}}{V_{CM}}, \quad (2)$$

where $\frac{\Delta V_{CM}}{V_{CM}}$ and $\frac{\Delta V_C}{V_C}$ are relative changes in the volume of mortar and volume of concrete, respectively, %; $\frac{\Delta V_{FA}}{V_{FA}}$, $\frac{\Delta V_{CA}}{V_{CA}}$ and $\frac{\Delta V_{CP}}{V_{CP}}$ show the radiation changes in the volume of fine aggregate, coarse aggregate and HPCP in the composition of concrete, respectively, %; C_{com}^{FA} and C_{com}^{CA} show the degree of compression of fine aggregate in mortar of concrete and coarse aggregate in concrete, determined by the formulas:

$$C_{com}^{FA} = \frac{V_{FA}}{V_{CA+FA}^{com} - V_{CA}}, \quad (3)$$

$$C_{com}^{CA} = \frac{V_{CA}}{V_{CA}^{com}}, \quad (4)$$

where V_{FA} and V_{CA} show the relative volume content of fine aggregate and coarse aggregate in concrete, respectively (in relative units); V_{CA+FA}^{com} is the maximum relative volume content of the mixture of fine aggregate and coarse aggregate in the case of their maximum compacted state (without layers of HPCP between particles) (in relative units), which is 0.77–0.93. By [9] $V_{CA+FA}^{com} = 0.86$ can be taken; V_{CA}^{com} is the maximum relative volume content of coarse aggregate in the case of its maximum compacted state (without layers of mortar between particles) (in relative units), which is 0.52–0.74. According to [9], we can take $V_{CA}^{com} = 0.63$.

On the basis of formulas (1) and (2), taking into account that the relative change in volume $\frac{\Delta V}{V}$ and linear dimensions $\frac{\Delta \ell}{\ell}$ are related by the ratio $\frac{\Delta V}{V} \approx 3 \frac{\Delta \ell}{\ell}$, according to the existing data of the research works [1, 2, 25] on radiation changes in the linear dimensions of Portland cement concretes under the influence of gamma radiation, changes in the dimensions of the mortar (on the 1st stage), and then the HPCP were calculated sequentially according to the formulas:

$$\frac{\Delta \ell_{CM}}{\ell_{CM}} = \frac{\frac{\Delta \ell_C}{\ell_C} - \frac{\Delta \ell_{CA}}{\ell_{CA}} \left(C_{com}^{CA} \right)^{\frac{1}{3}}}{\left[1 - \left(C_{com}^{CA} \right)^{\frac{1}{3}} \right]}, \quad (5)$$

$$\frac{\Delta \ell_{CP}}{\ell_{CP}} = \frac{\frac{\Delta \ell_{CM}}{\ell_{CM}} - \frac{\Delta \ell_{FA}}{\ell_{FA}} \left(C_{com}^{FA} \right)^{\frac{1}{3}}}{\left[1 - \left(C_{com}^{FA} \right)^{\frac{1}{3}} \right]}, \quad (6)$$

when calculating radiation changes in the strength of HPCP in the composition of concrete in the form of relative residual strength, the following formulas were used for the method of analytical determination of radiation changes in the strength of concretes and mortars according to data on radiation deformations and changes in the strength of their components (HPCP, fine aggregate, coarse aggregate), described in the research works [9, 15], given in a more convenient form:

$$\frac{R_C}{R_{C0}} = \frac{R_{CM}}{R_{CM0}} \left(\frac{R_{CA}}{R_{CA0}} \right)^{0.29} \left\{ 1 + \left[A_C \left(\frac{\Delta V_C}{V_C} \right)_{cr} \right]^2 \right\}^{-1}, \quad (7)$$

$$\frac{R_{CM}}{R_{CM0}} = \frac{R_{CP}}{R_{CP0}} \left(\frac{R_{FA}}{R_{FA0}} \right)^{0.29} \left\{ 1 + \left[A_C \left(\frac{\Delta V_{CM}}{V_{CM}} \right)_{cr} \right]^2 \right\}^{-1}, \quad (8)$$

where $\frac{R_C}{R_{C0}}$, $\frac{R_{CM}}{R_{CM0}}$, $\frac{R_{CA}}{R_{CA0}}$, $\frac{R_{CP}}{R_{CP0}}$, $\frac{R_{FA}}{R_{FA0}}$ is a relative after exposure to radiation residual strength of concrete, mortar, coarse aggregate, HPCP, fine aggregate, accordingly, unit fraction; A_C is parameter equal to:

$A_C = 0.31 \%^{-1}$ – for compressive strength;

$A_C = 0.53 \%^{-1}$ – for tensile strength;

$\left(\frac{\Delta V_C}{V_C} \right)_{cr}$ and $\left(\frac{\Delta V_{CM}}{V_{CM}} \right)_{cr}$ – radiation change in the volume of concrete and mortar due to the

formation of microcracks, respectively, in %, determined by the formulas:

$$\left(\frac{\Delta V_C}{V_C} \right)_{cr} = \frac{\Delta V_C}{V_C} - \frac{\Delta V_{CA}}{V_{CA}} V_{CA} - \frac{\Delta V_{CM}}{V_{CM}} (1 - V_{CA}), \quad (9)$$

$$\left(\frac{\Delta V_{CM}}{V_{CM}} \right)_{cr} = \frac{\Delta V_{CM}}{V_{CM}} - \frac{\Delta V_{FA}}{V_{FA}} \frac{V_{FA}}{1 - V_{CA}} - \frac{\Delta V_{CP}}{V_{CP}} \left(1 - \frac{V_{FA}}{1 - V_{CA}} \right), \quad (10)$$

Based on existing experimental data in the work after determination by formulas (5) and (6) values $\frac{\Delta l_{CM}}{l_{CM}}$ and $\frac{\Delta l_{CP}}{l_{CP}}$ based on values $\frac{\Delta V_{CM}}{V_{CM}} = 3 \frac{\Delta l_{CM}}{l_{CM}}$ and $\frac{\Delta V_{CP}}{V_{CP}} = 3 \frac{\Delta l_{CP}}{l_{CP}}$ using the formulas (9) and (10) calculated the values $\left(\frac{\Delta V_C}{V_C}\right)_{cr}$ and $\left(\frac{\Delta V_{CM}}{V_{CM}}\right)_{cr}$. After that, on the basis of the expressions (7) and (8) $\frac{R_{CM}}{R_{CM0}}$ and $\frac{R_{CP}}{R_{CP0}}$ were calculated according to the formulas:

$$\frac{R_{CM}}{R_{CM0}} = \frac{R_C}{R_{C0}} \left(\frac{R_{CA}}{R_{CA0}}\right)^{-0.29} \left\{ 1 + \left[A_C \left(\frac{\Delta V_C}{V_C}\right)_{cr} \right]^2 \right\}, \quad (11)$$

$$\frac{R_{CP}}{R_{CP0}} = \frac{R_{CM}}{R_{CM0}} \left(\frac{R_{FA}}{R_{FA0}}\right)^{-0.29} \left\{ 1 + \left[A_C \left(\frac{\Delta V_{CM}}{V_{CM}}\right)_{cr} \right]^2 \right\}, \quad (12)$$

The possibility of determining changes in the compressive strength of HPCP under the influence of gamma radiation was also considered from data on volume change. At the same time, the formula presented in the research works [9, 14] after irradiation in a nuclear reactor and heating was used:

$$\frac{R_{CP}}{R_{CP0}} = \left(A_{CP} + B_{CP} \frac{\Delta V_{CP}}{V_{CP}} \right)^{-1} \quad (13)$$

where A_{CP} and B_{CP} are parameters which values are [9, 14]: $A_{CP} = 0.724$; $B_{CP} = -0.0566 \%^{-1}$ for HPCP of "young" age (1 – 3 months of natural hardening); $A_{CP} = 1.00$; $B_{CP} = -0.23 \%^{-1}$ – for HPCP of "mature" age (more than 8 months of natural hardening or after thermo-humid treatment of a lower age).

Although it should be borne in mind that the expression (13) does not take into account the possible increase in the strength of HPCP when exposed to gamma radiation due to a decrease in the porosity of HPCP due to carbonization, shown in the research works [26, 29, 32]. In this regard, when using formula (13), radiation changes may be somewhat overestimated. Therefore, the formula can allow us to evaluate the maximum possible effect of gamma radiation.

To establish, on the basis of computational and analytical studies, the magnitude of radiation changes in HPCP under the influence of gamma radiation and their dependence on the absorbed dose were used experimental data from the research work [1, 2, 25] on studies of the effect of gamma radiation on concretes. Radiation changes in aggregates (fine aggregate and coarse aggregate) were taken on the basis of the calculated data of the research work [39].

In the research work of McDowell [25], samples with a diameter of 105 mm, a height of 305 mm of concrete made of Portland cement "Sulfacrete", coarse aggregate with a linear dimensions of approximately 20 mm of limestone and quartz fine aggregate were examined. In the manufacture of samples, a water-cement ratio of $W/C = 0.47$ and the ratio of aggregate consumption (coarse aggregate CA + fine aggregate FA) to the consumption of Portland cement PC $(CA+FA)/PC = 4.5$ were used. The plasticizer "Plastocrete" was injected in an amount of 0.005 by weight of cement. After aging for 24 hours in wet conditions, the samples were covered with POP (plaster of Paris), sealed in copper foil 0.127 mm thick and stored for a year until the tests. In this regard, samples of "mature" age were irradiated. Judging by the data of the granulometric composition of the aggregates based on the results of sieving, the proportion of coarse aggregate and fine aggregate consumption in the aggregate mixture was $CA/(CA + FA) = 0.61$ and $FA/(CA + FA) = 0.39$. The technological characteristics of the concrete mixture and concrete were determined on the basis of the above mentioned proportions of the components of the concrete mixture. At the same time, the density values of Portland cement, fine aggregate, coarse aggregate and concrete mixture took $\gamma_{PC} = 3100 \text{ Kg/m}^3$, $\gamma_{FA} = \gamma_{CA} = 2600 \text{ Kg/m}^3$, $\gamma_{MC} = 2400 \text{ Kg/m}^3$, as the most likely values. Portland cement consumption PC , coarse aggregate CA , fine aggregate FA and water W , as well as the volumetric content of the aggregates were taken to be equal to: $PC = 402 \text{ Kg/m}^3$,

$CA = 1105 \text{ Kg/m}^3$, $FA = 705 \text{ Kg/m}^3$, $W = 188 \text{ Kg/m}^3$, $V_{CA} = 0.42$, $V_{FA} = 0.27$. Calculated by formulas [3] and [4] the degree of compression of aggregates with $V_{CA+FA}^{com} = 0.86$, $V_{CA}^{com} = 0.63$ was:

$$C_{com}^S = \frac{V_{FA}}{V_{CA+FA}^{com} - V_{CA}} = \frac{0.27}{0.86 - 0.42} = 0.614;$$

$$C_{com}^{CA} = \frac{V_{CA}}{V_{CA}^{com}} = \frac{0.42}{0.63} = 0.667.$$

Irradiation of samples was carried out at $30 \text{ }^\circ\text{C}$ on a gamma device with a Co^{60} emitting gamma quanta with energy $E_\gamma = 1.17$ and 1.33 MeV at a dose rate $P_\gamma = 11.4 \cdot 10^3 \text{ rad/h} = 114 \text{ Gy/h}$ for $t = 10\text{-}314$ days. The maximum absorbed dose of gamma radiation was $D_G = P_\gamma t = 114 \cdot 314 \cdot 24 = 8.6 \cdot 10^5 \text{ Gy}$. We studied the change in the linear dimensions of samples as a result of creep under load $10 \text{ H/mm}^2 = 10 \text{ MPa}$ and shrinkage. Creep and shrinkage deformations were measured during irradiation (when processes took place and under the action of gamma radiation and with natural hardening and drying in time) and without irradiation (when the processes took place only due to natural hardening and drying in time).

The advantage of the results of the research work [25] is the absence of significant heating during irradiation and the possibility of taking into account natural shrinkage. This made it possible to obtain in the present work the effect of the influence of gamma radiation according to the formula:

$$\left(\frac{\Delta l_C}{l_C} \right)_G = \left(\frac{\Delta l_C}{l_C} \right)_R - \left(\frac{\Delta l_C}{l_C} \right)_{WR}, \quad (14)$$

where $\left(\frac{\Delta l_C}{l_C} \right)_G$, $\left(\frac{\Delta l_C}{l_C} \right)_R$ and $\left(\frac{\Delta l_C}{l_C} \right)_{WR}$ is reduction of the dimensions (deformation of shrinkage) of concrete under the action of gamma radiation only, with- and without irradiation, respectively.

The disadvantage is the relatively low values of absorbed doses.

The results obtained in the work [25] showing the dependence of the shrinkage of the studied concrete on time with irradiation and without irradiation were used in this work and are given in Fig. 1. In this figure and beyond, a decrease in dimensions (shrinkage) was not seen as a change with a minus sign, but as a decrease without specifying a sign, given that the decrease implies a negative change. This was convenient for automatically constructing trend lines, like approximation lines, on charts.

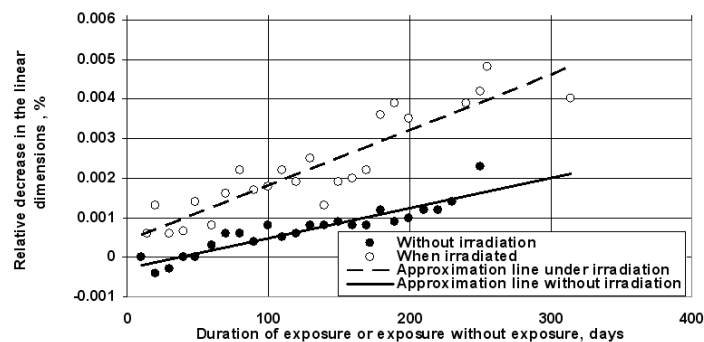


Figure 1. Dependence of the relative decrease in the linear dimensions of concrete (shrinkage) when irradiated with gamma radiation at an absorbed dose rate of 114 Gy/h at $30 \text{ }^\circ\text{C}$ and exposure without irradiation from the time of irradiation and exposure without irradiation according to [25].

In the research works [1, 2], samples in the form of disks with a diameter of 44.5 mm with a thickness of 12.7 mm of two types of concretes made on Portland cement with sandstone aggregates with a density of 2625 Kg/m^3 and with a limestone aggregate with a density of 2550 Kg/m^3 were examined. The ratio between the mass of Portland cement PC , coarse aggregate approximately up to 10 mm CA , fine aggregate FA and water W was the following:

$PC:CA:FA:W = 1:1.55:1.15:0.36$ – for concrete from limestone coarse aggregate and sandstone fine aggregate (hereinafter concrete from sandstone and limestone);

$PC:CA:FA:W = 1:1.77:0.93:0.36$ – for concrete from limestone coarse aggregate and limestone fine aggregate (hereinafter concrete from limestone).

The density of concrete from sandstone was $\gamma_C = 2310 \text{ Kg/m}^3$. The density of concrete from limestone was 2380 Kg/m^3 .

Based on the above-mentioned proportions and density of aggregates with the most likely density of the concrete mixture $\gamma_{MC} = \gamma_C + 100 \text{ Kg/m}^3$, the consumption of cement, aggregates and water, as well as the volume content of aggregates, were taken to be equal:

- $PC = 594 \text{ Kg/m}^3$, $CA = 921 \text{ Kg/m}^3$, $FA = 683 \text{ Kg/m}^3$, $W = 214 \text{ Kg/m}^3$, $V_{CA} = 0.361$, $V_{FA} = 0.260$ in concrete from limestone and sandstone;
- $PC = 611 \text{ Kg/m}^3$, $CA = 1081 \text{ Kg/m}^3$, $FA = 571 \text{ Kg/m}^3$, $W = 220 \text{ Kg/m}^3$, $V_{CA} = 0.424$, $V_{FA} = 0.224$ in concrete from limestone;

Calculated from formulas (3) and (4), the degree of compaction of aggregates at $V_{CA+FA}^{com} = 0.86$, $V_{CA}^{com} = 0.63$ was:

- $C_{com}^{FA} = \frac{V_{FA}}{V_{CA+FA}^{com} - V_{CA}} = \frac{0.26}{0.86 - 0.351} = 0.511$; $C_{com}^{CR} = \frac{V_{CA}}{V_{CA}^{com}} = \frac{0.361}{0.63} = 0.573$ – in concrete from limestone and sandstone;
- $C_{com}^{FA} = \frac{V_{FA}}{V_{CA+FA}^{com} - V_{CA}} = \frac{0.224}{0.86 - 0.424} = 0.514$; $C_{com}^{CA} = \frac{V_{CA}}{V_{CA}^{com}} = \frac{0.424}{0.63} = 0.673$ – in concrete from limestone.

Irradiation of concrete samples with gamma radiation was carried out in a pool with radioactive substances (apparently, in the storage pool of spent fuel elements of a nuclear reactor) at $20 \text{ }^\circ\text{C}$ at an absorbed dose rate of $5 \cdot 10^4 \text{ Gy/h} = 1.4 \cdot 10^1 \text{ Gy/s}$. The maximum absorbed dose was $4.7 \cdot 10^8 \text{ Gy}$. By the time of irradiation, the age of the samples was at least 3 months after manufacturing and storing them under normal conditions, so the material of "young" age was actually studied.

The results obtained in the research works [1, 2] of the change in linear dimensions, mass and strength of concretes after irradiation with gamma radiation used in this work are given in Table 1.

Table 1. Results* of irradiation of concretes with gamma radiation in the research works [1, 2].

Name of concrete by aggregates	Absorbed dose of gamma radiation, Gy	Relative linear dimension changes, % of the border average	Relative changes in mass, %	Relative residual strength, fractions of a unit
Concrete from limestone and sandstone	$2.27 \cdot 10^8$	-0.17 ... +0.076 -0.005±0.066	<u>-0.77...-1.01</u> -0.903±0.072	-
	$4.7 \cdot 10^8$	<u>-0.21 ... +0.04</u> -0.021±0.082	<u>-1.74...-2.14</u> -1.91±0.14	0.91±0.23
Concrete from limestone	$2.27 \cdot 10^8$	<u>-0.15 ... +0.04</u> -0.031±0.057	<u>-0.95...-1.70</u> -1.15±0.24	1.0±0.09
	$4.7 \cdot 10^8$	<u>-0.21 ... +0.04</u> -0.061±0.071	<u>-1.42...-3.38</u> -2.36±0.67	0.93±0.05

*The average quadratic deviations calculated by the authors of this research work

The advantage of the results of the research work [1, 2] is the higher values of the absorbed doses of gamma radiation than in the research work [25]. The disadvantage of these results is the significant variation in the magnitudes of the shrinkage deformations of individual samples associated with the peculiarities of using samples in the form of disks, as well as the lack of measurement results without irradiation. However, the average changes in the linear dimensions of concrete samples in the research

works [1, 2] are approximately proportional to the changes in mass, which have smaller spreads and are more reliable. In addition, since shrinkage changes in the dimensions of concretes are caused by the release of water, accompanied by a decrease in mass, the deformation of shrinkage can also be estimated by the change in mass based on the relationship between mass reduction and shrinkage after irradiation in reactors and heating, shown in the research work [9].

In this regard, the assessment of the change in the linear dimensions of HPCP under the influence of gamma radiation was also carried out according to the data on the decrease in the mass of concrete.

By reducing the mass of concrete, based on the density of concrete and the consumption of aggregates, the relative decrease in the mass of HPCP was determined by the formula:

$$\frac{\Delta M_{CP}}{M_{CP}} = \frac{\Delta M_C}{M_C} \cdot \frac{\gamma_C}{\gamma_C - CA - FA} \quad (15)$$

where $\frac{\Delta M_C}{M_C}$ and $\frac{\Delta M_{CP}}{M_{CP}}$ are relative reduction in the mass of concrete and HPCP; γ_C is concrete density, Kg/m³; CA and FA are consumption of coarse aggregate and fine aggregate, Kg/m³; $\gamma_C - CA - FA$ is value equal to the content of HPCP in concrete, Kg/m³.

Further, according to the magnitude of the decrease in the mass of HPCP according to the dependence shown in the research work [9], the change in volume was estimated, as well as decrease in the linear dimensions of the HPCP.

To do this, according to the ratio between the change in the volume and mass of the HPCP after irradiation in the reactors and heating, shown in the research work [9], the inverse relationship between the change in the mass and volume of the HPCP after these effects, presented in Fig. 2, was built and approximated.

According to the results of the approximation of the dependence of Fig. 2, the expression was used to determine the change in the linear dimensions of the HPCP by changing its mass:

$$\frac{\Delta \ell_{CP}}{\ell_{CP}} = \frac{1}{3} \cdot \frac{\Delta V_{CP}}{V_{CP}} = \frac{1}{3} \cdot 0.9304 \left(\frac{\Delta M_{CP}}{M_{CP}} \right)^{0.7282} \quad (16)$$

According to the formulas (9) – (12), on the basis of data on radiation changes in the dimensions of concrete, HPCP and aggregates under the influence of gamma radiation, as well as data on changes in the strength of concrete and aggregates, the values of radiation changes in the strength of HPCP were calculated (restored).

The effect of irradiation temperature on radiation changes in HPCP under the influence of gamma radiation was determined on the basis of data from the research works [35, 36] on irradiation of HPCP at 70–375 °C.

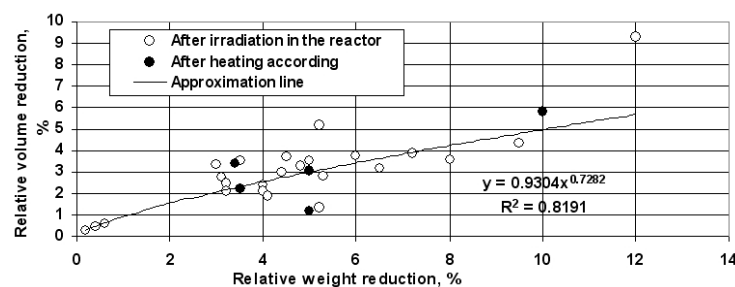


Figure 2. The relationship between the change in the mass and volume of the HPCP after irradiation in the reactor and after heating according to the data summarized in the research work [9].

3. Results and Discussion

The values obtained by formula (14) from the data of the research work [25] of the reduction in the linear dimensions of concrete only under the action of gamma radiation, as the difference between the change in dimensions during irradiation and without irradiation, are shown in Fig. 3 as a dependence on time and absorbed dose. It can be seen that with an increase in the irradiation time and the absorbed dose

of gamma radiation, the magnitude of the decrease in the volume of concrete increases and reaches 0.002–0.003 % after irradiation for 10 – 250 days before the absorbed doses $(0.38 – 6.8) \cdot 10^5$ Gy.

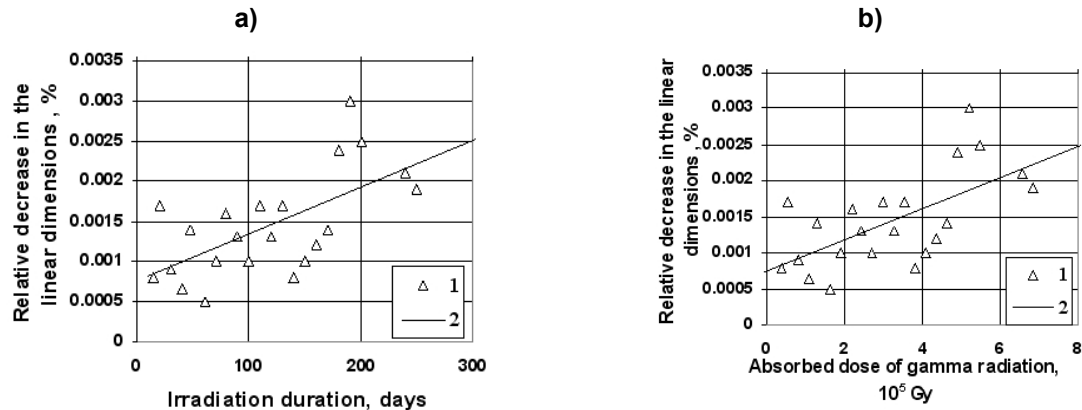


Figure 3. The dependence calculated from the data of the research work [25] on the irradiation time (a) and on the magnitude of the absorbed dose of gamma radiation (b) decrease in the linear dimensions of concrete under the action of gamma radiation, as the difference between the decrease in linear dimensions during irradiation and without irradiation.

1 – individual results; 2 – approximation line.

Calculated from the values of Fig. 3 according to the formulas (3) – (6) the values of the reduction in the linear dimensions of the HPCP under the action of gamma radiation and their dependence on the absorbed dose are shown in Fig. 4a. At the same time, in accordance with the calculated data of the research work [39], it was assumed that the radiation changes in the aggregates of concrete at the doses considered are zero, since the volume change is less than $6 \cdot 10^{-7}\%$, and the strength decreases by less than $1 \cdot 10^{-5}\%$. It can be seen that the degree of reduction in linear dimensions in the studied range of absorbed doses from $(0.38–1.6) \cdot 10^5$ to $(4.9–6.8) \cdot 10^5$ Gy is from 0.026–0.09 % to 0.1–0.16% and approximately linearly rises with an increase in the absorbed dose.

It was not possible to calculate the change in compressive strength using formulas (7) and (8) due to the lack of data on the change in the strength of concretes. In this regard, the change in the strength of HPCP was assessed according to the formula [13] with parameters for the material of "mature" age. The effect of reducing the porosity of HPCP due to carbonation, shown in the research works [26, 29, 32] in reserve was neglected. The calculated values of the relative residual strength of and their dependence on the absorbed dose are shown in Fig. 4b. It can be seen that in the studied range of absorbed doses $(0.38–1.6) \cdot 10^5$ to $(4.9–6.8) \cdot 10^5$ Gy, compressive strength decreases with an increase in the absorbed dose and the residual strength is from 0.94–0.98 to 0.9–0.935 from strength to irradiation.

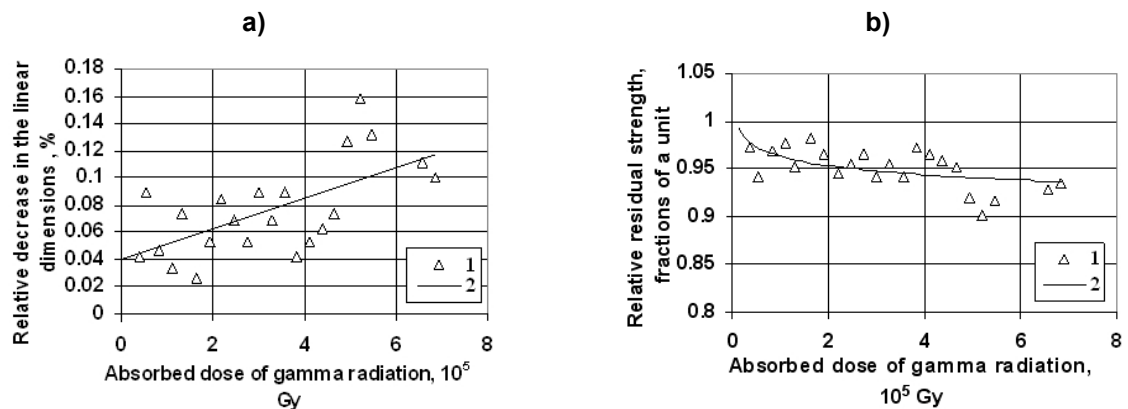


Figure 4. Calculated on the basis of the values shown in Fig. 3, the magnitudes of the linear dimensions reduction according to formulas (5, 6) (a) and the residual strength according to formula (13) (b) of HPCP under the action of gamma radiation as a function of the absorbed dose.

1 – individual results; 2 – approximation line.

When using these research works [1, 2], it is not possible to isolate the effect of irradiation alone, since there are no data on changes in concretes without irradiation. However, the absorbed doses of gamma radiation in the works [1, 2] are much higher than in the work [25]. In this regard, the contribution of natural changes in concrete in time is much lower and can be neglected.

The values of the reduction in the mass, linear dimensions and strength of HPCP under the action of gamma radiation calculated from these research works [1, 2] for concretes are shown in Table 2, as well as in Figure 5 as a dependence on the absorbed dose. At the same time, in accordance with the calculated data of the research work [39], it was assumed that the radiation changes in the aggregates of concrete at the considered doses are zero, since the volume change is less than $3 \cdot 10^{-4} \%$, and the strength decreases by less than $5 \cdot 10^{-3} \%$.

Table 2. Results of calculation of radiation changes* of HPCP according to the data of irradiation of concretes with gamma radiation at 30 °C in the research works [1, 2].

Name of concrete by aggregates	Absorbed dose of gamma radiation, Gy	Changes in the mass of HPCP, %	Relative changes in the dimensions of HPCP, %		Residual strength of HPCP, unit fraction	
			calculated from the change in the dimensions of concrete	calculated from the change in the mass of concrete	calculated from the change in the dimensions and strength of concrete	calculated from the change in the mass and strength of concrete
Concrete from limestone and sandstone	$2.27 \cdot 10^8$	-2.94 ± 0.23	-0.15 ± 1.94	-0.68 ± 0.11	-	-
	$4.7 \cdot 10^8$	-6.28 ± 0.46	-0.62 ± 2.11	-1.18 ± 0.15	1.01 ± 0.29	1.00 ± 0.24
Concrete from limestone	$2.27 \cdot 10^8$	-3.76 ± 0.78	-1.26 ± 2.31	-0.81 ± 0.23	1.10 ± 0.15	1.04 ± 0.10
	$4.7 \cdot 10^8$	-7.7 ± 2.2	-2.48 ± 2.88	-1.37 ± 0.45	1.28 ± 0.14	1.04 ± 0.07

*The average square deviations are given.

From Table 2 and Figure 5 it can be seen that under the influence of gamma radiation there is a decrease in the linear dimensions of the samples and mainly an increase in the strength of the HPCP. In the range of absorbed doses from $2.27 \cdot 10^8$ to $4.7 \cdot 10^8$ Gy, depending on the basis of calculations, there is a decrease in the linear dimensions of HPCP by 0.15–1.26 % to 0.62–2.48 %. At the same time, changes in HPCP obtained from data on changes in the linear dimensions of concretes have more significant standard deviations and variations of values than those obtained from changes in the mass of concrete, so they are less reliable statistically. However, changes in HPCP, obtained by changing the mass of concrete have a less reliable physical basis, since they are determined on the basis of the relationship of dimensional changes with changes in mass. At the same time, the average values obtained from the data on the two studied concretes, calculated from different data, are close to each other. This allows us to consider them sufficient to assess the radiation changes in HPCP under the conditions considered

The residual relative compressive strength increases from 1.04 – 1.1 to 1.0 – 1.28. The approximation line for the dependencies of changes on the absorbed dose has an approximately linear form, taking into account the fact that the change in linear dimensions and relative residual strength at the absorbed dose of zero are $\frac{\Delta V_{CP}}{V_{CP}} = 0$ and $\frac{R_{CP}}{R_{CP0}} = 1$.

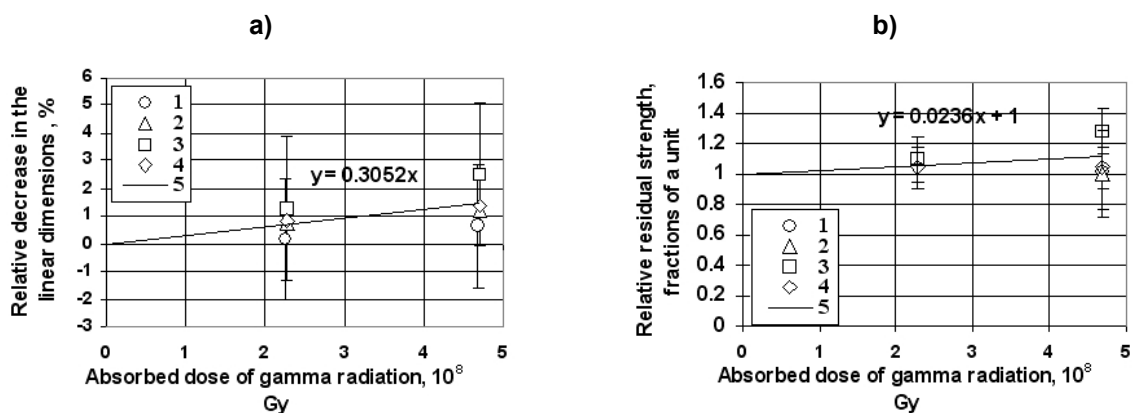


Figure 5. Calculated in Table 2 according to formulas (3) – (12) based on the data of the research works [1, 2] presented in Table 1, the magnitudes of the reduction in linear dimensions (a) and the compressive strength of HPCP under the action of gamma radiation as a dependence on the absorbed dose. 1 – reduce of the linear dimensions of concrete from limestone and sandstone; 2 – reduce of the mass of concrete from limestone and sandstone; 3 – reduce of the linear dimensions of concrete from limestone; 4 – reduce of the mass of concrete from limestone; 5 – approximation line.

Generalized for the values calculated from these research works [1, 2 and 25], the dependence of reducing the linear dimensions (shrinkage) of HPCP under the action of gamma radiation at 20–30 °C on the absorbed dose is shown in Fig. 6. It can be seen that the shrinkage of HPCP increases with an increase in the absorbed dose in the range from $3.8 \cdot 10^4$ to $4.7 \cdot 10^8$ Gy. Moreover, due to the absence of significant heating during irradiation, it can be considered that these changes occur only under the action of gamma radiation. Judging by the data [9], the effect of the composition, water-cement ratio, age of HPCP and the density of the flux of ionizing radiation on the shrinkage of HPCP under the action of ionizing radiation of the nuclear reactor is not observed. In this regard, the values of linear dimensions reduction calculated from the data of the research works [1, 2 and 25], where HPCP of different composition, W/C and age were used, irradiation was carried out at different rates of absorbed dose of gamma radiation can be considered as values of a single dependence on the absorbed dose. This dependence was approximated by the following expression:

$$\left(\frac{\Delta l_{CP}}{l_{CP}} \right)_G = a_G D_G^{b_G}, \quad (17)$$

where $\left(\frac{\Delta l_{CP}}{l_{CP}} \right)_G$ is a change in linear dimensions under the influence of gamma radiation, %; D_G is absorbed dose rate of gamma radiation; $a_G = -0.000894$, $b_G = 0.3497$ at D_G in Gy.

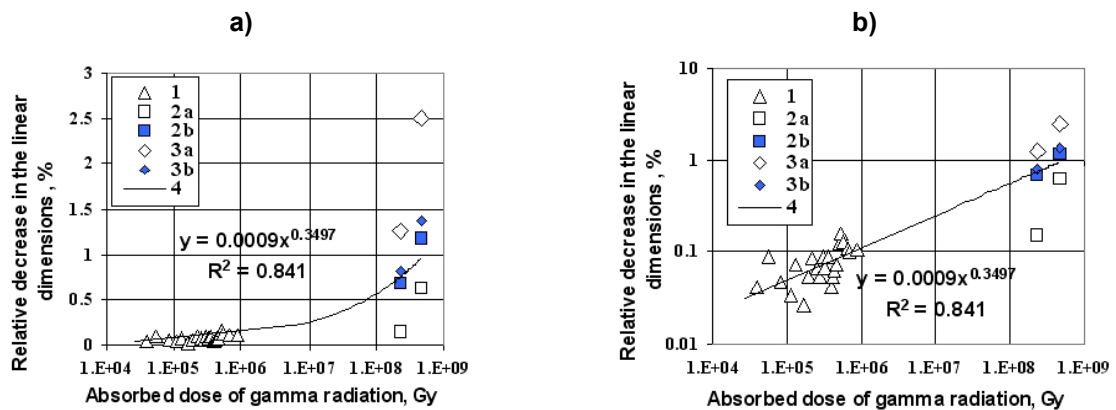


Figure 6. Generalized for the values calculated from these research works [1, 2, 25], the dependence of the reduction in linear dimensions (shrinkage) of HPCP under the action of gamma radiation at 20–30 °C on the absorbed dose in the semilogarithmic (a) logarithmic scale (b). 1 – from the data [25]; 2a – from the data [1, 2] on reducing the linear dimensions of concrete from limestone and sandstone; 2b – from the data [1, 2] on reducing the mass of concrete from limestone and sandstone; 3a – from the data [1, 2] on reducing the linear dimensions of concrete from limestone; 3b – from the data [1, 2] on reducing the mass of concrete from limestone; 4 – approximation line.

However, according to the results of irradiation with gamma radiation to absorbed doses of $1 \cdot 10^7$ – $5 \cdot 10^7$ Gy at temperatures from 70 to 375 °C in the research works [35, 36] it was noted that changes in HPCP under these conditions are mainly caused by the influence of heating accompanying irradiation. However, this conclusion was made on the basis of a comparison of the decrease in mass, and not the linear dimensions of HPCP after irradiation and heating without irradiation at irradiation temperatures and at sufficiently large spreads in results. In addition, the decrease in the mass of the studied HPCP after heating established in the research works [35, 36] exceeds all the data known to the authors at the same temperatures for unknown reasons. In addition, the relationship between the shrinkage of HPCP and the decrease in mass after irradiation differs significantly from the dependence shown in Fig. 2. This calls into question that the relationship between the established change in mass and linear dimensions is the same under irradiation and heating, and also calls into question the reliability of this inference based on changes in mass.

The addition of these research works [35, 36] after irradiation at temperatures from 70 to 375 °C to the dependence of Fig. 6 is shown in Fig. 7. It can be seen that the data of high-temperature irradiation, despite significant variations, mainly differ from the values of the approximation line obtained at 20–30 °C. It is most likely that this difference is due to the presence of additional changes under the influence of heating, since it is most likely that, as with neutron irradiation [9, 14], dimensional changes after irradiation can be represented as a sum of radiation and thermal changes and described by the formula:

$$\left(\frac{\Delta l_{CP}}{l_{CP}}\right)_{GT} = \left(\frac{\Delta l_{CP}}{l_{CP}}\right)_G + \left(\frac{\Delta l_{CP}}{l_{CP}}\right)_T, \quad (18)$$

where $\left(\frac{\Delta l_{CP}}{l_{CP}}\right)_{GT}$ is the total change in the dimensions of the HPCP after irradiation under the influence of gamma radiation and temperature; $\left(\frac{\Delta l_{CP}}{l_{CP}}\right)_G$, $\left(\frac{\Delta l_{CP}}{l_{CP}}\right)_T$ is changing the dimensions of HPCP after irradiation from exposure to gamma radiation only and from exposure to temperature only, respectively.

Since there are no data on changes in the linear dimensions of HPCP under the influence of heating in the research works [35, 36], it is not possible to determine purely radiation changes in the dimensions of HPCP under the influence of gamma radiation from these works. However, it is possible to use the data available in the research works [9, 40, 41] on the reduction in the dimensions of various HPCP of "mature" age after heating for a time commensurate with the time of irradiation, and compare them with the results of shrinkage after irradiation with gamma radiation at the same temperatures.

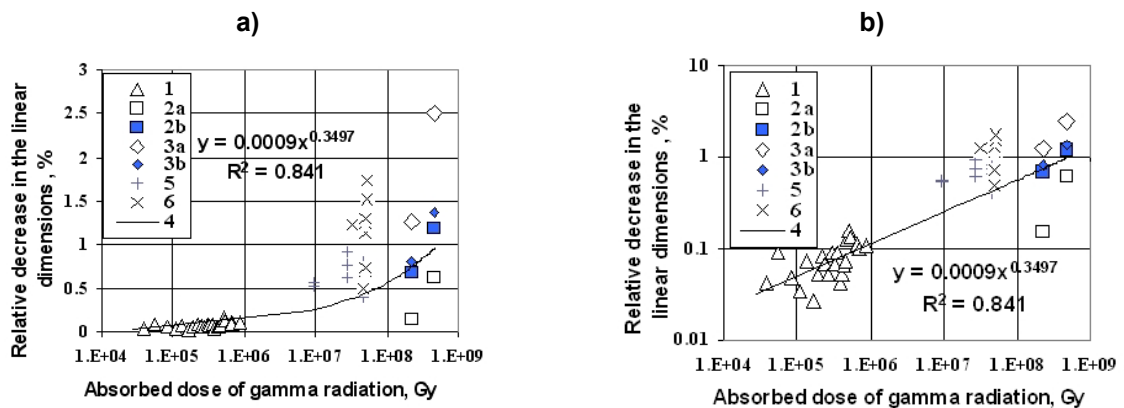


Figure 7. Generalized for the values calculated from the data of the research works [1, 2, 25], the dependence of reducing the linear dimensions (shrinkage) of HPCP under the action of gamma radiation at 20–30 °C on the absorbed dose with the addition of the research works [35, 36] after irradiation at temperatures from 70 to 375 °C at a semilogarithmic (a) logarithmic scale (b). 1 – from data [25]; Explanations of 1, 2a, 2b, 3a, 3b and 4 are given in Fig. 6; 5 – data of research works [35, 36], obtained at 70–120 °C; 6 – data of research works [35, 36], obtained at 260–375 °C.

A comparison of changes in the linear dimensions of HPCP after irradiation with gamma radiation at temperatures from 70 to 375 °C according to the data of the research works [35, 36] with changes in linear dimensions after heating without irradiation of various HPCP of "mature" age after heating for a time commensurate with the time of irradiation, according to the data of the research works [9, 40, 41] is shown in Fig. 8.

It can be seen that the changes in the linear dimensions of the HPCP studied in the research works [35, 36] mainly exceed the changes in the linear dimensions of various HPCP according to the data of the research works [9, 40, 41] after heating at the same temperatures during a commensurate heating time, although there are data spreads. This indicates that radiation changes under the influence of gamma radiation at temperatures higher than 30 °C occur as well. However, it can be seen that the differences between the data shown in the figure, and hence the contribution of radiation changes with increasing temperature decrease to about zero at a temperature of more than 550 °C.

This can be explained as follows. It is known that free and physically bound water is removed from the HPCP when heated in the range from 50 °C to 105 °C. Chemically bound water is removed in the range from 105 °C to 600 °C. After 600 °C, almost all water from HPCP is released. It is characteristic that after heating, the shrinkage of the HPCP according to [41] and the release of water according to the data [42] occurs most intensively in the initial heating period, and the contribution of gamma radiation is manifested mainly towards the end of irradiation, when the maximum absorbed dose to which the changes are tied is reached. In this case, the higher the irradiation temperature, the less water remains in the HPCP, which can be released under the influence of gamma radiation. In this regard, the rate of development of shrinkage of HPCP under the action of gamma radiation and shrinkage at a fixed absorbed dose decreases with an increase in the irradiation temperature.

To take into account the effect of temperature on radiation changes in the linear dimensions of HPCP under the influence of gamma radiation, it is possible to introduce a temperature influence coefficient K_T . For this, according to the data of the research works [35, 36], first, on the basis of Fig. 8, the radiation changes in the linear dimensions of the HPCP were determined as the difference between the change in dimensions after irradiation and the change in dimensions after heating at irradiation temperatures. Then the dependence of radiation changes from the temperature of irradiation was studied. Although the results of the research work [35, 36] were obtained at absorbed doses from $1 \cdot 10^7$ to $5 \cdot 10^7$ Gy, the effect of the absorbed dose in this range is not great, so the differences in the absorbed doses at different temperatures can be neglected. After that, we studied the coefficient K_T of the influence of temperature on the radiation change in the linear dimensions of the HPCP at absorbed doses of $1 \cdot 10^7$ – $5 \cdot 10^7$ Gy as the ratio of radiative changes in dimensions after irradiation at temperature T to radiation changes at 20°C obtained on the basis of extrapolation using the approximation line (-0.48%).

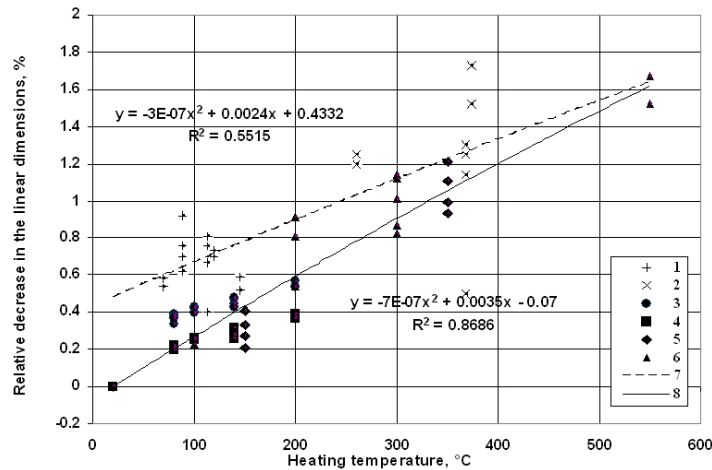


Figure 8. Comparison of changes in the linear dimensions of HPCP after irradiation with gamma radiation at temperatures from 70 to 375°C according to the data of the research works [35, 36] with changes in dimensions after heating of various HPCP of "mature" age after heating for a time commensurate with the time of irradiation, according to the data of the research works [9, 40, 41]. 1 – after irradiation of HPCP with $W/C = 0.4$ at the age of 1.5 years for 37.2 days at 70 – 120°C according to the data of the works [35, 36]; 2 – after irradiation of HPCP with $W/C = 0.4$ at the age of 1.5 years for 6.3 days at 260 – 375°C according to the data of the work [35, 36]; 3 – after heating HPCP with $W/C = 0.26$ – 0.35 at the age of 1 year for 30 days according to the work data [41]; 4 – after heating HPCP with $W/C = 0.26$ – 0.35 at the age of 1 year for 1 day according to the data of the work [41]; 5 – after heating HPCP with $W/C = 0.26$ – 0.35 at the age of 9 months for 5 hours according to work data [40]; 6 – after heating HPCP with $W/C = 0.28$ – 0.5 at the age of 30 months for 90–200 days according to the work data [9]; 7 – approximation line for the dependence of dimensions reduction after irradiation on temperature; 8 – approximation line for the dependence of reducing the dimensions after heating on the temperature.

The dependences of radiation changes in the linear dimensions of HPCP only under the influence of gamma radiation, calculated from the research works [35, 36] and the K_T coefficient on the irradiation temperature T , as well as the results of their approximation are shown in Fig. 9.

It can be seen that the changes in the linear dimensions of the cement stone only under the influence of gamma radiation and the values of the K_T coefficient at absorbed doses of $1 \cdot 10^7$ – $5 \cdot 10^7$ Gy decrease with increasing heating temperature and can be described by the expressions:

$$\left(\frac{\Delta l_{CP}}{l_{CP}} \right)_G = -3.74 \cdot 10^{-7} T^2 + 0.0011 T - 0.5032 \quad (19)$$

$$K_T = 7.77 \cdot 10^{-7} T^2 - 0.0023 T + 1.0454. \quad (20)$$

It is characteristic that at $T = 20^\circ\text{C}$ according to the formula (19) we get

$$\left(\frac{\Delta l_{CP}}{l_{CP}} \right)_G = -0.48\%$$

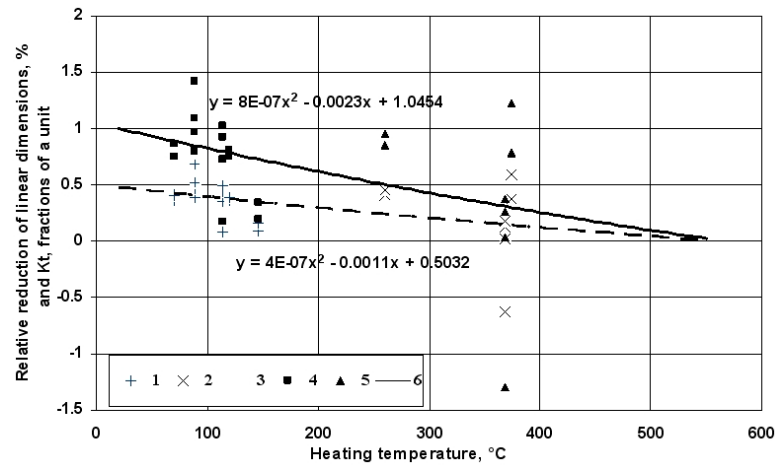


Figure 9. Dependencies of radiation changes in the linear dimensions of HPCP only under the influence of gamma radiation, calculated from research works [35, 36] and the coefficient K_T on the irradiation temperature, as well as the results of their approximation:
1 – reduction in linear dimensions only under the influence of gamma radiation after irradiation of HPCP for 37.2 days at 70–120 °C; 2 – reduction in linear dimensions only under the influence of gamma radiation after irradiation of HPCP for 6.3 days at 260–375 °C; 3 –approximation line for the dependence of linear dimensions reduction only under the influence of gamma radiation after irradiation of at 70–375 °C on temperature; 4 – values of the K_T coefficient after irradiation of HPCP at 70 – 120 °C; 5 – values of the K_T coefficient after irradiation of HPCP at 260–375 °C; 6 –approximation line for the dependence of the K_T coefficient on the irradiation temperature.

According to the formula (17) at absorbed doses from $1 \cdot 10^7$ to $5 \cdot 10^7$ Gy we get $\left(\frac{\Delta l_{CP}}{l_{CP}}\right)_G = -0.25 - -0.44$ %. This is commensurate with the value $\left(\frac{\Delta l}{l}\right)_P = 0.48$ %, obtained from the formula (19), therefore confirms the sufficient correctness of the formula (19) for the determination of radiation changes in the HPCP and at absorbed doses from $1 \cdot 10^7$ to $5 \cdot 10^7$ Gy. This allows us to recommend the obtained approximating dependence (17), taking into account the expression (20) for the calculated determination (assessment) of radiation changes in the linear dimensions of the HPCP only under the influence of gamma radiation in the following form:

$$\left(\frac{\Delta l_{CP}}{l_{CP}}\right)_G = K_T a_G D_G^{b_G}. \quad (21)$$

A comparison of the relationship between changes in compressive strength of HPCP with a decrease in volume calculated from the data of research work [1, 2] after gamma radiation and after irradiation in nuclear reactors and heating of HPCP of "young" age according to [9] is given in Fig. 10. It can be seen that these relationships are commensurate. In this regard, it can be concluded that the main thing for changes in the strength of HPCP, regardless of the type of impact that causes the release of water, is a decrease in its linear dimensions.

This gives grounds to recommend the use of the expression (13) for the analytical determination of radiation changes in the strength of HPCP under the influence of gamma radiation of both young and "mature" age. Although due to the fact that the reduction of porosity due to carbonation is not taken into account, the expression (13) will give an estimate of the maximum possible effect of gamma radiation.

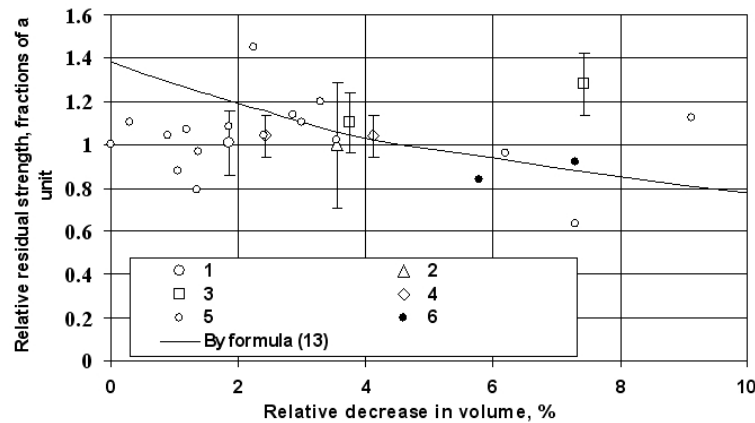


Figure. 10. Comparison of the relationship between changes in the compressive strength of HPCP with a decrease in volume under the influence of gamma radiation, calculated from the data of the research work [1, 2], with the relationship between these changes in HPCP of young "age" after irradiation in nuclear reactors and heating according to the data [9].

- 1 – reduce of the linear dimensions and strength of concrete from limestone and sandstone from the data [1, 2]; 2 – reduce of the mass and strength of concrete from limestone and sandstone from the data [1,2]; 3 – reduce of the linear dimensions and strength of concrete from limestone from the data [1, 2]; 4 – reduce of the mass and strength of concrete from limestone from the data [1, 2]; 5 – according to the data of the research work [9] after irradiation in nuclear reactors; 6 – according to the data of the research works [9] after prolonged heating without irradiation.

The results of calculations according to the formulas (21) and (13) of radiation changes in the linear dimensions and compressive strength of HPCP, caused only by the action of gamma radiation, after irradiation to the values of absorbed doses from $3 \cdot 10^4$ Gy to $1 \cdot 10^{10}$ Gy are shown in Fig. 11. It can be seen that the radiation decrease in linear dimensions increases, and the residual strength decreases with an increase in the absorbed dose and vice versa, the radiation decrease in linear dimensions decreases, and residual strength grows with rise of temperature associated with irradiation. With an absorbed dose of gamma radiation of 10^{10} Gy, the linear dimensions reduction will be 2.8 % after irradiation at 20–30 °C and 0.25 % after irradiation at 500 °C. With an absorbed dose of gamma radiation of 10^{10} Gy, the residual compressive strength will be 0.83 after irradiation of HPCP of "young" age and 0.34 after irradiation of HPCP of "mature" age at 20–30 °C; 1.3 after irradiation of "young" age material and 0.85 after irradiation of "mature" age material at 500 °C according to formulas (21) and (13), with (18) taking into account.

The results of estimated calculations of total changes under the influence of gamma radiation and concomitant heating of changes in the linear dimensions and strength (radiation-thermal changes) of HPCP after prolonged (more than 90 days) irradiation to absorbed doses from $3 \cdot 10^4$ Gy to $1 \cdot 10^{10}$ Gy at temperatures from 20 to 500 °C are shown in Fig. 12. At the same time, radiation changes in dimensions were determined by the formula (21). Thermal changes in the dimensions of the HPCP after prolonged heating were calculated on the basis of the data of the research work [9] according to the formula:

$$\left(\frac{\Delta l_{CP}}{l_{CP}} \right)_T = \frac{1}{3} \left(\frac{\Delta V_{CP}}{V_{CP}} \right)_T = \frac{1}{3} a_T T^{b_T}, \quad (22)$$

where T is temperature during irradiation (in °C); $a_T = -0.091$ %, $b_T = 0.73$ – for HPCP of "young" age by [9]; $a_T = -0.0146$ %, $b_T = 0.93$ – for HPCP of "mature" age according to the results of the approximation of the average shrinkage values presented in the research work [9].

Radiation-thermal changes in the strength of HPCP were calculated according to the formula (13) on the basis of radiation-thermal volume changes calculated from radiation-thermal changes in linear dimensions.

Fig. 12 shows that after irradiation of HPCP with gamma radiation at high temperatures the decrease in linear dimensions increases and the residual strength decreases with a rise in the absorbed dose to $2 \cdot 10^9$ Gy and the irradiation temperature. On the contrary, the radiation-thermal reduction in linear dimensions decreases and the residual strength increases with a rise in the absorbed dose above $2 \cdot 10^9$ Gy and with an increase in the temperature accompanying irradiation. With an absorbed dose of gamma radiation of 10^{10} Gy, the reduction in the linear dimensions of HPCP will be 2.8 % after irradiation at 20–30 °C and 0.25 % after irradiation at 500 °C. With an absorbed dose of gamma radiation of 10^{10} Gy, the residual compressive strength will be 0.83 after irradiation at the age of 1–3 months and 0.34 after

irradiation at the age of more than 8 months at 20–30 °C with; 1.3 after irradiation in HPCP of "young" age and 0.85 when irradiating HPCP of "mature" age at 500 °C. To obtain a more accurate result for a particular HPCP, it is necessary to use real thermal changes in the HPCP when performing estimates.

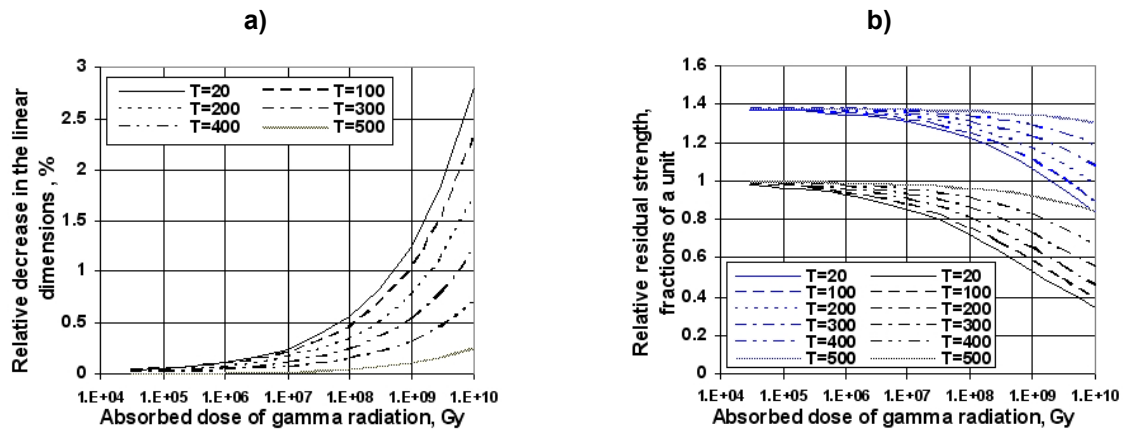


Figure 11. Results of calculations according to formulas (21) and (13) of radiation changes in the linear dimensions and compressive strength of HPCP caused only by the action of gamma radiation, after irradiation to the values of absorbed doses from $3 \cdot 10^4$ Gy to $1 \cdot 10^{10}$ Gy at different irradiation temperatures T in °C.

Blue lines are given for HPCP of "young" age. Black lines are given for HPCP of "mature" age.

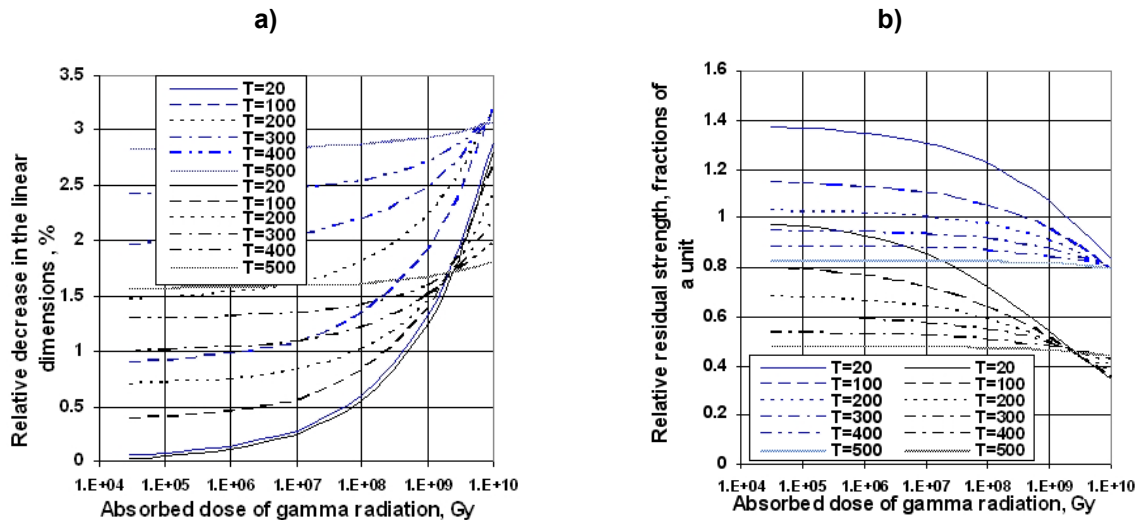


Figure 12. The results of the estimated calculations of the total changes under the influence of gamma radiation and the concomitant heating of changes (radiation-thermal changes) in the dimensions (a) and strength (b) of the HPCP after prolonged (more than 90 days) irradiation to the values of the absorbed doses from $3 \cdot 10^4$ Gy to $1 \cdot 10^{10}$ Gy at different irradiation temperatures T in °C. Blue lines are given for HPCP of "young" age. Black lines are given for HPCP of "mature" age.

The results obtained can be used to predict changes in the linear dimensions, volume and strength of HPCP and concrete under the influence of gamma radiation. At the same time, the effect of the mineral composition and water-cement ratio of W/C, the intensity of radiation on the radiation changes in the HPCP should not be significant, since, judging by [9] it is not noticeable during irradiation in nuclear reactors. The effect of age on radiation changes in linear dimensions with prolonged exposure should not be significant, since radiation changes are most pronounced by the end of irradiation, when the age of the materials will almost be sufficiently mature.

4. Conclusions

1. The research is based on the published data on the effect of gamma radiation on concretes at irradiation temperatures of 20–30 °C and on hardened Portland cement paste (HPCP) at 70–375 °C. The author carried out calculation and analytical studies to assess and establish the possibility of predicting radiation changes in HPCP under the influence of gamma radiation. The studies were conducted using the previously developed and tested method of analytical determination of radiation changes in concretes

according to data on changes in their components. The formulas used in this method made it possible to determine (restore) the radiation changes of HPCP from data on radiation changes in concretes and aggregates. When conducting computational and analytical studies, the author additionally used the existing relationship between the reduction in the mass of HPCP and its shrinkage, as well as known data on thermal changes in HPCP after its heating at different temperatures and holding time.

2. As a result of the studies carried out on the available results of irradiation of concretes, changes in linear dimensions and strength during compression of HPCP only under the action of gamma radiation are calculated (restored). The dependencies of radiation changes in HPCP on the magnitude of the absorbed dose in the range from $3.8 \cdot 10^4$ to $4.7 \cdot 10^8$ Gy after irradiation at 20–30 °C are provided. According to the available data on the irradiation of HPCP with gamma radiation at temperatures from 70 to 375 °C, the effect on radiation changes in the HPCP of the irradiation temperature is revealed. It is shown that radiation changes in HPCP increase with increasing absorbed dose and, conversely, radiation changes decrease with increasing temperature accompanying irradiation.

3. Based on the obtained approximating mathematical expressions, the paper provides the calculations of radiation changes in the dimensions and compressive strength of HPCP, caused only by the action of gamma radiation, after irradiation to absorbed doses from $3 \cdot 10^4$ Gy to $1 \cdot 10^{10}$ Gy. Using the results of these calculations and the available data on thermal changes in HPCP, the authors supplies the estimates of radiation-thermal changes in the linear dimensions and strength of HPCP under the action of gamma radiation and heating. These calculations were made after irradiation up to absorbed doses from $3 \cdot 10^4$ Gy to $1 \cdot 10^{10}$ Gy and concomitant heating at temperatures from 20 to 500 °C.

4. The obtained results can be used to predict radiation changes in the linear dimensions, volume and strength of HPCP under the influence of gamma radiation. Based on these changes in HPCP, using existing analytical methods makes it possible to predict radiation changes in concrete.

References

1. Kelly, B., Brocklehurst, J., Mottershead, D., McNearney, S. The Effects of Reactor Radiation on Concrete. Proceedings of the Second Information Meeting on Pre Stress Concrete and Reactor Pressure Vessels and their Thermal Isolation. EUR-4531, 1969. Pp. 237–265.
2. Gray, B.S. The Effect of Reactor Radiation on Cements and Concrete. Proceedings of an information exchange meeting on results of concrete irradiation programmes. EUR 4751 f-e Brussels (Belgium), April 19, 1971. Commission of the European Communities, Luxembourg, 1972. Pp. 17–39.
3. Elleuch, L., Dubois, F., Rappeneau, J. Effects of Neutron Radiation on Special Concretes and Their Components. Special Publication of The American Concrete Institute SP-34, 1972. Pp. 1071–1108.
4. Hilsdorf, H. K., Kropp, J., Koch, H.J. The effects of nuclear radiation on the mechanical properties of concrete. Proceedings of the Douglas McHenry International Symposium on Concrete and Concrete Structures. ACI SP 55-10. American Concrete Institute. Mexico City. Mexico, 1978. Pp. 223–251.
5. Kaplan, M.F. Concrete Radiation Shielding. Concrete Design and Construction Series. Harlow: Longman Scientific, 1989. 457 p.
6. Fillmore, D. L. Literature Review of the Effects of Radiation and Temperature on the Aging of Concrete. Technical Report INEL/EXT-04-02319. Idaho National Engineering and Environmental Laboratory. Bechtel BWXT Idaho, LLC. Prepared for the Central Research Institute of Electric Power Institute. September 2004.
7. Kontani, O., Ichikawa, Y., Ishizawa, A., Takizawa, M., & Sato, O. Irradiation effects on concrete structures. Int. Symp. On the Ageing Manag. of Nucl. P. P., 2010. Pp. 173–182. DOI: 10.1002/9781118536254.ch27
8. Maruyama, I., Kontani, O., Ishizawa, A., Takizawa, M., & Sato, O. Development of system for evaluating concrete strength deterioration due to radiation and resultant heat. Salt Lake City: Proceedings of 3rd International Conference on NPP Life Management for Long Term Operations. 2012.
9. Denisov, A.V., Dubrovskiy, V.B., Solovyev, V.N. Radiatsionnaya stoykost mineralnykh i polimernykh stroitelnykh materialov [Radiating stability of mineral and polymer building materials]. M.: Izdatelskiy dom MEI, 2012. 284 p. (rus)
10. William, K., Xi, Y., Naus, D. A review of the effects of radiation on microstructure and properties of concretes used in nuclear power plants. Tech. Rep. NUREG/CR-7171 ORNL/TM-2013/263, US Nuclear Regulatory Commission, Oak Ridge National Laboratory, 2013.
11. Field, K.G., Remec, I., Le Pape, Y. Radiation effects in concrete for nuclear power plants – Part I: Quantification of radiation exposure and radiation effects. Nuclear Engineering and Design. 2015. 282. Pp. 126–143.
12. Rosseel, T.M., Maruyama, I., Le Pape, Y., Kontani, O., Giorla, A.B., Remec, I., Wall, J. J., Sircar, M., Andrade, C., Ordonez, M. Review of the Current State of Knowledge on the Effects of Radiation on Concrete. Journal of Advanced Concrete Technology. 2016. 14. Pp. 368–383. DOI: 10.3151/jact.14.368
13. Muzalevskiy, L. P. Prognozirovaniye stepeni izmeneniya prochnosti i radiatsionnykh deformatsiy betona [Forecasting of degree of change of durability and radiating deformations of concrete]. Trudy Tret'yey Vsesoyuznoy nauchnoy konferentsii po zashchite ot ioniziruyushchikh iz-lucheniy yaderno-tehnicheskikh ustanovok. Vol. V. Tbilisi: Iz-vo TGU.1985. Pp. 116–125. (rus)
14. Denisov, A.V., Dubrovskiy, V.B., Yershov, V.Yu. et. al. Radiatsionno-temperaturnyye izmeneniya svoystv portlandsementnogo kamnya betona i zavisimosti dlya ikh prognozirovaniya [Radiation -thermal changes of properties of hardened cement paste and functions for their predictions]. Voprosy atomnoy nauki i tekhniki. 1989. 2. Pp. 20–35. (rus)
15. Denisov, A. V., Dubrovskiy, V. B., Muzalevskiy, L. P. Prognozirovaniye radiatsionnykh izmeneniy neorganicheskikh stroitelnykh materialov [Prediction of radiation changes in inorganic building materials]. Voprosy atomnoy nauki i tekhniki. Ser. Proyektirovaniye i stroitelstvo.1990. 3. Pp. 98–102. (rus)

16. Le Pape, Y., Field, K.G., Remec, I. Radiation effects in concrete for nuclear power plants, Part II: Perspective from micromechanical modeling. *Nuclear Engineering and Design*. 2015. 282. Pp. 144–157.
17. Giorla, A., Vaitova, M., Le Pape, Y., Stemberk, P. Meso-scale modeling of irradiated concrete in test reactor. *Nuclear Engineering and Design*. 2015. 295. Pp. 59–73.
18. Pomaro, B. A Review on Radiation Damage in Concrete for Nuclear Facilities. Experiments to Modeling. *Modelling and Simulation in Engineering*. 2016. Pp. 1–10. Article ID 4165746. DOI: 10.1155/2016/4165746 (date of application: 11.01.2023).
19. Giorla, A.B., Le Pape, Y., Dunant, C. F. Computing Creep-Damage Interactions in Irradiated Concrete. *Journal of Nanomechanics and Micromechanics*. 2017. 7(2). 04017001. DOI: 10.1061/(ASCE)NM.2153-5477.0000118
20. Le Pape, Y., Alsaïd, M.H.F., Giorla, A.B. Rock-forming minerals radiation induced volumetric expansion – revisiting the literature data. *Journal of Advanced Concrete Technology*. 2018. 16. Pp. 191–209. DOI: 10.3151/jact.16.191
21. Sasano, H., Maruyama, I., Sawada, S., Ohkubo, T., Murakami, K., Suzuki, K. Meso-Scale Modelling of the Mechanical Properties of Concrete Affected by Radiation-Induced Aggregate Expansion // *Journal of Advanced Concrete Technology*. 2020. 18(10). Pp. 648–677. DOI: 10.3151/jact.18.648
22. Khmurovska, Y., Štemberk, P. Catalogue of Radiation-Induced Damage of Rock Aggregates Identified by RBSM Analysis. *Journal of Advanced Concrete Technology*. 2021. 19. Pp. 668–686.
23. Alexander, S. Effects of Irradiation on Concrete Final Results. Technical Report HL.63/6438," Atomic Energy Research Establishment, Harwell 1963. In Hilsdorf 1978.
24. Sommers, J.F. Gamma radiation damage of structural concrete immersed in water. *Health Physics*. 1969. 16. Pp. 503–508.
25. McDowall, D.C. The Effect of Gamma Irradiation on the Creep Properties of Concrete. Proceedings of an information exchange meeting on results of concrete irradiation programmes. EUR 4751 f-e Brussels (Belgium), April 19, 1971. Commission of the European Communities, Luxembourg, 1972. Pp. 55–69.
26. Vodák, F., Trtík, K., Sopko, V., Kapičková, O., Demo, P. Effect of γ -Irradiation on Strength of Concrete for Nuclear Safety Structures. *Cement and Concrete Research*. 2005. 35. Pp. 1447–1451.
27. Lowinska-Kluge, A., Piszora, P. Effect of gamma irradiation on cement composites observed with XRD and SEM methods in the range of radiation dose 0-1409 MGy. *Acta Physica Polonica-Series A General Physic*, 2008. 114. p. 399–411.
28. Kitsutaka, Y., Matsuzawa, K. The effect of gamma radiation on the fracture properties of concrete. Proceedings of FraMCoS-7, May 23-28, 2010. *Fracture Mechanics of Concrete and Concrete Structures – Recent Advances in Fracture Mechanics of Concrete*. Korea Concrete Institute, Seoul, ISBN 978-89-5708-180-8. Pp. 61–64.
29. Vodák, F., Vydra, V., Trtík, K., Kapičková, O. Effect of γ -irradiation on Properties of Hardened Cement Paste. *Materials and Structures*. 2011. 44. Pp. 101–107.
30. Kontani, O., Ichikawa, Y., Ishizawa, A. Irradiation Effects on Concrete Durability of Nuclear Power Plants. Proceedings of ICAPP 2011. France, 2011. Paper 11361.
31. Kontani, O., Sawada, S., Maruyama, I., Takizawa, M., Sato, O. Evaluation of irradiation effects on concrete structure: gamma-ray irradiation tests on cement paste. Proceedings ASME 2013 Power Conference, Boston, USA 29 July-1 August 2013. New York, USA: American Society of Mechanical Engineers, 2013-98099.
32. Maruyama, I., Kontani, O., Takizawa, M., Sawada, S., Ishikawa, S., Yasukouchi, J., Sato, O., Etoh, J., Igari, T. Development of the soundness assessment procedure for concrete members affected by neutron and gamma-irradiation. *Journal of Advanced Concrete Technology*. 2017. 15. Pp. 440–523. DOI: 10.3151/jact.15.440
33. Ishikawa, S., Maruyama, I., Takizawa, M., Etoh, J., Kontani, O., Sawada S. Hydrogen Production and the Stability of Hardened Cement Paste under Gamma Irradiation. *Journal of Advanced Concrete Technology*. December 2019. 17. Pp. 673–685. DOI: 10.3151/jact.17.673
34. Varlakov, A.P., Kapustin, V.V., Varlakova, G.A., Zherebtsov, A.A., Petrov, V.G., Shirshin, E.A., Kalmykov, S.N. The effect of radiation doses typical for high-level waste on the properties of the cement matrix. *Radioactive Waste*. 2018. 1(2). Pp. 89–96 (rus).
35. Reches, Y.A multi-scale review of the effects of gamma radiation on concrete. *Results in Materials*. DOI: 10.1016/j.rinma.2019.100039 (date of application: 11.01.2023)
36. Sanchez, F., Kosson, D., Oskay, C. Development of a Nano-Modified Concrete for Next Generation of Storage Systems, US Department of Energy Nuclear Energy University Programs. Vanderbilt University, 2018. Nashville, TN2018. Project No. 13-4840.
37. Khmurovska, Y., Štemberk, P., Sikorin, S., Žák, J., Khaladkevich, Y., Pavalanski, E., & Fatseyeu, V. (2019b). Cement mortar creep under exposure to gamma-ray irradiation. *Journal of Nuclear Research and Development*, 18, 24–28.
38. Khmurovska, Y., Štemberk, P., Sikorin, S., Němeček, J., Józwiak Niedźwiedzka, D., Doleželová, M., Kaladkevich, Y., Pavalanski, E., Fatseyeu, V. Effects of Gamma-Ray Irradiation on Hardened Cement Mortar. *International Journal of Concrete Structures and Materials*. 2021. 15(3). Pp. 303–316. DOI: 10.1186/s40069-020-00452-7
39. Denisov, A.V. Radiation changes of concrete aggregates under the influence of gamma radiation. *Magazine of Civil Engineering*. 2020. 4(96). P. 94–109. DOI: 10.18720/MCE.96.8
40. Falikman, V.R., Vaselova, V.I., Yershov, V.Yu., Muzalevskiy, L.P. Povedeniye tsementnogo kamnya s khimicheskimi dobavkami v usloviyakh kratkovremennogo vozdeystviya vysokikh temperatur [Behavior of a cement stone with chemical additives in the conditions of short-term influence of high temperatures]. *Voprosy atomnoy nauki m tekhniki. Ser. Proyektirovaniye i stroitelstvo*. 1987, vyp. 1. P. 3–15.
41. Yershov, V. Yu., Dubrovskiy, V. B., Muzalevskiy, L.P. Kolesnikov, N. A. Povedeniye tsementnogo kamnya s khimicheskimi dobavkami v usloviyakh dlitelnogo vozdeystviya vysokikh temperatur [Behaviour of a cement stone with chemical additives in the conditions of long influence of high temperatures]. *Voprosy atomnoy nauki m tekhniki. Ser. Proyektirovaniye i stroitelstvo*. 1988. 2. Pp. 120–129. (rus)
42. Nekrasov, K.D., Zhukov, V. V., Gulyayev, V. F. Tyazhelyy beton v usloviyakh povyshennykh temperatur [Heavy concrete at elevated temperatures]. M.: Stroyizdat, 1972. 128 p. (rus)

Information about author

Aleksandr Denisov, PhD in Technical Sciences

ORCID: <https://orcid.org/0000-0002-8051-5914>

E-mail: den-al-v@inbox.ru

Received 05.03.2023. Approved after reviewing 24.10.2023. Accepted 24.10.2023.



Research article

UDC 693.5

DOI: 10.34910/MCE.124.4



Planting steel reinforcement for concrete columns

M.M. Kharnoob 

University of Baghdad, Baghdad, Iraq

 dr.majidkharnoob@coeng.uobaghdad.edu.iq

Keywords: column, implantation, pull-out, steel fiber, bond, slip

Abstract. This study presents a scenario where the embedding of dowel reinforcement for new columns was inadvertently omitted during the casting of concrete columns. This oversight necessitated the implantation of steel reinforcement into pre-existing cast areas. Owing to the high density of the primary slab reinforcement, implantation was feasible only up to half the slab's thickness. By modifying the superplasticizer (SP) dosage during mixing, we achieved a consistent slump of approximately 150 mm across various concrete mixes, ensuring that both slump and slump flow remained within expected limits. The properties of these mixes, both in their fresh and hardened states, are detailed in Table 2. The sieve segregation index consistently remained below 1.3 %, indicating exceptional cohesion in all concrete mixes. In fact, no segregation was observed, with all measured segregation widths being zero. In terms of strength, the cylinder strength increased significantly with the increase in fiber volume from 0 % to 2 %. This study also examines the impact of steel reinforcement, utilizing 8 mm diameter steel bars over a 30 cm length, planted at two different angles (90 and 45 degrees). The concrete column samples were subjected to uniaxial compressive load post-implantation. Results indicate that the implantation process generally led to an increase in the initial compressive strength of the concrete samples. Specifically, specimens with 30 cm reinforcement planted at distances of 55 mm and 35 mm exhibited an average strength increase of 23 % and 17 %, respectively.

Citation: Kharnoob, M.M. Planting steel reinforcement for concrete columns: In case of small distance at missing places in concrete columns. Magazine of Civil Engineering. 2023. 124(8). Article no. 12404. DOI: 10.34910/MCE.124.4

1. Introduction

This article introduces a novel integration technique for steel reinforcement in concrete columns, handy for temporary jack support in existing reinforced concrete structures. During the casting process, the inclusion of dowel reinforcement for new columns was inadvertently omitted, leading to the necessity of implanting steel reinforcement in pre-existing cast areas. The density of the primary slab reinforcement limited implantation to only half the slab's thickness. This study investigates the effect of steel reinforcement with an 8 mm diameter and 30 cm length, planted at 0 and 45 degrees angles. Post-implantation, the concrete column samples underwent uniaxial compressive load testing. Results indicated an enhancement in the initial compressive strength of the concrete samples. Specimens with 30 cm reinforcement, planted at distances of 55 mm and 35 mm, showed average strength increases of 23 % and 17 %, respectively [1–3].

Conventional reinforcement techniques include fiber-reinforced polymer (FRP) wrapping, steel cage addition, and concrete jacketing, with the latter being among the earliest and most effective methods. A recent advancement involves the application of high-performance fiber-reinforced cementitious composites (HPFRC) spray mortars with extra reinforcing bars [4]. This method demonstrated increased absorbed energy and improved cyclic response in column samples reinforced with HPFRC [5–6]. Further studies have shown that fiber-reinforced concrete significantly reduces fracture width and enhances energy

absorption. Concrete jacketing is also recognized as an effective method for restoring axial and lateral load capacities of damaged columns, though it may impose design and architectural constraints [7–9].

Alternative techniques, like FRP sheet external confinement, have gained attention. Research on FRP wrapping has highlighted its effectiveness in restoring damaged concrete columns, with reinforced columns showing increased axial load capacity [10–12]. However, the effectiveness of this strategy heavily relies on the column design.

Standard methods for curing concrete after completion include gluing for planting and planting machinery. The former involves drilling into concrete, inserting rebar, and filling the hole with adhesive, usually epoxy resin or cement [13–14]. This method is popular for its on-site applicability. Since the 1990s, cement-based materials for rebar planting have been replaced by various adhesives like polyester, vinyl ester, and epoxy. A pull-out test using two epoxies with steel models of the required 16 mm diameter indicated satisfactory performance [15–25].

It is recommended to use high-quality concrete for the monolithic construction of columns. In order to reduce their cost, it is advisable to use man-made raw materials and composite binders [26–29]. Recent studies have been carried out on the mechanical behavior and structural integrity of concrete structures using various additives, bringing new insights into innovative reinforcement techniques [30,31].

2. Methods

In this study, Ordinary Portland Cement (OPC) with a 52.5N strength rating, conforming to BS EN 197-1: 2000, was utilized for the concrete mix. The OPC exhibited a Blaine fineness of 354 m²/kg as per BS EN 196-6: 2010 standards. Both fine and coarse aggregates were derived from crushed granite rock, with the fine aggregate having a maximum size of 5 mm, and the coarse aggregate a maximum size of 10 mm. According to BS 812-2: 1995 protocols, the water absorption of the fine and coarse aggregates was determined to be 1.37 % and 1.89 %, respectively, with moisture contents measured at 0.79 % for fine aggregate and 1.04 % for coarse aggregate. To achieve the desired slump of 150 ± 25 mm in each concrete mix, a poly carboxylate-based superplasticizer (SP) was incorporated, characterized by a relative density of 1.03 and a solid mass content of 20 %. For the fiber-reinforced concrete component, hooked steel fibers branded as Dramix, 30 mm in length and classified as 3D 55/30, were employed, as depicted in Fig. 1.



Figure 1. Iron Fibres used.

Table 1 outlines the Mixtures of Plain and fiber-reinforced concrete. The volume of fiber in the concrete varied between 1 and 2 %. In contrast, the water/cement (W/C) ratio for both fiber-reinforced and plain concrete was adjusted within a range of 0.55 to 0.45. Additionally, the properties of Grade 500 high-strength ribbed steel bars, with a diameter of 12.0 mm, are detailed in the third row of Table 2. As per BS EN 10080: 2005 standards, these steel reinforcement bars feature a rib pattern with 1.05 mm rib height, 8.0 mm rib spacing, a 60° angle of inclination relative to the bar axis, and a 67° rib flank inclination angle.

For experimental purposes, a 150 mm concrete cube was cast, incorporating each reinforcing bar at a length of 30 mm. In adherence to RILEM guidelines, the bond length between the concrete and reinforcement bar was set at 50 mm, which is 4.2 times the diameter of the reinforcing bar. This bonded length of 236 mm was maintained in the middle third of the concrete cube. A 50 mm long plastic tubing was fitted around the implanted reinforcing bar to prevent bonding outside the designated area. The crevice was

sealed with clay to ensure no cement paste entered the gap between the reinforcing bar and the plastic tube.

The simple mixes and the fiber-reinforced concrete were prepared using a pan mixer. All specimens underwent a 28-day curing process in a tank of lime-saturated water at a temperature of 27 ± 3 °C, as shown in Table 1, which details the composition of the concrete mix.

Table 1. Mixtures of Plain and fiber-reinforced concrete.

Mix. Concentration	Cement (Kg/m ³)	Fine (Kg/m ³)	Water (Kg/m ³)	10 mm agg. (Kg/m ³)	Steel fibre (Kg/m ³)
0.0%	520	830	688	680	0
1.0%	523	820	819	671	70
2.0%	460	805	833	660	80

2.1. Testing program and procedure

To assess the efficacy of a friction reduction layer (comprising a PTFE film, stainless steel plate, and grease layer), three types of specimens were prepared from each concrete mix, both plain and fiber-reinforced. These specimens underwent testing with and without using a soft rubber pad or a friction reduction layer. Three distinct testing methods were employed, designated as SRNF (Soft Rubber No Friction layer), SRFR (Soft Rubber Friction Reduction layer), and NRNF (No Rubber No Friction layer). The NRNF setup did not include a friction reduction layer or a soft rubber pad. Conversely, the SRNF setup included a soft rubber pad but omitted the friction reduction layer. The SRFR method incorporated both a friction reduction layer and a soft rubber pad.

Testing was conducted on four samples from each concrete batch to establish the bond stress-slip curve and pull-out strength for each testing method and type of concrete. The average pull-out strength and its coefficient of variation were calculated based on the results of these four tests. All pull-out tests were conducted using an MTS testing apparatus with a 250 kN load capacity. Fig. 2(a) illustrates the testing device, while Fig. 2(b) depicts the test setup.

Given that the bond length was set at 50 mm, approximately 20 % of the testing machine's capacity, the expected pull-out load was estimated at 50 kN. The bond strength was calculated using a pull-out failure load testing apparatus, as per the formula:

$$\tau = F \pi d l / 268, \quad (1)$$

where τ is bond strength, d is diameter of the reinforcing bar, F is failure load

Workability of the new concrete was assessed through slump-flow and slump tests as per BS EN 12350-8: 2010 and BS EN 12350-2: 2009 standards. The slump cone was filled with fresh concrete to its brim, and upon lifting the cone, the concrete was allowed to flow and settle. The slump was measured as the decrease in height, and the slump-flow was determined by averaging the diameters of two parallel sides of the formed concrete patties. Additionally, the average width of any paste- or mortar-free strip around the concrete patties' edge was measured to ascertain the segregation width.

Cohesiveness of the fresh concrete was evaluated using a sieve segregation test as outlined in BS EN 12350-11: 2010. The concrete sample was placed in a 300 mm diameter plastic container and left undisturbed for 15 minutes. The top 2 litres of the sample were then gently poured onto a 5 mm sieve, and after two minutes of dripping, the passed-through portion was weighed. The weight of the concrete that seeped through the sieve was calculated as a percentage of the total weight dispensed onto the sieve.

The hardened concrete's strength was determined using standard cylinder compression testing as per BS EN 12390-3: 2009, except the curing temperature set at 27 ± 3 °C. Three cylinders, each with a diameter of 150 mm and height of 300 mm, were prepared from each concrete batch and tested after 28 days. The strength result was taken as the average strength of the three cylinders, calculated at 293.

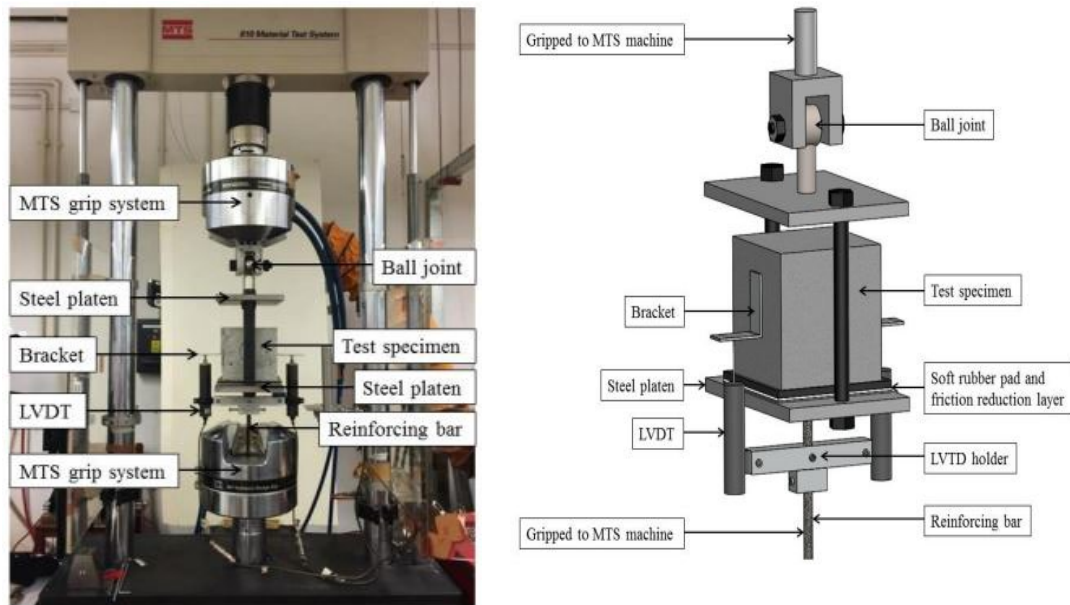


Figure 2. (a) Testing machine and test setup (b) Schematic diagram of pull out test setup.

3. Results and Discussion

3.1. Fresh and hardened Properties

During the mixing process, the superplasticizer (SP) dosage was carefully adjusted for each concrete mix, effectively achieving a target slump of approximately 150 mm. This adjustment ensured that both the slump and slump-flow values remained within the anticipated limits. The properties of these mixes, in both their fresh and hardened states, are detailed in Table 2. The sieve segregation index consistently registered below 1.3 %, indicating remarkably high cohesion across all concrete mixes, as evidenced by the cohesiveness data. Notably, actual segregation was absent in the samples, with all measured segregation widths being zero.

Regarding strength implications, a significant increase in cylinder strength was observed as the volume of fibers in the mix rose from 0 % to 2 %. This enhancement in structural integrity highlights the direct correlation between fiber volume and the compressive strength of the concrete, showcasing the efficacy of fiber reinforcement in concrete mixtures.

Table 2. The properties of the concrete mixes both Fresh and hardened.

Mix. Concentration	Slump (mm)	Slump-Flow (mm)	Cylindrical Strength (MPa)	Sieve Segregation Index (%)
0.0%	130	260	53.8	0.27
1.0%	135	240	56.4	0.15
2.0%	138	217	58.6	0.46

3.2. Bond stress-slip curves

Figure 3 displays the bond stress-slip curves for specimens with varying fiber volumes of 0.0 %, 1.0 %, and 2.0 %. Within this figure, sub-Fig. 3(a) illustrates the curve for specimens with a water/cement (W/C) ratio of 0.45, while sub-Fig. 3(b) presents the curve for those with a W/C ratio of 0.55. In each graph, a total of twelve curves are plotted, providing a comprehensive view of the bond stress-slip behavior across different fiber volumes and W/C ratios.

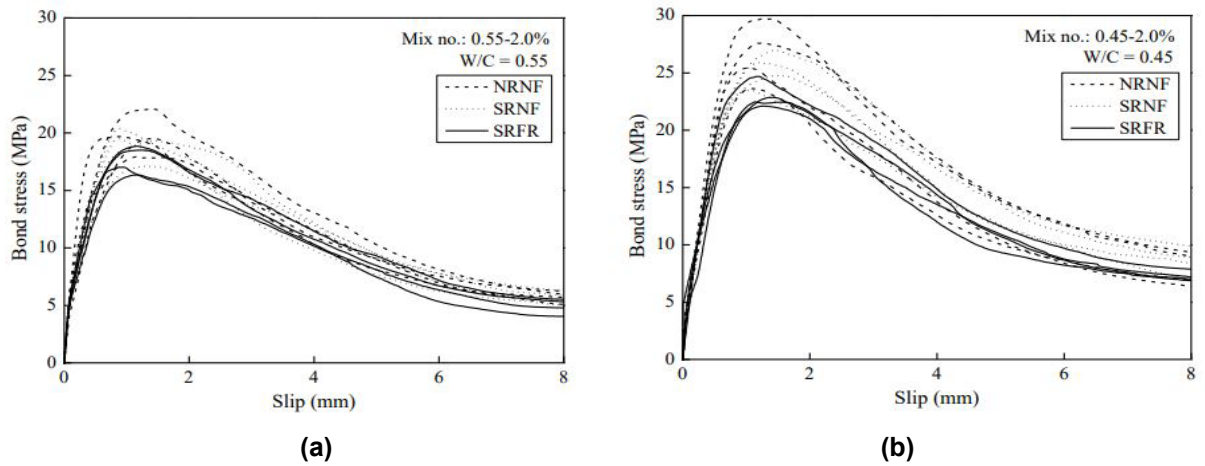


Figure 3. Bond stress-slip curves at fiber volume is 2.0 %.

Each of the twelve graphs in Fig. 3 encompasses three sets of curves corresponding to the three different test techniques (NRNF and SRNF) used for evaluating the four specimens. These curves illustrate the bond stiffness and strength derived from the bond stress-slip relationship. The specific values obtained from these curves are documented in Table 3. The subsequent section of this study delves into a detailed examination of these calculated bond stiffness and strength parameters.

Table 3. Characteristics of fresh and hardened properties of concrete mixes

Mix. Concentration	Test Technique	Individual bond Strength (MPa)			Mean of bond Strength (MPa)	Over-estimation	C.V. (%)
0.0%	SRNF	17.18	21.37	18.48	18.95	20.22	9.5
	NRNF	21.41	19.68	16.18	17.96	17.50	9.8
1.0%	SRNF	16.18	24.37	13.48	19.90	18.22	7.5
	NRNF	20.41	22.68	15.18	20.17	14.50	10.8
2.0%	SRNF	19.18	21.37	18.48	18.95	18.22	9.5
	NRNF	22.40	19.68	18.18	16.96	19.50	9.8

3.3. Mean and coefficient of variation of measured bond strength

The average bond strength can be determined by calculating the mean of four individual bond strength values obtained through a specific test procedure, as detailed in the seventh column of Table 3. Fig. 4 presents a graph illustrating the relationship between the mean calculated bond strength and the test technique, shedding light on the impact of the testing method on the measured bond strength. It was observed that the mean bond strength tended to decrease when transitioning from the NRNF to the SRNF testing technique. This decrease was expected due to the removal of the friction reduction layer and soft rubber pad from the interface between the concrete block and steel plate, which diminishes the confining stresses and consequently lowers the observed bond strength by allowing greater lateral expansion of the concrete. The SRFR method, combining a soft rubber pad with a friction reduction layer, yielded the lowest bond strength, likely offering a more accurate representation of the inherent bond strength. Other methods that exclude either the friction-reducing layer or the soft rubber pad tend to overestimate the bond strength.

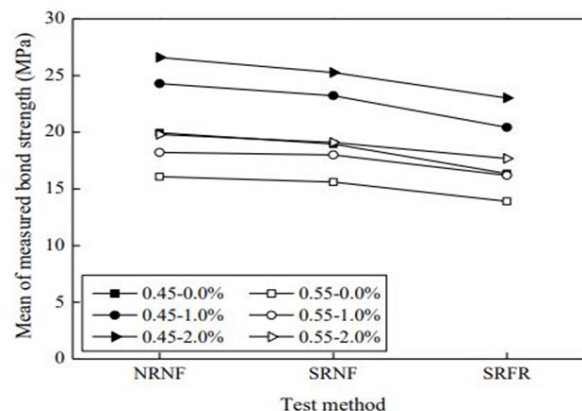


Figure 4. The effect of test procedure on the mean of measured bond strength.

The percentage overestimation of bond strength when using the NRNF method compared to the SRNF is documented in the eighth column of Table 3. These results show that the NRNF method overestimated bond strength by approximately 12.0 % to 22.0 %, whereas the SRNF method overestimated it by about 8.0 % to 16.0 %. This overestimation was more pronounced at lower W/C ratios and smaller fiber volumes. In scenarios lacking both a soft rubber pad and a friction reduction layer, the error in bond strength measurement could reach 20 %; however, with only a soft rubber pad present, the error could still be as high as 15 %. These findings highlight the necessity for improved test setups, especially at lower W/C ratios where inaccuracies in bond strength measurements could be more severe, indicating the importance of a more precise test apparatus for high-strength concrete.

The impact of internal confinement from additional fibers might explain the higher bond strength values at lower fiber volumes. Introducing fibers generally reduces the Poisson's ratio and lateral expansion of the concrete due to the fibers' internal restriction against lateral expansion. This internal confinement effect of the fibers would likely diminish the external confinement impact at the interface between concrete block and steel plate. The coefficient of variation (C.V.) of bond strength using all three test methodologies was also calculated, as shown in the final column of Table 3. Fig. 4 displays a graph correlating the estimated C.V. of measured bond strength with the test methodology, indicating that the test method significantly influences the variance in observed bond strength. For instance, the C.V. ranged from approximately 8.4 % to 13.2 % for NRNF, 4.5 % to 9.1 % for SRNF, and 4.4 % to 6.8 % for SRFR. The substantial reduction in C.V. achieved by the friction reduction layer can be attributed to its ability to minimize highly variable external confinement and the soft rubber pad's capacity to mitigate random fluctuations in contact pressure at the interface between concrete block and steel plate. This reduction in C.V. enhances the reliability and repeatability of the pull-out test, which is crucial for establishing design bond strength in structural analysis and design.

4. Conclusions

Despite the significant influence of bond properties of reinforcing bars on the structural behavior of reinforced concrete structures, there is currently no universally accepted test procedure for their measurement. Existing test methods often neglect the potential effects of boundary conditions at the interface between concrete block and steel plate. Addressing this gap, a finite element analysis was conducted to examine the impact of these boundary conditions, leading to the development of a new test method incorporating a soft rubber pad and a friction reduction layer at the interface. The primary goal of this novel method is to mitigate test errors caused by friction and uneven contact pressure. To assess the effectiveness of this approach, 72 specimens, both of plain and fiber-reinforced concrete with fiber volumes up to 2 %, were examined. The key conclusions drawn are as follows:

1. The discontinuous contact pressure and friction at the interface between concrete block and steel plate can significantly influence the confining stresses on the concrete around the reinforcing bar, consequently affecting the measured bond properties.
2. Introducing a soft rubber pad at the interface markedly reduces the measured bond strength and stiffness, thereby minimizing the overestimation of these bond properties. This addition also substantially diminishes the random variations in test results, enhancing the repeatability and reliability of the pull-out test.

References

1. Terai, M., Minami, K. Fracture behavior and mechanical properties of bamboo reinforced concrete members. *Procedia Engineering*. 2011. 10. Pp. 2967–2972.
2. Dahmani, L., Khennane, A., Kaci, S. Crack identification in reinforced concrete beams using ANSYS software. *Strength of materials*. 2010. 42 (2). Pp. 232–240.
3. Abed, F., El-Chabib, H., AlHamaydeh, M. Shear characteristics of GFRP-reinforced concrete deep beams without web reinforcement. *Journal of Reinforced Plastics and Composites*. 2012. 31(16). Pp. 1063–1073.
4. Chu, S.H., Kwan, A.K.H. A new method for pull out test of reinforcing bars in plain and fibre reinforced concrete. *Engineering Structures*. 2018. 164. Pp. 82–91. DOI: 10.1016/j.engstruct.2018.02.080
5. Jing, D., Cao, S., Krevaikas, T., Bian, J. A self-locking steel bearing connection for circular reinforced concrete columns. *Advances in Structural Engineering*. 2019. 22(12). Pp. 2605–2619. DOI: 10.1177/1369433219849810
6. Mohsin, S.S., Abbas, A., Cotsovos, D. Shear behaviour of steel-fibre-reinforced-concrete beams. In 11th International Conference on Concrete Engineering and Technology. 2012. 2014. Pp. 362–368.
7. Hashemi, N., Vatani Oskoue, A., Doostmohamadi, A. A Rehabilitation Experimental Program on Low-Strength Concrete with Steel Bar Planting. *Journal of Rehabilitation in Civil Engineering*. 2021. 9(2). Pp. 85–100.
8. Faisal, B., Izzet, A.F. Post Fire Residual Concrete and Steel Reinforcement Properties. *IOP Conference Series Earth and Environmental Science*. 2021. 856(1). 012058. DOI: 10.1088/1755-1315/856/1/012058
9. Tobbi, H., Farghaly, A.S., Benmokrane, B. Concrete Columns Reinforced Longitudinally and Transversally with Glass Fiber-Reinforced Polymer Bars. *ACI Structural Journal*. 2012. 109(4). 109-S48.

10. Aboukifa, M., Moustafa, M.A. Experimental seismic behavior of ultra-high performance concrete columns with high strength steel reinforcement. *Engineering Structures*. 2021. 232. 111885.
11. Mohammed, H., Said, A. Residual strength and strengthening capacity of reinforced concrete columns subjected to fire exposure by numerical analysis. *Journal of the Mechanical Behavior of Materials*. 2022. 31(1). Pp. 212–224. DOI: 10.1515/jmbm-2022-0026
12. Zhao, B., Taucer, F., Rossetto, T. Field investigation on the performance of building structures during the 12 May 2008 Wenchuan earthquake in China. *Engineering Structures*. 2009. 31(8). Pp. 1707–1723.
13. Hedebratt, J., Silfwerbrand, J. Full-scale test of a pile supported steel fibre concrete slab. *Materials and Structures*. 2014. 47(4). Pp. 647–666. DOI: 10.1617/s11527-013-0086-5
14. Eamon, C.D., Jensen, E. Reliability analysis of prestressed concrete beams exposed to fire. *Engineering Structures*. 2012. 43. Pp. 69–77. DOI: 10.1016/j.engstruct.2012.05.016
15. Garden, H.N., Hollaway, L.C., Thorne, A.M., Robust. A preliminary evaluation of carbon fibre reinforced polymer plates for strengthening reinforced concrete members. *Proceedings of the Institution of Civil Engineers – Structures and Buildings*. 1997. 122(2). Pp. 127–142. DOI: 10.1680/istbu.1997.29302
16. Johnson, R.P. *Composite Structures of Steel and Concrete: beams, slabs, columns and frames for buildings*. John Wiley & Sons, 2018.
17. Papakonstantinou, C.G., Petrou, M.F., Harries, K.A. Fatigue behavior of RC beams strengthened with GFRP sheets. *Journal of Composites for Construction*. 2001. 5(4). Pp. 246–253.
18. Engindeniz, M., Kahn, L.F., Abdul-Hamid, Z. Repair and strengthening of reinforced concrete beam-column joints: State of the art. *ACI Structural Journal*. 2005. 102(2). Pp. 1. 187–197
19. Fujikura, S., Bruneau, M. Experimental investigation of seismically resistant bridge piers under blast loading. *Journal of Bridge Engineering*. 2011. 16(1). Pp. 63–71.
20. Hanoon, A., Kharnoob, M. Push-Out Test of Steel-Concrete-Steel Composite Section for Pre-Installation and Post-Installation Techniques of Shear Connectors. *Key Engineering Materials*. 2020. 862. Pp. 12–16. DOI: 10.4028/www.scientific.net/KEM.862.12
21. Kharnoob, M.M., Hasan, A.J., Sabti, L.M. The Limitation and Application of geometric Buildings and Civil Structures. *E3S Web of Conferences*. 2021. 318(4). 04009. DOI: 10.1051/e3sconf/202131804009
22. Al-Ansari, A.A., Kharnoob, M.M., Kadhim, M.A. Abaqus Simulation of the Fire's Impact on Reinforced Concrete Bubble Deck Slabs. *E3S Web of Conferences*. 2023. 427(10). 02001. DOI: 10.1051/e3sconf/202342702001
23. Abbood, A.A., Kharnoob, M.M. Experimental Studies on the Fire Flame Behavior of Reinforced Concrete Beams with Construction Joints. *E3S Web of Conferences*. 2023. 427(1). 02018. DOI: 10.1051/e3sconf/202342702018
24. Kharnoob, M.M., Cepeda, L.C., Jácome, E., Choto, S., Alazbjee, A.A., Sapaev, I.B., Hussein, M.A.M., Yacin, Y., Alawadi, A.H.R., Alsalamy, A. Analysis of thermoelastic damping in a microbeam following a modified strain gradient theory and the Moore-Gibson-Thompson heat equation. *Mechanics of Time-Dependent Materials*. 2023. DOI: 10.1007/s11043-023-09632-w
25. Kharnoob, M.M., Hasan, F.F., Sharma, M.K., Zearah, S.A., Alsalamy, A., Alawadi, A.H.R., Thabit, D. Dynamics of spinning axially graded porous nanoscale beams with rectangular cross-section incorporating rotary inertia effects. *Journal of Vibration and Control*. 2023. DOI: 10.1177/10775463231222531
26. Klyuev, S.V., Kashapov, N.F., Radaykin, O.V., Sabitov, L.S., Klyuev, A.V., Shchekina, N.A. Reliability coefficient for fibreconcrete material. *Construction Materials and Products*. 2022. 5(2). Pp. 51–58. DOI: 10.58224/2618-7183-2022-5-2-51-58
27. Strelkov, Yu.M., Sabitov, L.S., Klyuev, S.V., Klyuev, A.V., Radaykin, O.V., Tokareva, L.A. Technological features of the construction of a demountable foundation for tower structures. *Construction Materials and Products*. 2022. 5(3). Pp. 17–26. DOI: 10.58224/2618-7183-2022-5-3-17-26
28. Kashapov, R.N., Kashapov, N.F., Kashapov, L.N., Klyuev, S.V., Chebakova, V.Yu. Study of the plasma-electrolyte process for producing titanium oxide nanoparticles. *Construction Materials and Products*. 2022. 5(5). Pp. 70–79. <https://doi.org/10.58224/2618-7183-2022-5-5-70-79>
29. Kashapov, R.N., Kashapov, N.F., Kashapov, L.N., Klyuev, S.V. Plasma electrolyte production of titanium oxide powder. *Construction Materials and Products*. 2022. 5 (6). P. 75 – 84. DOI: 10.58224/2618-7183-2022-5-6-75-84
30. Hussein, O.H., Ibrahim, A.M., Abd, S.M., Najm, H.M., Shamim, S., Sabri, M.M.S. Hybrid Effect of Steel Bars and PAN Textile Reinforcement on Ductility of One-Way Slab Subjected to Bending. *Molecules*. 2022. 27. DOI: 10.3390/molecules27165208
31. Zeybek, Ö., Özkılıç, Y.O., Çelik, A.İ., Deifalla, A.F., Ahmad, M., Sabri, M.M. Performance evaluation of fiber-reinforced concrete produced with steel fibers extracted from waste tire. *Frontiers in Materials*. 2022. 9. DOI: 10.3389/fmats.2022.1057128

Information about authors:

Majid Kharnoob, PhD

ORCID: <https://orcid.org/0000-0001-5922-5122>

E-mail: dr.majidkharnoob@coeng.uobaghdad.edu.iq

Received 05.03.2023. Approved after reviewing 10.07.2023. Accepted 08.12.2023.



Research article

UDC 691.3

DOI: 10.34910/MCE.124.5



Cementless binder based on high-calcium fly ash with calcium nitrate additive

K. Usanova¹ , Yu.G. Barabanshchikov¹ , S. Dixit^{2, 3, 4}

¹ Peter the Great St. Petersburg Polytechnic University, St. Petersburg, Russian Federation

² Division of Research, Uttarakhand University, Dehradun, India

³ Division of Research and Development, Lovely Professional University, Phagwara, Punjab, India

⁴ Khalifa University, Abu Dhabi, United Arab Emirates

✉ plml@mail.ru

Keywords: fly ash, microsilica, silica fume, early strength agent, calcium nitrate, X-ray diffraction analysis, strength, heat release, differential thermal analysis, heat of hydration, phase composition

Abstract. Fly ash from Berezovskaya Thermal Power Plant, containing a lot of CaO, in combination with silica fume does not expand and exhibits the properties of a binder. However, the strength of this binder is low. The addition of Ca(NO₃)₂ significantly increases the strength of the binder. The work aims to study the effect of Ca(NO₃)₂ additive on the strength, heat of hydration, and phase composition of hydration products of the binder based on high-calcium fly ash and silica fume. The results of X-ray diffraction and Differential Thermal Analysis show that the main phases formed during the hydration of binder with the calcium nitrate additive in various dosages are lime, calcium hydroxide, ettringite, CSH(II) type silicates and calcium aluminosilicates, corresponding to such minerals as gismondine, yugaveralite, goosecreekite. When hardening in water, the residual amount of lime after 7 days is sharply reduced. An increase in the dosage of Ca(NO₃)₂ from 1.5 to 11.8 % leads to a decrease in the CaO content by almost 2 times. With an increase in the dosage of calcium nitrate, the content of portlandite noticeably decreases, and a significant increase in the amount of calcium hydroaluminosilicates, especially the composition of CAS₂H₄, is observed. A study of the heat release process showed that calcium nitrate greatly accelerates the process in the first 60 minutes of hydration. However, then the composition with the addition of Ca(NO₃)₂ is inferior in the rate of heat release to binder without the additive. When testing a mortar with polyfractional sand, the addition of Ca(NO₃)₂ more than doubled the compressive strength of the mortar.

Funding: Russian Science Foundation No. 21-19-00324, <https://rscf.ru/project/21-19-00324/>

Citation: Usanova, K., Barabanshchikov, Yu.G., Dixit, S. Cementless binder based on high-calcium fly ash with calcium nitrate additive. Magazine of Civil Engineering. 2023. 124(8). Article no. 12405. DOI: 10.34910/MCE.124.5

1. Introduction

Numerous theoretical and practical studies, as well as world experience, show that industrial waste is a suitable raw material for replacing natural resources in the construction industry [1–7]. Such wastes include wastes from coal combustion at thermal power plants, blast-furnace slags and fly ash [8, 9]. A well-known solution to obtain cementless binders is also the use of fly ash [10–12].

Due to the limited supply of class “F” fly ash in the building materials market, there is a growing interest in high calcium fly ash [13, 14]. Recently, much research has been done on the use of high-calcium fly ash to produce cementless binders. Studies show that fly ash with a high content of calcium oxide has a low degree of polymerization of silicate anions and a high content of free lime, so it has a high hydration

activity and a large volume expansion upon hydration. Because the free lime crystal size in the high calcium oxide fly ash is smaller and the lattice distortion is greater, the development of expansion during hydration of this fly ash is faster. It can be made into an effective additional binder with some appropriate technical measures [15].

It has been established that three types of fly ash from the Kansk-Achinsk fuel and energy complex provide the possibility of obtaining cementless compositions with a strength of up to 35–36 MPa. It has been shown that the additional introduction of silica fume and salt effluents into the ash stone modifies the phase composition of neoformations and the microstructure, transforming it into a denser one due to the formation of new compounds in the system – gyrolite and hydrochloraluminates [16]. The features of formation of the composition and hydraulic activity of high-calcium fly ash obtained by burning Kansk-Achinsk brown coals are studied. Fly ash, selected in a dry state, can be used as a kind of binding agents, provided that they are pre-treated, which reduces the uneven change in the volume of the fly ash paste during hydration [17].

Expansion studies of a mixture of cement and mineral admixtures show that "F" class fly ash increases the expansion of cement pastes, while "C" class fly ash and silica fume decrease expansion [18]. Studies of the fly ash hydration products from the circulating fluidized bed show that the expansion of the hardened paste occurs mainly due to the formation of dihydrate gypsum and ettringite. In addition, free lime indirectly causes expansion due to its effect on ettringite crystallization [19]. There are three hypotheses that explain the mechanism of action of fly ash to enhance the expansion of mixtures. The first hypothesis is that expanding mixtures containing fly ash produce more ettringite than mixtures without fly ash. The second hypothesis is that the lower stiffness of concrete containing fly ash results in higher expansion. The third hypothesis says that fly ash delays the hydration of expanding compounds in mixtures [20].

The reactions of hydration of expanding type K cement pastes and the effect of silica fume have been studied. In pastes with and without silica fume, expansion is associated with the formation of ettringite. The expansion continues until ettringite is formed. The rate and magnitude of expansion at an early age (the first two days of hydration) are higher when silica fume is added to the expanding cement paste. Solid phase analysis and rate curves of the pastes also show that the addition of silica fume accelerates the hydration of the paste [21]. Studies related to pore fluid analysis show that in expanding type K cement paste without silica fume, ettringite formation and subsequent expansion cease due to depletion of SO_4^{2-} in the pore fluid after 11 days of hydration. In the presence of silica fume, the initial formation of ettringite is accelerated, which leads to an increase in the rate and magnitude of expansion [22]. However, as shown in [23], in the case of using high-calcium fly ash as an independent binder, silica fume is an agent that blocks the expansion of fly ash mixtures. The low hardening rate and low strength of the fly ash-silica binder suggests the study of additives that accelerate the hardening of cement compositions.

One of the accelerating agents is calcium nitrate, which effectively increases the setting and hardening rate of Portland cement. The mechanism of action of $\text{Ca}(\text{NO}_3)_2$ in the cement paste is to increase the concentration of Ca^{2+} ions, which contributes to the saturation of the solution and more rapid formation of $\text{Ca}(\text{OH})_2$ [24]. A comparison of three accelerating agents for pozzolanic Portland cement [25] shows that calcium nitrate is inferior in efficiency to calcium formate, which, in turn, is inferior to triethanolamine in the compressive strength of the cement mortar. It should be borne in mind that the effectiveness of calcium nitrate depends on the type of cement used. The results [26] show that calcium nitrate itself acts as a set accelerator, but it has a relatively small positive effect on the long-term development of mechanical strength. The combined addition of calcium nitrate and triisopropanolamine has shown significant and promising results at a very early age in terms of both setting acceleration and hardening acceleration.

The effect of calcium nitrate on white Portland cements is presented in [27] in various compositions of fresh cement paste after 7 and 28 days of hardening. The addition of calcium nitrate reduced the setting time and setting time of the specimens. In addition, the smaller size of the ettringite needles was established, and the plasticizing effect of calcium nitrate observed at an early stage of hydration. Flexural and compressive tests on cement specimens without the addition of sand or aggregates were carried out after curing at 7 and 28 days. The results showed a non-monotonic evolution of mechanical strength with calcium nitrate content. Diffractometry, SEM, and NMR relaxometry performed on specimens after final bending tests revealed changes in C-S-H gel morphology, an increase in the proportion of capillary pores, and an increase in the degree of carbonation with calcium nitrate content for older specimens.

Tests of commercial CEM I 52.5 R show that $\text{Ca}(\text{NO}_3)_2$ accelerates the silicate reaction and significantly influences the initial formation of the AFm and ettringite phases. In the presence of $\text{Ca}(\text{NO}_3)_2$, the dissolution rates of gypsum and anhydrite increase, and the formation of ettringite increases, especially at the highest analyzed dosage of 5 % $\text{Ca}(\text{NO}_3)_2$ by weight. In addition, significant amounts of NO_3 -AFm are formed in the presence of $\text{Ca}(\text{NO}_3)_2$. Calcium nitrate shortens the time it takes for alite to rapidly hydrate. In addition to a significant increase in Ca^{2+} ions, there is a decrease in the concentration of Al^{3+} in the pore solution, which can also accelerate the hydration of alite in the presence of $\text{Ca}(\text{NO}_3)_2$ [28]. An increase in

the amount of ettringite present in the cement structure in the form of non-oriented needles is evidenced by SEM micrographs taken on the 28th day of cement slurry curing using NC [29].

A study [30] considers class C fly ash in the presence of various concentrations of calcium nitrate. Tests have shown that calcium nitrate accelerates the hydration of the calcium aluminate phases with respect to dosage. The new products consist of calcium aluminate hydrate and nitrate. Evidence suggests that modified nitrate hydrates compete with or inhibit calcium aluminate sulfate hydrates.

The work aims to study the effect of $\text{Ca}(\text{NO}_3)_2$ additive on the strength, heat of hydration, and phase composition of hydration products of the binder based on high-calcium fly ash and silica fume.

Tasks of the research:

1. Determination based on the results of X-ray Diffraction Analysis (XRD) what interactions occur in the "fly ash – silica fume – $\text{Ca}(\text{NO}_3)_2$ " system and how these interactions affect the hydration.
2. Differential Thermal Analysis (DTA) of cementless binder specimens with different content of $\text{Ca}(\text{NO}_3)_2$ additive.
3. Experimental study of the $\text{Ca}(\text{NO}_3)_2$ additive on the heat release of cementless binder.
4. Experimental study of the effect of the $\text{Ca}(\text{NO}_3)_2$ additive on the compressive strength of specimens from a mortar with polyfractional standard sand.

2. Materials and Methods

2.1. Characteristics of Fly Ash Collected from Electrostatic Precipitators

The work uses high-calcium fly ash from Berezovskaya Thermal Power Plant. The bulk density is 1.09 g/cm^3 , the true density is 3.09 g/cm^3 , the median particle size is $7.7 \text{ }\mu\text{m}$, and the Blaine specific surface area is $2815 \text{ cm}^2/\text{g}$. The chemical composition of coal fly ash from the Berezovsky deposit is given in Table 1.

Table 1. Chemical composition of the fly ash specimen.

CaO	SiO ₂	Al ₂ O ₃	Fe ₂ O ₃	MgO	P ₂ O ₅	SO ₃	K ₂ O	Na ₂ O	Chlorine ion	C	Loss on ignition
42.2	26.8	6.49	6.09	7.05	<0.1	2.86	0.23	0.43	<0.05	2.33	3.44

The results of X-ray diffraction analysis (XRD) obtained earlier in [23] showed that about 15 % of free calcium oxide is contained in fly ash. In addition, the main minerals of this fly ash include aluminates, silicates, aluminosilicates, calcium ferrites, and aluminum and magnesium oxides (Table 2). TiO₂, MnO₂, P₂O₅ are present in small amounts. Minerals such as brownmillerite, andradite, merwinite, grossular, and quartz have been identified [23].

High-calcium fly ash, when mixed with water, seizes and hardens. However, due to the presence of a large amount of free lime, its hardening is accompanied by strong expansion and cracking.

Table 2. Composition of fly ash according to X-ray phase analysis.

Crystal phases	Chemical composition of phases	Conditional content [%]
Lime	Ca O	62.39
Graphite	C	12.81
Periclase	Mg O	7.3
Brownmillerite	4CaO·Al ₂ O ₃ ·Fe ₂ O ₃	3.71
Andradite	3CaO·Fe ₂ O ₃ ·3SiO ₂	3.62
Merwinite	3CaO·MgO·2SiO ₂	3.39
Millosevichite	Al ₂ (SO ₄) ₃	1.97
Calcium Aluminum Oxide	3CaO·Al ₂ O ₃	1.92
Grossular	3CaO·Al ₂ O ₃ ·3SiO ₂	1.06
Aluminum Oxide	Al ₂ O ₃	0.54
Yeelimite	3CaO·Al ₂ O ₃ ·CaSO ₄	0.51
Kilchoanite	3CaO·2SiO ₂	0.41
Quartz	SiO ₂	0.38

The X-ray diffraction pattern corresponding to Table 2 is shown in Fig. 1.

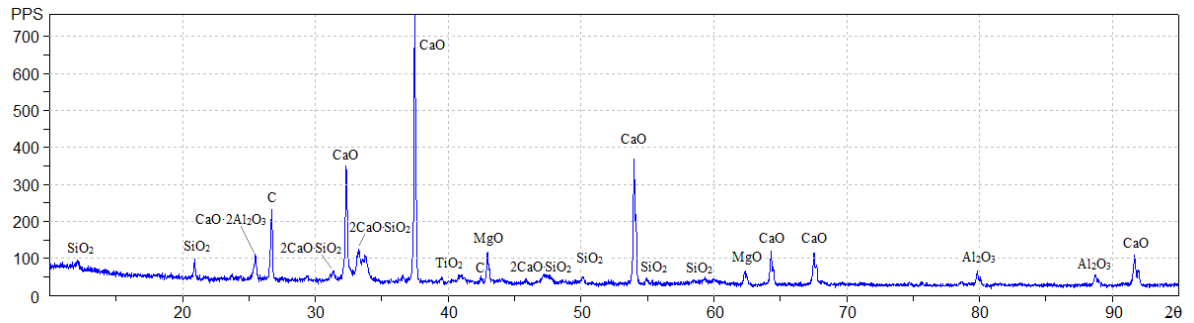


Figure 1. X-ray diffraction pattern of fly ash.

2.2. Determination of Compressive Strength

The compressive strength of the specimens consisting of fly ash-silica fume binder with $\text{Ca}(\text{NO}_3)_2$ additive was determined on test cube with dimensions of $32 \times 32 \times 32$ mm. 4 mixtures were tested, differing in the dosage of $\text{Ca}(\text{NO}_3)_2$ additive (from 1.5 to 11.8 % of the fly ash mass). The content of silica fume in the mixture was 30.4 % of the fly ash mass. The additive was introduced into the mixture in the form of an aqueous solution. The water content in the solution was considered in the calculation of the water/binder ratio (W/B). The water content in the finished mixture was selected so as to obtain mixtures with the same consistency. At the same time, W/B increases with increasing dosage of $\text{Ca}(\text{NO}_3)_2$ from 0.41 to 0.43. 6 specimens of each mixture were prepared. Demolding of the specimens was carried out after 2 days. Immediately after demolding, 3 out of 6 specimens were placed in water, and the other 3 were left to harden in sealed containers. This prevented the specimens from drying out and excluded their contact with the outside air in the laboratory, the temperature of which was regulated and amounted to (20 ± 2) °C. The specimens of both dry and wet hardening were tested for compressive strength after 7 days from the date of manufacture. Before testing, the state of the specimens was visually assessed, the presence of expansion and cracks.

The compressive strength of the specimens of fly ash-sand mortar (Table 3) was determined on test cube with dimensions of $7 \times 7 \times 7$ cm. Specimens were tested at the age of 28 days, in the amount of 3 pieces per test. The specimens were stored in a laboratory room with a temperature of (20 ± 2) °C, for the first 7 days in covered forms, and the rest of the time in a desiccator above water.

Table 3. Compositions and designation of specimens for determining strength and heat release.

Material	Consumption of materials [kg/m ³]		
	Q1	Q4	Q6
Fly ash	210	210	210
Silica Fume MKU-85	-	90 (42.9 %)	90 (42.9 %)
$\text{Ca}(\text{NO}_3)_2$ (dry)	-	-	24.8 (11.8 %)
Polyfractional sand	1645	1476	1451
Water	318	340	330
Total	2173	2116	2106

The compressive strength of all specimens was determined using a PGM-50MG4 hydraulic test press with a maximum force of 50 kN. During the test, the loading rate was maintained (50 ± 10) kPa/s.

2.3. Influence of Calcium Nitrate on Phase Composition of Hydration Products of Fly Ash-Silica Fume Binder

The use of X-ray diffraction analysis and differential thermal analysis was aimed at establishing what interactions occur in the fly ash-silica fume- $\text{Ca}(\text{NO}_3)_2$ system and how they affect the hydration and strength of the fly ash stone. Both analyzes were performed as described in [23].

The analyses were performed on specimens of the fly ash-silica fume binder compositions listed in Table 4.

Table 4. Component content of binder.

Component type	Component content in composition of binder [%]		
	Mix 1	Mix 2	Mix 3
Fly ash	100	70	64.7
Silica Fume MKU-85	–	30	27.7
Ca(NO ₃) ₂	–	–	7.6
Water-solid ratio	1.2	0.42	0.50

Semiquantitative analysis of crystalline phases in the specimens was carried out on a Dron 7 X-ray diffractometer produced by JSCE "Burevestnik"(Russia) with the following parameters: CuK α radiation, $\lambda = 0.15406 \text{ \AA}$, 2θ shooting range from 8° to 94° with a step of 0.02° , and an exposure of 3 and 5 s.

Differential thermal analysis (DTA) was performed on the device "Termoscan" produced by LLC "Analitpribor" (Russia). The specimens for DTA had a mass of about 0.7–0.8 g. The specimens were heated to a temperature of 950–1000 °C.

2.4. Influence of Calcium Nitrate on Heat release of Fly Ash-Silica Fume Binder

The heat release of the specimens consisting of fly ash-silica fume binder and sand was determined experimentally by the semi-adiabatic (thermos) method according to EN 196-9:2010. The test procedure is described in detail [23]. To obtain comparable results, the heat release of concrete obtained by the semi-adiabatic method at an initial concrete temperature of 20 °C was calculated to an isothermal hardening regime at a temperature of 20 °C using the reduced time hypothesis [31].

The heat release of the binder was determined in the composition of a mortar with standard polyfractional sand on cylindrical specimens with a diameter of 62 mm and a height of 160 mm. Three compositions of the mortar were tested (designation Q1, Q4, Q6) with the same amount of fly ash, but with a different combination of additives (Table 3).

3. Results and Discussion

3.1. Compressive strength test results

The test results are shown in Table 5. For comparison Table 5 also shows the strength of the same fly ash-silica binder with the addition of MgCl₂ according to [23].

Table 5. Compressive strength of specimens with different accelerating agents.

Ca(NO ₃) ₂ content [% by weight of fly ash]	Compressive strength [MPa]			
	Ca(NO ₃) ₂		MgCl ₂	
	dry	in water	dry	in water
1.5	3.5	0	2.9	0
4.7	2.7	0	8.3	0
8.2	8.8	0.38	9.8	1.92
11.8	10.4	1.15	15.2	2.3

The addition of Ca(NO₃)₂ showed a relatively low result compared to the addition of MgCl₂. With the same additive content of 11.8 %, the compressive strength of the specimens was 10.4 and 15.2 MPa, respectively.

The appearance of specimens with Ca(NO₃)₂ is shown in Fig. 2. It can be seen that the specimens of dry hardening with a low content of Ca(NO₃)₂ (1.5 % and 4.7 %) underwent cracking. In water, specimens of these compounds swelled and cracked even more. Specimens with a high content of Ca(NO₃)₂ (8.2 %–11.8 %) passed the test without cracking during dry hardening. In water, however, there was a slight expansion of these specimens and slight cracking.

The addition of Ca(NO₃)₂ is inferior in strength to magnesium chloride, but unlike chloride salts, it does not cause corrosion of steel reinforcement and therefore can be considered as an accelerator for reinforced concrete. Calcium nitrate does not cause cracking and expansion at high dosages (8.2%–11.8 %) and dry curing conditions, however, does not provide water resistance (Fig. 2). The softening coefficient is 0.04–0.11.

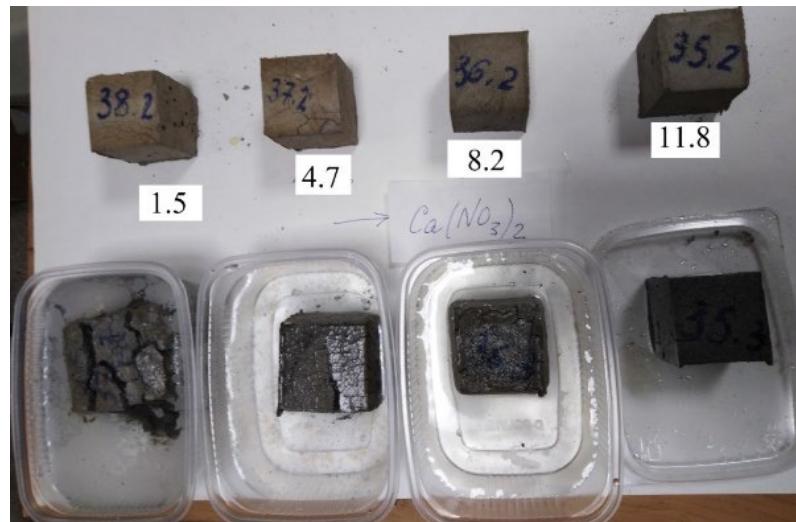


Figure 2. Specimens with $\text{Ca}(\text{NO}_3)_2$ additive. The top row is specimens hardening in dry conditions; bottom row is specimens hardening in water.

3.2. Results of X-ray diffraction analysis

X-ray patterns of the specimens of mixes presented in Table 4 after curing are shown in Fig. 3.

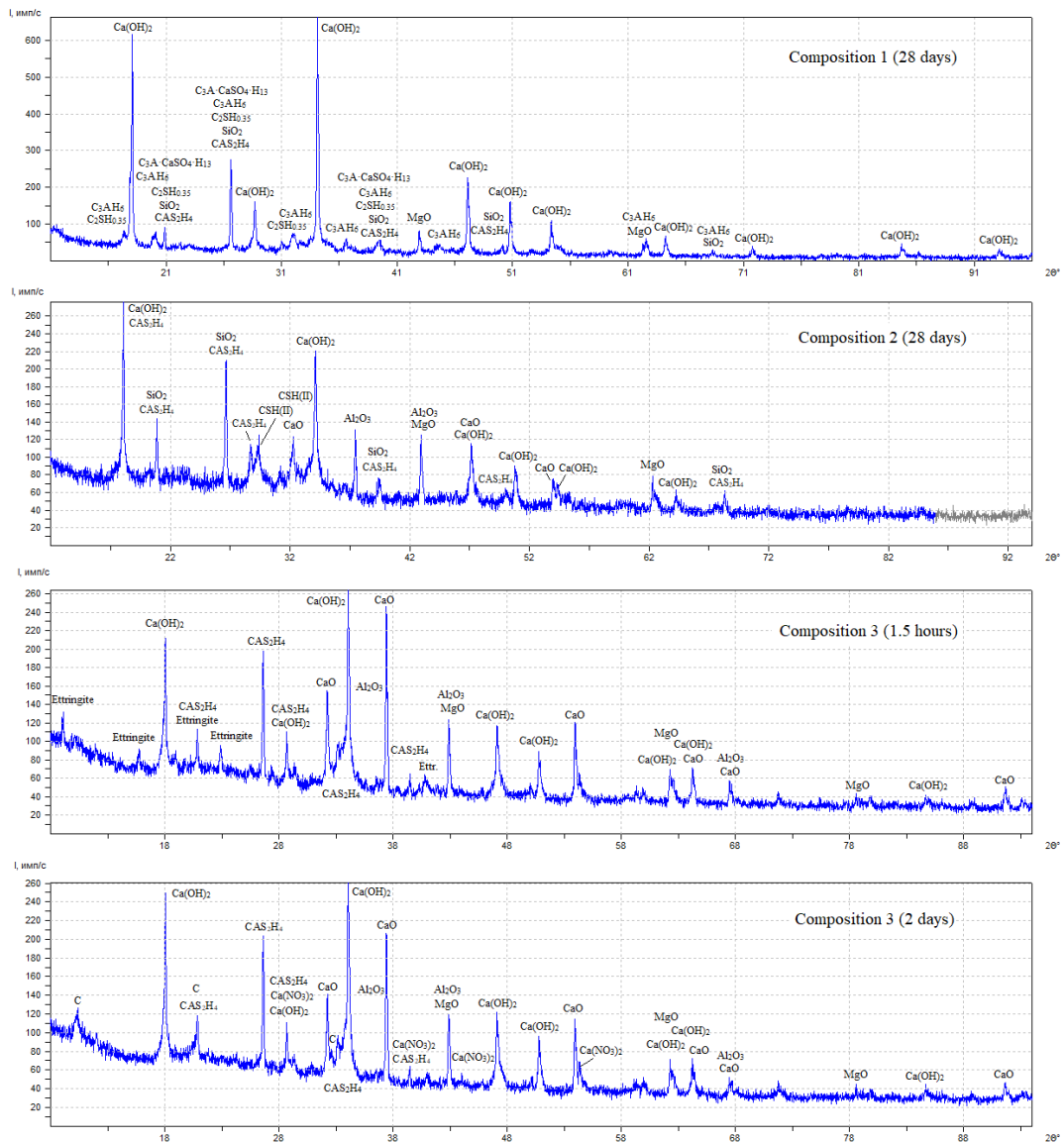


Figure 3. X-ray diffraction pattern of mixes after curing (Table 4).

A semi-quantitative analysis was carried out using the integral values of the intensity of the X-ray peaks. The obtained conditional values of the percentage of identified hydrated phases are given in Table 6.

Table 6. Conventional values of percentage of identified phases.

Phase	Chemical composition of phase	Mix 1 (28 days)	Mix 2 (28 days)	Mix 3	
				1.5 h	2 days
Lime	CaO	-	12.8	43.0	30.2
Portlandite	Ca(OH) ₂	85.4	41.8	37.2	35.0
Katoite	C ₃ AH ₆	11.1	-	-	-
Gismondine	CAS ₂ H ₄	-	27.5	11.2	18.9
Calcium Aluminum Silicate Hydrates	CAS ₆ H ₄	-	-	-	7.1
Katoite silication	C ₃ ASH ₄	-	2.7	-	-
Calcium Silicate Hydrates	CSH(II)	-	15.2	-	8.7
Calcium Aluminum Oxide Sulfate Hydrate	C ₃ A·CaSO ₄ ·H ₁₃	3.5	-	-	-
Ettringite	C ₃ A·3CaSO ₄ ·H ₃₂	-	-	8.6	-

Consideration of the data in Table 6 allows us to draw the following conclusions.

1. In the absence of silica fume and Ca(NO₃)₂ (mix 1), the interaction of fly ash with water for 28 days led to the complete hydration of CaO_{free}. At the same time, calcium hydroxide was formed in the overwhelming amount from the products of hydration. Its amount was 85.4 % of the mass of the identified phases. Hydrosilicates in crystalline form were not found. Of the calcium hydroaluminates, C₃AH₆ was present (11.1 %). A small proportion (3.5 %) was the low sulfate form of calcium hydrosulfoaluminate.

2. The addition of silica fume to the fly ash (mix 2) slowed down the hydration of lime. This corresponded to the effect of silica impurities on the rate of quenching of air lime. After 28 days of hydration, the fly ash still contained a significant amount of unreacted CaO_{free} (12.8 %) and the Ca(OH)₂ content almost halved compared to mix 1 as a result of the action of silica fume. This was indicated by the significant content of calcium silicates and aluminosilicates formed. The effect of silica fume on the hydration of high-calcium fly ash was considered by us in more detail in [23].

3. The effect of Ca(NO₃)₂ (mix 3) was investigated for two hydration periods. After 1.5 hours, a significant amount of unreacted CO_{free} (43 %) remained in the binder, and 37.2 % Ca(OH)₂ was formed. Calcium silicate hydrates were absent, which was explained by insufficient time for reactions to occur and crystallization of hydration products. An analysis of the literature shows that, the interaction between Ca(OH)₂ and SiO₂ was noticeable approximately 3 days after the onset of hydration. Aluminosilicate CAS₂H₄, corresponding in composition to the natural mineral Gismondine, and calcium hydrosulfoaluminate of the trisulfate form (ettringite) were quite clearly identified. By the age of 2 days, calcium silicate hydrates of the tobermorite group CSH(II) according to Taylor were formed, the content of gismondine increased, and calcium aluminosilicate of composition CAS₆H₄ appeared.

A semi-quantitative X-ray phase analysis was also carried out for specimens of fly ash-silica fume binder with the calcium nitrate additive, which were previously tested for strength (Table 5). The results of X-ray phase analysis are given in Table 7, and the X-ray diffraction pattern is given in Fig. 4.

Table 7. Conventional values of percentage of identified phases resulting from hydration of binder consisting of fly ash and silica fume.

Phase	Chemical composition of phase	Dry curing				Water curing	
		Ca(NO ₃) ₂ content [% by weight of fly ash]					
		1.5	4.7	8.2	11.8	1.5	11.8
Portlandite	Ca(OH) ₂	47.4	34.0	24.4	20.8	33.6	32.1
Lime	CaO	21.8	21.1	25.6	17.4	6.8	3.5
Calcite	CaCO ₃	0.8	0.7	9.7	2.0	13.2	0.8
Ettringite	C ₃ A·3CaSO ₄ ·H ₃₂	8.4	9.4	14.2	9.3	10.8	10.8
Gismondine	CAS ₂ H ₄	-	8.7	23.9	37.2	8.2	21.5
Yugawaralite	CAS ₆ H ₄	7.9	-	2.2	1.0	2.9	3.9
Goosecreekite	CAS ₆ H ₅	-	16.6	-	12.4	9.5	7.7
Calcium Silicate Hydrate	CSH(II)	13.8	9.6	-	-	15.0	19.7

Table 7 shows only those phases that are formed in the binder as a result of hydration and accompanying reactions and which are most often repeated in the studied compositions. The total content of these phases is taken as 100 %.

The main identified phases that satisfy this condition are lime, calcium hydroxide, ettringite, CSH(II) type silicates, and calcium aluminosilicates corresponding to such minerals as gismondine, yugavalite, and goosecreekite. The influence of $\text{Ca}(\text{NO}_3)_2$ on CaO hydration during dry hardening is manifested to a small extent. The residual content of free lime slightly fluctuates relative to the average value of 21.4 % with a tendency to decrease with an increase in the $\text{Ca}(\text{NO}_3)_2$ amount. With water curing, the amount of lime is sharply reduced to an average of 5.2 %. In this case, an increase in the dosage of $\text{Ca}(\text{NO}_3)_2$ from 1.5 to 11.8 % leads to a decrease in the CaO content by almost 2 times. With an increase in the dosage of calcium nitrate, the content of portlandite noticeably decreases, obviously due to the reaction with silica, and the amount of calcium hydroaluminosilicates increases significantly, the total content of which increased by 6.4 times during dry curing, and 1.6 times during water curing. However, calcium hydrosilicates during dry storage are observed only in the case of a low dosage of $\text{Ca}(\text{NO}_3)_2$ additive (1.5 % and 4.7 %). At higher dosages they are not identified. Specimens hardened in water show the presence of hydrosilicates in a significant amount and, the greater, the higher of the additive content. Ettringite does not show a pronounced dependence on the additive dosage and hardening conditions; its content in all compositions remained approximately the same. Thus, the addition of calcium nitrate mainly intensifies the formation of calcium aluminosilicate hydrates, especially of the composition CAS_2H_4 . Reaction products of $\text{Ca}(\text{NO}_3)_2$ with calcium silicates and aluminates, such as calcium hydroxynitrates and hydronitroaluminates, which are usually formed during hardening of Portland cement with the calcium nitrate addition, are not found. Perhaps their formation occurs at the molecular level in the form of X-ray amorphous mass.

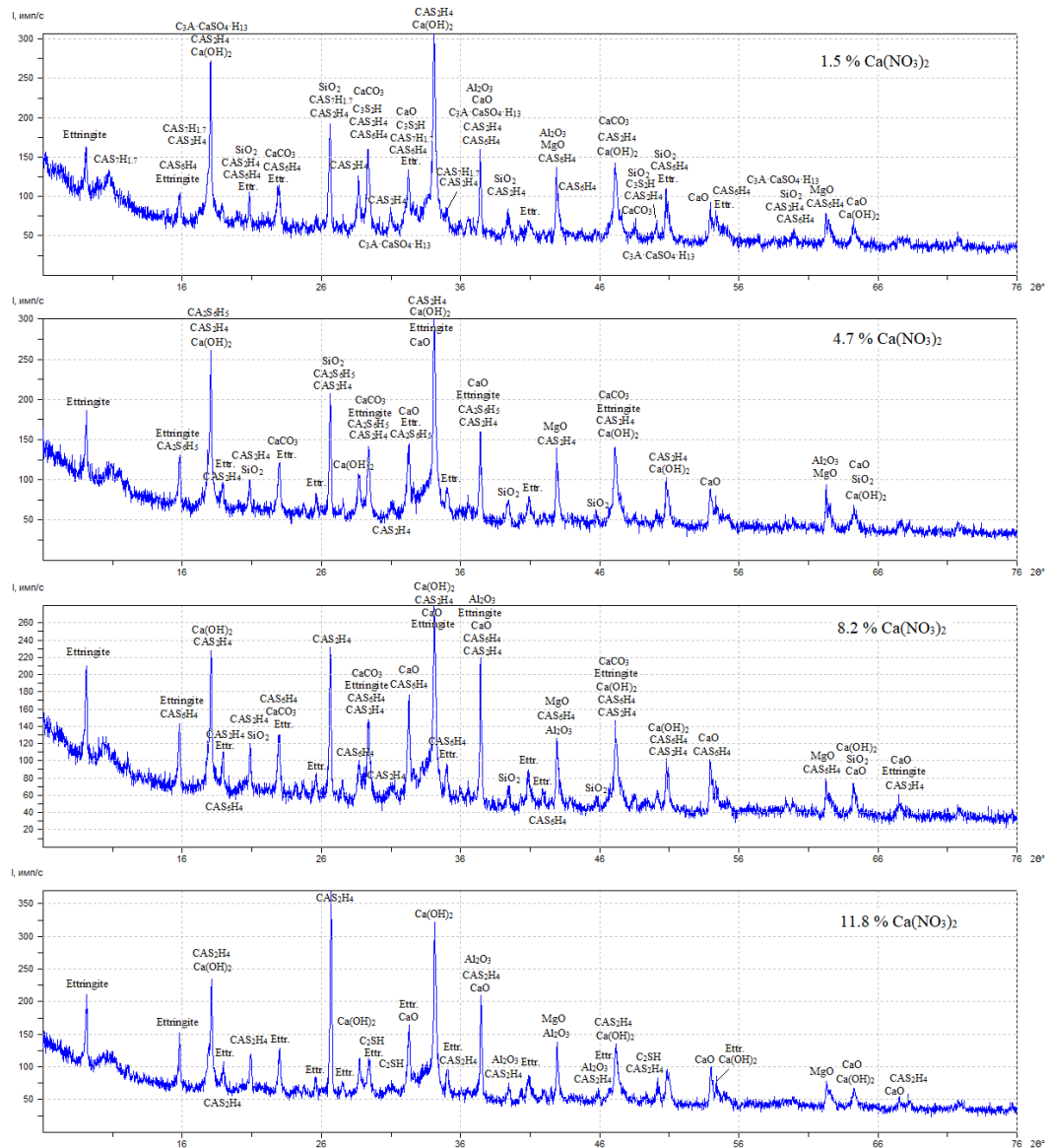


Figure 4. X-ray diffraction pattern of mixes with $\text{Ca}(\text{NO}_3)_2$ additive pre-tested for strength (Table 5).

3.3. Results of differential thermal analysis

Fig. 5 shows the DTA curves for mixes 2 and 3 at different ages (Table 4).

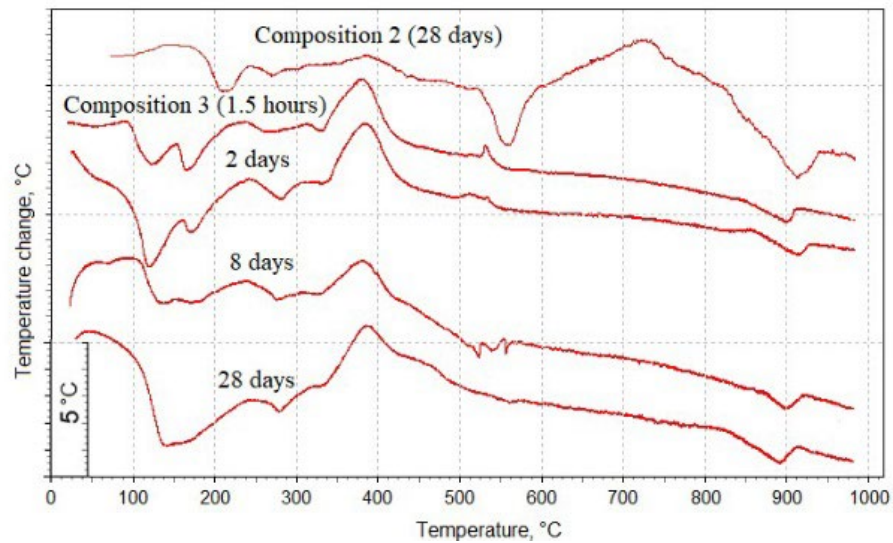


Figure 5. DTA curves of mix 2 (without $\text{Ca}(\text{NO}_3)_2$) and mix 3 with $\text{Ca}(\text{NO}_3)_2$ additive of 11.8 % at different ages.

The thermogram of mix 2 shows 3 pronounced endothermic peaks at 210, 560, and 915 °C. The first of them may correspond to the loss of interlayer water in tobermorite. The effects at 560 and 915 °C refer to the decomposition of $\text{Ca}(\text{OH})_2$ and CaCO_3 , respectively. The exoeffect at 730 °C shows the presence of tobermorite in mix 2, which transforms into wollastonite — $5\text{CaO} \cdot 6\text{SiO}_2 \cdot 9\text{H}_2\text{O}$.

Other thermograms show a number of effects caused by the $\text{Ca}(\text{NO}_3)_2$ influence. There are two endothermic peaks in the temperature range of 120–180 °C, which may be associated with the presence of gypsum and the reaction of ettringite formation. It is possible that gypsum is formed as a result of the reaction of $\text{Ca}(\text{OH})_2$ with aluminum sulfate. The intensity of the first endoeffect increases with the specimens age, which may indicate an increase in the ettringite amount. The decrease in the second peak intensity is associated with the consumption of gypsum for the reaction. In this temperature range, the loss of adsorbed and interlayer water by hydrosilicates also usually occurs. The effect at 170–180 °C may be associated with the dehydration of the $\text{C}_2\text{S}_2\text{H}_4$ compound or other calcium alumina hydrosilicates. Endothermic peak at 280 °C observed after cement hydration for 5 hours, O.P. Mchedlov-Petrosyan et al. attribute the presence of C_2AH_7 [32]. The authors of [33] believe that at a temperature of about 280 °C, the process of dehydration of C_2AH_8 and CAH_{10} begins. Endothermic peaks at 140, 280, and 560 °C can also be attributed to calcium hydronitroaluminate $\text{C}_3\text{A} \cdot \text{Ca}(\text{NO}_3)_2 \cdot 10\text{H}_2\text{O}$.

A slight endothermic effect at 330–340 °C is associated with C_3AH_6 presence, and an exothermic peak at 380 °C indicates the transformation of soluble anhydrite into insoluble one.

The thermograms of mix 3 (Fig. 5) show almost no endothermic effect of $\text{Ca}(\text{OH})_2$ decomposition, although according to X-ray diffraction analysis, it should be present. At the same time, in the temperature range of 520–550 °C, small areas of exothermic peaks are observed, which are superimposed on the effect of $\text{Ca}(\text{OH})_2$ dehydration, blocking the heat input for the decomposition of portlandite. Since mix 2 does not show a similar effect, the addition of calcium nitrate can be considered responsible. Unfortunately, it has not yet been possible to decipher this exoeffect. Probably in this case, the burnout of unburned carbon particles occurs.

The thermograms shown in Fig. 6 characterize the effect of the $\text{Ca}(\text{NO}_3)_2$ dosage on the phase composition of the specimens consisting of fly ash, silica fume and $\text{Ca}(\text{NO}_3)_2$ additive.

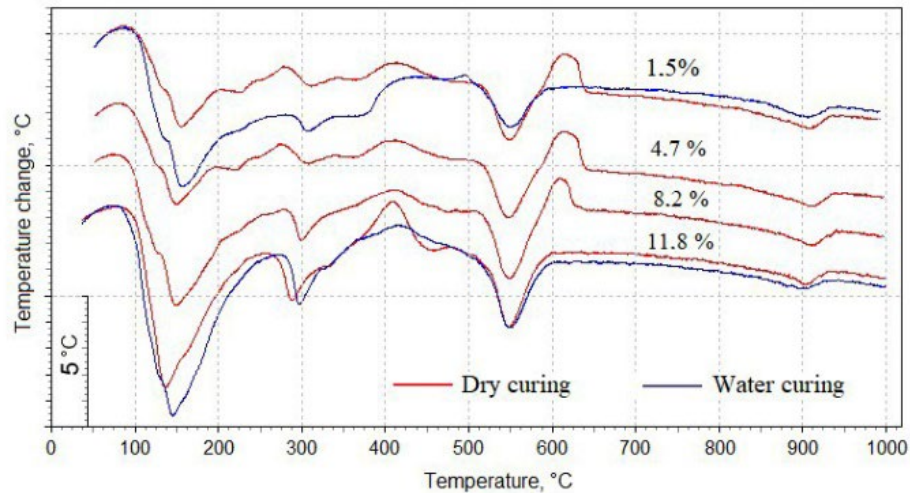


Figure 6. DTA curves of specimens with different content of calcium nitrate.

Fig. 7 shows that with an increase in the $\text{Ca}(\text{NO}_3)_2$ content, the depth of the endothermic peak sharply increases at a temperature of about 150°C , which indicates an increase in the growth of hydrates of aluminates and calcium aluminosilicates in the presence of $\text{Ca}(\text{NO}_3)_2$. In this case, the intensity of the endothermic peak at 550°C corresponding to the decomposition of $\text{Ca}(\text{OH})_2$ decreases. In these specimens, after 7 days of hydration, two endothermic effects at temperatures around 300 and 460°C can be attributed to cubic C_3AH_6 . The peak at 300°C can also be seen as offset from the effect at 280°C in the previous diagram (Fig. 5). On the thermograms in Fig. 7, two exothermic peaks are observed. The first one, at 410°C , is especially pronounced on the curve for the mix with the highest content of the $\text{Ca}(\text{NO}_3)_2$ additive (11.8 %) during dry hardening. On thermograms with a lower content of calcium nitrate, this effect is more blurred and insignificant. A similar exothermic effect (also at 11.8 % $\text{Ca}(\text{NO}_3)_2$) is observed on thermograms for mix 3 at the age from 1.5 h to 28 days, however, at 280°C (Fig. 5). The second exothermic peak on the thermograms of the dry curing specimens with the addition of 1.5–8.2 % $\text{Ca}(\text{NO}_3)_2$ at 610 – 620°C is presumably associated with the burnout of carbonaceous particles.

3.4. Results of Heat Release Determination

The specific heat release of a mortar consisting of fly ash and sand, per 1 kg of fly ash at a temperature of 20°C , depending on the composition, is shown in Fig. 7.

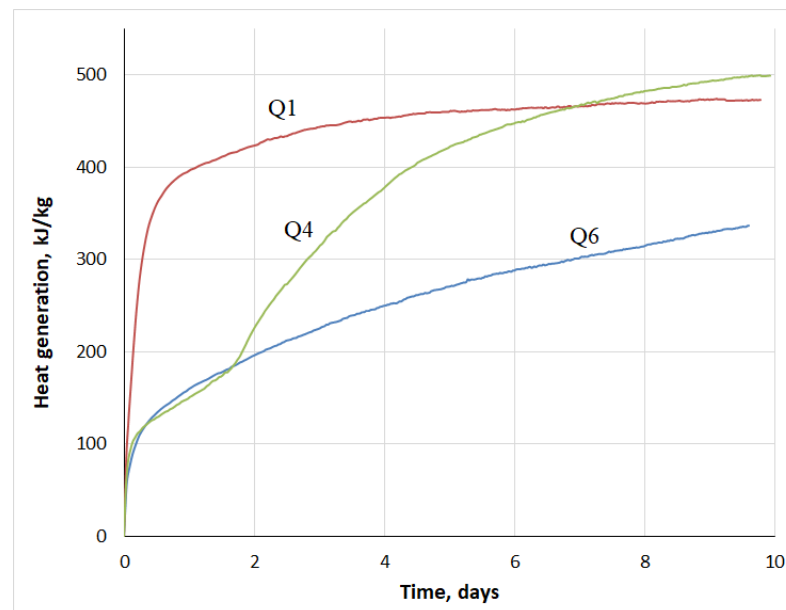


Figure 7. Specific heat release of mortar per 1 kg of fly ash at temperature of 20°C , depending on composition: Q1 is mix without additives; Q4 is mix with MS additive of 42.9 %; Q5 is mix with additives: MS of 42.9 % and $\text{Ca}(\text{NO}_3)_2$ of 11.8 %.

Pure fly ash (curve Q1) reacts very violently with water due to the slaking of free lime. Approximately 1 day after intense heat release, the process slows down sharply and ends by the fourth day. In the

presence of silica fume (curve Q4), a sharp slowdown of the heat release process is observed. By the end of the second day, the reaction rate increases again and on the 10th day the heat release is higher than that of pure fly ash. The addition of $\text{Ca}(\text{NO}_3)_2$ (curve Q6) provides a reduced heat release of the mortar. In the initial period up to 1.5 days, curves Q4 and Q6 practically coincide. This indicates that the hydration process during this period is controlled by silica fume, and the retarding effect of calcium nitrate begins to affect later. At the same time, the heat release rate (the angle of inclination of the tangent to curves Q4 and Q6) for mix Q6 is higher than for mix Q4, and it should be expected that by a certain long term of hydration, the integral values of their thermal effects will become equal. Thus, the $\text{Ca}(\text{NO}_3)_2$ additive blocks the accelerating effect of silica, starting from 1.5-2 days of hydration.

Heat release experiments require a certain amount of time for preparing the mix, preparing the specimens, placing the specimens in thermoses, etc. In our case, this time is about 30 minutes. During this period, intense heat release occurs, however, it is not recorded in the experiment. Therefore, we made additional tests to increase the temperature of the paste based on fly ash and additives during the first 1 hour of hydration. The mixes of the test are given in Table 8.

Table 8. Mixes for determining temperature in initial period of hydration.

Material	Consumption of materials [kg/m ³]		
	T1	T4	T6
Fly-ash	30	30	30
Silica Fume MKU-85	–	12.9 (42.9 %)	12.9 (42.9 %)
$\text{Ca}(\text{NO}_3)_2$ (dry)	–	–	3.54 (11.8 %)
Water	19.5	27.9	30.2
Total	49.5	70.8	76.64

The test procedure was presented in detail in [23]. Each mix was tested twice and the average value was taken. The results of measuring the temperature of the paste consisting of fly ash and silica fume are shown in Fig. 8.

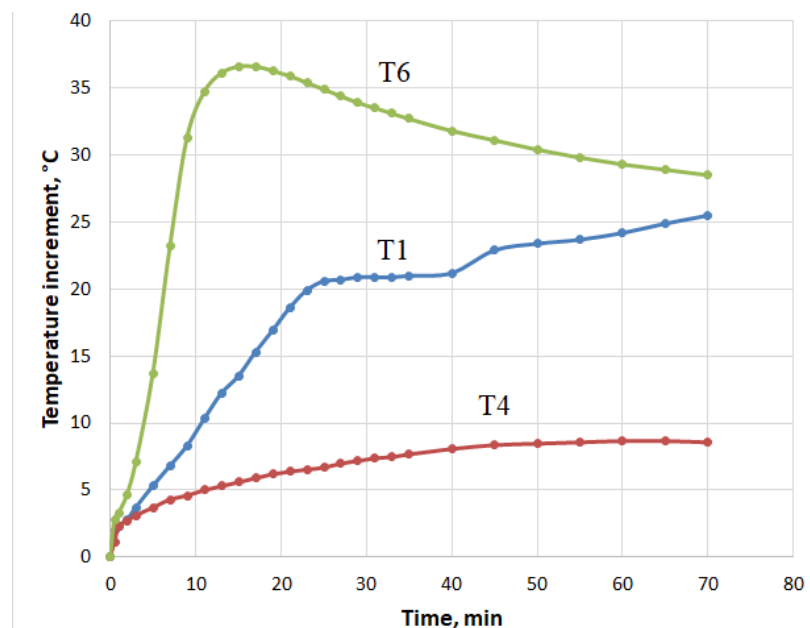


Figure 8. Temperature increase of specimens depending on mix: T1 is fly ash without additives; T4 is fly ash with MS additive of 42.9 %; T6 is fly ash with MS additive of 42.9 % and $\text{Ca}(\text{NO}_3)_2$ additive of 11.8 %.

Fig. 8 shows that the temperature of the fly ash (mix T1) for 1 hour of hydration increased by 24.2 °C against the initial one. At the same time, in the presence of silica fume (mix T2), the hydration rate dropped sharply, and the temperature of the paste increased by only 8.7 °C. Here, the same regularity of silica fume effect was observed as in the initial period of hardening of the mortar consisting of fly ash and silica fume (Fig. 7). The introduction of the $\text{Ca}(\text{NO}_3)_2$ additive led to an exceptionally sharp rise in temperature in the first 15 min after mixing. The temperature increase during this time was 36.6 °C.

Thus, calcium nitrate is a strong accelerator of the initial stage of the hydration process, which can be estimated at 30–60 minutes. After the initial stage, up to a period of about 1.5 days, there follows a

period when the heat release of binder, both with and without the $\text{Ca}(\text{NO}_3)_2$ additive, proceeds practically at the same level. That is, the supplement during this period does not accelerate or slow down the hydration process. In the next third period, a low monotonous increase in heat release Q6 continues (Fig. 7), while the composition without additive shows a sharp increase in heat release (curve Q4)

3.5. Influence of Calcium Nitrate on Strength of mortar consisting of Fly Ash and Sand

The results of determining the compressive strength of the specimens are shown in the diagram in Fig. 9.

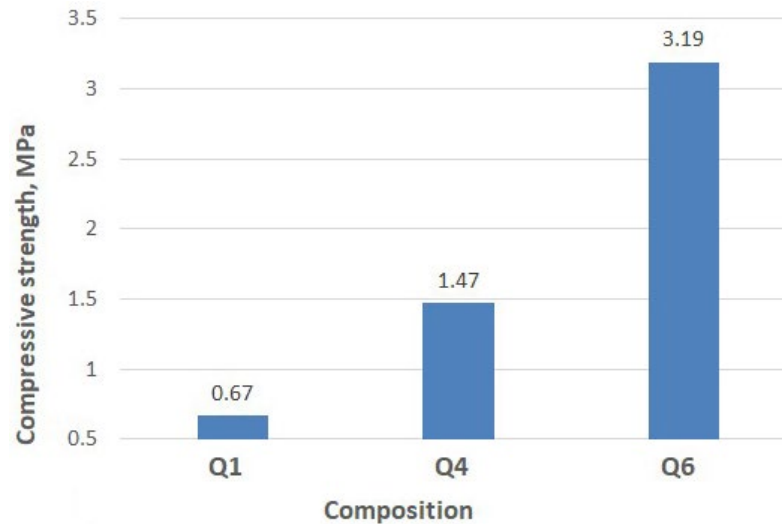


Figure 9. The results of determining compressive strength of specimens of mortar: Q1 is mix without additives; Q4 is mix with MS additive of 42.9 %; Q5 is mix with additives: MS of 42.9 % and $\text{Ca}(\text{NO}_3)_2$ of 11.8 %.

Fig. 9 shows, that the silica fume additive increased the strength of the specimens by approximately 100 %, and when $\text{Ca}(\text{NO}_3)_2$ was added to the mortar consisting of fly ash, silica fume and sand, the strength increased by more than two times.

It should be noted the low strength of the tested mixes of the mortar, however, it must be borne in mind that the binder/sand ratio in these mixes ranges from 1:5 to 1:7.

4. Conclusions

This paper presented the results of experimental studies conducted to evaluate the influence of $\text{Ca}(\text{NO}_3)_2$ additive on the strength, heat of hydration, and phase composition of hydration products of the binder based on high-calcium fly ash and silica fume. The following key conclusions were drawn from this study:

1. The effect of $\text{Ca}(\text{NO}_3)_2$ (mix 3, Table 4) was studied using XRD and DTA. After 1.5 h of hydration, a significant amount of unreacted CO_{free} (43 %) remains in the paste and 37.2 % $\text{Ca}(\text{OH})_2$ is formed. Aluminosilicate CAS_2H_4 , corresponding in composition to the natural mineral gismondine, and calcium hydrosulfoaluminate of the trisulfate form (ettringite) are quite clearly identified. By the age of 2 days calcium silicate hydrates of the tobermorite group are formed, the content of gismondine increases, and calcium aluminosilicate of the composition CAS_6H_4 appears. The main phases identified in specimens aged 7 days at different $\text{Ca}(\text{NO}_3)_2$ content are lime, calcium hydroxide, ettringite, CSH(II) type silicates, and calcium aluminosilicates, corresponding to such minerals as gismondine, yugaveralite, and goosecreekite. The influence of $\text{Ca}(\text{NO}_3)_2$ on CaO hydration during dry hardening is manifested to a small extent. The residual content of free lime slightly fluctuates relative to the average value of 21.4 % with a tendency to decrease with an increase in the $\text{Ca}(\text{NO}_3)_2$ amount. With water curing, the amount of lime is sharply reduced to an average of 5.2 %. In this case, an increase in the $\text{Ca}(\text{NO}_3)_2$ content from 1.5 to 11.8 % leads to a decrease in the CaO content by almost 2 times. With an increase in the dosage of calcium nitrate, the content of portlandite noticeably decreases, obviously due to the reaction with silica, and a significant increase in the amount of calcium hydroaluminosilicates, the total content of which increased by 6.4 times during dry curing, and 1.6 times during water storage. The specimens hardened in water show the presence of hydrosilicates in a significant amount and in positive relation to the additive content. Thus, the calcium

nitrate additive mainly intensifies the formation of calcium aluminosilicate hydrates, especially of the composition CAS_2H_4 .

2. With an increase in the $\text{Ca}(\text{NO}_3)_2$ content in the binder based on fly ash and silica fume after 7 days of hydration, the depth of the endothermic peak at 150 °C on the DTA curves increases, which confirms the intensive growth of hydrates of aluminates and calcium aluminosilicates in the presence of $\text{Ca}(\text{NO}_3)_2$. In this case, the intensity of the endothermic effect at 550 °C, corresponding to the decomposition of $\text{Ca}(\text{OH})_2$, decreases. Two endothermic peaks are observed at temperatures around 300 and 460 °C, which may belong to cubic C_3AH_6 . There are also two exothermic peaks. The first one, at 410 °C, increases with the content of the $\text{Ca}(\text{NO}_3)_2$ additive. Its nature has not been elucidated. The second exothermic peak at 610–620 °C is presumably associated with the burnout of carbonaceous particles.

3. A study of the heat release process showed that pure fly ash reacts very violently with water, due to the slaking of free lime. During the first day, 85 % of heat is released from the value for 10 days. Silica fume significantly slows down the heat release of fly ash in the initial period of hardening up to 1.5 days, after which a sharp rise follows, and by the end of the experiment, the heat release of the binder exceeds the value for pure fly ash. Calcium nitrate greatly accelerates the process in the first 60 minutes of hydration. However, then the mix with the $\text{Ca}(\text{NO}_3)_2$ additive is inferior in the rate of heat release to binder without additive.

4. When testing a mortar consisting of fly ash, silica fume and sand, the $\text{Ca}(\text{NO}_3)_2$ additive more than doubled the compressive strength of the mortar.

References

- Ahmad, J., Zhou, Z., Usanova, K.I., Vatin, N.I., El-Shorbagy, M.A. A Step towards Concrete with Partial Substitution of Waste Glass (WG) in Concrete: A Review. *Materials* (Basel). 2022. 15(7). P. 2525. DOI: 10.3390/ma15072525
- Ahmad, J., Martínez García, R., de Prado Gil, J., Irshad, K., El-Shorbagy, M., Fediuk, R., Vatin, N. Concrete with Partial Substitution of Waste Glass and Recycled Concrete Aggregate. *Materials*. 2022. 15. 430. DOI: 10.3390/ma15020430
- Klyuev, S., Sevostyanov, V., Sevostyanov, M., Ageeva, M., Fomina, E., Klyuev, A., Protsenko, A., Goryagin, P., Babukov, V., Shamgulov, R., Fediuk, R., Sabitov, L. Improvement of Technical Means for Recycling of Technogenic Waste to Construction Fiber. *Case Studies in Construction Materials*. 2022. 16. e01071. DOI: 10.1016/j.cscm.2022.e01071
- Petrov, V.V., Protsenko, A.E., Sapozhnik, K.R. Solid-cabide tool waste recycling technology. *Construction Materials and Products*. 2022. 5(3). Pp. 27–34. DOI: 10.58224/2618-7183-2022-5-3-27-34
- Zakrevskaya, L.V., Gavrilenko, A.A., Kapush, I.R., Lyubin, P.A. Creating ground concrete and strengthening substrates using mining waste. *Construction Materials and Products*. 2022. 5 (3). Pp. 35–44. DOI: 10.58224/2618-7183-2022-5-3-35-44
- Kashapov, R.N., Kashapov, N.F., Kashapov, L.N., Klyuev, S.V., Chebakova, V.Yu. Study of the plasma-electrolyte process for producing titanium oxide nanoparticles. *Construction Materials and Products*. 2022. 5 (5). Pp. 70–79. DOI: 10.58224/2618-7183-2022-5-5-70-79
- Kashapov, R.N., Kashapov, N.F., Kashapov, L.N., Klyuev, S.V. Plasma electrolyte production of titanium oxide powder. *Construction Materials and Products*. 2022. 5 (6). Pp. 75–84. DOI: 10.58224/2618-7183-2022-5-6-75-84
- Barabanshchikov, Y., Usanova, K., Akimov, S., Uhanov, A., Kalachev, A. Influence of Electrostatic Precipitator Ash "Zolest-Bet" and Silica Fume on Sulfate Resistance of Portland Cement. *Materials*. 2020. 13(21). 4917. DOI: 10.3390/ma13214917
- Fediuk, R., Smoliakov, A., Timokhin, R., Batarshin, V., Yevdokimova, Yu. Using thermal power plants waste for building materials. *IOP Conference Series: Earth and Environmental Science*. 2017. 87(9). 092010. DOI: 10.1088/1755-1315/87/9/092010
- Salamanova, M., Murtazaev, S.-A., Saidumov, M., Alaskhanov, A., Murtazaeva, T., Fediuk, R. Recycling of Cement Industry Waste for Alkali-Activated Materials Production. *Materials*. 2022. 15(19). 6660. DOI: 10.3390/ma15196660
- Klyuev, S.V., Kashapov, N.F., Radaykin, O.V., Sabitov, L.S., Klyuev, A.V., Shchekina, N.A. Reliability coefficient for fibreconcrete material. *Construction Materials and Products*. 2022. 5 (2). Pp. 51–58. DOI: 10.58224/2618-7183-2022-5-2-51-58
- Alani, A., Lesovik, R., Lesovik, V., Fediuk, R., Klyuev, S., Amran, M., Ali, M., de Azevedo, A.R.G., Vatin, N.I. Demolition Waste Potential for Completely Cement-Free Binders. *Materials*. 2022. 15(17). 6018. DOI: 10.3390/ma15176018
- Giergiczny, Z. Fly ash and slag. *Cement and Concrete Research*. 2019. 124. 105826. DOI: 10.1016/j.cemconres.2019.105826
- Vatin, N., Barabanshchikov, Y., Usanova, K., Akimov, S., Kalachev, A., Uhanov, A. Cement-based materials with oil shale fly ash additives. *IOP Conf Ser Earth Environ Sci*. 2020. 578(1). 012043. DOI: 10.1088/1755-1315/578/1/012043
- Shi, H.-S. Research on intrinsic characteristics and hydration properties of fly ash with high calcium oxide. *Tongji Daxue Xuebao/Journal of Tongji University*. 2003. 31(12). Pp. 1440–1443.
- Shevchenko, V.A., Artemieva, N.A., Ivanova, L.A., Kiselev, V.P., Vasilovskaya G.V. Cement-free binder from ash-silica compositions. *Modern problems of science and education*. 2015. 1. Pp. 1–8.
- Domanskaya, I., Oleynik, V., Minyazev, D. ICSC Problems and Perspectives of high-calcium fly ash from heat power plants in the composition of "green" building materials. *E3S Web of Conferences*. 2016. 6. 01014. DOI: 10.1051/e3sconf/20160601014
- Chaunsali, P., Mondal, P. Physico-chemical interaction between mineral admixtures and OPC-calcium sulfoaluminate (CSA) cements and its influence on early-age expansion. *Cement and Concrete Research*. 2016. 80(1). Pp. 10–20. DOI: 10.1016/j.cemconres.2015.11.003
- He, S., Zhu, X.Y., Bao, W.Z., Zhao, W.X., Jin, D.M. Study on Expansion of Circulating Fluidized Bed Combustion Coal Ash. *Advanced Materials Research*. 2012. 518–523. Pp. 3501–3506. DOI: 10.4028/www.scientific.net/AMR.518-523.3501
- Bich Thi Nguyen, T., Chatchawan, R., Saengsoy, W., Tangtermsirikul, S., Sugiyama, T. Influences of different types of fly ash and confinement on performances of expansive mortars and concretes. *Construction and Building Materials*. 2019. 209. Pp. 176–186. DOI: 10.1016/j.conbuildmat.2019.03.032

21. Lobo, C., Cohen, M.D. Hydration of type K expansive cement paste and the effect of silica fume: I. Expansion and solid phase analysis. *Cement and Concrete Research*. 1992. 22(5). Pp. 961–969.
22. Lobo, C., Cohen, M.D. Hydration of type K expansive cement paste and the effect of silica fume: II. Pore solution analysis and proposed hydration mechanism. *Cement and Concrete Research*. 1993. 23(1). P. 104–114.
23. Barabanshchikov, Y., Usanova, K. Influence of Silica Fume on High-Calcium Fly Ash Expansion during Hydration. *Materials*. 2022. 15(10). 3544. DOI: 10.3390/ma15103544
24. Kicaite, A. The effect of calcium nitrate on the properties of Portland cement pastes and concrete hardening at low temperatures. *Ceramics – Silikaty*. 2020. 64(3). Pp. 1–9. DOI: 10.13168/cs.2020.0015
25. Derakhshani, A., Ghadi, A., Vahdat, S.E. Study of the effect of calcium nitrate, calcium formate, triethanolamine, and triisopropanolamine on compressive strength of Portland-pozzolana cement. *Case Studies in Construction Materials*. 2023. 18(18). e01799. DOI: 10.1016/j.cscm.2022.e01799
26. Chikh, N., Zouaoui, M., Aggoun, S., Duval, R. Effects of calcium nitrate and triisopropanolamine on the setting and strength evolution of Portland cement pastes. *Materials and Structures*. 2008. 41. Pp. 31–36. DOI: 10.1617/s11527-006-9215-8.
27. Rusu, M., Vulpoi, A., Vilau, C., Dulescu, M., Pășcuță, P., Ardelean, I. Analyzing the Effects of Calcium Nitrate over White Portland Cement: A Multi-Scale Approach. *Materials*. 2022. 16(1). 371. DOI: 10.3390/ma16010371.
28. Dorn, T., Hirsch, T., Stephan, D. Working mechanism of calcium nitrate as an accelerator for Portland cement hydration. *Journal of the American Ceramic Society*. 2023. 106(1). Pp. 752–766.
29. Belmonte, I., Soler, M., Benito, F., Costa, C., López, C., Martín, J., Pacheco, V., Torrano, P. Mineralization Reaction of Calcium Nitrate and Sodium Silicate in Cement-Based Materials. *Crystals*. 2022. 12(4). 445. DOI: 10.3390/cryst12040445
30. Russell Hill, K.D. The interaction of calcium nitrate and a Class C fly ash during hydration. *Cement and Concrete Research*. 1996. 26(7). Pp. 1131–1143.
31. Zaporozhec, D.I. Osnovy teorii teplovydeleniya betona [Fundamentals of the theory of heat generation of concrete]. Doctor Thesis. Leningrad. 1965. 33 p. (rus)
32. Ramachandran, V.S. Applications of Differential Thermal Analysis in Cement Chemistry. Chemical Publishing Company, 1969. 328 p.
33. Krivopustov, D.Yu. Fazovye prevrashcheniya cementnogo kamnya na osnove alyuminatnogo klinkera [Phase transformations of cement stone based on aluminate clinker]. *Mezhdunarodnaya nauchno-tehnicheskaya konferenciya molodyh uchenyh BGTU im. V.G. Shuhova [Conference proceedings]*. Belgorod. 2019. Pp. 2519–2522.

Information about authors

Kseniia Usanova,

ORCID: <https://orcid.org/0000-0002-5694-1737>

E-mail: plml@mail.ru

Yuriy Barabanshchikov, Doctor of Technical Sciences

ORCID: <https://orcid.org/0000-0001-7011-8213>

E-mail: ugb@mail.ru

Saurav Dixit,

E-mail: sdixit@ricsbe.edu.in

Received 20.07.2023. Approved after reviewing 15.09.2023. Accepted 21.09.2023.



Research article

UDC 624.1

DOI: 10.34910/MCE.124.6



Shear strength and chemical properties of soft clayey soil treated with magnetized water

S.I. Jawad^{1,2} , M.O. Karkush¹ 

¹ University of Baghdad, Baghdad, Iraq

² Bilad Alrafidain University College, Diyala, Iraq

✉ mahdi_karkush@coeng.uobaghdad.edu.iq

Keywords: magnetized water, magnetic field, shear strength, soft soil, vane shear, unconfined compressive strength

Abstract. Design criteria of any type of foundation are mainly depending on the shear strength of the soil founded on/in it. In this research, investigation of the effect of magnetized water (MW) on shear strength and chemical properties of soft clayey soil was investigated. The shear strength of soft soil before and after treatment by MW was measured by an unconfined compressive strength test (UCST) and vane shear test (VST). Tap water used to treat the soft soil was modified by different magnetic field intensities (2000, 4000, 6000, and 8000 Gauss). Two-time intervals were used to conduct the shear strength tests for all intensities: first, after 7 days of treatment of the soil by MW, and second after 14 days. The circulating of MW through soft clayey soil samples for 7 days shows increasing the unconfined shear strength by 17, 39, 42, and 45% for soil treated with MW of intensity 2000, 4000, 6000, and 8000 G, respectively compared to the reference soil sample treated under the same conditions with tap water (TW). Increasing the duration of treatment up to 14 days showed increasing in the UCS of soft soil by 35, 49, 92, and 120% for soil treated with MW of intensity 2000, 4000, 6000, and 8000 G, respectively. On the other hand, the shear strength (S_{uv}) measured by the vane shear device increased with increasing the intensity of the magnetic field for the same duration of treatment. The magnetized water technique can be considered as a promising and sustainable technology to be employed in geotechnical engineering to improving the geotechnical properties of soil.

Citation: Jawad, S.I., Karkush, M.O. Shear strength and chemical properties of soft clayey soil treated with magnetized water. Magazine of Civil Engineering. 2023. 124(8). Article no. 12406. DOI: 10.34910/MCE.124.6

1. Introduction

Iraq is one of the countries that have significant ratios of regions formed by sedimentation deposits, especially in the middle and southern regions. This stratigraphy consists mainly of weak soils classified as soft to very soft, which often make unfavorable conditions for construction activities. Therefore; the assessment and design of any geotechnical structures requires a good knowledge of the most important engineering issues such as the bearing capacity and settlement of these challenging types of soils. Depending on the cohesion (c) and angle of internal friction (ϕ), the shear strength of soil can be affected by several factors such as the liquid and plastic limits and the water and clay content [1]. Many criteria were adopted in order to consider the soil as soft, such as the high tendency to flow, the high plasticity behavior, saturation conditions, and also consistency index (I_c) < 0.75. Moreover, a wide range of techniques has been used to improve the geotechnical properties of soft soils such as grouting and stone columns which are considered popular techniques to reinforce the underlying foundation of the structures [2]. Sand compaction pile (SCP), dynamic compaction (DC), prefabricated vertical drain (PVD), and microbially induced calcite precipitation (MICP) are also recently used to improve soft soils [3,4]. The rapid increase in

population and growing infrastructures made the requirement of problematic soils, therefore, geotechnical engineers make a challenge to improve the soft soils in order to be used for many infrastructures facilities.

Many studies were conducted to investigate the variation of shear strength of soft soils after using different improvement techniques. Additives such as cement and lime [5], the common agents adopted as a binder for improving the strength of soil and ground improvement can be used as an additional mixture with Nano-MgO to improve strength properties and micro-structure of soft soil with a significant resulting role in unconfined compressive strength of stabilized soil [6]. Additionally, the vertical drains and pre-loading can be used to improve disturbed zone containing soft soil deposits [7]. Many categories of chemical and mechanical stabilization methods have been applied to various types of problematic soils, these types of methods are mainly based on vibration, loading of soil, soil grouting, admixtures, and other methods [8,9]. General soil stabilization methods of soft soil concluded that the soft soil properties and the strength characteristics can be improved significantly by using additives other than using mechanical stabilization methods which were depending on the decreasing voids ratio in the soil by compaction [10,11].

The current study focuses on the application of magnetized water (MW) as green technology which has an increasingly significant effect on many fields of science. In general, water can be found at the nanoscale as clusters which can be affected by factors such as temperature, pressure, and the forces applied to it [12-14]. As the water is subjected to a magnetic field, certain properties of this water will be altered, due to alteration in the water cluster and consequently the water density. Therefore, many variations in these anomalous and unique properties of water occur at the macroscopic level (the hydrogen bonds and van der Waals forces will change due to the conditions of exposing the water to the dominant existing magnetic fields [15-17]. Studies on the treatment of water magnetic field stated that the hydrogen bonds get stronger when subjected to the magnetic forces, that is to say, the increase in the energy of hydrogen bonds directly reflects the increase in the surface tension of the water [18-20]. The majority point of the study considers the MW as an environmentally friendly technology in the remediation of water and consequently the improvement of soil properties depending mainly on the bonds among soil particles as well as the intensity of the magnetic field applied to the modified water.

Various laboratory tests have been conducted to investigate the influence of using MW to improve some properties of construction materials (e.g. soil and concrete) with various purposes and different intensities of magnetized water. The previous studies showed that the MW is considered a factor that can enhance the fresh-state and hardened-state properties of the concrete when using the small intensities of magnetization technique (0, 6000, 12000, and 18000 Gauss) as well as the improvement of the mechanical performance of the concrete due to the decrement in the numbers of pores and getting more dense concrete with MW [21,22]. It has also been shown that MW can be used as an injection fluid in oil fields to substitute the extracted oil [23]. In the field of soil mechanics, the MW is used to enhance the chemical and swelling properties of expansive soil type treated by MW with several intensities of magnetic fields (500, 1000, 1500, and 2000 Gauss). The treatment by MW led to a decrease in the liquid limit and free swelling by a significant amount, resulting in the mitigation of the potential of expansive soils [24]. MW technology proved sufficient satisfactory effects in many fields of science such as agriculture, medicine, and engineering.

The shear strength of soil refers to the resistance of soil particles to sliding along each other when subjected to shear stress. It is related to the bonding between soil particles and the frictional forces that act between them. The shear strength of soil is influenced by various factors such as particle size, shape, surface roughness, mineralogy, water content, and compaction. It can be determined using various laboratory tests such as the direct shear test, triaxial shear test, vane shear test, and unconfined compression test. Overall, the shear strength of soil is an important property that influences the stability and behavior of soil in different geotechnical applications, such as foundation design, slope stability analysis, and underground excavations. The overall objective of the current study aims to investigate the influence of using several intensities of MW on the chemical properties and shear strength of the soft clayey soil for two-time intervals of the treatment process. The shear strength of soil was measured by the unconfined compressive strength test (UCST) and vane shear test (VST) after 7 and 14 days of treatment by MW.

2. *Materials and Methods*

The material used herein basically includes the water and the soil samples. In this study, tap water was used for the treatment of soft soil.

2.1. *Magnetic Water Technique*

Magnetized water is generally obtained by passing water through a magnetic field to induce some alteration in the properties of the selected water type. The manufacturing of water magnetization equipment consisted of two Poly Vinyl Chloride (PVC) pipes, the first pipe of 25 mm in diameter and has a different length to transport the water from the pump to the tank of water and passes through the second pipe of a

larger diameter which contains the magnetic rocks. The ends of the second pipe are closed by a plastic cover as shown in Figure 1 (a,b). The schematic diagram of a physical model of the water magnetization system is shown in Figure 2. The magnetic devices were placed in a way that provided the ease of the circulation route of the water in the container of soil. The water passes through the magnetic field of several intensities (2000, 4000, 6000, and 8000 Gauss) by a plastic pipe of 12 mm diameter. The magnetizing system consists of magnetic rocks, a container made of PVC with a submersible pump of 25 watts, a head of 1.8 m, a flow rate of 1000 l/h, and connecting PVC tubes. The container was filled with tap water and circulate in the magnetic field for a two-time duration; firstly, the water circulated for 7 days through the magnetic field and increased the time of circulation up to 14 days, and test the soil samples after each treatment.

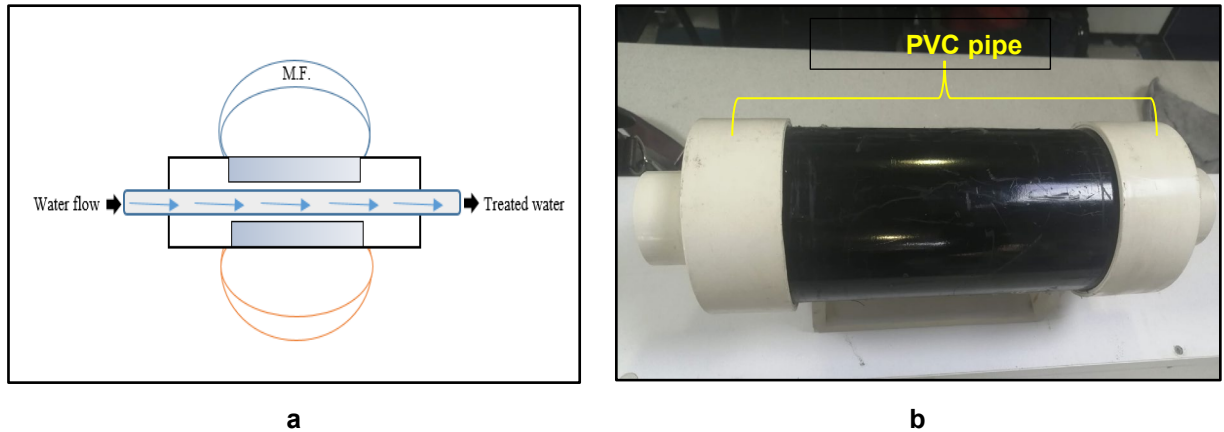


Figure 1. (a) Schematic diagram of magnetic device represent the inflow section, the magnets, and the outflow section and (b) magnetic device.

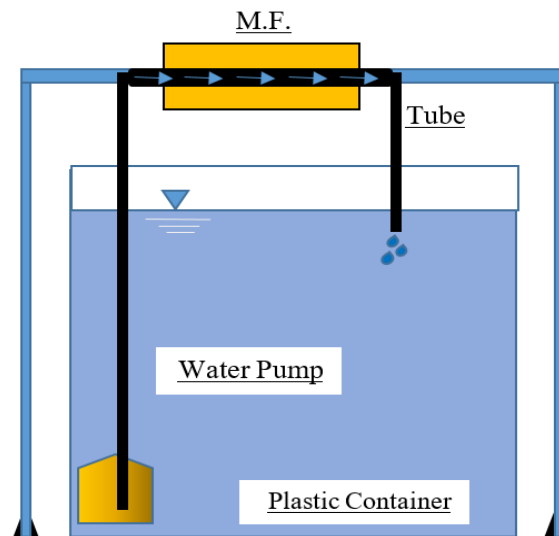


Figure 2. Schematic diagram of water magnetization system.

2.2. Soil Tests

The shear strength of soil refers to the strength of the soil at the microscopic level, which is governed by the interactions between soil particles and the pore fluid. The shear strength of soil is an important parameter in geotechnical engineering, as it plays a key role in determining the stability and bearing capacity of foundations, slopes, and retaining walls. Experimental methods, such as direct shear tests, triaxial tests, and torsional shear tests, can be used to measure the shear strength of soil in the laboratory. However, it is important to note that the measured shear strength can be influenced by factors such as sample preparation, testing conditions, and the stress history of the soil. Therefore, it is important to carefully consider the testing methodology and interpretation of the results when evaluating the micromechanical shear strength of the soil.

In this study, the clayey soil samples were obtained from one of the residential complexes in Baghdad, Iraq. The soil investigation program included drilling a borehole extended to a depth of (1.5–2) m below the natural ground level. Subsequent analysis and laboratory tests were accomplished to determine the physical, chemical, and shear strength characteristics of the soil sample. However, the general

classification of the natural soil result is clayey soil (CL) which is accomplished according to the unified soil classification system (USCS). The geotechnical properties of soil were examined before and after treatment by MW. Additionally, the laboratory tests were conducted according to the ASTM specifications, where the shear strength was represented by an unconfined compressive strength test (UCST), direct shear test (DST), and vane shear test (VST) were conducted according to ASTM D2166, ASTM D3080, and ASTM D4972 standards, respectively. The description of the soil and physical properties are given in Table 1. The results of shear strength tests conducted on the natural soil are listed in Table 2, which was conducted according to ASTM D2166 and ASTM D3080.

Table 1. Soil description and physical properties.

Depth, m	% Passing No. 200 sieve	γ_{wet} , kN/m ³	Natural water content, %	γ_{dry} , kN/m ³	LL, %	PL, %	PI, %	Gs	Fines, %		USCS
									Clay	Silt	
1.5–2.0	95	20.01	27.5	22.6	47	20	27	2.75	51.2	40.8	CL

Table 2. Results of undrained shear strength of natural soil.

Depth, m	UCST		DST		Consistency [25]
	q_u , kPa	c_u , kPa	c_u , kPa	ϕ , degree	
1.5–2.0	92.8	46.4	28	3	Medium

The current study focuses on determining the effect of the MW on the geotechnical properties of soft clayey soil. The aforementioned type of soil was prepared artificially from the natural clayey soil. Before preparing the soft soil, many tests were carried out to measure the relationship between the undrained shear strength of the soil and moisture content. Based on the results of tests shown in Figure 3, the soft soil used in this study can be prepared by mixing a moisture content approximately equal to 34% with natural clayey soil to produce a soft clayey soil has undrained shear strength, $c_u = 40$ kPa.

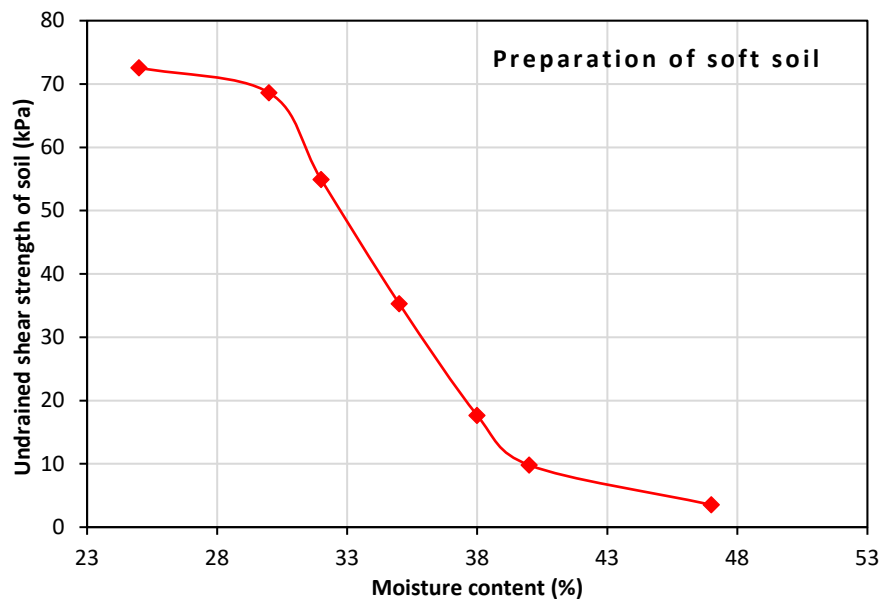


Figure 3. Variation of undrained shear strength versus water content for the remolded clay after 48 hrs.

3. Results and Discussion

The effect of magnetized water on the shear strength of soil is not well established and is currently a subject of ongoing research and debate. While some studies have suggested that magnetized water may have beneficial effects on soil properties, including shear strength, the results have been mixed and the underlying mechanisms of action are not well understood. One proposed mechanism is that the magnetic field may alter the structure and behavior of water molecules, leading to changes in soil structure and properties. Another proposed mechanism is that the magnetic field may enhance the activity of soil microorganisms and improve soil fertility, which could indirectly affect shear strength. However, these mechanisms have not been conclusively proven, and further research is needed to better understand the potential effects of magnetized water on soil properties and behavior, including shear strength. It is important to note that any claims about the effects of magnetized water on soil properties should be viewed

with caution until they are supported by rigorous scientific evidence. In the meantime, established soil testing methods and principles should continue to be used for evaluating soil properties and behavior. The shear strength of soil samples was tested by the portable vane shear device as well as the unconfined compressive strength test as shown in Figure 4. The chemical test of the soil had also been tested before and after the treatment by the magnetized water with different time duration and different magnetic field intensities.

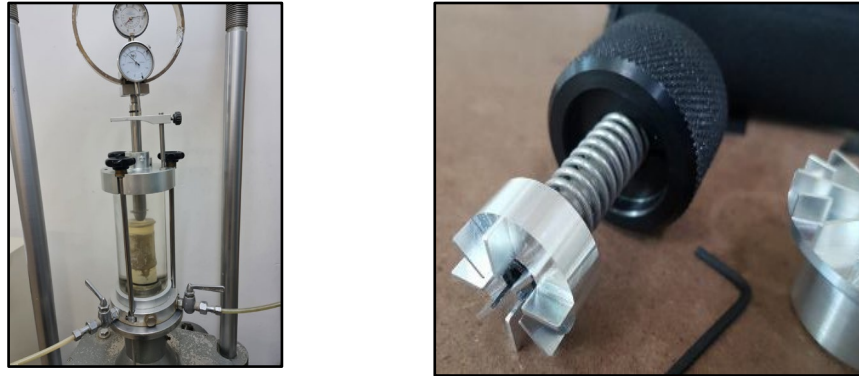


Figure 4. Unconfined compressive strength test (UCST) and portable vane shear test (VST) devices.

3.1. Influence of MW on Chemical Properties of Soil

The magnetic field applied to the water is thought to alter the structure and behavior of water molecules, which can affect the solubility and availability of soil nutrients and minerals. Some studies have reported that magnetized water can reduce the total soluble salt content of the soil, particularly in soils with high salinity. This effect is thought to be due to changes in the electrical charge and surface tension of the water, which can enhance the ability of the water to dissolve and transport nutrients while reducing the accumulation of salts in the soil. However, other studies have reported no significant effect of magnetized water on the total soluble salt content of the soil. The mechanisms of action are not well understood, and the results of studies on the effects of magnetized water on soil-soluble salt content have been mixed. In order to study the chemical alteration of the properties of soft clayey soil when treated with MW, the chemical tests listed in Table 3 were conducted on the soil samples before and after treatment. The analysis of variance showed that the effects of MW treatment on the chemical properties were significant under the highest intensity of 8000 G. Some studies have suggested that magnetized water can increase microbial activity in the soil, which could potentially lead to an increase in the decomposition of organic matter. This effect may be due to the increased solubility and availability of nutrients in the soil, as well as changes in the electrical charge and surface tension of the water. However, other studies have reported no significant effect of magnetized water on soil organic matter content (OMC) or decomposition rates. The mechanisms of action are not well understood, and the results of studies on the effects of magnetized water on soil organic matter have been mixed. The concentration of OMC decreased by 16.3% after 7 days and 26.2% after 14 days.

Table 3. Chemical test results were conducted on soft soil treated with magnetized water.

Property	7 days					14 days
	TW	2000 G	4000 G	6000 G	8000 G	8000 G
Organic matter content (OMC), %	4.35	4.25	4.01	3.78	3.64	3.21
Gypsum content, %	2.37	2.15	2.01	1.62	1.31	1.01
pH value	7.81	7.89	8.24	8.46	8.52	8.66
Sulfate content (SO ₄), %	2.39	1.96	1.45	1.36	0.86	0.61
Total soluble salts content (TSS), %	4.47	4.11	4.06	3.65	3.16	2.64

Gypsum is a common mineral in soil and can play an important role in soil fertility and structure. There is limited research on the effect of magnetized water on the gypsum content of the soil. One study reported that magnetized water had no significant effect on the solubility or availability of gypsum in soil. However, the study had a limited sample size and further research is needed to confirm these results. Overall, more research is needed to better understand the potential effects of magnetized water on the gypsum content of the soil and to determine the optimal conditions and application methods for achieving any potential benefits. It is important to note that claims about the effects of magnetized water on soil gypsum content should be viewed with caution until they are supported by rigorous scientific evidence. Gypsum content decreased by 44.7% after 7 days and 57.3% after 14 days, respectively. The decrement

in the sulfate content may be due to the decline in the solubility of the gypsum content in water, and increased rates of crystal growth and nucleation instead, which leads to the precipitation of gypsum.

Magnetized water has also been shown to affect the pH and conductivity of soil solutions, potentially influencing the availability of other nutrients and minerals. Some studies have reported that magnetized water can increase soil pH, while others have reported no significant effect. However, the results of studies on the effects of magnetized water on soil chemical properties have been mixed, and the mechanisms of action are not well understood. Further research is needed to better understand the potential effects of magnetized water on soil chemistry and nutrient availability and to determine the optimal conditions and application methods for achieving any potential benefits. Also, the pH value of the soil was influenced by the magnetic field of different intensities. The water treated with the magnetic intensity of 8000 G circulated through the soil, and the pH value gets also increased to about 8.34% after 7 days and 9.82% after 14 days, respectively. Increasing the value of the pH of the soil resulted from increasing the concentration of the hydrogen ions in the magnetized water.

The sulfate concentration in the soil was measured before and after treatment by different magnetic intensities and the analysis results showed the increase in the magnetic intensity for the treated water will cause a lower concentration measurement of sulfate 64% after 7 days and 74.48% after 14 days at the intensity of 8000 G. The total soluble salts (TSS) in the soil were decreased under the treatment by the magnetized water, as the efficiency of the magnetic treatment to reduce the concentration was 29.3% after 7 days and 36.9% after 14 days at the intensity of 8000 G. This is due to that the MW is working on increasing the leaching of the excess soluble salts due to that when water passes the magnetic field becomes more energetic and modifying the ability of the flow of the water, and dissolving slightly the soluble salts like carbonates, phosphates, and sulfates. However, other studies have reported no significant effect of magnetized water on the sulfate content of the soil. The mechanisms of action are not well understood, and the results of studies on the effects of magnetized water on soil sulfate content have been mixed.

3.2. Influence of MW on Shear Strength of Soil

On the other hand, the shear strength of soft soil has been measured by two tests, UCST and VST. Each has been conducted on soil samples before and after the treatment process by several intensities of MW. Each increment of the magnetic field intensity has led to increasing the shear strength of soft clayey soil. The tests can be grouped into two classes as varying the time of conducting tests after being treated by magnetized water. The soil was first tested when treated by MW for 7 days and the treatment continued for 14 days and then the soil was tested again. Figure 4 shows the influence of magnetic treatment on the unconfined compressive strength (q_u) of soft clay after 7 days of treatment which compared with that of the reference soil sample treated with tap water (TW). Generally, circulation of the water in magnetic field for 7 days and soft clay indicates an increase in q_u value by 52, 68, 43, and 45% for soil samples treated with MW of intensity 2000 G, 4000 G, 6000 G, and 8000 G, respectively.

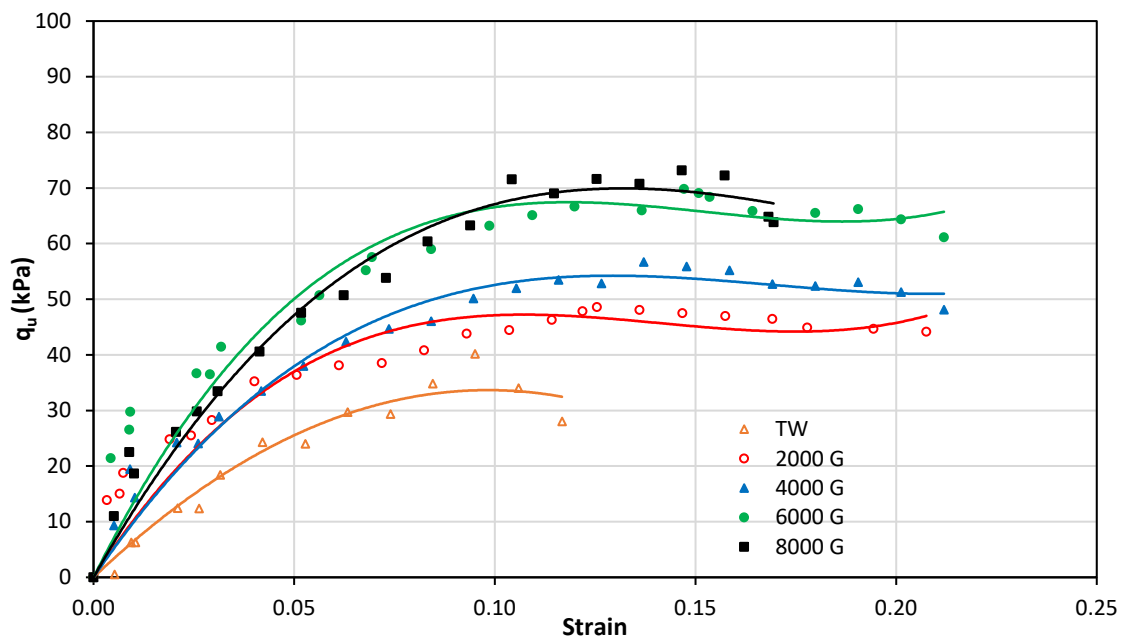


Figure 5. Variation of unconfined compressive strength with strain for soil samples treated with MW after 7 days.

Also, the unconfined compressive strength (q_u) of soft clayey soil was measured after 14 days of treatment as shown in Figure 5. Increasing the duration of treatment by MW from 7 days to 14 days showed increasing the unconfined compressive strength of soft soil by 21, 41, 74, and 82% corresponding to that treated with MW of intensity 2000 G, 4000 G, 6000 G, and 8000 G, respectively. The average of increasing q_u ranged from 1.25 to 2.65 times that gained after 7 days of treatment. It can be concluded that increasing the unconfined compressive strength of soil (i.e., the cohesion values) can be attributed to increasing the concentration of the salts and minerals in the pores of soil which provide additional internal bonds between the particles of soil. Also, decreasing the thickness of the double-diffusive layer causes a reduction in the antiparticle's repulsion force and increasing the attraction force between the soil particles.

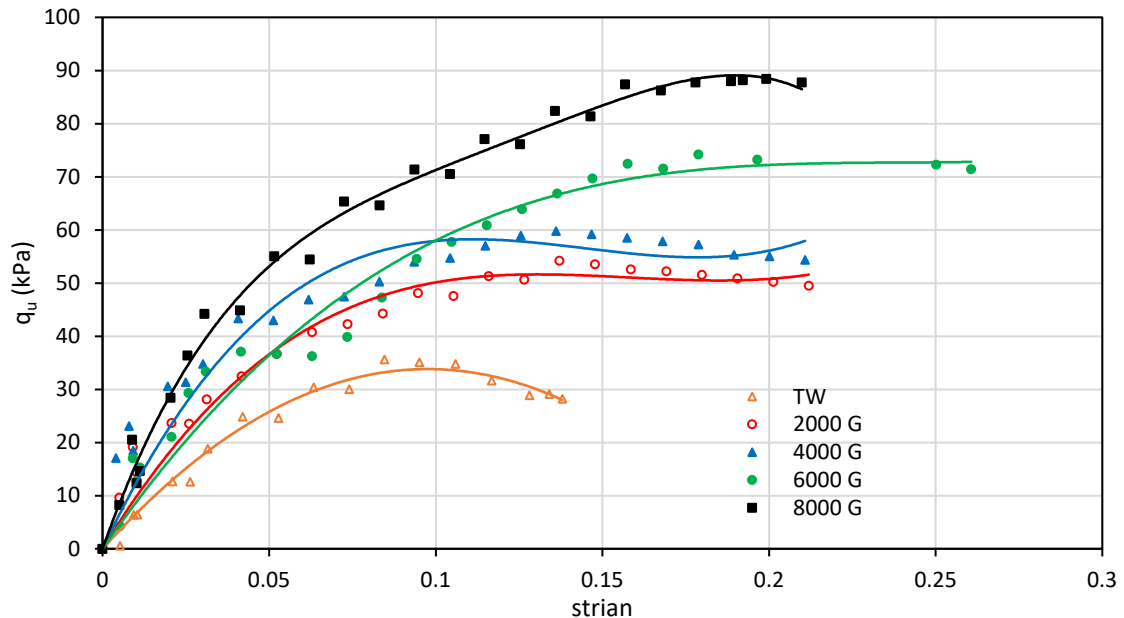


Figure 6. Variation of unconfined compressive strength with strain for soil samples treated with MW after 14 days.

The vane shear test is a type of in-situ test used to determine the undrained shear strength of soft soils. This test is particularly useful for cohesive soils, such as clays, silts, and muds. In the vane shear test, a four-bladed vane is inserted into the soil at a known depth and rotated at a constant rate. The torque required to rotate the vane is measured and used to calculate the undrained shear strength of the soil. The test is typically performed in situ, which means that the soil sample is not disturbed during the testing process. This makes it an ideal test for soft soils where disturbance can significantly alter the soil properties. The vane shear test is commonly used in geotechnical engineering to assess the stability of slopes, embankments, and other earth structures. It can also be used to evaluate the stability of shallow foundations and to determine the shear strength of soils for use in design calculations.

Figures 6 and 7 show the variation of undrained shear strength (S_{uv}) measured by a vane shear device for soft soil samples treated with several intensities of MW after 7 and 14 days of treatment. The treatment of soft soil by MW of intensities 2000 G and 4000 G showed a slight increase in the undrained shear strength, but the soil samples treated with intensities of 6000 G and 8000 G showed a significant increase in the undrained shear strength (S_{uv}) of soft clayey soil. Based on the results displayed, there is a slight effect of treatment duration on the magnitude of undrained shear strength.

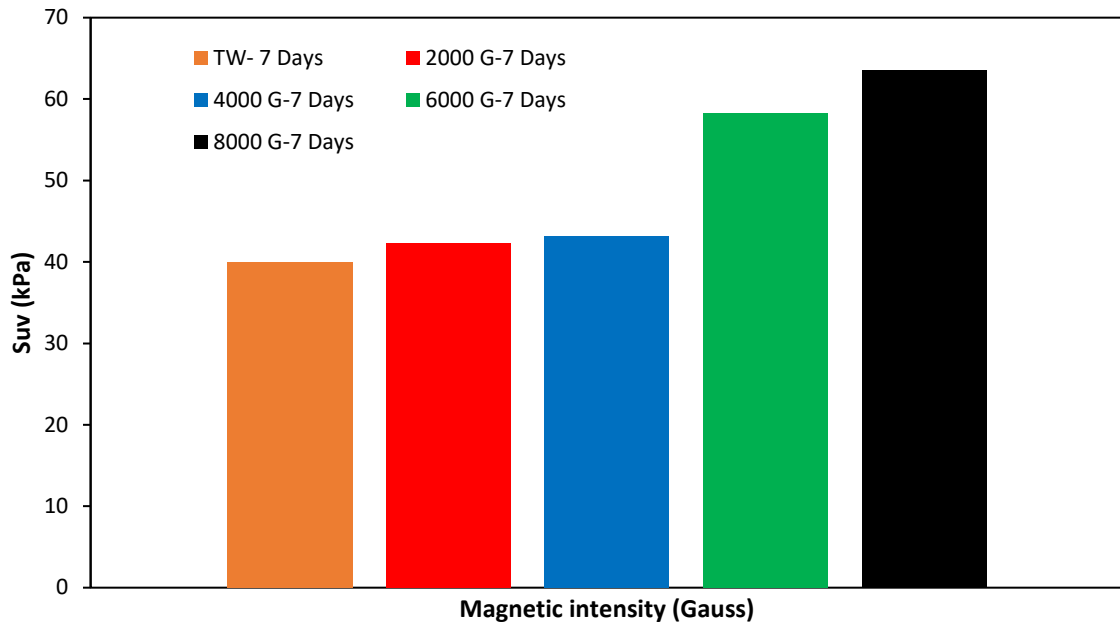


Figure 7. Results of vane shear tests after 7 days of soft clay samples treated by MW.

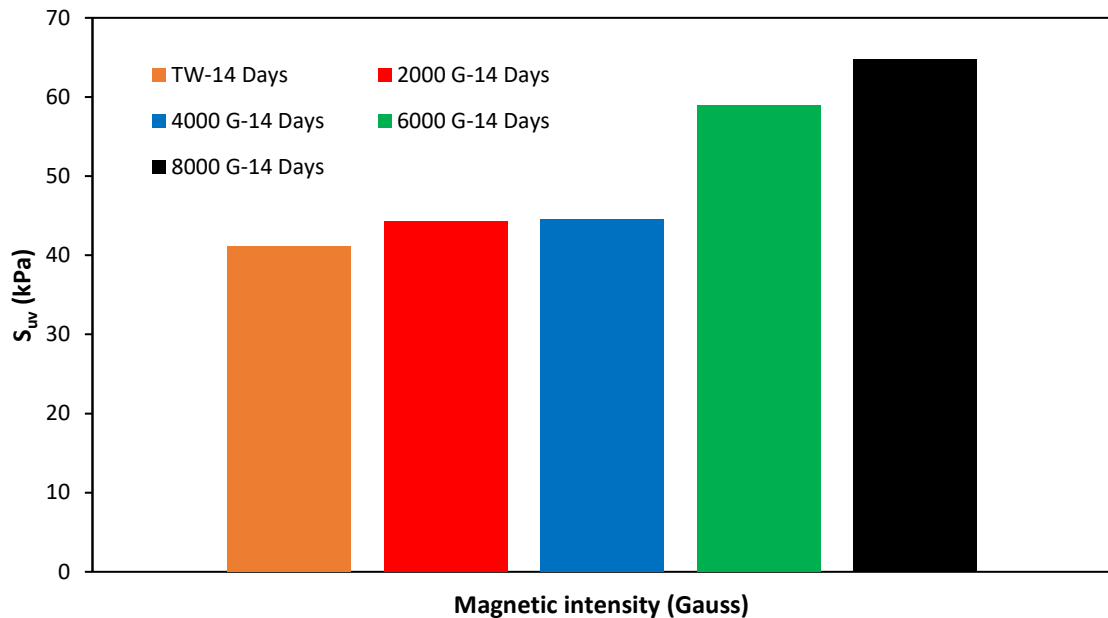


Figure 8. Results of vane shear tests after 14 days of soft clay samples treated by MW.

The summary of results of unconfined compressive strength (q_u) and undrained shear strength (S_{uv}) for soft clayey soil samples treated by several intensities of MW after 7 and 14 days of treatment are given in Table 4. The VST gives results of undrained shear strength higher than the unconfined shear strength test. Also, the rate of growth of undrained shear strength after 7 days of treatment is higher than that after 14 days of treatment, but still, the shear strength after 14 days of treatment is higher than that obtained after 7 days of treatment by MW.

Table 4. Summary of shear strength of soft clay treated by MW obtained from UCST and VST.

Soil sample	7 days					14 days				
	q_u , kPa	c_u , kPa	% change	S_{uv} , kPa	% change	q_u , kPa	c_u , kPa	% change	S_{uv} , kPa	% change
MW	34	17.00	0.00	40.00	0.00	35.11	17.56	0.00	41.10	0.00
2000 G	47.82	23.91	40.65	42.30	5.75	51.27	25.64	45.99	44.32	7.83
4000 G	53.47	26.74	57.26	43.10	7.75	58.93	29.47	67.80	44.51	8.30
6000 G	66.61	33.31	95.91	58.24	45.60	73.19	36.60	108.40	58.88	43.26
8000 G	70.69	35.35	107.91	63.60	59.00	88.19	44.10	151.11	64.71	57.45

4. Conclusions

The main objective of this work was studying the influence of several intensities (2000, 4000, 6000, and 8000 G) of magnetized water on the chemical properties and shear strength of soft clayey soil after 7 and 14 days of treatment by MW. Based on the results of this study, the following points can be drawn out:

- The influence of the magnetized water with different intensities also showed a significant variation in the chemical composition of the soil after 7 and 14 days.
- Water magnetization increased the alkalinity of the soil, where pH value increased from 7.81 to 8.52, but the OMC, gypsum, SO₃, and TSS contents decreased with increasing the intensity of MW due to adsorption and sedimentation of salts.
- The treatment of soft soil by MW improved the shear strength measured by UCST and VST, where the shear strength increased with increasing the intensity of the magnetic field.
- The shear strength of the soil was also increased as the curing time of the magnetized water circulation increased from 7 days up to 14 days.
- In general, the overall response of the treated soil depicts a promising and bright application of the magnetized water sustainability system used for alteration and improvement of the shear strength and chemical properties of soft clayey soil. The sustainable effects of using MW technique on the soil properties is not only limited to the cost, but also reduce using chemicals that could spread in the soil, which in turn would be very expensive and toxic. In addition, in large sites, the MW technique can be easily applied compared with other techniques. Furthermore, one of the main advantages of MW technique is the low cost, as it relies mainly on water circulating through a magnetized metal field device, and the validity of this device extends for many years.

References

1. Das, B.M., Sobhan, K. Principles of geotechnical engineering. Cengage Learning; 2021.
2. Karkush, M.O., Abdulkareem, M.S. Deep remediation and improvement of soil contaminated with residues oil using lime piles. *International Journal of Environmental Science and Technology*. 2019. 16. Pp. 7197–7206. DOI: 10.1007/s13762-019-02244-3
3. Hore, R., Ansary, M.A. Different Soft Soil Improvement Techniques of Dhaka Mass Rapid Transit Project. *Journal of Engineering Science*. 2020. 11(2). Pp. 37–44. DOI: 10.3329/jes.v11i2.50896
4. Ali, N.A., Karkush, M.O. Improvement of unconfined compressive strength of soft clay using microbial calcite precipitates. *Journal of Engineering*. 2021. 27(3). Pp. 67–75.
5. Karkush, M.O., Almurshedi, A.D., Karim, H.H. Investigation of the Impacts of Nanomaterials on the Micromechanical Properties of Gypseous Soils. *Arabian Journal for Science and Engineering*. 2023. 48(1). Pp. 665–675. DOI: 10.1007/s13369-022-07058-z
6. Mir, B.A., Hariprasad Reddy, S. Enhancement in shear strength characteristics of soft soil by using nanomaterials. *Sustainable Environment and Infrastructure: Proceedings of EGRWSE 2019*. 2020. Pp. 421–435. DOI: 10.1007/978-3-030-51354-2_39
7. Feng, T.W. Compressibility and permeability of natural soft clays and surcharging to reduce settlements. University of Illinois at Urbana-Champaign, 1991.
8. Kazemian, S., Huat, B.B. Assessment of stabilization methods for soft soils by admixtures. *International Conference on Science and Social Research (CSSR 2010)*. IEEE, 2010. Pp. 118–121. DOI: 10.1109/CSSR.2010.5773714
9. Marto, A., Mohd Yunus, N.Z., Pakir, F., Latifi, N., Mat Nor, A.H., Tan, C.S. Stabilization of marine clay by biomass silica (non-traditional) stabilizers. *Applied Mechanics and Materials*. 2015. 695. Pp. 93–97. DOI: 10.4028/www.scientific.net/AMM.695.93
10. Hasmda, W., Hassan, W. Strength Characteristic of Soft Soil Reinforced with Coir Fibre. Pahang: Universiti Malaysia Pahang, 2010.
11. Kasim, F., Marto, A., Rahman, N.A., Tan, C.S. Unconfined compressive strength and microstructure of clay soil stabilised with biomass silica. *Jurnal Teknologi*. 2015. 77(11). DOI: 10.11113/jt.v77.6382
12. Esmailnezhad, E., Choi, H.J., Schaffie, M., Gholizadeh, M., Ranjbar, M. Characteristics and applications of magnetized water as a green technology. *Journal of Cleaner Production*. 2017. 161. Pp. 908–921. DOI: 10.1016/j.jclepro.2017.05.166
13. Kadhim, K.N., Alghazali, N.O. Effect of magnetization of saline irrigation water of Almasab Alam on some physical properties of soil. *Journal of the Mechanical Behavior of Materials*. 2022. 31(1). Pp. 225–332. DOI: 10.1515/jmbm-2022-0031
14. Kadhim, K.N., Alghazali, N.O. Effect of magnetization on some physical properties of Almasab Alam salty water. *IOP Conference Series: Earth and Environmental Science*. 2021. 856(1). 012045. DOI: 10.1088/1755-1315/856/1/012045
15. Karunanayaka, S.D. Studies of magnetic filtration techniques to purify potable water and wastewater. M.Sc. Thesis in Information and Telecommunications Engineering, Massey University, Palmerston North, New Zealand. 2007.
16. Jawad, S.I., Karkush, M., Kaliakin, V.N. Alteration of physicochemical properties of tap water passing through different intensities of magnetic field. *Journal of the Mechanical Behavior of Materials*. 2023. 32(1). 20220246. DOI: 10.1515/jmbm-2022-0246
17. Karkush, M.O., Ahmed, M.D., Al-Ani, S.M. Magnetic field influence on the properties of water treated by reverse osmosis. *Engineering, Technology and Applied Science Research*. 2019. 9(4). Pp. 4433–4439. DOI: 10.48084/etasr.2855
18. Fujimura, Y., Iino, M. Magnetic field increases the surface tension of water. *Journal of Physics: Conference Series*. 2009. 156(1). 012028. DOI: 10.1088/1742-6596/156/1/012028
19. Iwasaka, M., Ueno, S. Structure of water molecules under 14 T magnetic field. *Journal of Applied Physics*. 1998. 83(11). Pp. 6459–6461. DOI: 10.1063/1.367737

20. Hosoda, H., Mori, H., Sogoshi, N., Nagasawa, A., Nakabayashi, S. Refractive indices of water and aqueous electrolyte solutions under high magnetic fields. *The Journal of Physical Chemistry A*. 2004. 108(9). Pp. 1461–1464. DOI: 10.1021/jp0310145
21. Karimipour, A., Edalati, M., de Brito, J. Influence of magnetized water and water/cement ratio on the properties of untreated coal fine aggregates concrete. *Cement and Concrete Composites*. 2021. 122. 104121. DOI: 10.1016/j.cemconcomp.2021.104121
22. Reddy, B.S., Ghorpade, V.G., Rao, H.S. Influence of magnetic water on strength properties of concrete. *Indian Journal of Science and Technology*. 2014. 7(1). Pp. 14–18. DOI: 10.17485/ijst/2014/v7i1.7
23. Esmailnezhad, E., Choi, H.J., Schaffie, M., Gholizadeh, M., Ranjbar, M. Characteristics and applications of magnetized water as a green technology. *Journal of Cleaner Production*. 2017. 161. Pp. 908–921. DOI: 10.1016/j.jclepro.2017.05.166
24. Al-Ani, S.M., Karkush, M.O., Zhussupbekov, A., Al-Hity, A.A. Influence of magnetized water on the geotechnical properties of expansive soil. *Modern Applications of Geotechnical Engineering and Construction: Geotechnical Engineering and Construction. Lecture Notes in Civil Engineering*. 2021. Pp. 39–50. DOI: 10.1007/978-981-15-9399-4_5
25. Terzaghi, K., Peck, R.B. *Soil mechanics in engineering practice*, 2nd Ed. John Wiley and Sons, Inc., New York, N.Y., 1967.

Information about authors

Saba Jawad, Doctor of Technical Sciences

ORCID: <https://orcid.org/0000-0002-16579-0942>

E-mail: saba@bauc14.edu.iq

Mahdi Karkush, Doctor of Technical Sciences

ORCID: <https://orcid.org/0000-0003-1304-0303>

E-mail: mahdi_karkush@coeng.uobaghdad.edu.iq

Received 07.04.2023. Approved after reviewing 29.04.2023. Accepted 29.11.2023.



Research article

UDC 691

DOI: 10.34910/MCE.124.7



Properties of grey marl bricks with additions of rice husks

P. Zlateva¹ , R. Petkova-Slipets² , K. Yordanov¹ 

¹ Technical University of Varna, Varna, Bulgaria

² Varna Free University "Chernorizets Hrabar", Varna, Bulgaria

✉ pzlateva@tu-varna.bg

Keywords: rice husks, grey marl, bricks, thermal properties, heat capacity, thermal conductivity

Abstract. This article presents the results of experimental research on the impact of environmentally efficient materials developed on the basis of grey marl and sand with the addition of 3 % to 6 % of rice husk on the thermophysical characteristics: coefficient of thermal conductivity, specific heat capacity and thermal diffusivity. The thermal indicators are measured with a device based on the non-stationary method. The purpose of the research is to investigate the impact of a new type of a light natural organic additive material, the husk of rice grains, on the properties of the resulting composite. The task is to develop a new material which is both thermally efficient and eco-friendly. The results of the research show that the addition of rice husks reduces the coefficient of thermal conductivity by 42 %, of the thermal diffusivity by 38 %, and increases the specific heat capacity by 10 % compared to the reference sample.

Citation: Zlateva, P., Petkova-Slipets, R., Yordanov, K. Properties of grey marl bricks with additions of rice husks. Magazine of Civil Engineering. 2023. 124(8). Article no. 12407. DOI: 10.34910/MCE.124.7

1. Introduction

Over the recent years, more and more efforts have been made to reduce the harmful impact of traditional building materials and to find solutions to construction-induced air pollution responsible for climate changes. Therefore, the needs of construction industry demand harmless and eco-friendly materials to be developed [1–3]. There are many opportunities to construct buildings with environmentally friendly materials and to use renewable energy sources in order to reduce energy consumption in buildings [4, 5]. One of these opportunities for ecologically clean construction is the use of waste biomass from agricultural crops [6, 7]. Globally, large amounts of raw materials are obtained from agricultural waste biomass such as straw, corn stalks, rice husks, etc., which can be used to produce building materials such as bricks, cladding boards, etc. [8–10]. Raw materials from waste biomass are easily available and cheap on the one hand, and on the other hand, they contribute to the reduction of air pollution, thus having a favourable effect on the climate change, which makes them a preferred choice for use in construction [11, 12]. Bricks are the main material in construction because of their compactness and light weight, easy transfer of heat, which is preserved for a long time, etc. The usefulness of brick in construction has been proven over time and has been used since ancient times. Two of the important characteristics of bricks produced from agricultural waste materials in combination with cement, sand and water are the coefficient of thermal conductivity and the specific heat capacity [13, 14]. The lower the value of the coefficient of thermal conductivity, the better the thermal insulation properties of the material. The higher the value of the specific heat capacity, the better the accumulative properties of the material, i.e. the heat is retained for a longer time [15–18]. The search for and implementation of newer building materials in construction requires knowledge of their thermophysical characteristics such as thermal conductivity, specific weight, specific heat capacity, etc [19–22].

According to the investigations carried out so far, there is a significant lack of information on the development of ecological marl bricks with the addition of biomass, in particular rice husks (RH) in different quantities. This motivated conducting research on the thermophysical characteristics of composites made of grey marl, sand, rice husks and water. The publication presents the obtained results for thermal conductivity coefficient k , specific heat capacity C_p and thermal diffusivity a , as well as their analysis.

The aim of the present research is to study the impact of different amounts of rice husks added to a mixture of grey marl and sand on the thermophysical characteristics of the obtained samples. In the literature, there are no similar studies focused on the thermal characteristics of environmentally friendly materials. The growing trend towards sustainable architecture and construction with sustainable materials, including natural materials, the established principles of green and circular economy require continuing and profound search for new materials adapted to modern trends for construction purposes. Therefore, it is vital to point out the real advantages that materials with a slight addition of biomass have with a view to supporting the comfort of buildings. This article investigates eco-friendly materials based on grey marl, sand and rice husk, in response to the growing interest in new environmentally friendly and energy-efficient materials from agricultural crop waste materials.

2. Methods

Experimental studies were carried out on samples of ecological composite materials with different additions of rice husks in order to identify their basic thermophysical characteristics such as: coefficient of thermal conductivity, specific heat capacity and thermal diffusivity.

2.1. Preparation of the samples

For the purposes of the study, four types of samples were made based on grey marl and sand with different addition of rice husks (Table 1 and Fig. 1). The water binding ratio was 0.5. Each mixture was shaped into five cubes with a side of 0.10 m.

Table 1. Composition and density of the samples.

Sample No	Weight ratio			Rice husks wt%	Bulk density kg/m ³
	grey marl	sand	water		
1	1	2	0.5	0	1920±
2	1	2	0.5	3.0	1840±
3	1	2	0.5	4.0	1760±
4	1	2	0.5	6.0	1625±



Figure 1. General view of the rice husks.

The bulk density of the dry samples was measured on the 14th day of age. Table 1 shows the data on the average volume density of the samples. The addition of rice husks from 3 % to 6 % resulted in a density decrease by about 9 % to about 20 %, respectively, compared to the density of the reference sample without light addition.

2.1.1. Sample preparation methodology

The experimental samples were made by following the following steps. First, the natural grey marl was mixed with water, where it plasticized, and then medium-grained dry quartz sand was added. For the

production of samples 2, 3 and 4, the pre-weighed amounts of rice husks were added in weight percentage ratios as indicated in Table 1. All ingredients were mixed with a blender until a homogeneous mixture was obtained. Next was the moulding of cubes with a side size of 0.10 m in wooden moulds (Fig. 2).



Figure 2. Manufacturing stage.



Figure 3. General look of the finished samples.

Laboratory conditions at air temperature of 23 ± 3 °C and humidity 65 % for 5 days. On the sixth day, the samples were removed from the wooden mould (Fig. 3). The samples were smoothed with sandpaper to avoid measurement errors. Until the time of conducting the tests, the samples were stored in laboratory conditions at a temperature of 23 ± 3 °C and humidity of 65 %.

2.2. Methodology of experimental measurement

The measurement of the thermophysical characteristics (thermal conductivity coefficient k , volumetric heat capacity $C_v(C, \rho)$ and thermal diffusivity a of the samples being tested was carried out with an Isomet 2114 device [23]. The device affords a wide range of direct measurements of isotropic materials, such as dense and porous materials, plastics, glass and minerals. The measurement range of the coefficient of thermal conductivity is from 0.015 to 7.0 W/(m.K). and for the volume specific capacity – from $4.0E+04$ to $4.0E+06$ J/(m³.K). The measuring device has two types of probes: a needle probe for soft materials and a surface flat probe for hard materials. The measurement data is saved in the internal memory of the device or exported to a computer, as shown in Fig. 4.

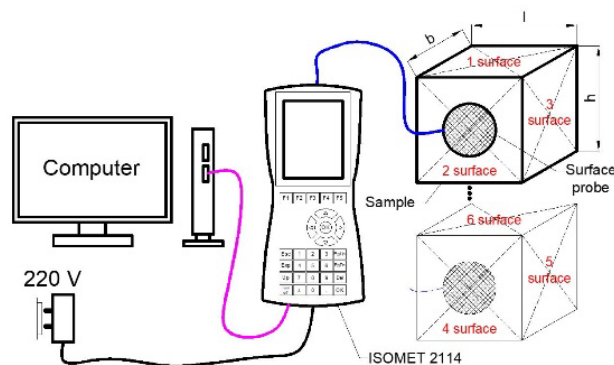


Figure 4. Scheme of the experimental measurement of thermophysical characteristics.

The experimental studies were carried out in compliance with the methodology for using the device. The measurements were carried out under non-stationary conditions. The measurement method was based on an analysis of the measured temperature difference during heating or cooling of the tested sample at heat flow pulses. The heat flow was induced by an electrical heating resistor embedded in the probe, which is in direct thermal contact with the sample being tested.

The measurements for the present study were carried out with a surface probe IPS 1105 on the surface of the sample in the range indicated in Table 2. The surface probe has long-term stability in the measurement range used. Before the measurements, the accuracy of the device was verified by using the cork calibration standard which comes with the device, and the calibration coefficient was given as per the requirements of the ASTM 5334-08 standard [24].

Table 2. Technical characteristics of the measurement [23].

Characteristic	Measurement range	Accuracy in the measuring range
Temperature t , °C	-15...+50	n.a.
Volumetric heat capacity $C_v(C, \rho)$, J/(m ³ .K)	1.5E+06...3.0E+06	15 % of reading + 1E+03 J/m ³ .K
Thermal conductivity coefficient k , W/(m.K)	0.30–2.00	in a range 0.015 .. 0.70 W/m.K -5 % of reading + 0.001 W/m.K in a range 0.70 .. 6.0 W/m.K – 10 % of reading

After setting the measuring range, a measurement followed within about 20 min. Throughout the measurement process, the amount of heat generated by the device was known. The heat in the tested samples dissipated radially. The increase in temperature of the tested sample changed linearly with the logarithm of time. In this way, it was possible for the coefficient of thermal conductivity of the tested sample to be obtained directly, and also the data to be transferred to a computer.

The experimental measurements were carried out on the levelled surfaces of the tested samples (Fig. 5 and 6).

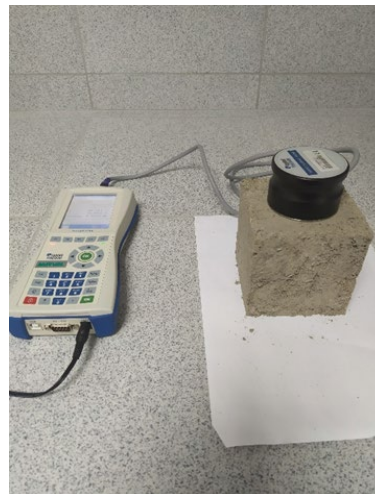


Figure 5. Experimental measurements.

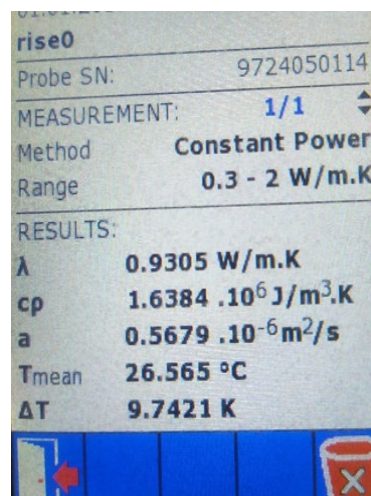


Figure 6. Measurement of sample No. 2.

Equation 1 is used for the samples tested.

$$y = a \times x \pm b. \quad (1)$$

On the basis of the measured thermal parameters, the specific heat capacity C_p was calculated using the formula [25]:

$$C_p = k / (a \times \rho). \quad (2)$$

3. Results and Discussion

As a result of the conducted measurements of the thermophysical characteristics of all samples, values were obtained for the coefficient of thermal conductivity, the volumetric heat capacity and thermal diffusivity. Six series of measurements were carried out for each sample. The values for reference sample No.1 are given in Table 3.

Table 3. Measurement results of the reference sample No. 1

Sample No. 1	k W/(m.K)	a m ² /s	C_v J/(m ³ .K)
Average value	1.0698	6.3742E-07	1.6801E+06
Median	1.0687	6.3664E-07	1.6793E+06
Standard deviation	0.0236	1.8007E-08	7.9280E+04
Coefficient of variation, %	2.20	2.82	4.72

Due to the large amount of data from the measurements, after transferring them to a computer from the measuring device, the data were processed statistically to obtain values for average value, median value, standard deviation and coefficient of variation. The results of the measurements for samples No. 2, No. 3 and No. 4 are presented in Tables 4, 5 and 6, respectively.

Table 4. Results for sample No. 2.

Sample No. 2	k W/(m.K)	a m ² /s	C_v J/(m ³ .K)
Average value	0.9018	5.4681E-07	1.6502E+06
Median	0.9009	5.4495E-07	1.6556E+06
Standard deviation	0.0168	1.4887E-08	5.4574E+04
Coefficient of variation, %	1.86	2.72	3.31

Table 5. Results for sample No. 3.

Sample No.3	k W/(m.K)	a m ² /s	C_v J/(m ³ .K)
Average value	0.7828	4.8614E-07	1.6098E+06
Median	0.7984	4.9685E-07	1.6094E+06
Standard deviation	0.0807	4.9016E-08	5.8319E+03
Coefficient of variation, %	10.32	10.08	0.36

Table 6. Results for sample No. 4.

Sample No. 4	k W/(m.K)	a m ² /s	C_v J/(m ³ .K)
Average value	0.6242	3.9776E-07	1.5672E+06
Median	0.6341	4.0697E-07	1.5646E+06
Standard deviation	0.1104	6.6663E-08	1.8376E+04
Coefficient of variation, %	17.68	16.76	1.17

The research results show that the addition of rice husks has a positive effect on the thermo-technical characteristics.

The coefficient of thermal conductivity changes from 1.0698 W/(m.K) for the material without addition of rice husk to 0.6242 W/(m.K) for the material with 6 wt% light additive, which is a reduction of approximately 42 %. The specific structure of rice husks and the inhomogeneous structure of the tested samples exert a significant effect on the coefficient of thermal conductivity, and, in particular, on the repeatability of the data. As can be seen from Tables 3–6, with the increase of the proportion of rice filler, the thermal conductivity of the materials decreases, but along with this, there is also an increase in the standard deviation of the results. This could be explained, on the one hand, by the fact that the measurement is superficial and local (below the surface of the sensor with a diameter of 60 mm) and the results that are reported are for volumes with different structure, different distribution of the additive material and mould share. On the other hand, the shape of the rice particles is not perfectly spheroidal, but rather spindle-shaped and slightly tapering in one direction (Fig. 1). From a structural point of view, this is seen as a prerequisite for anisotropy and inhomogeneity. Moreover, the particles are randomly located in the volume of the tested samples, which leads to the so-called quasi-isotropy.

The volumetric specific capacity also changes with the change in the amount of added rice husks in the samples, whereby the increase in the proportion of biomass results in decrease of C_v .

The obtained values for the thermal diffusivity range from 6.3742E-07 m²/s to 3.9776E-07 m²/s depending on the percentage content of rice husks – from 3 % to 6 %, respectively.

The statistically processed results of the samples tested for coefficient of thermal conductivity, volumetric specific capacity and thermal diffusivity versus on the percentage content of rice husks are shown in Fig. 7, 8 and 9.

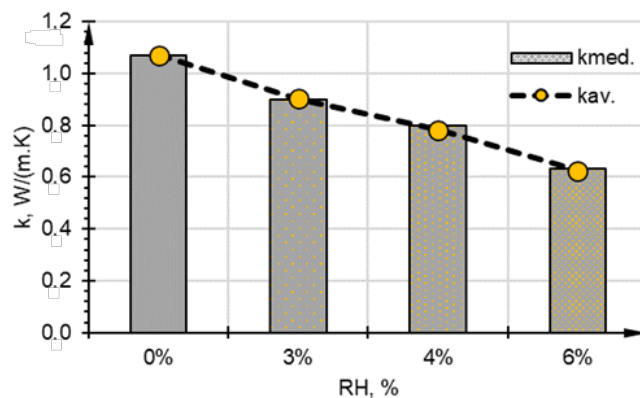


Figure 7. Statistically processed results of the samples tested for coefficient of thermal conductivity versus on the percentage content of rice husks.

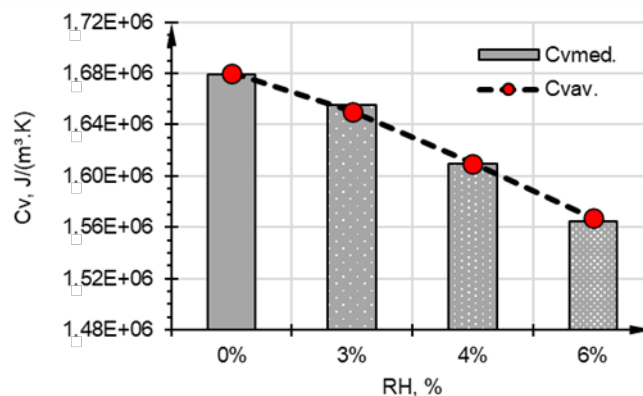


Figure 8. Statistically processed results of the samples tested for volumetric specific capacity versus on the per-centage content of rice husks.

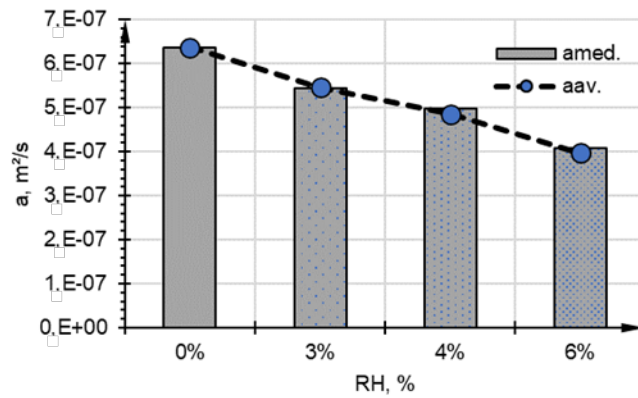


Figure 9. Statistically processed results of the samples tested for thermal diffusivity versus on the percentage content of rice husks.

The graphs in Fig. 7, 8 and 9 clearly show the tendency towards decrease of the studied thermophysical characteristics with the increase of the content of rice husks.

Table 7. Calculated values of the specific heat capacity

Sample	1	2	3	4
$C_p, J/(kg.K)$	875.1	896.9	914.7	964.4

The results (Table 7) show that the addition of rice husks improves the specific heat capacity of the tested materials. The analysis shows that the addition of 6 % rice husk increases the specific heat capacity from 875.1 J/(kg.K) for the base material without a light additive to 964.4 J/(kg.K), which is an increase of about 10 %.

Fig. 10, 11 and 12 shows the relationships between the coefficient of thermal conductivity, thermal diffusivity and the specific heat capacity as a function of the density of the samples.

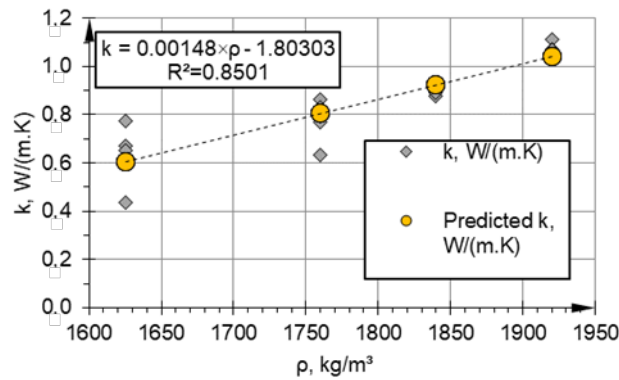


Figure 10. Dependence of the thermal conductivity coefficient as a function of the density – $k = f(\rho)$.

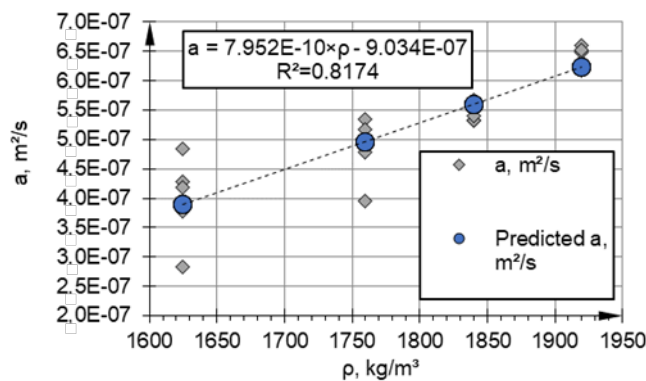


Figure 11. Dependence of the thermal diffusivity as a function of the density – $a = f(\rho)$.

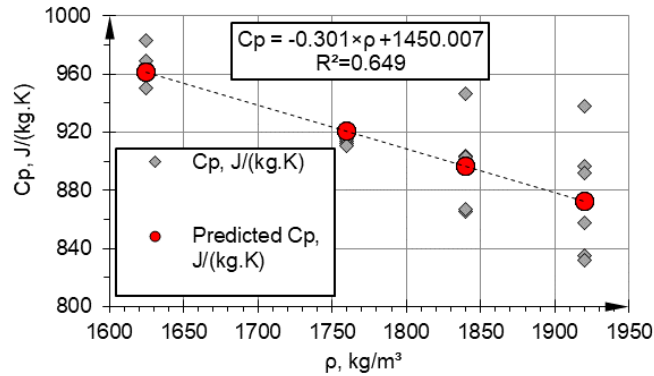


Figure 12. Dependence of the specific heat capacity as a function of the density – $C_p = f(\rho)$.

The increase in rice husk additives can be useful in the development of thermally efficient lightweight eco-friendly building materials.

Fig. 10 and Fig. 11 show the same direction of the two parameters of the tested samples, and Fig. 12 shows the opposite direction compared to the previous two figures. As the coefficient of thermal conductivity decreases, a decrease in thermal diffusion and an increase in specific heat capacity are observed. The relationship between these parameters can be indirectly attributed to the density of the studied samples.

For the tested samples, dependencies equations from 3 to 5 were proposed.

$$k = 0.00148 \times \rho - 1.80303, \text{ W}/(\text{m.K}); \quad (3)$$

$$a = 7.952.E - 10 \times \rho - 9.034.E - 07, \text{ m}^2/\text{s}; \quad (4)$$

$$C_p = -0.301 \times \rho + 1450.007, \text{ J}/(\text{kg.K}). \quad (5)$$

The additions of rice husks, as used in the samples, lead to higher air content, specific porosity and a respective decrease in thermal conductivity and heat transfer.

The authors of paper [20], present hand-mixed clay with different percentages of sawdust (0 %, 4 %, 6 %) to evaluate its effect on the thermal performance of unfired bricks. The obtained composites were characterized by densities of 2133 kg/m³, 1883 kg/m³ and 1876 kg/m³. The corresponding values of thermal conductivity were 0.8954 W/(m.K), 0.7996 W/(m.K) and 0.7395 W/(m.K). Experimental results show that the addition of both rice husk and sawdust positively affects the quality of building materials and other heat transfer properties.

In article [26], the authors also used clay with different percentage additions of rice husks. The researchers obtained that bulk density of clay bricks was decreasing with increasing rice husk content. The results indicated that the values of bulk density of the samples containing rice husk (0 %–10 %) varied from 1890 to 1370 kg/m³.

4. Conclusion

1. This research work presents the results of experiments carried out with samples based on grey marl, sand and different ratios of rice husks: 0 %, 3 %, 4 % and 6 %. We studied the basic thermophysical characteristics of the materials such as: coefficient of thermal conductivity k , thermal diffusivity a and specific heat capacity C_p . The addition of rice husks as a light additive results in reduction of density by 15 % and an improvement of thermal insulation properties of the material.
2. It was found that with a content of rice husks of 6 wt%, all the studied thermal characteristics change significantly. The coefficient of thermal conductivity decreases by 42 % and the thermal diffusivity decreases by 38 %, while the specific heat capacity increases from 875.1 J/(kg.K) to 964.4 J/(kg.K), resulting in an improvement of about 10 % compared to the reference case.
3. The research shows that the combination of grey marl and sand with addition of rice husks gives good results, which can potentially be used in the development of low-cost eco-friendly and energy-efficient materials.

References

1. Kubule, A., Komisarova, T., Blumberga, D. Optimization Methodology for Complete Use of Bio-resources. *Energy Procedia*. 2017. 113. Pp. 28–34. DOI: 10.1016/j.egypro.2017.04.009
2. Faludi, J. Ecological Payback Time of an Energy-Efficient Modular Building. *Journal of Green Building*. 2012. 7. Pp. 100–119. DOI: 10.3992/jgb.7.1.100
3. Czopka, P. Sustainable materials in ecological buildings. *Economic and Environmental Studies*. 2018. 18 (1). Pp. 93–102. DOI: 10.25167/ees.2018.45.6
4. Tachaudomdach, S., Hempao, S. Investigation of compression strength and heat absorption of native rice straw bricks for environmentally friendly construction. *Sustainability* 2022. 14(19). 12229. DOI: 10.3390/su141912229
5. Wan, S., Ding, G., Runeson, G., Liu, Y. Sustainable buildings' energy-efficient retrofitting: a study of large office buildings in Beijing. *Sustainability*. 2022. 14(2). 1012. DOI: 10.3390/su14021021
6. Sasui, S., Jinwuth, W., Hengrasmee, S. The effects of raw rice husk and rice husk ash on the strength and durability of adobe bricks. *Civil Engineering Journal*. 2018. 4(4). Pp. 732–742. DOI: 10.28991/cej-0309128
7. Zhang, Z., Wong, Y.C., Arulrajah, A., Horpibulsuk, A. A review of studies on bricks using alternative materials and approaches. *Construction and Building Materials*. 2018. 188. Pp. 1101–1118. DOI: 10.1016/j.conbuildmat.2018.08.152
8. Ahmed, H., Ibrahim, I.M., Radwan, M.A., Sadek, M.A., Elazab, H.A. Preparation and analysis of cement bricks based on rice straw. *International Journal of Emerging Trends & Technology in Computer Science*. 2020. 8(10). Pp. 7393–7403. DOI: 10.30534/ijeter/2020/1188102020
9. Liang, X.C., Zhang, M., Tian, S.C. Research on composite rice straw-cement brick for high-rise building. *INMATEH - Agricultural Engineering*. 2020. 60. Pp. 71–78. DOI: 10.35633/inmateh-60-08
10. Chen, J., Elbashiry, E.M.A., Yu, T., Ren, Y., Guo, Z., Liu, S. Research progress of wheat straw and rice straw cement-based building materials in China. *Magazine of Concrete Research*. 2018. 70. Pp. 84–95. DOI: 10.1680/jmacr.17.00064
11. Selvaranjan, K., Gamage, J.C.P.H., De Silva, G.I.P., Navaratnam, S. Development of sustain-able mortar using waste rice husk ash from rice mill plant: Physical and thermal properties. *Journal of Building Engineering*. 2021. 43(7). 102614. DOI: 10.1016/j.jobe.2021.102614
12. Hwang, C.L., Huynh, T. Investigation into the use of unground rice husk ash to produce eco-friendly construction bricks. *Construction and Building Materials*. 2015. 93. Pp. 335–341. DOI: 10.1016/j.conbuildmat.2015.04.061
13. Raheem, A.A., Oriola, K.O., Kareem, M.A., Abdulwahab, R. Investigation on thermal properties of rice husk ash-blended palm kernel shell concrete. *Environmental Challenges*. 2021. 5. 100284. DOI: 10.1016/j.envc.2021.100284
14. Adamczyk, J., Dylewski, R. The impact of thermal insulation investments on sustainability in the construction sector. *Renewable and Sustainable Energy Reviews*. 80(3). Pp. 421–429. DOI: 10.1016/j.rser.2017.05.173
15. Meral, O. Cost analysis for optimum thicknesses and environmental impacts of different insulation materials. *Energy and Buildings*. 2012. 49. Pp. 552–559. DOI: 10.1016/j.enbuild.2012.03.002
16. Madurwar, M.V., Ralegaonkar, R.V., Mandavgane, S.A. Application of agro-waste for sustainable construction materials: A review. *Construction and Building Materials*. 2013. 38. Pp. 872–878. DOI: 10.1016/j.conbuildmat.2012.09.011
17. Shafiq, P., Asadi, I., Mahyuddin, N.B. Concrete as a thermal mass material for building applications – A review. *Journal of Building Engineering*. 2018. 19. Pp. 14–25. DOI: 10.1016/j.jobe.2018.04.021
18. Lamrani, M., Khalfou, M., Laaroussi, N., Khabbazi, A. Thermal characterization of a new effective building material based on clay and olive waste. *MATEC Web Conf*. 2018. 149(3). 02053. DOI: 10.1051/mateconf/201714902053
19. Subashi De Silva, G.H.M.J., Perera, B.V.A. Effect of waste rice husk ash (RHA) on structural, thermal and acoustic properties of fired clay bricks. *Journal of Building Engineering*. 2018. 18. Pp. 252–259. DOI: 10.1016/j.jobe.2018.03.019
20. Asadi, I., Shafiq, P., Hassan, Z.F.B., Mahyuddin, N.B. Thermal conductivity of concrete – A review. *Journal of Building Engineering*. 2018. 20. Pp. 81–93. DOI: 10.1016/j.jobe.2018.07.002
21. Hadipramana, J., Riza, F.V., Ali, N., Somad, A., Basri, N. Thermal conductivity of aerated concrete containing rice husk ash as partially sand replacement. *IOP Conference Series: Materials Science and Engineering*. 2019. 674(1). 012023. DOI: 10.1088/1757-899X/674/1/012023
22. Sathurshan, M., Yapa, I., Thamboo, J., Jeyakaran, T., Navaratnam, S., Siddique, R., Zhang, J. Untreated rice husk ash incorporated high strength self-compacting concrete: Properties and environmental impact assessments. *Environmental Challenges*. 2021. 2. 100015. DOI: 10.1016/j.envc.2020.100015
23. ISOMET 2114 – Thermal properties analyzer. User's Guide. Bratislava. Slovakia. 2011. Pp. 3–33.
24. ASTM Standards. Standard Test Method for determination of thermal conductivity of soil and soft rock by thermal needle probe procedure D-5334-08. 2008. Pp. 1–8.
25. Charai, M., Sghouri, H., Mezrhab, A., Karkri, M., Elhammouti, K., Nasri, H. Thermal Performance and Characterization of a Sawdust-Clay Composite Material. *Procedia Manufacturing*. 2020. 46. Pp. 690–697. DOI: 10.1016/j.promfg.2020.03.098
26. Phonphuak, N., Saengthong, C., Srisuwan, A. Physical and mechanical properties of fired clay bricks with rice husk waste addition as construction materials. *Materials Today: Proceedings*. 2019. 17 (4). Pp. 1668–1674. DOI: 10.1016/j.matpr.2019.06.197

Information about authors

Penka Zlateva, PhD

ORCID: <https://orcid.org/0000-0002-8615-4208>

E-mail: pzlateva@tu-varna.bg

Rositsa Petkova-Slipets, PhD

ORCID: <https://orcid.org/0000-0003-2449-7173>

E-mail: rositsa.petkova@vfubg

Krastin Yordanov, PhD

ORCID: <https://orcid.org/0000-0002-6714-6480>

E-mail: krastin_yordanov@tu-varna.bg

Received 07.08.2022. Approved after reviewing 21.11.2023. Accepted 21.11.2023.



Research article

UDC 624.074.5

DOI: 10.34910/MCE.124.8



Optimum space frames with rectangular plans

V.F. Mushchanov , A.M. Mushchanov, A.N. Orzhehivskiy, M.N. Tcepliaev 

Donbas National Academy of Civil Engineering and Architecture, Makeevka

✉ mvf@donnasa.ru

Keywords: truss, truss structure, shape optimization, optimum design, structural optimization

Abstract. In this article, the object of research is spatial framed systems, one of the most commonly used types of spatial structures. The main feature of the research is the expansion of proven design solutions to the area of large-span frames with rectangular plan with an aspect ratio of less than 1:2, which is an urgent research and practical task. In this regard, the main purpose of the research study is to establish a connection between the main parameters of the projected object (geometric characteristics, structural loads) and their metal intensity. The study was based on a number of research methods. We used the finite element method in the numerical study of the coating stability of rods loaded in the axial direction. The method of physical modeling helped in experimental studies of models and coatings of their elements. Finally, the method of optimal design, specifically the Nelder–Mead method, was used to find the basic shape of a structure with a long-span rectangular plan. Main results. First, the data from theoretical and experimental studies confirmed a decrease in the estimated length of the compressed elements by 5...25 % due to their partial pinching in the ball nodes-connectors. Secondly, we developed an optimal design algorithm of spatial frames with long-span rectangular plans with an aspect ratio of less than 1:2. It differs from the previously developed ones due to a clarification of the load-carrying ability of axially loaded rods from the stability condition and the project designer's advanced capabilities in terms of their shaping. It provides an opportunity to use clear correspondences at the trial design stage and to clarify the specific metal consumption to set the optimal geometric parameters of the projected structure. We found patterns that make it possible to design optimal material consumption flat and spatial structural forms of spatial frames on rectangular large-span plans with an aspect ratio of less than 1:2, while taking into account the refined bearing capacity of rods loaded in the axial direction. The results obtained make it possible to use a proven limited range of structural elements in the form of round-section rods and connecting elements (ball-and-socket plug-connectors).

Funding: Russian Science Foundation "Conducting fundamental scientific research and exploratory scientific research by small individual scientific groups", No. 22-29-00139

Acknowledgments: The authors express their deep gratitude to all employees of the Department of Metal Constructions and Structures Federal State Educational Budgetary Institution of Higher Education Donbass National Academy of Civil Engineering and Architecture (FSEBI HE DNACEA) in Makeevka, who assisted in organizing and conducting experimental research, as well as to employees of the Department of Theoretical and Applied Mechanics FSEBI HE DNACEA for valuable advice formulated in the development of the optimization algorithm.

Citation: Mushchanov, V.F., Mushchanov, A.M., Orzhehivskiy, A.N., Tcepliaev, M.N. Optimum Space Frames with Rectangular Plans. Magazine of Civil Engineering. 2023. Article no. 12408. DOI: 10.34910/MCE.124.8

1. Introduction

Space frames (Fig. 1 a, b) are among the most commonly used types of spatial bar structures for coverings. Therefore, further research studies for improving structural forms are the basic improvement of the calculation, design, and construction procedures. The analysis of the stress-strain state of space frames is carried out in various software systems for calculation and design. The structural model contains multiple statically indeterminate hinge-rod systems. In such a case, the resulting stress in the selected section is the longitudinal stress that presents itself in a single element.



Figure 1a. Fragment of space frames (Donetsk, DPR, Russia)



Figure 1b. Plug-connector node (pinned)

The space frame structures designed earlier for mass use have some typical limitations [1]:

- maximum span is 42 m;
- standard aspect ratio in the plan is 1:1...1:2;
- limited assortment of elements and nodes designed for spans up to 42 m and for the aspect ratio from 1:1 to 1:2 in the plan (Table 1).

Table 1. Geometric and strength characteristics of a limited range of elements used*.

No.	Calculated force in the rod, N	Mechanical characteristics of the material, MPa		Type of the element	Section, mm × mm
		σ_{yield}	$\sigma_{tensile_strenght}$		
1	36800				48×3
2	50400				60×3.2
3	64600				76×3.2
4	83000				89×3.5
5	95600				102×3.5
6	122000	240	360	Rod	114×4
7	138300				127×4.5
8	201300				127×6
9	277300				133×8
10	377100				146×10
11	489100				159×12
12	-				Ø120
13					Ø150
14	-	785	980	Connector	Ø170
15	-				Ø200

* - the data given in Table 1 are taken from [1–3]

The approximating solutions as a discrete-continuous model, proposed by V.Z. Vlasov [4–6], are used for a multi-connected plate. Vlasov's concepts have been developed in [1–3]. However, the structural plates should be considered multiple statically indeterminate hinge-rod systems. In addition, in design, the forces in the rods of different zones of the plate are calculated depending on the structure's geometry, means of support, load applications, etc. Therefore, the use of such methods is possible at the stage of outline design of the grid.

Numerical approaches implemented in finite element analysis are the most common method of SSS analysis. The finite element analysis displays all the rod elements of the space frames that form the system. Such a system is a multiple statically indeterminate hinge-rod system. And the selection of sections is made for each individually modeled element. The authors performed a critical analysis of a number of scientific works, which can be divided into 3 large groups:

Papers in which the problem of stability of centrally compressed rods is considered from various positions. One of the most important indicators when choosing sections of rods with axial load is their stability. Since a huge number of works are devoted to this problem, we will consider only a few of them concerning the issues of studying stability using finite element models. Naturally, the matrices of shape functions used in finite element models gradually developed from the simplest, based on the hypotheses of L. Euler [7] (the initial deflection in the form of a half-wave of a sinusoid during elastic operation of the rod material is considered), to the more complex ones of F. Engesser [8] and F.S. Yasinsky [9] (the elasto-plastic work of the material in an approximate formulation is taken into account. By the way, the authors Y. Zheng, H. Zheng [10], who in their work substantiate application of a design solution that reduces the value of the calculated eccentricity in an eccentrically compressed rod). Finally, the classic papers of B.G. Galerkin [11] and N.S. Streletsky [12] made it possible to generalize the experience of numerous theoretical and experimental studies for centrally, eccentrically compressed and compressed-bent rods, loss of spatial stability of solid rods, and features of the operation of through rods. A.R. Rzhansyn supplemented these materials with the solution of a number of stability problems from the standpoint of probability theory, which served as the basis for assigning values of the safety factor, and the results of studies of the stability of rod systems [13]. Integration of the results into a unified system for describing the process of buckling, taking into account the influence of rod bending, is presented in the scientific papers of S.P. Timoshenko, J. Geer [14] and S.D. Leites [15]. A certain generalization of methods for calculating the stability of centrally and eccentrically compressed rods at the present stage was given by I.D. Anikeev, A.V. Golikov in article [16], within the framework of which a comparative analysis of methods for calculating the stability of rods, which form the basis of regulatory documents of the CIS countries, was carried out and Europe. The different methodological basis in determining the value of random eccentricity is emphasized.

Standing somewhat apart from this list are the results of a study of the stability of centrally and eccentrically compressed rods made of composite materials. Although composite materials range from traditional (B. Li, H. Luo, H. Wang, M. Bosco [17] defective steel bars reinforced with CFRP) to exotic (W. Zhao, Z. Chen, B. Yang [18] steel and bamboo), the authors use the above described methodological framework to conduct their research. And the most complete modern representation of the capabilities of the finite element method in solving stability problems, corresponding to the problems solved in this article, is presented in the papers:

- A.V. Perelmuter, V.I. Slivker, S.Yu. Fialko [19–22], which discuss the peculiarities of using universal calculation systems from the standpoint of assessing the complexity of systems and its components, the correctness of finite element models, the scale of the problems being solved, the heterogeneity of the finite elements and their relationships;
- F. Yunfeng, W. Li, T.E.E. Kong Fa [23], in which the implicit function apparatus was used to calculate the reliability index of steel coating structures in the presence of a large amount of data. The Monte Carlo method is used as a method for determining the numerical value of the probability of failure.

Papers devoted to the features of a refined analysis of the stress-strain state of spatial rod systems in the form of structural structures:

- in the research paper of A.B. Bondarev and A.M. Yugov [24], the influence of random imperfections acquired by a spatial structural structure at the installation stage, the method for calculating the accuracy of large-span metal rod systems and its mathematical model are considered. Very close to it in terms of the formulation of the problem and research methods is the study of M. Gordini and M. Habibi [25], in which the problem of the influence of installation imperfections is considered for two-layer lattice space trusses (DLGST). Differences in the length of elements were modeled by random variables generated in accordance with using the normal distribution law;

- Structural structures are considered from the same positions in the research of E. Gaylord, K. Gaylord and J. Stollmeyer [26], which presents calculation and design methods that make it possible to analytically assess the stress-strain state of a spatial frame. The authors went somewhat further in this direction: S. Liu, L. He, Z. Wu, J. Yuan [27], who take into account the influence of the deformability of the node, when it is considered as a deformable semi-rigid connection, on the change in the geometry of the elements converging in it when creating a stochastic element models;
- the problem of improving the design of a node for connecting elements of structural structures is considered in the paper of V. Hassani [28] (the possibilities of designing nodes focused on the technological capabilities of 3D printing for metal are presented. In this case, the procedure for optimal design of a node is performed using a genetic algorithm to minimize the maximum background stress von Mises as an objective function depending on the node mass as a constraint function). Close in meaning is the article of T. Sathish, S. Dinesh Kumar, S. Karthick [29], where the problem of improving the reliability of a unit is solved based on a comparative analysis of the results of using aluminum alloys AA2014, AA6061 and AA7075. In the same series are the papers of the authors J. Lange, T. Feucht, M. Erven [30] and K. Buchanan, L. Gardner [31], where the issues of forming units at the design and manufacturing stage are solved using additive manufacturing technologies. However, we immediately note that in all the analyzed works there is no feedback in the form of the influence of the selected node shape on the stress-strain state of the rod;
- very interesting and close in one of the final goals of our research is the paper of S. Lan, H. Tu, J. Xue and others [32], in which the problem of shaping a structural structure is solved using the proposed adaptive method for determining the shape. However, in contrast to the approach proposed in this research, here the problem of forming an effective structure is solved on the basis of minimizing the lengths of the rods;
- also, the problems of shaping spatial rod structures are solved in the article of S. Li, J. Xu, G. Feng, Z. Zhu [33] (the features of the stress-strain state of 2 structural systems of vertical and inverted hexagonal pyramids are analyzed), and the features changes in the dynamic characteristics of spatial rod structures due to the magnitude and nature of the application of snow load are discussed in detail in the research of H. Guan, H. Chen, J. He, H. Sun [34].

The majority of two factors in studying the buckling process using the FEM are noted:

- the difference between the actual fastenings of the rod from the idealized ones;
- different forms of stability loss and the ability to predict them.

The structural model simplifies in all the works studied. Namely, the detailed modeling of nodes and their influence on the load structure is not considered. Therefore, clarified modeling will allow the implementation of the followings:

- keeping the actual restraints due to the applied structural concept for nodes of space frames elements;
- the creation of such a grid of nodes in the structural model will allow describing most accurately the initial mistakes, which is characteristic of the subsequent deformation of the rod in the process of buckling.

It should be noted that all the researchers presented above dealt mainly with the issues of SSS of space frames' nodes. Less attention was paid to the stability of space frames' loaded elements. The influence of the initial geometric imperfections of the rods and rigidity of the nodes on the load-carrying ability of the diagonal member from the stability condition was not considered.

Papers devoted to the problem of optimization of structural structures: Works devoted to the problem of variant and optimal design represent a huge body of research, the analysis of which should be devoted to separate works. The standard criterion for the quality of the project (optimality criterion), namely, the objective function (effectiveness function), is the extreme value of the function with the required parameters. The most common quality criterion for a project is metal intensity. Therefore, without claiming to be a complete review on this issue, the authors would like to note that the practical application of variant and optimal design in the design of structural structures is associated, first of all, with researches of Ya.M. Likhtarnikov [35], in which the basis of the method was developed, within which the main approaches to the formulation of the goal function in the form of a minimum mass, labor intensity or cost of manufacturing and installation, cost in business or the present value of the structure were detailed. Optimization of standard and unique core slabs, shells and domes according to a complex economic criterion – reduced costs – was carried out in the paper of V.N. Shimanovsky, V.N. Gordeev, M.L. Grinberg [36]. Also, considerable attention is paid to the assessment of metal intensity, labor intensity of

manufacturing and installation, and energy intensity of the structural form. The closest to the approach being developed is the paper of I.V. Romensky [37], in which the optimization of the goal function in the form of a minimum of mass, labor intensity or cost of manufacturing and installation, cost in the case of spatial long-span membrane coverings using the Nelder-Mead method.

Optimization based on the minimum mass criterion was used in the research of N. Petrović, N. Kostić, N. Marjanović, J. Živković, I.I. Cofaru [38], where optimization was performed by refining the geometric shape of four different topological variations of a typical trapezoidal roof truss, taking into account their effect on the total external surface area.

M. Kurniawan and A. Adha [39] present the results of a study of trusses that must satisfy an optimum of minimum cost while maximizing the use of load-bearing capacity. Due to the significant number of variables taken into account in the calculation, a feature of this study was the use of iterative procedures using genetic algorithms, in which the process proceeds in a stochastic manner.

The article by T. Zhang, K. Kawaguchi, M. Wu [40] presents a methodology for searching for an optimal strategy for folding frame structures, which is created on the basis of a generalized inverse theory and a genetic algorithm. A similar approach using a two-phase genetic optimization algorithm was used in the work of M. Kociecki, H. Adeli [41] for free-form steel space-frame roof structures. In [42] by the same authors, the algorithm was extended to optimize the topology and shape of free-form steel space-frame roof structures with complex geometry using evolutionary calculations. What is especially unusual is that in the proposed shape optimization algorithm, heuristic restrictions are introduced to achieve the goal, which make it possible not to distort the original architectural design during the optimization process.

As a brief conclusion based on the results of the critical analysis, it should be noted that in all the cases analyzed above, the rods that make up the structure are considered from the classical idealized positions of the hinge-rod model, when either the deviation of the length of the rod from the idealized value or the idealized (simplified) shape was considered in the form of an initial imperfection initial curvature, far from the geometry of the rod corresponding to the moment of loss of stability. And this factor has a huge impact on the final result of the calculation – the value of the critical force.

The approaches to optimizing the structural form of structural coverings discussed above do not take into account a number of important factors in the form of a refined load-bearing capacity of compressed rods from the stability condition, expanded possibilities for shaping structural coverings from a limited set of elements due to the transition from a flat shape to a shell of positive Gaussian curvature, and the influence of the length ratio sides of a rectangular covering plan. The above works disclose the optimization of long-span structures on traditional square plans or similar to them. These processes are possible per the current design standards with various variable parameters. However, the issue of optimizing structures on a rectangular plan with an aspect ratio less than 1:2, with the refined calculation models of space frame elements, was not addressed.

The results of the critical analysis made it possible to identify a number of key issues that were not properly reflected in the analyzed works and require further research. It is supposed to establish the relation between the main parameters of the designed object (geometric characteristics, structural design loads) and their metal intensity for large-span shells on a rectangular plan up to 126 meters in size and an aspect ratio up to 1:2. These conditions stand considering the current trend toward increasing spans and the transition to non-standard geometric shapes. The optimum design shape finding for overlapping such plans with space frames involves testing and subsequent use of two hypotheses:

- increasing the stability of axially loaded rods by taking into account their partial restraint in nodes (ball-and-socket connectors);
- lowering the maximum design forces in the chord elements of the space frames by changing their flat shape into deflected ones.

The combination of these two approaches in one design algorithm has a positive effect on:

- improvement of technical and economic indicators of the designed structures;
- the possibility of using a limited assortment of elements and nodes, designed for spans up to 42 m and for the aspect ratio from 1:1 to 1:2 in the plan.

This research aims to exploit the optimal space frame design shape on rectangular plans with an aspect ratio of less than 1:2. The significant design parameters and clarified load-carrying ability of axially loaded rods are considered. Thus, the possibility of using a limited range of structural elements provides.

Research objectives:

- to undertake the theoretical and experimental evaluation of the nodes' structural concept influence on the stability of axially loaded rods for space frames;

- to build an algorithm for the optimal design of space frames on rectangular plans, including those with an aspect ratio less than 1:2. The clarified load-carrying ability of axially loaded rods and extended approaches to shaping in the form of shallow shells of positive Gaussian curvature;
- to evaluate the influence of support compliance on the stress-strain state of the space frame structure on a non-standard plan.
- to give recommendations for the space frames' design of long-span rectangular plans with an aspect ratio of less than 1:2. Thus, the possibility of using a limited range of structural elements provides (rods, connecting elements).

2. Materials and Methods

2.1. Numerical methods

Clarifying the load-carrying ability of axially loaded rods from the condition of stability is carried out using the FEM through the displacement method. The process is possible by considering the structural design of the nodes and the spatial working of the rod elements. It should be noted that the structural model designed as a spatial shell-bar (Fig. 2) confirms its accuracy. Moreover, there is a possibility of further use in the numerical analysis of the rods' stability, taking into account the influence of nodes (Table 2). Also, the control of the stress-strain state makes it possible to more correctly take into account the change in the geometry of the rod in the process of its deformation. The process takes place during step-by-step load application in the calculation model.

The Nelder-Mead method is a preferable solution for the problem of optimizing the geometric shape of an initially flat space frame on a rectangular plan with an aspect ratio of 1:1 ... 1: 2.8 due to its main features:

- the zero-order method uses only the value of the objective function. It is easily applied to non-smooth and noisy functions. Thereby it does not apply restrictions on functions;
- the lack of the theory of convergence (the algorithm can diverge even on smooth functions);
- it does not depend on the number of control parameters;
- it allows control of the information at each iteration of optimum seeking.

2.2. Experimental methods

The method of physical modeling is chosen as an observation method. In this case, a space frame unit is taken as a model on a scale of 1:1 in relation to the full-scale structure. The full compliance with the material similarity is kept. This decision is justified by the possibility of observing the actual behavior of the structure on load and the strain capacity of nodes. Table 3 and Fig. 3 justify the accuracy of the used equipment.

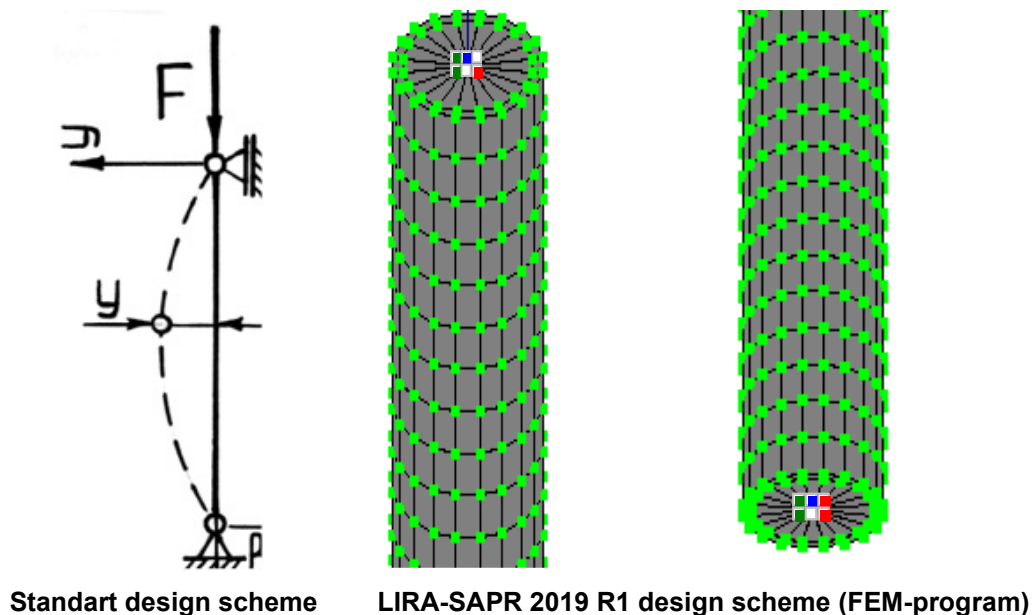


Figure 2. Design scheme for the model verification.

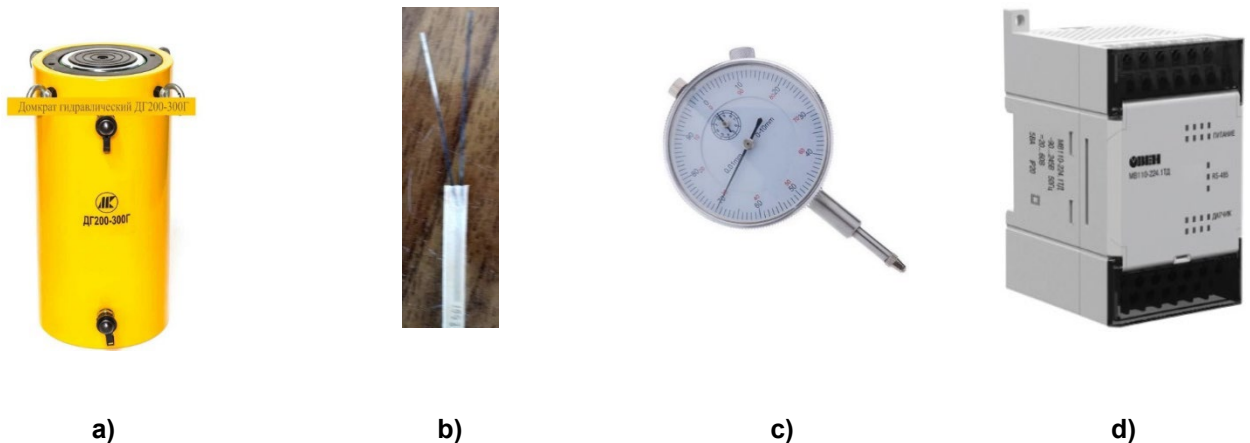
Table 2. Comparison of the results of verification calculation.

λ	Calculation results	Analytical solving (standart design scheme)	Finite element method solving (LIRA-SAPR 2019 R1)	Error between columns 3 and 4 (%)
80	σ_{cr} (Pa)	2.188e+8	2.175e+8	0.6
	N_{cr} (N)	92770	92250	
100	σ_{cr} (Pa)	2.042e+8	2.069e+8	1.3
	N_{cr} (N)	86810	87750	

λ is the flexibility of rod
 σ_{cr} is the critical stress in the rod
 N_{cr} is the critical longitudinal force in the rod

Table 3. Support the possibility of the measuring equipment.

Research rate	Type of equipment	Description of equipment			The graduation of a device	Measurement error
		Name	Country	Manufacturer		
Load	Jack Hydraulic (Fig. 3.a)	DG 100-200G	Russia	Consul Ltd.	1.0e+5 Pa	-
Relative deformation	Resistive strain gage (Fig 3.b)	KF5P1-20-200-A-12-S1	Russia		-	± 1 Ohm
Displacement	Dial indicator (Fig 3.c)	ICH-10	Russia	JSC KP KRIN	0.01 mm	From 15 to 20 micron
Ohmic resistance change	Input module of resistive strain gage signals (Fig 3.d)	OWEN MV110-224.4.TD	Ukraine	OWEN	1.0e+4 Pa	± 0.05 %

**Figure 3. Experimental equipment.**

The physical model under analysis is created in line with geometric and physical similarity principles. At the same time, it has the same qualitative sense as the model object. There is a regulatory assortment for both rods and nodes. Thus, the indicators for scales (EI , EF geometric dimensions) are taken on a full scale of 1:1. Two experimental setups are used as experimental research for laboratory tests:

- the separate unit of the space frame in which diagonals lose stability in the elastic stage of material behavior (λ of diagonal is 120) (Fig. 4–5, a, b);
- a rod that loses stability in the elastic stage ($\lambda = 120$) (Fig. 4-5, c, d).

Based on the preliminary calculation results, the level of designed load on the tested model No. 1 is 22755 kg. The level of critical load in the inclined rods of the pyramid is $N_{cr(FEM)} = -79.545$ kN. The level of designed load on the tested model No. 2 is 8800 kg and $N_{cr(FEM)} = -64.35$ kN.

The load on the experimental models was applied using hydraulic jacks. For model No. 1, hydraulic jack DG-100 to the upper node is used. For model No. 2, hydraulic jack DG-20 to the lower node was used. The step of load applying for the first model is 550 kg, and for the second model is 100 kg (41 and 88 load steps, respectively).

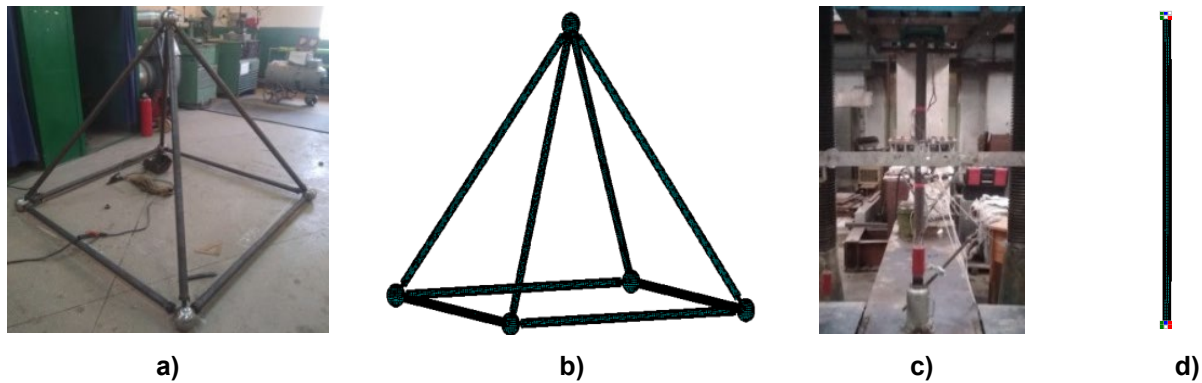


Figure 4. Experimental models.

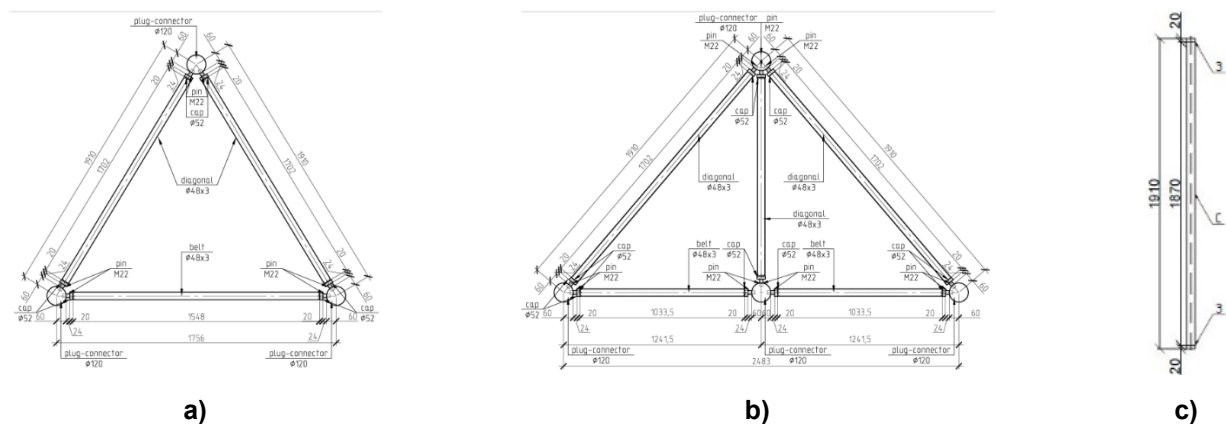


Figure 5. Model sizes.

The holding time of each stage is 35–55 seconds (for the load accommodation and distribution in the structure). The main reason is that the polling rate of all active strain gauges connected to the OVEN strain gauge station equals 7 polls per second. It makes it possible to average all the received data as clearly as possible. Moreover, it allows identifying the moment of distribution and stabilization in the structure of strain gauge readings. They were recorded using the MasterSCADA program as a text file. The dial gauge readings were recorded on video cameras and written down manually.

3. Results and Discussion

3.1. Results

3.1.1. Stability of centrally compressed rods

The axially loaded rods' buckling was studied using finite element analysis. Variable parameters are the sizes of the node structure and the flexibility of the rods.

The dimensions of the structural elements were taken per the limited assortment] (Table 1). The value of the flexibility of the elements varied in the range of 50–140. The models of shell finite elements were developed in the LIRA-SAPR 2019 R1 software package. Such elements make it possible to consider the nonlinear relation of both deformations and material properties on the load. In models, all rods have the following properties:

- initial imperfection in the form of rod's axis deviation along with the half sine wave $f/l = 1/700$ (Fig. 6);
- tensile stress-deformation diagram for steel S245 ($R_y = 240$ MPa) (for rod and plug) and 40X "Select" ($R_y = 785$ MPa) (for bolt and connector).

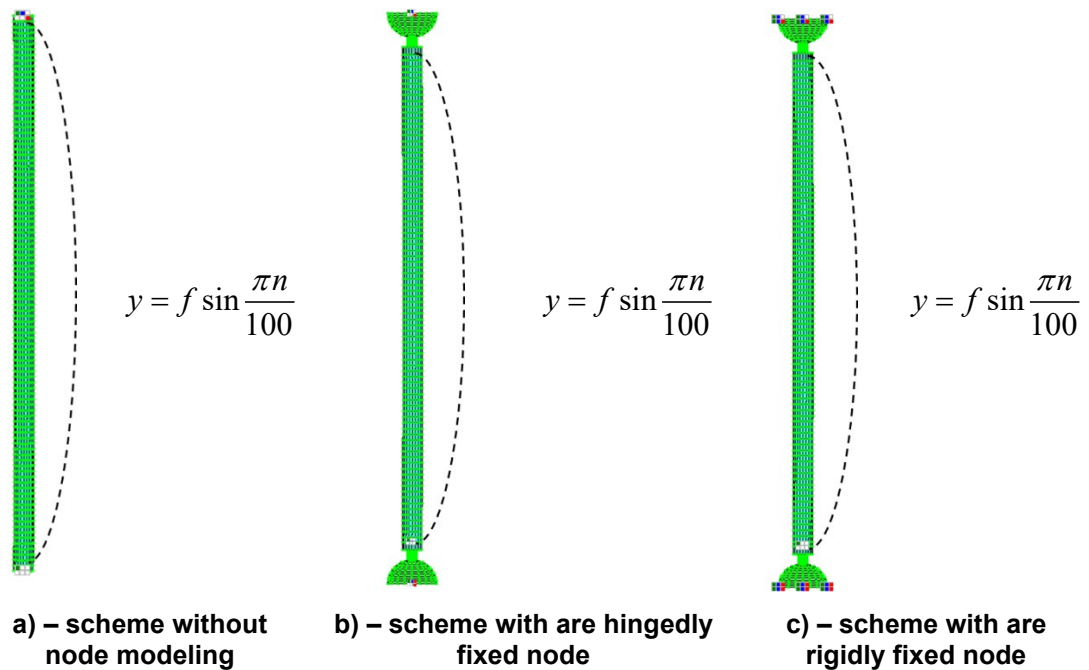


Figure 6. Design schemes with initial geometric imperfection in the form of a deviation from the rod axis along a half-wave of a sinusoid.

The methodological framework of the research work was based on the comparison of critical stresses with different modeling of rods:

- a rod without node modeling (Fig. 6, a);
- a hinged rod (Fig. 6, b);
- a rod with rigid fixing, reflecting the work of the rod in the space frame (Fig. 6, c).

Fig. 7 represents the influence of nodal connection modeling on the rod's bearing capacity as load-displacement relations.

A comparison of the data array of critical loads and stresses with the corresponding solutions is held to analyze the results of numerical studies. The results were obtained using the classical Euler method [7] and Engesser-Yasinskiy [8, 9] method, adopted in the latest scientific research over the past five years [16, 18, 43]. The results of numerical studies presented in Fig. 7 allow us to assert the need to consider the influence of pinching of the rod in the nodes when analyzing its stability. The main differences in the calculation results for the schemes presented in Fig. 6 are expressed by the following:

- there is a significant difference in the form of rod axis curvature at the moment of buckling from the deformation scheme in the form of a half sine wave used in the classical solutions of the stability problem;
- there is a pinching of a part of the length of the rod's support section in the plug-connector nodes. This pinching causes a reduction in its effective length. Therefore, the flexibility lowers, and the load-carrying ability rises from the condition of stability. The fact of lowering flexibility is confirmed by the lowering in the values of the maximum rod's deviations, corresponding to the moment of buckling (W_{\max} by 3–4 times), due to the influence of the rigidity of the node (Fig. 7 a–d).

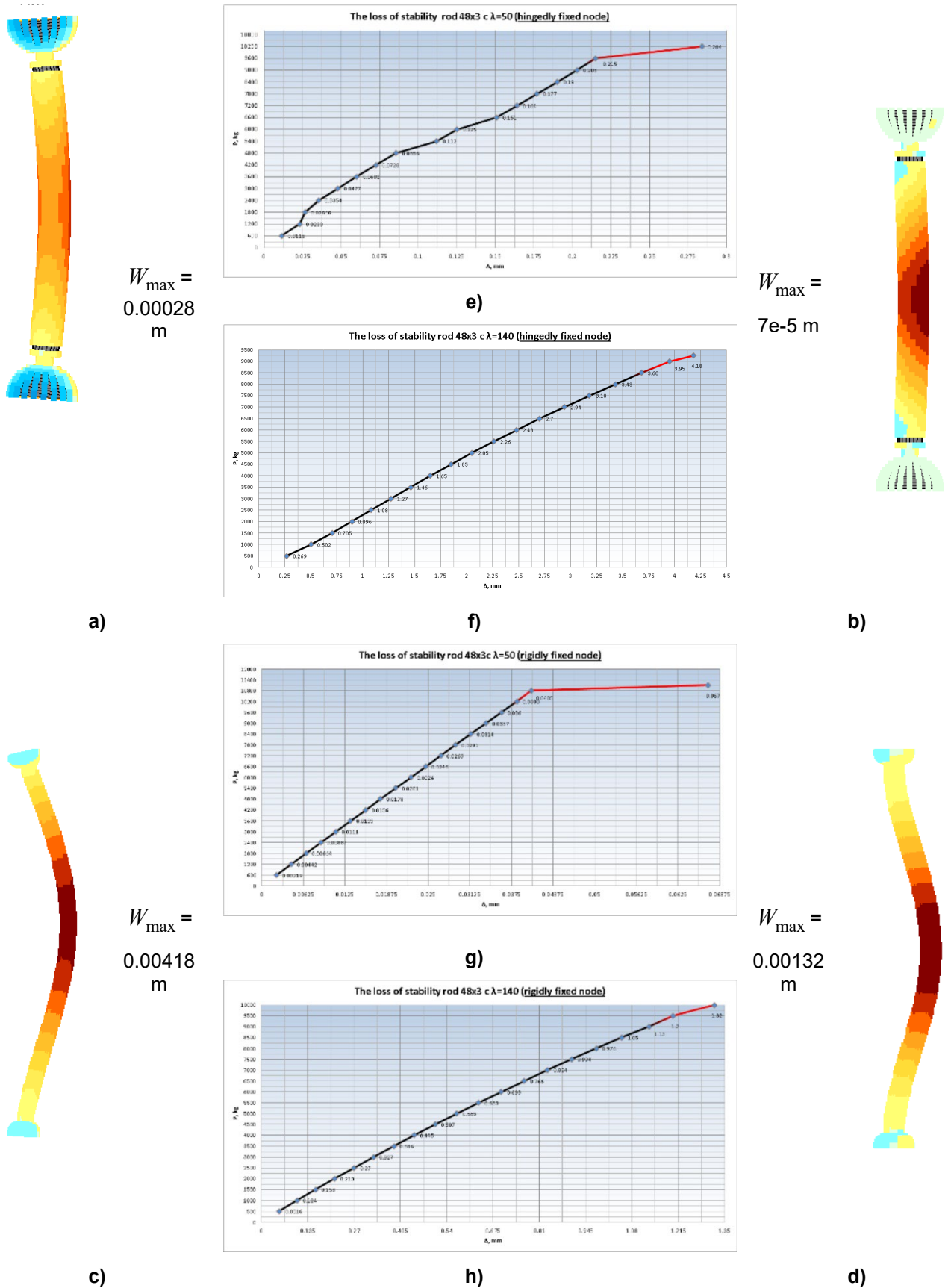


Figure 7. View of a deformed steel rod in a moment of loss of stability.

As a result, the load-carrying ability of the axially loaded rods of space frames is refined from the stability condition (1). Stability condition (1) considers the influence of nodes on the form of the rod's deformed axis, and the spatial work of the rod-shell was taken into account. The correspondence σ can be described by stability condition (1) with sufficient accuracy for practical calculations $\sigma_{cr} - \lambda$:

$$\sigma_{cr} = 0.0004\lambda^2 - 0.1536\lambda + 26.681. \quad (1)$$

Moreover, this formula (1) is the basis for the values of the conversion factor from geometrical length to calculation one (μ) and the factor of the longitudinal bending φ (for steel $R_y = 240$ MPa), which take into account the flexibility and pinching of the rod in the joints of structures with ball-and-socket plug-connectors. (Table 4).

Table 4. Dependences $\mu - \lambda, \varphi - \lambda$

λ	50	60	70	80	90	100	110	120
μ	0.83	0.88	0.91	0.93	0.94	0.95	0.95	0.95
φ	0.933	0.892	0.854	0.820	0.789	0.760	0.739	0.721

μ is the conversion factor from geometrical length to the calculation length of rod; φ is the factor of the longitudinal bending of rod; λ is the flexibility of rod;

3.1.2. Experimental verification of theoretical studies

Experimental studies of the influence of space frames' nodes on the stability of axially loaded rods were carried out on the basis of numerical studies [44]. Some test results are presented in tables 5 and 6 (critical longitudinal forces and their comparison with numerical studies). Figure 8 a–c shows buckled elements in experimental models.



a) Rod 1 (first model, structural covering cell)



b) Rod 2 (first model, structural covering cell)



c) Rod 3 (second model, single rod)

Figure 8. View of the unstable rod.

Table 5. Massive of critical loads (the first tests).

Massive of critical loads					Difference	
$N_{cr(FEM)}$, N	$N_{cr(UCC)}$, N	$N_{cr(rod1)}$, N	$N_{cr(rod.2)}$, N	$N_{cr(aver.)}$, N	Δ_{1-5} , %	Δ_{2-5} , %
-79545	-47000	-65801	-80245	-73023	8.2	35.64

$N_{cr(FEM)}$ is the critical longitudinal force on the finite element method.

$N_{cr(UCC)}$ is the critical longitudinal force on the Ukrainian Construction Code. Steel Structures design code..

$N_{cr(rod1)}$ is the critical longitudinal force in the first rod on the experimental model.

$N_{cr(rod.2)}$ is the critical longitudinal force in the second rod on the experimental model.

$N_{cr(aver.)}$ is the average critical longitudinal force on the experimental model.

Table 6. Massive of critical loads (the second tests).

Massive of critical loads				Difference		
$N_{cr(FEM)}$,	$N_{cr(UCC)}$,	$N_{cr(aver.)}$,	$N_{cr(s.rod)}$,	$\Delta 1-4$,	$\Delta 2-4$,	$\Delta 3-4$,
N	N	N	N	%	%	%
-64350	-47200	-73023	-57410	10.78	17.78	21.038

$N_{cr(FEM)}$ is the critical longitudinal force on the finite element method.

$N_{cr(UCC)}$ is the critical longitudinal force on the Ukrainian Construction Code.

$N_{cr(aver.)}$ is the average critical longitudinal force on the experimental model.

$N_{cr(s.rod)}$ is the critical longitudinal force in the single rod (second experimental model).

The experimental studies confirm the correctness of the numerical studies' results. The hypothesis of an increase in the load-carrying ability of the axially loaded rods of the space frames due to their pinching in ball-and-socket plug-connectors is proved (the divergence of results is within 8–11 %).

3.1.3. Research results on optimization of design concepts

The search for the optimal constructive solution for space frames on rectangular plans with an aspect ratio up to 1:1 ... 1:2.8 was based on minimizing the theoretical mass of the structure. The mass of the structure is calculated from the final geometric parameters of the structural elements that make up the structure

$$G \rightarrow \min \left[\rho \left(\sum_{i=1}^n A_i l_i + \sum_{j=1}^m V_j \right) \right], \quad (2)$$

where G is the optimized mass of the structure, ρ is the steel density, $i = 1 \dots n$ is the number of nod elements of the space frame, A_i is the cross-sectional area of the i -th element, l_i is the theoretical length of the i -th element (by the centers of nodes), $j = 1 \dots m$ is the number of connecting nodes, V_j is the true volume (excluding slots) of the j -th connector.

The space framing optimization algorithm on a rectangular plan with an aspect ratio up to 1:1...1:2.8 was based on the objective function (2). This algorithm considers the possibility of selecting sections for axially loaded rods, both per the requirements of regulatory documents and using dependence (1). According to the MATHLAB algorithm, a program optimizes the structural form of the space frame on a rectangular plan with an aspect ratio up to 1:1...1:2.8 (Fig. 9).

The optimization of the initial design solutions is carried out in two versions, using the capabilities of the algorithm:

- it is a preservation of the flat shape of the original design solution and searching for the optimal solution by varying a single parameter which is the relative height of the covering (h/b).
- the original flat shape of the design solution bending and transformation into a flat rod shell with the search for the optimal solution by varying two parameters: the relative height of the covering (h/b) and the relative camber (f/b) [45].

The following limitations are set when developing an optimal design algorithm:

- the studies are conducted for structural elements made of steel with a design resistance of 240 MPa. In the optimization process, a limited range of rod elements and ball-and-socket plug-connectors, shown in Table 1, was used;
- the relative height varies within $(1/10 \dots 1/30) b$ here b is the short side of the plan. The reason for this is recommendations for the design of structures;
- the relative camber varies within $(0 \dots 1/4.5) b$. It is due to the possibility of preservation of a uniformly distributed snow load in the structural models for all optimal designs;

Table 7. Results of optimization of design solutions for the constructive form of coverings on a non-standard plan.

Structure covering in plan	Calculation load (N/m ²)	Optimization of geometric parameters			Mass of the structure (kg)	
		One parameter	Two parameters		Before optimization	After optimization (two param.)
		<i>h</i> (m)	<i>h</i> (m)	<i>f</i> (m)		
45×45	400	1.523	0.7031	7.856	22674.10	19610.10
	1000	1.934	0.7031	6.071	25155.60	21775.70
	1600	2.508	0.7031	5.174	28600.30	23384.00
	2400	2.836	0.7031	9.999	33275.80	25806.20
45×68	400	1.523	0.7031	4.285	30834.70	27360.60
	1000	2.344	0.7031	7.142	35591.70	30921.40
	1600	2.672	0.7031	7.856	41305.80	33750.50
	2400	3.000	0.7031	9.999	49.89960	37.10420
45×90	400	1.523	0.7031	4.107	40.82280	36.59150
	1000	2.508	0.7031	7.142	47.85630	40.68090
	1600	2.672	0.7031	9.999	56.22520	43.97220
	2400	3.000	0.7031	8.571	68.27860	48.92690
45×108	400	1.523	0.7031	4.285	50.16080	45.18870
	1000	2.508	0.7031	7.856	59.24530	49.39490
	1600	2.672	0.7031	8.928	69.07500	52.60220
	2400	3.492	0.7031	9.999	85.05950	59.66300
45×126	400	1.605	0.7031	5.000	57.59710	51.77130
	1000	2.508	0.7031	9.999	69.58510	58.43290
	1600	2.672	0.7031	9.999	82.64190	63.10020
	2400	3.328	0.7031	9.999	100.48210	70.88510

Table 8. Resulting regression formulas.

$$y = b_0 \pm b_1 x_1 \pm b_2 x_2, \quad (3)$$

y is the required indicator; *x*₁ is the covering calculation load; *x*₂ is the aspect ratio in plan; *b*₀, *b*₁, *b*₂ is the support factors.

Formula	Description	Correl. factor
$G_{ucc} = 8.56004 + 0.03523 \times q - 0.038389 \times a/b$	Specific gravity calculated from the height of the covering. The application of the formula for the selection of axially loaded rods is possible according to the current regulatory documents	0.99007
$G_{meth} = 8.52905 + 0.03384 \cdot q - 0.2448 \cdot a/b$	Specific gravity calculated from the height of the covering. The application of the formula for the selection of axially loaded rods is possible according to the proposed technique	0.99004
$h/b_{ucc} = 0.03809 + 0.0019 \cdot q - 0.0138 \cdot a/b$	Relative height calculated from the height of the covering. The application of the formula for the selection of axially loaded rods is possible according to the current regulatory documents	0.91866
$h/b_{meth} = 0.0393 + 0.0018 \cdot q - 0.0161 \cdot a/b$	Relative height calculated from the height of the covering. The application of the formula for the selection of axially loaded rods is possible according to the proposed technique	0.91912
$G_{ucc} = 8.24686 + 0.01873 \cdot q + 0.47052 \cdot a/b$	Specific gravity calculated from the height of the covering and camber. The application of the formula for the selection of axially loaded rods is possible according to the current regulatory documents	0.98861
$G_{meth} = 8.20306 + 0.01541 \cdot q + 0.73692 \cdot a/b$	Specific gravity calculated from the height of the covering and camber. The application of the formula for the selection of axially loaded rods is possible according to the proposed technique	0.98379

$$y = b_0 \pm b_1 x_1 \pm b_2 x_2, \quad (3)$$

y is the required indicator; x_1 is the covering calculation load; x_2 is the aspect ratio in plan; b_0, b_1, b_2 is the support factors.

Formula	Description	Correl. factor
$h/b_{ucc} = 0.22617 + 0.000003 \cdot q - 0.0234 \cdot a/b$	Relative height calculated from the height of the covering and camber. The application of the formula for the selection of axially loaded rods is possible according to the current regulatory documents	0.54018
$h/b_{Meth} = 0.23334 + 0.0000046 \cdot q - 0.0429 \cdot a/b$	Relative height calculated from the height of the covering and camber. The application of the formula for the selection of axially loaded rods is possible according to the proposed technique	0.76918

The flexibility of supports affects the metal intensity of the covering and its optimal geometric parameters [46]. It should be considered when developing a design solution. Table 9 shows the results for the plan of 45×90 m with different ratios of the flexural rigidity of the supports and the span of the covering.

Table 9. Results of optimization of design solutions for the constructive form of coverings on a 45×90 plan with the account of the pliability of the supports.

Stiffness ratio k_1^*	Calculation load (N/m ²)	Optimization for two parameters		Optimal structural covering weight (kg)	
		h, m	f, m	On the fixed supports	On the pliability supports
∞	400	0.7031	10	36591.50	-
	1000	0.7031	10	40680.09	-
	1600	0.7031	10	43972.20	-
	2400	0.7031	10	48926.90	-
10:1	400	2.344	10	-	41189.10
	1000	3.574	9.582	-	44460.70
	1600	3.574	10	-	47992.30
	2400	2.139	10	-	52885.80
1:1	400	3.574	10	-	35478.00
	1000	3.369	10	-	39401.60
	1600	3.164	10	-	44270.90
	2400	2.344	10	-	48124.40
1:10	400	3.369	9.791	-	35801.50
	1000	2.344	6.666	-	42738.10
	1600	2.344	10	-	45771.00
	2400	2.344	10	-	50983.60

* - Note: $k_1 = EI/D \cdot b$, here k_1 is a coefficient considering the influence of the flexural rigidity of the span and supports on the optimal design parameters ratio; EI is the rigidity of supports (columns); D is the bending stiffness of the slab, b is the distance between the supports (columns) in the cross direction.

Table 10 gives the calculated regressional dependencies. It is possible to specify the main geometric parameters of the designed structure. These specifications can provide the optimal steel consumption considering the flexibility of the supports.

We conclude a significant reduction in the metal intensity of the space frame according to the analysis. This approach, based on the appointment of the change in geometry and the usage of a refined assessment to the load-carrying ability of axially loaded rods, fact confirms the correctness of the hypotheses underlying the research work.

Table 10. Resulting regression formulas with account the pliability of the supports

Formula	Description	Correl. factor
$G_{calc} = 8.63805 - 0.00034 \cdot k1 + 0.01923 \cdot q_{calc}$	Specific gravity calculated from the height of the covering and camber. The application of the formula for the selection of axially loaded rods is possible according to the current regulatory documents	0.958859
$G_{calc} = 8.74417 - 0.00037 \cdot k1 + 0.01587 \cdot q_{calc}$	Specific gravity calculated from the height of the covering and camber. The application of the formula for the selection of axially loaded rods is possible according to the proposed technique	0.933453
$h / b_{calc} = 0.064894 - 0.000046 \cdot k1 - 0.000021 \cdot q_{calc}$	Relative height calculated from the height of the covering and camber. The application of the formula for the selection of axially loaded rods is possible according to the current regulatory documents	0.784184
$h / b_{calc} = 0.072853 - 0.000048 \cdot k1 - 0.000066 \cdot q_{calc}$	Relative height calculated from the height of the covering and camber. The application of the formula for the selection of axially loaded rods is possible according to the proposed technique	0.907314

The final form of the covering structure and its geometric parameters based on the results of optimization is presented in Fig. 10 a–d.

3.2. Discussion

In this paper, the authors improved the process of designing space frames on rectangular large-span plans with an aspect ratio up to 1:1... 1:2.8. The following step-by-step improvements are made:

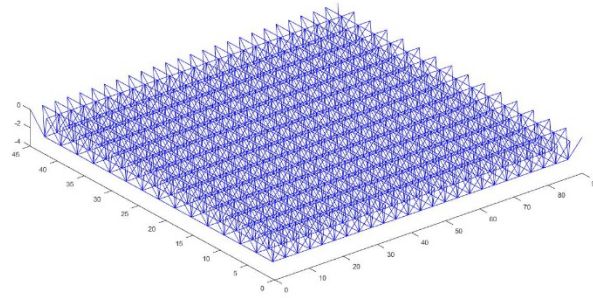
1. clarification of the traditional structural model;
2. clarification of the bearing load-carrying ability of rod elements;
3. optimization of the design shape.

The hypothesis on the influence of the node's design on the load-carrying ability of loaded rods from the condition of stability is confirmed. The results correlate with the data of A.V. Perelmuter, V.I. Slivker, S.Y. Fialko [19–22], I.D. Anikeev, A.V. Golikov [16], F. Yongfeng, W. Li, T.E.E. Kong Fah [23]. The experimental data by Central Research Institute of Building Structures named after Kucherenko (Moscow, Russia) [1] correlates in cases of coincidence of slenderness and conditions of jointing of the studied rods.

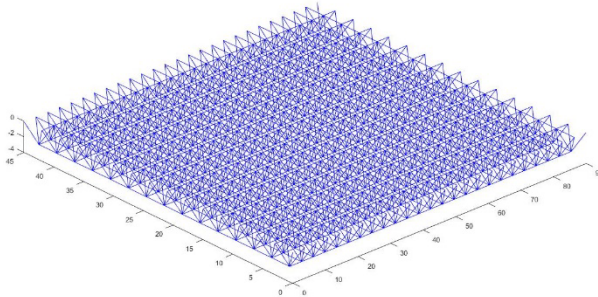
An important practical outcome of the research results is recommendations for project designers on using certain factors. These are the factor of the longitudinal bending φ and the conversion factor from geometrical length to calculation one (μ). The values of these factors for the rods jointed by nodes are given. Practical recommendations for the optimal parameters of the designed structure, which can be used at the initial design stage, are presented in the paper too.

At the same time, there are several topics for further research:

- expanding the research area for the nodal joint design and the load-carrying ability of the loaded rods of space frames by considering other types of nodes and steel classes;
- conducting additional research related to the type and parameters of the specified initial geometric imperfection while studying the stability of axially loaded rods. An additional issue of this line may be a connection between the design of the node and the given initial geometric imperfection of the rod element shape;
- developing the constructive form optimization algorithm associated with the expansion of the number of variable parameters and the specified structural forms.

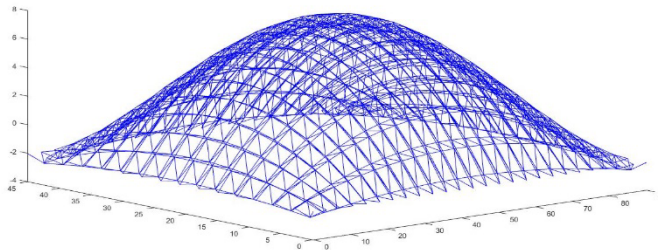


a) – the original scheme



b) – optimization for one parameter

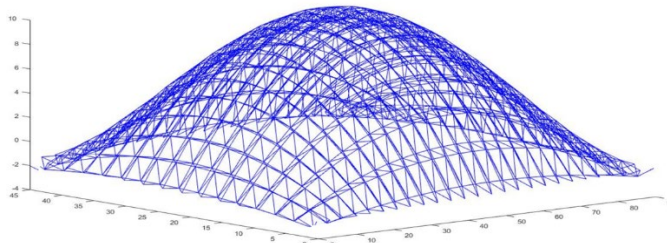
$$\left(\frac{1}{12} < h_{opt} / b < \frac{1}{22} \right)$$



c) – optimization for two parameters

$$\left(h_{opt} / b \approx \frac{1}{64} \right);$$

$$\left(\frac{1}{4.5} < f_{opt} / b < \frac{1}{6} \right)$$



d) – optimization for two parameters taking into account the pliability of the supports

$$\left(\frac{1}{12} < h_{opt} / b < \frac{1}{19} \right);$$

$$\left(f_{opt} / b \approx \frac{1}{4.5} \right)$$

Figure 10. A graphic representation of geometry optimization of structural covering.

4. Conclusions

1. A correspondence of refining the load-carrying ability of axially loaded rods and the stability condition is presented. This correspondence was based on the approximation of multiple linear regression and has the stability condition (1). It fits for axially loaded rods of space frames connected at the nodes with ball-and-socket plug-connectors. The values of μ and φ factors considering the rod's flexibility and degree of pinching are presented.

We proposed an algorithm for the optimal design of space frames with rectangular plans and with an aspect ratio up to 1:1...1:2.8 presented as a block-diagram in Fig. 9. It differs from the previously developed ones by the possibility of:

- clarification of the load-carrying ability of axially loaded rods from the stability condition;
- considering the possibilities in the manufacturing and installation of the development of an optimal design solution in a traditional flat form, or in the form of a two-layer rod shell of positive Gaussian curvature;

- considering the flexibility of the supports when assigning the optimal geometric parameters of the designed structure.
2. The influence of support flexibility on the optimal parameters of the designed structure is presented in the paper. The analysis of changes in design parameters for a shell on a rectangular plan is represented by an example. It is found that:
- an increase in the supporting structures' flexibility using two control parameters (h/b and f/b) necessitates an increase of the camber $f/b = 1/4.5 \approx 0.222$. If it is necessary to increase the height of the covering to $h/b = 1/16 \dots 1/20$, due to the need to increase the rigidity of the span of the covering;
 - the average increase of the metal intensity of the system due to the increase of the support's flexibility reaches 8 ... 12 %. There is a slight lowering in the metal intensity of the covering (up to 3 %) in some cases with a high level of support's flexibility and a low level of the design loads.

References

1. TSNIISK behalf Kucherenko. Recommendations for structural design. Moscow: Stroyizdat, 1984. 303 p. (rus). URL: <https://meganorm.ru/Data2/1/4293792/4293792341.pdf> (application date: 09.11.2023).
2. Lekhnitskii, S.G. Theory of elasticity of an anisotropic elastic body. First Edit. New York, Holden-Day, 1963. 404 p. URL: <https://archive.org/details/lekhnikskii-theory-of-elasticity-of-an-anisotropic-body-mir-1981> (application date: 09.11.2023).
3. Trofimov, V.I., Begun, G.B. Strukturnyye konstruksii (Issledovaniye, raschet i proyektirovaniye) [Constructions (Calculation and design studies)] Moscow: Stroyizdat, 1972. 271 p. (rus). URL: <https://search.rsl.ru/ru/record/01008417770> (application date: 09.11.2023).
4. Vlasov, V.Z. Tonkostennyye prostranstvennyye sistemy [Thin-Walled Space Systems]. Moscow: Science, 1964. 481 p. (rus). URL: <https://search.rsl.ru/ru/record/01006118791> (application date: 09.11.2023).
5. Vlasov, V.Z. Obschchaya teoriya obolochek [General theory of envelopes]. Moscow: Science, 1962. 528 p. (rus)
6. Vlasov, V.Z. Thin-Walled Elastic Beams. Washington: US Department of Commerce, 1961.
7. Euler, L. Methodus Inveniendi Lineas Curvas. Academia Imperialis Scientiarum Petropolitana, 1744. URL: https://ia902207.us.archive.org/23/items/methodus-inveniendi-lineas-curvas/Methodus_inveniendi_lineas_curvas.pdf (application date: 09.11.2023).
8. Engesser, F. Knickfestigkeit gerader Stäbe. Zentralblatt der Bauverwaltung. 1889. 11. Pp. 483–486. DOI: 10.5445/IR/1000026122.
9. Yasinskiy, F.S. Izbrannyye raboty po ustoychivosti szhatykh sterzhney [Selected papers on stability of compressed bars]. Moscow-Leningrad, State publishing house of technical literature, 1952. (rus) URL: <https://search.rsl.ru/ru/record/01006069480> (application date: 09.11.2023).
10. Zheng, Y., Zheng, H. Steel rod stability and inelastic buckling study. Applied Mechanics and Materials. 2013. 357–360. Pp. 626–630. DOI: 10.4028/www.scientific.net/AMM.357-360.626.
11. Galerkin, B.G. Sterzhni i plastinki : Ryady v nekotorykh voprosakh uprugogo ravnovesiya sterzhney i plastinok [Rods and plates. Series occurring in various questions concerning the elastic equilibrium of rods and plates]. Petrograd: Stroitel', 1915. (rus)
12. Streletskiy, N.S. Rabota szhatykh stoyek [The work of compressed racks] (In Russian). Moscow, State publishing house for building and architecture, 1959. 283 p. (rus) URL: <https://dwg.ru/dnl/4805> (application date: 09.11.2023).
13. Rzhaniysyn, A.R. Raschet sooruzheniy s uchetom plasticheskikh svoystv materialov [Calculation of structures taking into account the plastic properties of materials] Moscow: State publishing house for building and architecture, 1954. 287 p. (rus) URL: <https://dwg.ru/dnl/1758> (application date: 09.11.2023).
14. Timoshenko, S.P., Gere, J. Theory of Elastic Stability, 2nd Edition. New York, McGraw-Hill, 1985. 280 p.
15. Leites, S.D. Ustoychivost' szhatykh stal'nykh sterzhney [Stability of compressed steel rods]. Moscow: State publishing house for building and architecture, 1954. 309 p. (rus) URL: <https://dwg.ru/lib/1503> (application date: 09.11.2023).
16. Anikeev, I.D., Golikov, A.V. Derivation and analysis of methods for calculation of axially loaded steel compression members based on different building codes. RUDN Journal of Engineering Researches. 2018. 19(3). Pp. 299–316. (rus)
17. Li, B., Luo, H., Wang, X., Bosco, M. Failure analysis of locally damaged slender steel bars strengthened with CFRP composites: experiments, theory, and computational simulations. Advances in Civil Engineering. 2020. 2020. 8831701. DOI: 10.1155/2020/8831701.
18. Zhao, W., Chen, Z., Yang, B. Axial compression performance of steel/bamboo composite column. Procedia Engineering. 2017. 210. Pp. 18–23. DOI: 10.1016/j.proeng.2017.11.043
19. Perelmuter, A.V., Fialko, S.Y. Problems of computational mechanics relate to finite-element analysis of structural constructions. International Journal for Computational Civil and Structural Engineering. 2005. 1(2). Pp. 72–86. DOI: 10.1615/intjcompstructeng.v1.i2.70
20. Perelmuter, A.V., Slivker, V.I. Ustoychivost' ravnovesiya konstruksiy i rodstvennyye problem [Design balance stability and related problems]. Vol. 1. Moscow, SCAD-Soft, 2010. 681 p. (rus)
21. Perelmuter, A.V., Slivker, V.I. Ustoychivost' ravnovesiya konstruksiy i rodstvennyye problem [Design balance stability and related problems]. Vol. 2. Moscow, SCAD-Soft, 2010. 663 p. (rus)
22. Perelmuter, A.V., Slivker, V.I. Ustoychivost' ravnovesiya konstruksiy i rodstvennyye problem [Design balance stability and related problems]. Vol. 3. Moscow, SCAD-Soft, 2011. 388 p. (rus)
23. Yongfeng, F., Li, W., Kong Fah, T.E.E. Analysis of the steel structural reliability under the big data. IOP Conference Series: Materials Science and Engineering. 2020. 958(1). 012001. DOI: 10.1088/1757-899X/958/1/012001
24. Bondarev, A.B., Yugov, A.M. The method of calculating the accuracy of large-span metal rod systems. Magazine of Civil Engineering. 2016. (1). Pp. 60–73. DOI: 10.5862/MCE.61.6
25. Gordini, M., Habibi, M.R., Tavana, M.H., Amiri, M., Roudsari, M.T. Influence of Member Length Imperfection on the Capacity of Spatial Structures. The Open Civil Engineering Journal. 2019. 12 (1). Pp. 481–494. DOI: 10.2174/1874149501812010481

26. Gaylord, E., Gaylord, C., Stallmeyer, J. Structural Engineering Handbook. New York, McGraw-Hill, 1996. 1248 p.
27. Liu, C., He, L., Wu, Z., Yuan, J. Experimental study on joint stiffness with vision-based system and geometric imperfections of temporary member structure. Journal of Civil Engineering and Management. 2018. 24(1). Pp. 43–52. DOI: 10.3846/jcem.2018.299.
28. Hassani, V., Khabazi, Z., Raspall, F., Banon, C., Rosen, D.W. Form-finding and structural shape optimization of the metal 3D-printed multi-branch node with complex geometry. Computer-Aided Design and Applications. 2020. 17 (1). Pp. 205–225. DOI: 10.14733/cadaps.2020.205-225
29. Sathish, T., Dinesh Kumar, S., Karthick, S. Modelling and analysis of different connecting rod material through finite element route. Materials Today: Proceedings. 2020. 21. Pp. 971–975. DOI: 10.1016/j.matpr.2019.09.139
30. Lange, J., Feucht, T., Erven, M. 3D printing with steel: Additive Manufacturing for connections and structures. Steel Construction. 2020. 13 (3). Pp. 144–153. DOI: 10.1002/stco.202000031
31. Buchanan, C., Gardner, L. Metal 3D printing in construction: A review of methods, research, applications, opportunities and challenges. Engineering Structures. 2019. 180. Pp. 332–348. DOI: 10.1016/j.engstruct.2018.11.045
32. Lan, C., Tu, X., Xue, J., Briseghella, B., Zordan, T. Adaptive form-finding method for form-fixed spatial network structures. International Journal of Advanced Structural Engineering. 2018. 10 (2). Pp. 99–109. DOI: 10.1007/s40091-018-0179-z
33. Li, C., Xu, J., Feng, G., Zhu, Z. Design and static analysis of cellular double-layer grid roof structure with hexagonal cone system. IOP Conference Series: Materials Science and Engineering. 2019. 493 (1). DOI: 10.1088/1757-899X/493/1/012131
34. Guan, X., Chen, H., He, J., Sun, X. Investigation of snow load effects on modal parameters of a steel structure roof. Shock and Vibration. 2018. 2018. 7018325. DOI: 10.1155/2018/7018325
35. Likhtarnikov, Y.M. Variantnoye proyektirovaniye i optimizatsiya stal'nykh konstruksiy [Variant design and optimization of steel structures]. Moscow: Stroyizdat, 1979. 319 p. (rus)
36. Shimanovskiy, V.N., Gordeev, V.N., Grinberg, M.L. Optimal'noye proyektirovaniye prostranstvennykh reshetchatykh pokrytiy [Optimal design of spatial rod surfaces]. Kyiv, Budivel'nik, 1987. 224 p. (rus)
37. Romenskiy, I.V. Optimizatsiya konstruksiy membrannykh pokrytiy polozhitel'noy gaussovoy krivizny na pryamougol'nom i kruglom plane [Optimization of the designs of positive Gaussian rectangular and circular]. PhD Thesis. TSNIISK behalf Kucherenko, 1990. (rus)
38. Petrović, N., Kostić, N., Marjanović, N., Živković, J., Cofaru, I.I. Effects of structural optimization on practical roof truss construction. Applied Engineering Letters. 2020. 5 (2). Pp. 39–45. DOI: 10.18485/aeletters.2020.5.2.1
39. Kurniawan, M., Adha, A. Truss structure optimization for two design variable elements using Genetic Algorithm with stress and failure probability constraints. IOP Conference Series: Materials Science and Engineering. 2019. DOI: 10.1088/1757-899X/615/1/012091
40. Zhang, T., Kawaguchi, K., Wu, M. Optimization of frame structures with kinematical indeterminacy for optimum folding. Journal of Engineering Mechanics. 2019. 145 (9). Pp. 04019072. DOI: 10.1061/(asce)em.1943-7889.0001646.
41. Kociecki, M., Adeli, H. Two-phase genetic algorithm for size optimization of free-form steel space-frame roof structures. Journal of Constructional Steel Research. 2013. 90 (2013). Pp. 283–296. DOI: 10.1016/j.jcsr.2013.07.027.
42. Kociecki, M., Adeli, H. Shape optimization of free-form steel space-frame roof structures with complex geometries using evolutionary computing. Engineering Applications of Artificial Intelligence. 2015. 38. Pp. 168–182. DOI: 10.1016/j.engappai.2014.10.012.
43. Zverev, V.V., Liubavskaya, I.V., Meshcheryakova, E.V., Sotnikova, M.V. The stability of a compressed resiliently supported rod of variable stiffness. IOP Conference Series: Materials Science and Engineering. 2018. 456 (1). DOI: 10.1088/1757-899X/456/1/012032
44. Gorokhov, E.V., Vasylev, V.N., Mushchanov, A.V., Volchkov, A.N. Experimental study of the influence of node joints of structural structures on the stability of central compressed rods. Metal Constructions. 2020. 26 (2). Pp. 87–101. (rus)
45. Mushchanov, A.V., Mushchanov, V.F., Romenskiy, I.V. Rational geometric and stiffness parameters of long-span structural roof. Construction of Unique Buildings and Structures. 2016. 2 (41). Pp. 18–29. DOI: 10.18720/CUBS.41.2 (rus)
46. Mushchanov, A.V., Mushchanov, V.F., Romenskiy, I.V. The impact of support on the compliance of the stress-strain state of structural elements covering. Construction of Unique Buildings and Structures. 2016. 1 (40). Pp. 7–19. (rus)

Information about authors:

Vladimir Mushchanov, Doctor of Technical Sciences

ORCID: <https://orcid.org/0000-0003-3188-3400>

E-mail: mvf@donnasa.ru

Alexander Mushchanov,

E-mail: mushchanov93@gmail.com

Anatoliy Orzhehovski, PhD in Technical Sciences

E-mail: orzhehovskiy@bk.ru

Maxim Tcepliaev, PhD in Technical Sciences

ORCID: <https://orcid.org/0000-0002-1729-4127>

E-mail: m.n.cepliaev@donnasa.ru

Received 15.09.2022. Approved after reviewing 08.11.2023. Accepted 09.11.2023.



Research article

UDC 691.32 + 691.328.1 + 691.335 + 624.042.5

DOI: 10.34910/MCE.124.9



Concrete heat liberation in thermal stressed state analysis

E.N. Ivanov , K.S. Semenov, Yu.G. Barabanshchikov , S.V. Akimov , A.S. Kuleshin, N.S. Titov 

Peter the Great St. Petersburg Polytechnic University, St. Petersburg, Russian Federation

✉ 79602615868@yandex.ru

Keywords: concrete construction, reinforced concrete structures, construction period, thermo-stressed state, concrete heat liberation

Abstract. This paper presents the results of numerical studies of the temperature regime and the thermal stressed state of the reinforced concrete wall of the nuclear power plant foundation block during the construction period with continuous concreting at full height. Calculations were done both using the dependence of the change in heat liberation over time on the hardening temperature, according to the theory of I.D. Zaporozhets, as well as the experimental data. It is established that if Zaporozhets equation is used in calculations, the correction of heat release values should be performed in the first 45 hours of concrete hardening. In order to correct the theoretical values of the specific heat, the last one should be multiplied by the correction factor. The dependence of the factor on the time within the range of 4 to 45 hours is approximated with sufficient accuracy by the obtained fifth degree polynomial. The crack resistance of the structure was determined using a deformation criterion, taking into account the change in the ultimate elongation of concrete over time. In this particular case of concreting a structure it is shown that when the correction function is introduced into the calculation program there is no need to use thermal insulation. The direct economic effect, as well as the indirect one associated with the decrease in the construction period, allow avoiding the rise of the construction costs. It is proposed to use the developed methodology in practical calculations of thermal crack resistance of massive concrete and reinforced concrete structures during the construction period.

Citation: Ivanov, E.N., Semenov, K.S., Barabanshchikov, Yu.G., Akimov, S.V., Kuleshin, A.S., Titov, N.T. Concrete heat liberation in thermal stressed state analysis. Magazine of Civil Engineering. 2023. 124(8). Article no. 12409. DOI: 10.34910/MCE.124.9

1. Introduction

The hardening of massive concrete and reinforced concrete structures has a number of features. During the building period, the formation and development of cracks are possible. The main reasons for that are non-uniform temperature distribution in the concrete body and the temperature gradient between the core and surface of the block [1–3]. In turn, temperature non-uniformity is caused by fluctuations of the ambient temperature, the heat release due to cement hydration, as well as difference between the maximum temperature in the block and the temperature of its faces, the rate of block cooling [4–6]. The presence of such damage in structures of high responsibility level is unacceptable.

The problem of assessing the thermal crack resistance of massive concrete and reinforced concrete structures in early period consists of determining the temperature fields based on the solutions of heat conductivity equations [7–10] and stresses, and verifying certain conditions meeting the thermal cracks formation. The allowable core-surface temperature gradient was accepted as a crack resistance criterion in papers [11–13]. The energy [1] and the deformation criterion [13] are more accurate and approved in national design codes of concrete structures. The latter one is used in the current work.

The heat liberation due to the cement hydration contributes greatly to the formation of non-uniform temperature fields of massive concrete and reinforced concrete structures during the building period. Special attention is paid to this factor [14–29].

The theory of I.D. Zaporozhets describes the kinetics of concrete heat release depending on temperature and time of hardening [14]. The experimental studies show that at the initial stage the heat release of concrete differs from the results obtained on the basis of the I.D. Zaporozhets equation used in computer programs [15, 16]. Moreover, the hydration temperature influence on the heat liberation process should be taken into account [13].

Neglecting the above-specified factors causes the error in the concrete thermal stressed state analysis. As a result, the calculated characteristics of concrete protection measures against cracking may be overestimated (thickness of thermal insulation, terms of its removal).

Therefore, the aim of the current work is to develop the procedure for refining the design heat release function based on the experimental data for more accurate application of specific measures against cracking.

2. Methods

2.1. Analysis Procedure

The TERM program developed at the Department of Building Structures and Materials of Peter the Great St. Petersburg Polytechnic University (SPbPU) was used in analysis [13]. An important feature of the program is the ability to take into account the influence of time and temperature on the deformative and thermophysical characteristics of concrete, which is relevant for the construction period.

The first block of the program solves the problem of determining non-stationary temperature fields in a concrete structure in contact with the base and other elements. The inhomogeneous differential heat conductivity equation for 2D calculation cases is as follows:

$$c\gamma = \lambda \left(\frac{\partial^2 t}{\partial x^2} + \frac{\partial^2 t}{\partial y^2} \right) + \frac{\partial Q}{\partial \tau} \quad (1)$$

where Q is the heat of the cement hydration exothermic reaction;

c is concrete specific heat capacity;

λ is concrete internal heat conductivity coefficient;

γ is concrete density;

t is temperature;

τ is time.

Concrete heat liberation according to I.D. Zaporozhets is treated as a function of time and temperature not depended on the coordinates of an element:

$$Q(\tau) = Q_{max} \left[1 - (1 + A_T \tau)^{-\frac{1}{m-1}} \right] \quad (2)$$

where Q_{max} is the limit, which the concrete heat liberation goes for;

A_T is the increase rate of heat liberation coefficient providing the constant temperature T in time;

m is reaction order with respect to water, which is 2+2.3 for Portland cement;

The temperature influence on the heat liberation is taken into account with the temperature function:

$$f(t) = 2^{\frac{t_1 - t_2}{\varepsilon}} \quad (3)$$

where ε is the characteristic temperature subtraction which shows the times of heat liberation velocity alteration providing the temperature variation in ε degrees. The characteristic temperature subtraction depends on temperature: $\varepsilon = kt + l$, where $k \approx 0.13$; $l \approx 8$ are characteristics revealed with experiment.

On the outer contour of structure the 3-d kind boundary conditions are accepted, assuming that the heat exchange between the concrete surface and the air environment occurs according to Newton's convective heat transfer law. In this case, the heat flow, coming from the inner concrete layers to the surface, must be accepted by the environment. This condition is written as equality of two flows:

$$\lambda \frac{\partial t}{\partial n} = -\beta(t_{cs} - t_{em}) \quad (4)$$

where β is the heat exchange coefficient depended on surface heat exchange conditions (wind velocity and direction in the open air, curing conditions: into the temporary hide, the presence on the concrete surface the membrane, thermal insulation, framework);

t_{cs} u t_{em} is the concrete surface and environment temperature respectively;

n is the normal vector to the concrete surface.

The reduced heat transfer coefficient allows to take in account the thermal insulation, covering, framework influence:

$$\beta_{np} = \frac{1}{\frac{1}{\beta} + R} \quad (5)$$

where R is the insulation thermal resistance.

At the border of contact with the base or other elements of the concrete structure, boundary conditions of the 4-th kind are accepted. From the condition of the continuity of the temperature field, it follows that at the contact of two bodies in an infinitely thin layer the temperature of the first body is equal to the temperature of the second one. In addition, the equality of heat flows at the border of two bodies must be satisfied:

$$\lambda_1 \left(\frac{\partial t}{\partial n} \right)_1 = \lambda_2 \left(\frac{\partial t}{\partial n} \right)_2 \quad (6)$$

The second block of the program calculates the values of thermal stresses. The resolving system of integral-differential equations is obtained by substituting dependencies describing deformations taking into account the hypothesis of flat sections. Also the relationship between stresses and deformations considers creep through the relaxation function according to the linear hereditary theory of aging, and the condition of static equivalence to zero of the temperature forces across the section. When solving the system, the finite element method and numerical integration are used.

The third block of the program evaluates the thermal crack resistance of a concrete structure. The criterion proposed by P.I. Vasiliev, suggesting the appearance of cracks due to the insufficient ability of concrete to deform under the tensile stresses, is used:

$$\sigma(t) = \gamma_{b3} \gamma_{b6} \varepsilon_{lim} \varphi(t) E_b(t) \quad (7)$$

where $\sigma(t)$ is the thermal stresses at time t ;

γ_{b6} is the working condition coefficient;

γ_{b3} is the coefficient taking in account the gradient of strain across the section influence on the strength of concrete in tension;

ε_{lim} is limit concrete elongation;

$\varphi(t)$ is the coefficient taking in account dependence of ε_{lim} from the age;

$E_b(t)$ is initial elasticity modulus of concrete at age less than 180 days.

2.2. Initial Data

We investigated the thermally stressed state of the monolithic reinforced concrete wall of the NPP foundation block, continuously concreted to the entire height with and without taking into account corrections in the heat release equation. Despite the reinforcement of the wall, the work of the reinforcement is neglected due to approximately the same thermal expansion coefficient as that of concrete. Since the length of the wall significantly exceeds its thickness and height, the analysis in plane strain way is considered in this paper. The design characteristics and design parameters are presented in Tables 1 and 2, respectively.

Table 1. Construction parameters.

No	Name	Material	Thickness, m	Height, m
1	Foundation slab	Concrete B40	2.6	–
2	Wall	Concrete B30	2.0	5.4

Table 2. Design parameters for the thermal stress state analysis.

No	Design parameter	Property
1	Concrete strength class	B30
2	Cement consumption for concrete, C	230 kg/m ³
3	Deformation modulus of concrete, E_b	33.1 GPa
4	Environment temperature	10 °C
5	Concrete mixture temperature before casting	20 °C
6	Reduced heat transmission coefficient of 20 mm plywood timbering and 10 mm heat insulation	2.64 W/m ² ·°C
7	Concrete maximum heat liberation, Q_{max}	102.4 MJ/m ³
8	Heat liberation growth rate coefficient, A_{20}	0.61
9	Power index, m	2.2

The comparative assessment of the calculation results is presented using Equation (2) in the original and corrected versions. The correction was made by introducing the correction factors equal to the ratio of experimental data to theoretical ones.

2.3. Heat Liberation Experimental Results

The heat release of concrete was determined experimentally: in a semi-adiabatic calorimeter, as well as by calculation: using the temperature function [14] with a reduction to isothermal hardening under a temperature of 20 °C. In order to reveal the dependence of the specific heat release on time, the average values of four samples were used. The laboratory results and theoretical values are presented in Table 3 and Figure 1.

Table 3. Concrete unit heat liberation.

Time τ , h	4.0	8.0	12.1	16.0	20.3	24.2	28.2	32.4	35.8	40.0
q_{test} , kJ/kg	6.0	12.6	32.5	62.2	97.3	125.5	149.6	169.0	181.5	194.4
q_{calc} , kJ/kg	34.5	63.6	89.2	110.1	130.3	146.4	161.5	175.4	185.5	197.0
$(q_{calc} - q_{test}) / q_{test}$	4.75	4.05	1.74	0.77	0.34	0.17	0.08	0.04	0.02	0.01
$k = q_{test} / q_{calc}$	0.174	0.198	0.364	0.565	0.747	0.857	0.926	0.964	0.978	0.987

NOTE: q_{test} is the experimental specific heat liberation of; q_{calc} is the theoretical specific heat liberation: according to Equation (2).

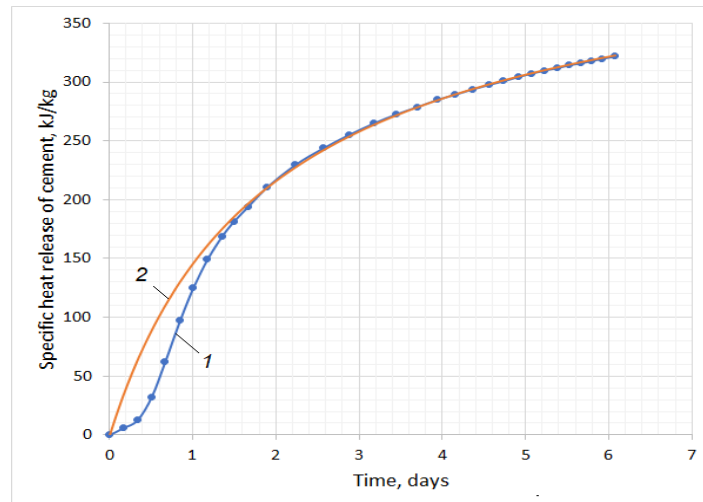


Figure 1. Specific concrete heat liberation: 1 – experimental; 2 – theoretical.

Fig. 1 and Table 3 show that the curves are different from each other in the first 40 hours. The excess of the theoretical value of heat release over the experimental one is from 1 to 475%. The closer the time is to the beginning of concrete hardening, the more significant the distinction is, what may be explained by the impossibility to take into account the retarding action of gypsum, softeners and other additives in Equation (2).

Correction of theoretical values of specific heat release is carried out by multiplying the correction factor k . The dependence of factor k on time τ in the range from 4 to 45 hours with sufficient accuracy ($R^2 = 0.9999$) is approximated with the fifth degree polynomial (Fig. 2).

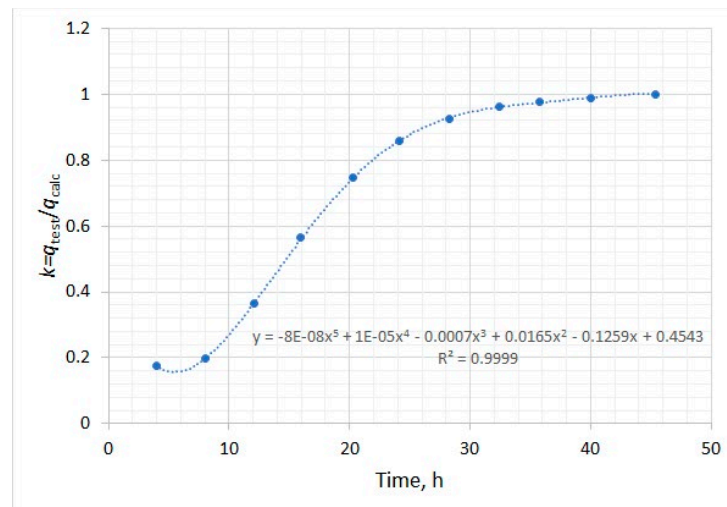


Figure 2 Approximation of the correction factor $k = f(\tau)$ with the fifth degree polynomial.

3. Results and Discussion

The plane problem of determining the temperature fields and stresses of a reinforced concrete wall for two cases of taking into account the heat release of concrete was solved: 1) heat release was taken according to the equation of I.D. Zaporozhets (Eq. (2)); 2) heat release is taken according to the equation of I.D. Zaporozhets with a correcting function $k = f(\tau)$. Thermal insulation and formwork are dismantled 10 days after placing the concrete mixture.

3.1. The first design case

Temperature and stress distributions in the center and on wall surface according to the I.D. Zaporozhets heat liberation theory that was not corrected with the experimental data are presented in Fig. 3 and 4 respectively. The notional strength is the right part of the equation (7).

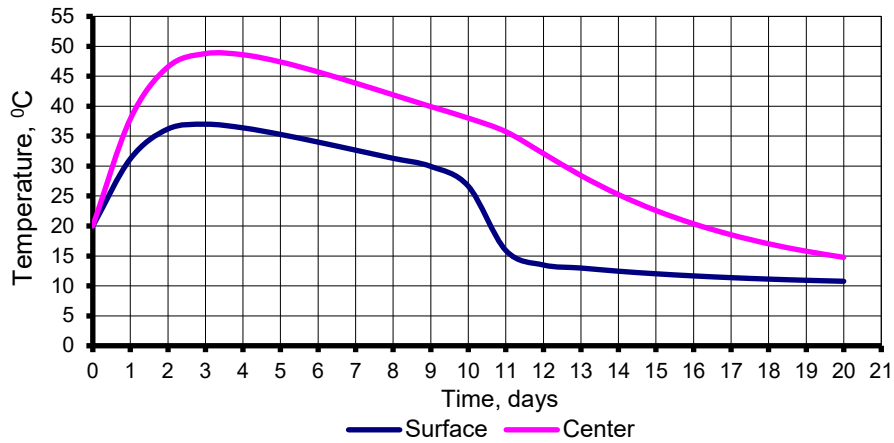


Figure 3. Temperature variation in the center and on the surface of the wall (the 1st case).

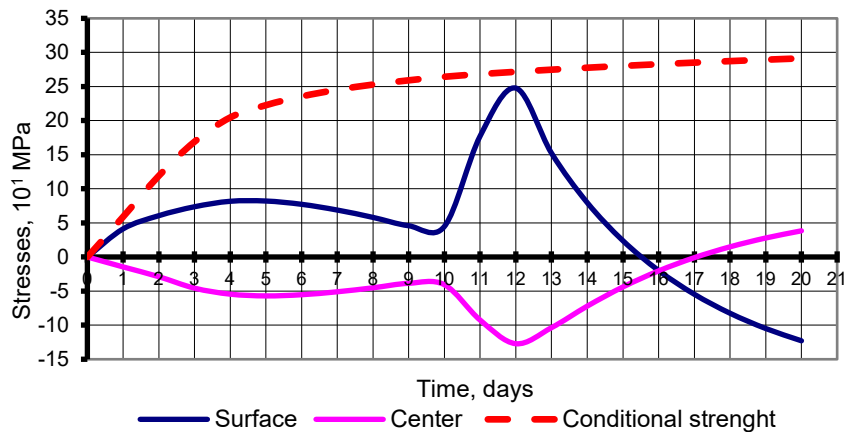


Figure 4. Stress variation in the center and on the surface of the wall (the 1st case).

Figure 3 shows that 3 days later the temperature in the center of the wall rose to a maximum value of 49 °C, and the surface temperature was 37 °C. Ten days later, as a result of thermal insulation and formwork removing, a sharp drop in the surface temperature from 30 °C to 14 °C is observed. Along with it, a sharp jump up to 2.5 MPa of tensile stresses is observed. This phenomenon is called the heat stroke.

3.2. The second design case

Temperature and stress distributions in the center and on the surface of the wall according to the I.D. Zaporozhets heat liberation theory that was not corrected with the experimental data are presented in Fig. 3 and 4 respectively.

Temperature and stress distributions in the center and on the wall surface using the correction function $k = f(\tau)$ to the equation of I.D. Zaporozhets heat liberation theory are presented in Fig. 5 and 6, respectively.

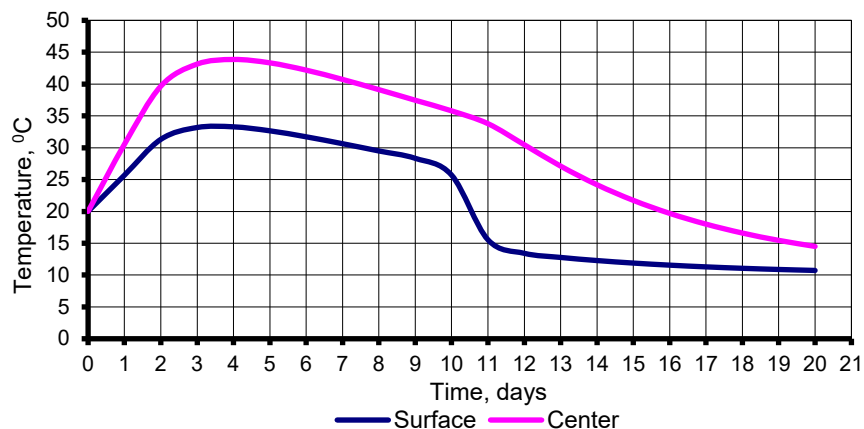


Figure 5. Temperature variation in the center and on the surface of the wall (the 2nd case).

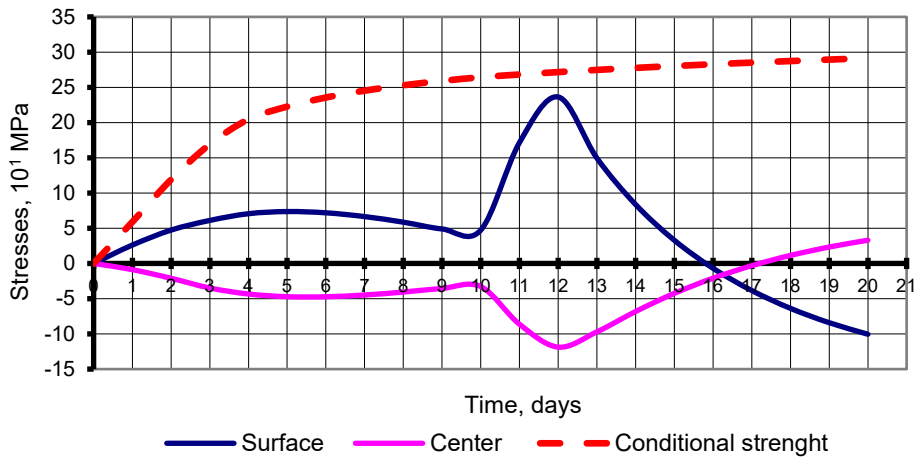


Figure 6. Stress variation in the center and on the surface of the wall (the 2nd case).

In this case, there is a decrease in the maximum temperature in the wall center to 44 °C and in the surface layer to 33 °C. In addition, the temperature drop and the stress jump after the thermal insulation removal decreased to 11 °C and 2.3 MPa respectively.

3.3. Refusal from insulation

Reducing temperature differences and thermal stresses as a result of applying the corrective function and obtaining more reliable results allows us to reject the insulation and reduce the cost of concrete work, which is confirmed by the calculations (see Figures 7 and 8).

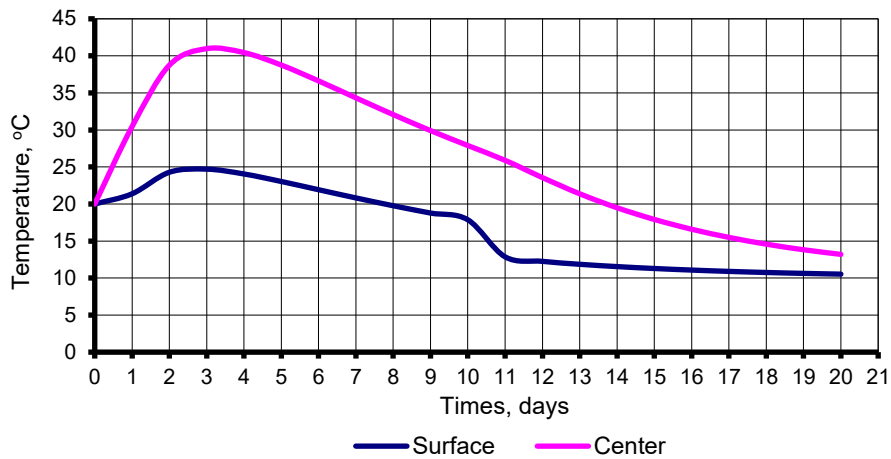


Figure 7. Temperature variation in the center and on the surface of the wall (the 3rd case).

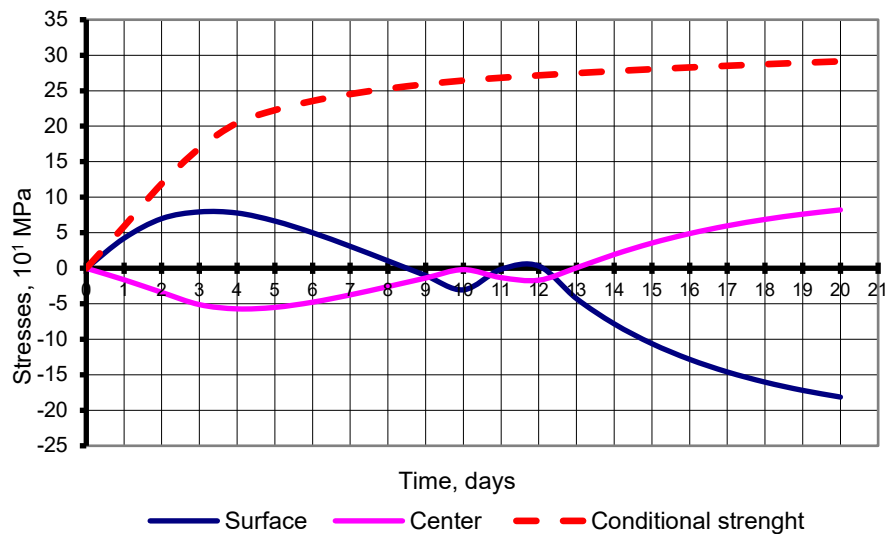


Figure 8. Stress variation in the center and on the surface of the wall (the 3rd case).

The concrete thermal stress state results obtained for the 3 design cases are presented in Tables 4 and 5.

Table 4. Thermal stressed state calculation results on the 1st day after concrete pouring.

No	Calculation case	Time, days	Max temperature center/surface, °C	Max temperature contrast, °C	Tensile stresses, MPa
1	Heat liberation not corrected	1	38/31	7	0.41
2	Heat liberation corrected	1	31/26	5	0.26
3	Heat liberation corrected and without insulation	1	30/21	9	0.42

The results of the thermal stressed state analysis on the 1st day after concrete pouring are presented in Table 4. Such a time step is indicative from comparing the old method of determining the heat liberation of concrete and the new point of view. For this purpose, the crack resistance calculation was carried out separately, taking into account the heat liberation according to the old method in the absence of thermal insulation on the upper face of the wall. As a result, on the 1st day, the crack resistance criterion is not met: the operating stresses are 0.66 MPa, the notional strength is 0.58 MPa, which requires a thermal insulation. When the calculations of crack resistance use a new method for estimating heat liberation (case 3 of Table 4), crack resistance is met and thermal insulation is not required.

Table 5. Thermal stressed state calculation results for the maximum temperature rise.

No	Calculation case	Time, days	Max temperature center/surface, °C	Max temperature contrast, °C	Tensile stresses, MPa	Maximum tensile stresses due to thermal stroke, MPa
1	Heat liberation not corrected	3	49/37	12	0.82	2.5
2	Heat liberation corrected	4	44/33	11	0.74	2.3
3	Heat liberation corrected and without insulation	3	41/25	16	0.78	0.05

Turning attention to Table 5, in the first case, to ensure the thermal crack resistance of concrete, according to the calculation, it is necessary to apply thermal insulation. Here, the largest temperature difference between the center and the wall surface is observed on the 3rd day and amounted to 12 °C, with the corresponding tensile stress of 0.82 MPa. Tensile stresses acquire the highest value (2.5 MPa) on the 10th day after the insulation and formwork removal. However, by this age concrete has time to gain the necessary strength and elasticity to resist cracking.

In comparison with the previous case, the correction of the heat liberation formula gave a delay of one day for the onset of the largest temperature difference and the corresponding stress at their lower values (11 °C and 0.74 MPa). In addition, there was a decrease in the peak of tensile stresses during thermal stroke.

Thus, the refinement of the heat release parameters on the basis of experimental data allows us to obtain more reliable calculation results and reject the unreasonable use of insulation. The removal of the formwork does not lead to the phenomenon of heat stroke (Fig. 8), and the terms of removal can be assigned without consideration of the thermal stressed state of the structure.

Due to the specifics of the study made, the results can be compared with the data of other researchers only without taking into account the introduction of a corrective function, which are close to the similar calculations [2–4].

4. Conclusions

1. The work shows that the theoretical dependence of the heat liberation of concrete on the hardening time used in the calculations of the thermal stress state differs from the experimental one and gives not entirely reliable results on the crack resistance of concrete.

2. Due to the difficulties in the analytical description of the real curve of the cement exotherm, which has a double curvature, the possibility of bringing the theoretical dependence of heat release on time to a

more reliable form is shown by multiplying by correcting function obtained on the basis of experimental data.

3. The work established that, using the equation of I.D. Zaporozhets, heat release values must be corrected in the first 40 hours of concrete hardening. During this period, the actual heat release is lower than the calculated one.

4. It is shown that when the correction function is introduced into the calculation program, in this particular case of concreting a massive structure, there is no need to use thermal insulation. A direct economic effect, as well as an indirect one, associated with a reduction in the construction period of massive structures, will help to avoid a rise in the cost of construction. Therefore, the proposed methodology can be recommended for practical calculations of thermal crack resistance of massive concrete and reinforced concrete structures during the construction period.

5. The offered methodology of estimating the thermal stresses of massive concrete structures during the building period is applicable when the concrete has acquired elastic properties.

References

1. Trapeznikov, L.P. *Temperaturnaya treshchinostoykost massivnykh betonnykh sooruzheniy* [Thermal cracking resistance of mass concrete structures]. Moscow: Energoatomizdat, 1986. 272 p. (rus)
2. Aniskin, N., Chuc Nguyen, T., Kiet Bui, A. The use of ice to cool the concrete mix in the construction of massive structures. E3S Web of Conferences. Tashkent, 2021. 264. 02047. DOI 10.1051/e3sconf/202126402047.
3. Wang, D.B., Song, X.B., Nie, H.Y. Cracking analysis of massive concrete with large-diameter pipes during construction. *Construction and Building Materials*. 2022. 338. 127636. DOI 10.1016/j.conbuildmat.2022.127636.
4. Usanova, K., Barabanshchikov, Yu.G., Pakrastins, L., Akimov, S.V., Belyaeva, S.V. Heat release and thermal conductivity of expanded-clay concrete for 3D printer. *Magazine of Civil Engineering*. 2021. 102(2). Article No.10210. DOI: 10.34910/MCE.102.10.
5. Maruyama, I, Lura. P. Properties of early-age concrete relevant to cracking in massive concrete. *Cement and Concrete Research*. 2019. 123. 105770. DOI: 10.1016/j.cemconres.2019.05.015.
6. Lacarrière, L., Knoppik, A., Leal da Silva, W.R., Honorio, T., Šmilauer, V., Asamoto, S., Fairbairn, E.M.R. Hydration and heat development. *RILEM State-of-the-Art Reports*. 2019. 27. Pp. 13-46. DOI: 10.1007/978-3-319-76617-1_2.
7. Pustovgar, A.P., Lavdansky, P.A., Yesenov, A.V. Research work report. Study of the distribution of temperatures and stresses in selected designs of nuclear power plants during hardening of concrete mix. *Concrete production offers*. 2012. 137 p.
8. Aleksandrovskiy, S.V. *Raschet betonnykh i zhelezobetonnykh konstruksiy na izmeneniya temperatury i vlazhnosti s uchetom polzuchesti* [Calculation of temperature change and humidity in terms of concrete creep in concrete and reinforced concrete structures], Moscow: Stroyizdat, 1973. 444 p. (rus).
9. Lesovik, V.S., Popov, D.Y., Fediuk, R.S., Sabri, M.M., Vavrenyuk, S.V., Liseitsev, Yu.L. Shrinkage of ultra-high performance concrete with superabsorbent polymers. *Magazine of Civil Engineering*. 2023. 121(5). Article no. 12108. DOI: 10.34910/MCE.121.8.
10. Nemova, D.V., Vatin, N.I., Gorshkov, A.S., Kashabin, A.V., Rymkevich, P.P, Tceitin, D.N. Technical and economic assessment on actions for heat insulation of external envelopes of an individual house. *Construction of Unique Buildings and Structures*. 2014. 23(8). Pp. 93-115. (rus). DOI: 10.18720/CUBS.23.7
11. Teleshev, V.I. *Raschet dopustimogo temperaturnogo rezhima betonnoy kladki iz usloviy obespecheniya yeye treshchinostoykosti* [Calculation of the permissible temperature regime of concrete masonry from the conditions for ensuring its crack resistance]. Leningrad: LPI, 1985. 37 p. (rus).
12. Teleshev, V.I. *Konstruktivno-tekhnologicheskiye meropriyatiya po obespecheniyu treshchinostoykosti i monolitnosti massivnykh betonnykh gidrotekhnicheskikh sooruzheniy* [Structural and technological measures to ensure crack resistance and monolithicity of massive concrete hydraulic structures. Leningrad: LPI, 1983. 79 p.
13. Semenov, K.V., Barabanshchikov, Yu.G. Maintenance of thermal cracking resistance in massive concrete base slabs during winter concreting. *Construction of Unique Buildings and Structures*. 2014. 17(2). Pp. 125-135. (rus). DOI: 10.18720/CUBS.17.10
14. Zaporozhets, I.D., Okorokov, S.D., Pariyskiy, A.A. *Teplovydeleniye betona* [Heat Liberation of concrete]. Leningrad; Moscow: Stroyizdat, 1966. 316 p. (rus).
15. Pulyaev, S., Pulyaev, I., Korovyakov, V., Sitkin, A. Research of hydration heat of Portland cement used in bridge construction of Kerch Strait. *MATEC Web of Conferences*. 2018. 251. 7.
16. Linderoth, O., Wadsö, L., Jansen, D. Long-term cement hydration studies with isothermal calorimetry. *Cement and Concrete Research*. 2021. 141. 106344. DOI: 10.1016/j.cemconres.2020.106344
17. Hai, T.H., Thuc, L.V. The effect of splitting concrete placement on controlling thermal cracking in mass concrete. *Journal of science and technology in civil engineering*. 2017. Vol. 11. No. 6. Pp. 22-28. <http://stce.nuce.edu.vn/index.php/en/article/view/932>
18. Vatin, N.I., Gorshkov, A.S., Nemova, D.V. *Energoeffektivnost ograzhdayushchikh konstruksiy pri kapitalnom remonte*. [Energy efficiency of envelopes at major repairs. *Construction of Unique Buildings and Structures*. 2013. 8(3). Pp. 1–11. (rus). DOI: 10.18720/CUBS.8.1
19. Miyazawa, S., Koibuchi, K., Hiroshima, A., Ohtomo, T., Usui T. Control of thermal cracking in mass concrete with blast-furnace slag cement. *Concrete Under Severe Conditions*. 2010. 7–9. Pp. 1487–1495.
20. Shengxing, W., Donghui, H. Estimation of cracking risk of concrete at early age based on thermal stress analysis. *Journal of Thermal Analysis and Calorimetry*. 2011. 105(1). Pp. 171–186. DOI: 10.1007/s10973-011-1512-y
21. Zhang, Z., Zhang, X., Wang, X., Zhang, T. Merge concreting and crack control analysis of mass-concrete base slab of nuclear power plant. *Applied Mechanics and Materials*. 2011. 94–96. Pp. 2107–2110. DOI: 10.4028/www.scientific.net/AMM.94-96.2107
22. Larson, M. *Thermal crack estimation in early age concrete-models and methods for practical application*. Doctoral Thesis. Division of Structural Engineering, Lulea University of Technology, 2003. 190 p.

23. Lee, M.H., Khil, B.S., Yun, H.D. Influence of cement type on heat of hydration and temperature rise of the mass concrete. *Indian Journal of Engineering & Materials Sciences*. 2014. 8(5). Pp. 536–542.
24. Usanova, K., Barabanshchikov, Yu.G., Dixit, S. Cementless Binder Consisting of High-Calcium Fly Ash, Silica Fume and Magnesium Chloride. *Magazine of Civil Engineering*. 2023. 123(7). Article no. 12305. DOI: 10.34910/MCE.123.5.
25. Bingqi, L., Zhenhong, W. Temperature control and crack prevention during constructio in steep slope dams and stilling basins in high-altitude areas. *Advances in Mechanical Engineering*. 2018. 10(1). Pp. 1–15. DOI: 10.1177/1687814017752480
26. Korotchenko, I.A., Ivanov, E.N., Manovitsky, S.S., Borisova, V.A., Semenov, K.V., Barabanshchikov, Yu.G. Deformation of concrete creep in the thermal stress state calculation of massive concrete and reinforced concrete structures. *Magazine of Civil Engineering*. 2017. 69(1). Pp. 56–63. DOI: 10.18720/MCE.69.5.
27. Bamforth P.B. Early-age thermal crack control in concrete. CIRIA C660. London. 2007. 113 p..
28. Nguyen, T.C., Huynh, T.P., Tang, V.L. Prevention of crack formation in massive concrete at an early age by cooling pipe system. *Asian Journal of Civil Engineering*. 2019. 20(8). Pp. 1101–1107. DOI: 10.1007/s42107-019-00175-5
29. Vasilyev, P.I. Svyaz mezhdu napryazheniyami i deformatsiyami v betone pri szhatii s uchetom vliyaniya vremeni [Relationship between stresses and deformations in concrete under compression, taking into account the influence of time]. *VNIIG News*. 1951. 45. Pp. 78–93.

Information about authors

Ernest Ivanov,

ORCID: <https://orcid.org/0000-0003-3420-9518>

E-mail: 79602615868@yandex.ru

Kirill Semenov, PhD in Technical Sciences

E-mail: kvsemenov@bk.ru

Yuriy Barabanshchikov, Doctor of Technical Sciences

ORCID: <https://orcid.org/0000-0001-7011-8213>

E-mail: ugb@mail.ru

Stanislav Akimov

ORCID: <https://orcid.org/0000-0002-2908-4565>

E-mail: akimov_sv@spbstu.ru

Alexey Kuleshin

E-mail: alex_kulesh4@mail.ru

Nikita Titov

ORCID: <https://orcid.org/0000-0001-6384-4989>

E-mail: tns93@mail.ru

Received 01.11.2022. Approved after reviewing 21.11.2023. Accepted 05.12.2023.



Research article

UDC 691

DOI: 10.34910/MCE.124.10



Environmental analysis of residential exterior wall construction in temperate climate

D.V. Kokaya , D.D. Zaborova , T.A. Koriakovtseva  

Peter the Great St. Petersburg Polytechnic University, St. Petersburg, Russian Federation

 tamusorina@mail.ru

Keywords: enclosing structures, global warming potential, production of building materials, greenhouse gas emissions, life cycle assessment, heat-losses, insulating materials, thermal transmittance

Abstract. With the growth of the construction industry market there is an urgent need to evaluate the use of building materials from the sustainable point of view. Product stage of construction materials has a significant negative impact on the environment. This work represents environmental assessment of the construction materials of a low-rise residential building located in the temperate climate zone. To conduct such an analysis, we used a comprehensive methodology, product life cycle assessment (LCA), complying with international standards ISO 14044 and ISO 14025. The global warming potentials were calculated for the building life cycle product stages (A1-A3) in the equivalent of the carbon dioxide emissions (CO_{2e}). It was found that external walls have the greatest negative impact on the environment compared to other building elements. Production of construction materials for external wall structures is responsible for 45 % of the total CO_{2e} emissions. Based on the performed calculations, alternative options for exterior wall construction are proposed. Heat losses were calculated for each type of enclosing structures, as well as greenhouse gas emissions from burning fuel for heating the building. It was found that an aerated concrete wall with ventilated facade has the least negative impact on the environment, even though heating a building with such an enclosing structure requires more energy than other wall options. Environmentally reasonable approach of the enclosing structure selection allowed a reduction of greenhouse gas emission by 16.7 %, from 402.85 tons to 335.65 tons CO_{2e}.

Funding: This work is supported by the Russian Science Foundation under grant 21-79-10283, date 29.07.2021 <https://rscf.ru/project/21-79-10283/>

Citation: Kokaya, D.V., Zaborova, D.D., Koriakovtseva, T.A. Environmental analysis of residential exterior wall construction in temperate climate. Magazine of Civil Engineering. 2023. 124(8). Article no. 12410. DOI: 10.34910/MCE.124.10

1. Introduction

Climate change is one of the leading problems in the global community today. The specificity of the problem of global warming lies in the irreversibility of the consequences caused by the widespread emission of greenhouse gases, as well as in the direct impact on all spheres of human life. The climate map of the world for the periods 1980–2016 and 2071–2100 clearly shows cardinal climate changes due to global warming in different regions of the earth [1].

The development of clean energy technologies and the problem of climate change occupy one of the central places in the modern international economic agenda. The key achievement of recent years has been the conclusion of the Paris Agreement in 2015 under the auspices of the UN Framework Convention on Climate Change (COP-21). The energy transition taking place at the present stage involves the active introduction of low-carbon energy sources [2]. The European climate legislation, numbering dozens of

directives, norms, and decisions, regulates the entire spectrum of the climate, energy, and economic agenda [3].

According to [4], the industrial sector's contribution to the global Warming Potential (GWP – Global Warming Potential) was 21 % in 2010. Urban population growth requires a constant increase in residential buildings and the construction of urban infrastructure. If the world's population increases to 9.3 billion people by 2050, then there will be a need to develop urban infrastructure. However, the production of building materials for this infrastructure alone, using technologies available today, will lead to greenhouse gas emissions of approximately 470 Gt CO₂ eq. According to the UN, the world's population has already surpassed the mark of 8 billion people [5] as of November 2022.

Life Cycle Assessment (LCA) of buildings and structures makes it possible to assess the contribution of construction industry to the Global warming by calculating greenhouse gas emissions, energy consumed and other parameters at various stages of construction. These stages include materials production, their transportation to the construction site, building demolition and waste recycling [6, 7]. The LCA data of buildings show that 70–80 % of all greenhouse gas emissions occur precisely at the stage of materials production. According to [8], buildings are responsible for 40% of energy consumption, and for 36 % of greenhouse gas emissions throughout the EU.

LCA of building materials is part of the Environmental Product Declaration (EPD) and comply with EN 15804+A21 and ISO 14025 standards (Fig. 1). The presence of EPD for a particular product is a convenient tool that allows you to compare analogous materials on their impact on the environment and choose the best option from it.

LCA stages A1-A3 are responsible for the largest share of energy consumed and greenhouse gas emissions in construction, reflect the impact of processing of natural raw materials, its transportation, and production of building materials.

Product stage			Construction process stage		Use stage							End of life stage				Benefits and loads beyond the system boundary
Raw material supply	Transport	Manufacturing	Transport	Construction-installation process	Use	Maintenance	Repair	Replacement	Refurbishment	Operational energy use	Operational water use	Demolition	Transport	Waste processing	Disposal	Reuse - Recovery- Recycling Potential
A1	A2	A3	A4	A5	B1	B2	B3	B4	B5	B6	B7	C1	C2	C3	C4	D

Figure 1. LCA of building materials, stages.

Use phase of building also impacts environment during the life cycle. For example, building orientation (rational use of solar radiation), building configuration (reducing the area of external enclosing structures by combining several residential buildings in-to a block [9]), use of energy-efficient engineering systems, service life of enclosing structures and building retrofitting measures [10–13].

The market provides a variety of building materials [14] with different compositions, physical properties obtained through the use of various production technologies. There is an urgent need to evaluate the use of building materials from the sustainable point of view. Preference should be given to materials with minimal GHG emissions, minimal energy costs and minimal waste during production, as well as optimization of solutions in accordance with today's environmental agenda. Furthermore, the construction industry must minimize the consumption of both embodied and operational energies to achieve a sustainable built environment [15–16].

The purpose of this study is an environmental assessment of the construction materials of a low-rise residential building. This goal was reached through the following steps:

1. Design of a low-rise residential building considering materials selection;
2. LCA of building materials (stages A1-A3);
3. Analysis of LCA results, conclusions and design optimization;
4. Calculation of heat losses and greenhouse gas emissions for building heating.

Results analysis provides an opportunity to optimize accepted decisions and reduces the negative impact of construction on the environment.

2. Materials and Methods

The object of the study is a two-storey blocked residential building (Fig. 2) with a living area of 261 m². The dimensions of the building are 11.5x15.2 m. Enclosing structures and reinforced concrete columns are loadbearing structures. Internal walls are made of aerated concrete.

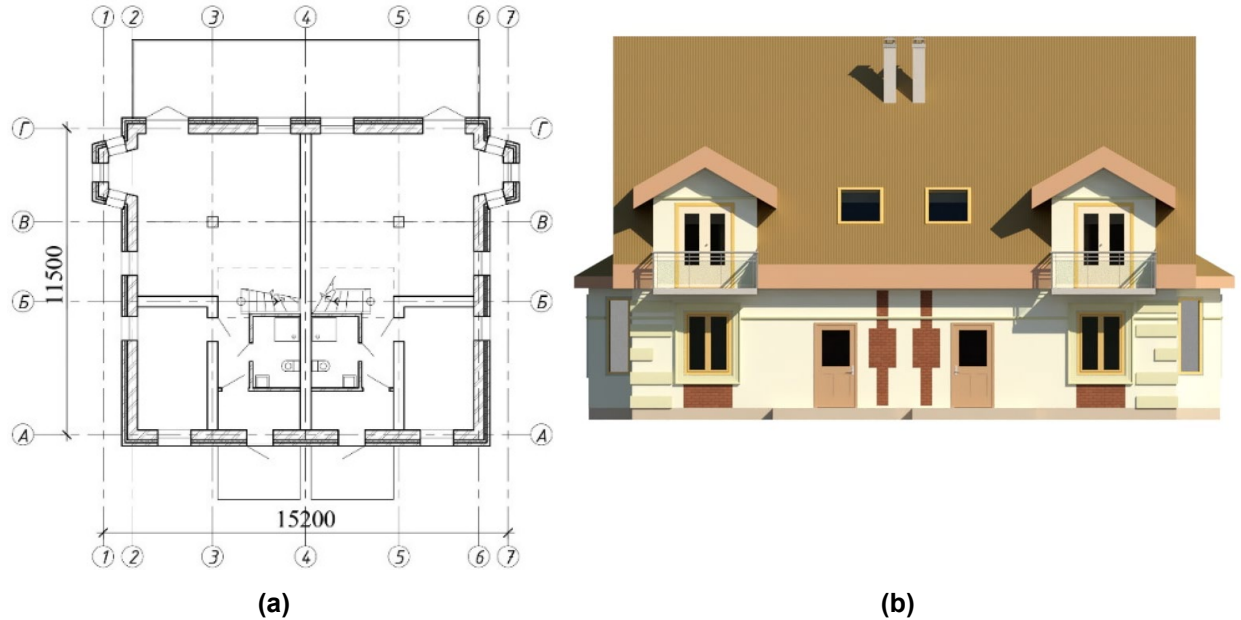


Figure 2. Two-storey residential house: (a) Building plan; (b) Building facade.

The building is located in the temperate climate zone (St. Petersburg, Russia). The thickness and composition of the enclosing structures of the walls, roof and foundation were determined in accordance with local requirements. The building materials used as part of various structures are presented in Table 1, where the mass and volume of materials are indicated. LCA results of used materials allow us to estimate the contribution of each of them to the total amount of greenhouse gas emissions from construction. One Click LCA software was used to calculate the amount of greenhouse gas emissions at stages A1-A3 of the materials life cycle, which is also shown in Table 1. The software is compliant with EN 15978 standard and followed by Environmental Product Declarations (EPDs) based on the ISO 14044 and EN 15804 standards.

Materials shown in Table 1 were quantified by using a 3D model of the object. The aforementioned software allows the user to specify the materials applied in the project and assign manufacturers to existing materials. One Click LCA¹ can assess the potential environmental impacts associated with product quantifying lifetime environmental impacts. The program uses the following information, such as material quantity and its environmental performance derived from EPD of each material or generic database. All materials are divided into structures in which they were considered during the project design, making it possible to divide total building emissions into structure groups. LCA assesses several environmental impact categories, with Global Warming Potential (GWP) being the most widely recognized. Table 1 shows the assessment result of carbon footprint from the material product stage (A1-A3).

Table 1. Building materials.

Material	Weight, ton	Volume, m ³	Emission, ton of CO ₂ e, (stage A1-A3)
1. Foundation – 44.76 t CO ₂ e ~ 13 %			
Sand	43.93	26.12	0.1
Extruded polystyrene	0.55	17.42	9.65
Sawn timber	1.82	1.74	1.56
Reinforced concrete	108.85	43.54	33.2
Geotextile	0.063	0.17	0.25

¹ URL: <https://www.oneclicklca.com>

Material	Weight, ton	Volume, m ³	Emission, ton of CO ₂ e, (stage A1-A3)
2. Vertical structures – 214.2 t CO ₂ e ~ 63 %			
External load-bearing walls			
Stone wool	2.25	22.5	4.6
Bricks	176	110	149
Columns			
Reinforced concrete	13.5	5.4	2.5
Internal walls			
Aerated concrete	26.77	53.54	28.2
Bricks	35.2	22	29.9
Gypsum	0.2	0.24	0.02
3. Horizontal structures – 75.7 t CO ₂ e ~ 23 %			
Floor slab			
Reinforced concrete	61.025	24.41	18.6
Gypsum	2.6	3.5	0.76
Extruded polystyrene	0.44	14	7.76
Sawn timber	1.47	1.41	0.91
Vapour barrier	0.02	0.03	0.84
Roof			
Gypsum	5.3	7.13	1.54
Sawn timber	16	35.54	11.2
Extruded polystyrene	0.45	14.2	7.86
Stone wool	4.27	42.67	8.62
Shingles	12.5	3.41	14.5
Waterproofing membrane	0.66	0.43	1.4
Vapour barrier	0.04	0.06	1.7
4. Doors & windows – 3.4 t CO ₂ e ~ 1 %			
Sawn timber	2	4.4	1.51
Glass	0.89	0.4	1.91
Total:			339

3. Results and Discussion

The total contribution of each type of construction to greenhouse gas emissions is shown in Fig. 3.

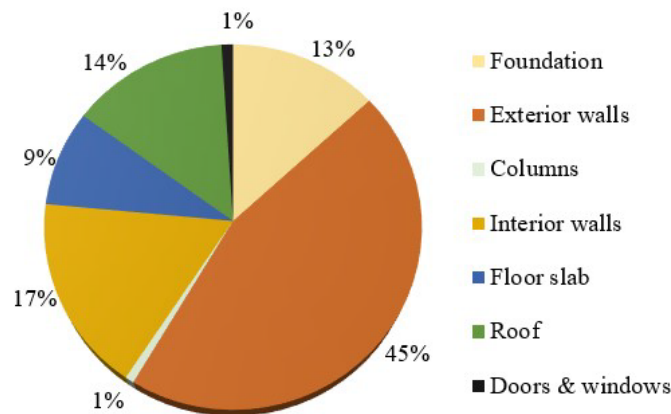


Figure 3. Building structures contribution to the total greenhouse gas emissions.

The greatest impact of material production on the carbon footprint is exerted by materials of the exterior walls (45 %). Fig. 4 shows the composition of the initial structure of the three-layer external wall of the considered residential building.

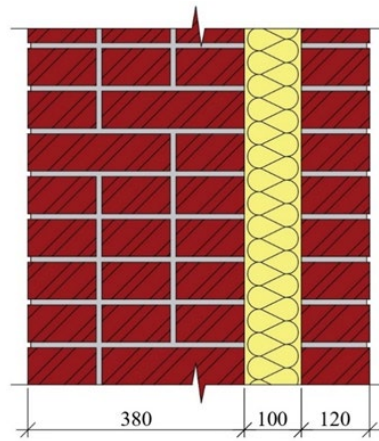


Figure 4. Exterior wall I, $U_I = 0.28 \text{ W}/(\text{m}^2 \cdot \text{K})$.

Assessment results of the contribution of each material to the total greenhouse gas emissions at the A1-A3 LCA stages (Fig. 5) show that bricks, mainly as part of exterior walls, are responsible for 53 % of greenhouse gas emissions. Therefore, in order to reduce the initial value of emissions, first of all it is necessary to optimize the design of external walls by changing its composition so that its properties meet the requirements for thermal protection for the relevant construction region [17–19].

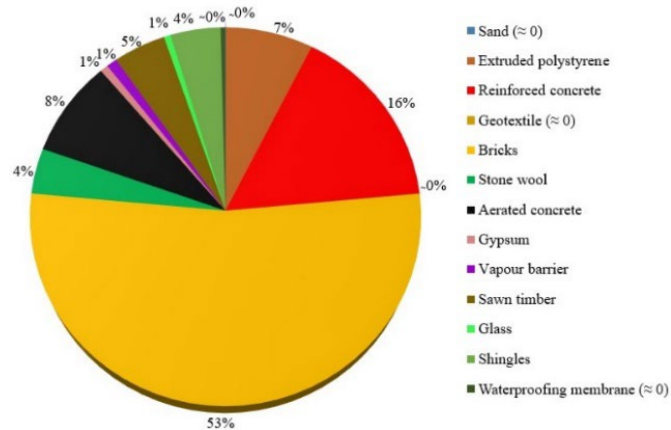


Figure 5. Materials contribution to the total greenhouse gas emissions.

The purpose of the environmental assessment is mainly the choice optimization of building materials based on the LCA analysis results. Alternative designs of exterior walls, which are shown in Fig. 6, were chosen based on their popularity among private residential construction.

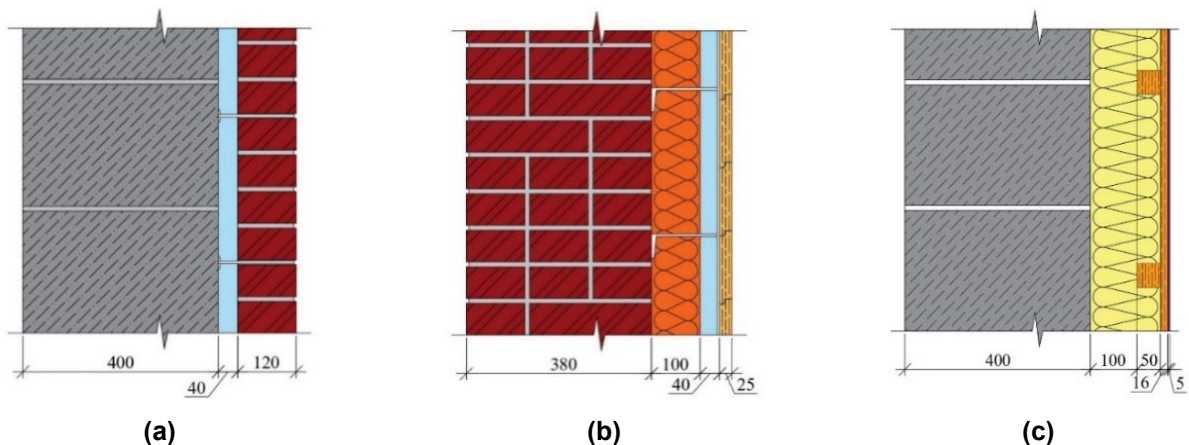


Figure 6. Types of exterior walls: (a) Type II, $U_{II} = 0.29 \text{ W}/(\text{m}^2 \cdot \text{K})$; (b) Type III, $U_{III} = 0.27 \text{ W}/(\text{m}^2 \cdot \text{K})$; (c) Type IV, $U_{IV} = 0.13 \text{ W}/(\text{m}^2 \cdot \text{K})$.

CO₂ emissions from the production of 4 different types of enclosing structures are shown in Table 4. According to the calculations, the exterior walls II-IV are the most environmentally friendly compared to the

original version. All walls meet the requirements for thermal transmittance. It can be concluded that the exterior wall IV is the most optimal choice for the construction of a two-storey residential building.

Table 2. Exterior walls constructions comparison.

No	Material	Thickness, m	U-value, W/(m ² · K)	Emission, ton of CO ₂ e (stage A1-A3)	Construction contribution to total greenhouse gas emissions, %	Total emissions from materials, ton of CO ₂ e (stage A1-A3)
I	Solid brick M150	0.38	0.28	153.6	45	339
	Stone wool	0.10				
	Hollow brick M150	0.12				
II	Aerated concrete D500, B3,5	0.40	0.29	83.7	31	270
	Air layer	0.04				
	Hollow brick M150	0.12				
III	Solid brick M150	0.38	0.27	130.4	41	318
	Extruded polystyrene	0.10				
	Air layer	0.04				
IV	Sawn timber	0.025	0.13	59,5	24	244
	Aerated concrete D500, B3,5	0.40				
	Stone wool	0.1				
	Stone wool	0.05				
	Oriented strand boards (OSB) panels	0.016				
Façade tiles	0.005					

The heat loss of the building through the enclosing structures is calculated to determine the amount of heat needed for building heating. The calculation was carried out only for external walls in order to select the most effective design. The amount of heat lost by the building through the enclosing structures of the exterior walls is determined by the formula (1):

$$Q = S \cdot \Delta t \cdot T \cdot U, \quad (1)$$

where S is wall area, [m²], Δt is temperature difference, [K], T is heating period, [h], U is thermal transmittance of the wall, [W/(m² · K)].

The area of the facade remains unchanged for each type of structure and it is equal to 225 m². The following values were taking for the calculation based on local climate data and technical standards [20]: external temperature is (-24 °C); internal temperature is (+18 °C); heating period is 224 days.

Thermal transmittance was calculated earlier and given in Table 2. It is considered that 1 kW = 1 kJ/s, 1 kWh = 3600 kJ, and 1 Gcal = 1163 kWh. It is necessary to know the calorific value of natural gas, the density and the amount of emissions per 1 kg of used natural gas in order to calculate the amount of greenhouse gas emissions. Natural gas was chosen as the most widely used type of fuel for building heating in Russia. The calculation is made in tabular form (Table 3).

Table 3. Calculation of heat losses and greenhouse gas emissions.

Parameter	External wall I	External wall II	External wall III	External wall IV
U-value of the wall, W/(m ² ·K)	0.28	0.29	0.27	0,13
Facade area, m ²	225	225	225	225
Temperature difference, K	42	42	42	42
Heating season, h	5064	5064	5064	5064
Heat loss through external walls, W·h	13399344	13877892	12920796	6221124
Heat loss through external walls, MJ	48238	49960	46515	22396
Calorific capacity of natural gas for 1 MJ/m ³	33.5	33.5	33.5	33.5
Natural gas consumption per year, m ³	1439.9	1491.3	1388.5	668.5
Natural gas density, kg/m ³	0.68	0.68	0.68	0.68
Mass of consumed natural gas, kg	979.1	1014.1	944.2	454.58
Greenhouse gas emissions, kg CO ₂ e per 1 kg of consumed gas	2.64	2.64	2.64	2.64
Total greenhouse gas emissions, kg CO ₂ e per year	2585	2677	2493	1200
Heat loss through external walls, Gcal	11.53	11.94	11.12	5.35

Let us assume that service life of the building is 50 years and calculate the total CO₂ emissions (Table 4):

Table 4. Total calculation of CO₂ emission.

Wall type	External wall I	External wall II	External wall III	External wall IV
CO ₂ e emission from the materials production, ton	339	270	318	244
CO ₂ e emission from burning fuel for building heating, ton	129.25	133.85	124.65	60
Total CO ₂ e emission, ton	468.25	403.85	442.65	304

4. Conclusions

It follows from the calculation results (Table 3) that the most environmentally friendly and cost-effective option in operation is the external wall IV. Low U-value of this wall type makes the mass of consumed fuel several times less than value of fuel consumption in other cases. It is important to note that wall structures with that low U-value are rarely applied in given region because construction standards in Russia do not require such a low value of thermal transmittance of external walls (U-value of 0.2–0.3 is sufficient to meet existing requirements). Considering the data in Table 2, which shows the results of calculating the amount of greenhouse gas emissions during material product stage, the most environmentally friendly option also is external wall IV. It can be explained that prevailing material used in producing this type of external wall (aerated concrete) has low CO₂ emission per unit of mass. Moreover, this type of external wall does not have brick in its composition, which has the greatest amount CO₂ emission per unit of mass.

Operation stage of the building (building heating) does not cause such harm to the environment as the production of building materials despite the fact that calculations were carried out for the service life of

50 years. According to the results in Table 4, CO₂ emissions from building heating do not exceed 1/3 of the total CO₂ emissions. Furthermore, the lower the U-value is, the smaller this ratio is.

The possibilities of optimization, such as the number of alternative options of certain structures as well as the number of materials suitable for use, have their strict limits in each specific situation, depending on the type of building being designed, its features, dimensions, requirements for strength, stability and rigidity of load-bearing structures, thermal protection of enclosing structures, etc. [21]. The calculations carried out in this study are an example of the fact that the choice of building materials should be comprehensive. It means that it is necessary to consider the criterion of environmental friendliness, which has a direct impact on the environment, in addition to the standard criteria.

In many ways, a similar assessment of the building materials of a residential low-rise building was carried out in the study [20]. As a result, materials that have the greatest contribution to the total amount of greenhouse gases from the construction of the building (at A1-A3 stages of LCA) are concrete and wood as part of the foundation structures, ceilings and exterior walls. Also, in cases [22–24], it was found that concrete is the most dangerous in terms of its contribution to the total amount of greenhouse gases. In the study [25], ceramic bricks make the greatest contribution to the total amount of emissions. The assessment of the life cycle of an industrial building [26] shows that in buildings of this type, concrete (reinforced concrete) is the material responsible for the largest percentage of greenhouse gas emissions, due to massive load-bearing reinforced concrete structures.

Thus, based on the results of this study, confirmed by other works, we can conclude that the most popular building materials, such as concrete and brick, which are used everywhere, are the reason for the large GWP in the construction industry. According to [27], in terms of the amount of greenhouse gas emissions and the amount of energy consumption, the use of a wooden frame is the best option for the construction of low-rise residential buildings. However, replacing concrete and brick with wood is not always possible. Therefore, it is worth paying attention to manufacturers of building materials and their environmental product declarations (EPD). Emissions from the same material but from different manufacturers may differ by several times.

This work evaluated the product stages of building LCA (A1-A3). In further studies, it is planned to evaluate the construction stage (transportation to construction site A4 and installation A5).

References

1. Beck, H.E., Zimmermann, N.E., McVicar, T.R., Vergopolan, N., Berg, A., Wood, E.F. Present and future Köppen-Geiger climate classification maps at 1-km resolution. *Scientific Data*. 2018. 5(1). DOI: 10.1038/sdata.2018.214
2. Garanina, O.L. Povestka energeticheskogo perekhoda: vyzovy dlya Rossii v kontekste pandemii [Energy Transition Agenda: Challenges for Russia under the Pandemic]. *Russian Foreign Economic Journal*. 2021. 4. DOI: 10.24411/2072-8042-2021-4-40-52. (rus).
3. Zhavoronkova, N.G., Agafonov, V.B. Klimaticheskoe zakonodatel'stvo Rossijskoj Federacii: vozmozhnosti i potencial v usloviyah energeticheskogo perekhoda [Climate Legislation of the Russian Federation: Opportunities and Potential in the Conditions of Energy Transition]. *Lex Russica*. 2022. 75(1). Pp. 29–37. DOI: 10.17803/1729-5920.2022.182.1.029-037. (rus)
4. Edenhofer, O., Pichs-Madruga, R., Sokona, Y., et al. IPCC, Climate Change 2014: Mitigation of Climate Change. Contribution of Working Group III to the Fifth Assessment Report of the Intergovernmental Panel on Climate Change. Cambridge University Press, Cambridge, United Kingdom and New York, NY, USA. 2014. 16 p.
5. Zeifman, L., Hertog, S., Kantorova, V., Wilmoth, J. A World of 8 Billion. United Nations. 2022. 140. DOI: 10.18356/27081990-140
6. Cabeza, L.F., Rincón, L., Vilariño, V., Pérez, G., Castell, A. Life cycle assessment (LCA) and life cycle energy analysis (LCEA) of buildings and the building sector: A review. *Renewable and Sustainable Energy Reviews*. 2014. 29. Pp. 394–416. DOI: 10.1016/j.rser.2013.08.037
7. Ben-Alon, L., Loftness, V., Harries, K.A., DiPietro, G., Hameen, E.C. Cradle to site Life Cycle Assessment (LCA) of natural vs conventional building materials: A case study on cob earthen material, *Building and Environment*. 2019. 160. 106150. DOI: 10.1016/j.buildenv.2019.05.028
8. European Parliament. Directorate general policy department A: For internal policies economic and scientific policy. Boosting Building Renovation: What potential and value for Europe. 2016. 72 p.
9. Bastante-Ceca, M.J., Cerezo-Narváez, A., Piñero-Vilela, J.-M., Pastor-Fernández, A. Determination of the Insulation Solution that Leads to Lower CO₂ Emissions during the Construction Phase of a Building. *Energies*. 2019. 12. 2400. DOI: 10.3390/en12122400
10. Zaborova, D., Musorina, T. Environmental and Energy-Efficiency Considerations for Selecting Building Envelopes. *Sustainability*. 2022. 14(10). 5914. DOI: 10.3390/su14105914
11. Zubarev, K.P., Gagarin, V.G. Experimental Comparison of Construction Material Vapor Permeability in Case of Horizontal or Vertical Sample Position. *IOP Conference Series: Materials Science and Engineering*. 2018. 463. 032082. DOI: 10.1088/1757-899x/463/3/032082
12. Borodiņecs, A., Prozuments, A., Zajacs, A., Zemītis, J. Retrofitting of Fire Stations in Cold Climate Regions. *Magazine of Civil Engineering*. 2019. 90(6). Pp. 85–92. DOI: 10.18720/MCE.90.8
13. Prozuments, A., Borodiņecs, A., Zemītis, J., Strelets, K. The Effect of the Air Duct Tightness on the Stability of the Indoor Air Parameters. *Magazine of Civil Engineering*. 2020. 5. Pp. 1–7. DOI: 10.18720/MCE.97.10
14. Kumar, D., Alam, M., Zou, P.X.W., Sanjayan, J.G., Memon, R.A. Comparative analysis of building insulation material properties and performance, *Renewable and Sustainable Energy Reviews*. 2020. 131. 110038. DOI: 10.1016/j.rser.2020.110038

15. Abouhamad, M., Abu-Hamd, M. Life Cycle Assessment Framework for Embodied Environmental Impacts of Building Construction Systems. *Sustainability*. 2021. 13. 461. DOI: 10.3390/su13020461
16. Grygierek, K., Ferdyn-Grygierek, J. Analysis of the Environmental Impact in the Life Cycle of a Single-Family House in Poland. *Atmosphere*. 2022. 13. 245. DOI: 10.3390/atmos13020245
17. Gamayunova, O., Petrichenko, M., Mottaeva, A. Thermotechnical calculation of enclosing structures of a standard type residential building. *Journal of Physics: Conference Series*. 2020. 1614. 012066 DOI: 10.1088/1742-6596/1614/1/012066
18. Gagarin, V.G., Kozlov, V.V., Zubarev, K.P. Determination of maximum moisture zone on enclosing structures. *Cold Climate HVAC*. 2018. *Sustainable Buildings in Cold Climates*. 2019. Pp. 925–932. DOI: 10.1007/978-3-030-00662-4_78
19. Zubarev, K., Zobnina, Y. Methods of achieving energy efficiency in buildings and their evaluation. *E3S Web of Conferences*. 2023. 389. 06025. DOI: 10.1051/e3sconf/202338906025
20. Gumerova, E., Gamayunova, O., Shilova, L. The optimal decision of insulation in cladding structures for energy efficient buildings. *MATEC Web of Conferences*. 2017. 106. 06020. DOI: 10.1051/matecconf/201710606020
21. Kheiri, F. A review on optimization methods applied in energy-efficient building geometry and envelope design, *Renewable and Sustainable Energy Reviews*. 2018. 92. Pp. 897–920. DOI: 10.1016/j.rser.2018.04.080
22. Petrovic, B., Myhren, J.A., Zhang, X., Wallhagen, M., Eriksson, O. Life Cycle Assessment of Building Materials for a Single-family House in Sweden. *Energy Procedia*. 2019. 158. Pp. 3547–3552. DOI: 10.1016/j.egypro.2019.01.913
23. Asif, M., Muneer, T., Kelley, R. Life cycle assessment: A case study of a dwelling home in Scotland. *Building and Environment*. 2007. 42(3). Pp. 1391–1394. DOI: 10.1016/j.buildenv.2005.11.023
24. Emami, N., Heinonen, J., Marteinson, B., Säynäjoki, A., Junnonen, J.-M., Laine, J., Junnila, S. A Life Cycle Assessment of Two Residential Buildings Using Two Different LCA Database-Software Combinations: Recognizing Uniformities and Inconsistencies. *Buildings*. 2019. 9. DOI: 10.3390/buildings9010020
25. Traverso, M., Rizzo, G., Finkbeiner, M. Environmental performance of building materials: life cycle assessment of a typical Sicilian marble. *The International Journal of Life Cycle Assessment*. 2010. 15(104) DOI: 10.1007/s11367-009-0135-z
26. Rodrigues, V., Martins, A.A., Nunes, M.I., Quintas, A., Mata, T.M., Caetano, N.S. LCA of constructing an industrial building: focus on embodied carbon and energy, *Energy Procedia*. 2018. 153. Pp. 420–425. DOI: 10.1016/j.egypro.2018.10.018
27. Bahramian, M., Yetilmezsoy, K. Life cycle assessment of the building industry: An overview of two decades of research (1995–2018). *Energy and Buildings*. 2020. 219. 109917. DOI: 10.1016/j.enbuild.2020.109917

Information about authors:

David Kokaya,

ORCID: <https://orcid.org/0009-0001-3191-5663>

E-mail: kokaya.dv@edu.spbstu.ru

Daria Zaborova, PhD in Technical Sciences

ORCID: <https://orcid.org/0000-0002-8346-549X>

E-mail: zaborova-dasha@mail.ru

Tatiana Koriakovtseva, PhD in Technical Sciences

ORCID: <https://orcid.org/0000-0002-8380-0067>

E-mail: tamusorina@mail.ru

Received 06.07.2023. Approved after reviewing 21.11.2023. Accepted 27.11.2023.



Research article

UDC 532.517

DOI: 10.34910/MCE.124.11



Digital models for retrospective analysis of the structure of currents in the Neva Bay

D.K. Zotov , G.L. Kozinetc, P.V. Kozinets, P.V. Chernov , V.L. Badenko 

Peter the Great St. Petersburg Polytechnic University, St. Petersburg, Russian Federation

 zotovdk@gmail.com

Keywords: Neva Bay, Neva River, fairway, water area, hydrodynamic problem, finite element method, boundary conditions, anthropogenic impact, digital models, shallow water equation, velocity field, water exchange, hydrological regime

Abstract. The Neva Bay is a body of water located between the delta of the Neva River and Kotlin Island. The goal of the study was to develop a method for numerical modeling of the shallow water equation in the Neva Bay, based on the finite element method. To achieve this goal, we solved a number of tasks. First, we selected characteristic periods in the history of the Neva Bay and formed numerical modeling options while determining boundary conditions. Secondly, we determined the geometric characteristics of the computational domain for modeling options and formed a finite element mesh for each of the options. Then, we found a numerical solution of hydrodynamic problems in terms of determining values of current velocity vectors. Finally, we conducted a comparative analysis of the results of solving the hydrodynamic problem of the structure of currents in the Neva Bay in different periods of history. The changes in the velocity field occurred because of the construction of the fairway and the dams for the Complex of flood protection structures (CFPS) in St. Petersburg. Today there is practically no water flow south of the Sea Canal. Water exchange between the Neva Bay and the Gulf of Finland is carried out due to culvert structures in the northern part of the CFPS and navigation facilities. The average flow of the Neva River during the calculation period did not change and was about 2500 m³/s (depends on the water level in Lake Ladoga); an increase in speeds occurs north of the Sea Canal.

Funding: The research was supported by the Russian Science Foundation grant No. 23-19-20062, <https://rscf.ru/project/23-19-20062/>, and the St. Petersburg Science Foundation grant No. 23-19-20062.

Citation: Zotov, D.K., Kozinetc, G.L., Kozinets, P.V., Chernov, V., Badenko, V.L. Digital models for retrospective analysis of the structure of currents in the Neva Bay. Magazine of Civil Engineering. 2023. Article no. 12411. DOI: 10.34910/MCE.124.11

1. Introduction

The Neva Bay is in the eastern part of the Gulf of Finland and is its shallowest part, where the full-flowing Neva River has an average flow of about 2500 m³/sec [1–3]. Historically, this water area, starting from the 18th century, was subject to anthropogenic impact and its geometric parameters changed, and to date the area of the water surface is about 329 km², and the depths do not exceed 5–6 m [4–6]. The strongest impact on the hydrological regime of the Neva Bay was exerted by the construction of the Complex of Flood Protection Structures of St. Petersburg (CFPS), which was completed in 2011 and turned Neva Bay into a “technogenic lagoon”, a kind of internal marine area of the metropolis [2, 7–9].

The Neva Bay has been the subject of practical and theoretical research since the 18th century [10]. Special attention has always been paid to the study of the causes of the Neva floods, their development, and consequences [11–13]. It should be noted that many field observations and theoretical studies were

carried out based on various hydrodynamic models, which were constantly modernized to improve the quality of forecasts [6, 14–16]. At the same time, the methods and instrumental support for field observations were constantly improved during numerous expeditionary studies using the latest instruments and remote sensing data – satellite images [3, 4, 17]. Many publications have been devoted to environmental problems and their connection with changes in anthropogenic load [2–4, 7–9, 17, 18]. Scientists were also interested in the impact of currently observed climate changes on the hydrodynamics of the Neva Bay [2, 17, 19]. It should be noted that all researchers highlighted the importance of retrospective analysis of changes in the structure of currents to identify trends and make forecasts, but such an analysis was not systematically carried out. Such retrospective studies are always carried out using numerical models, but due to the lack of detailed information about the modeling features, they are difficult to replicate.

In the world you can find estuaries that are to some extent similar to the Neva Bay and which raise similar problems related to sedimentation characteristics and changes in the ecological situation for the worse [20–24]. Typically, estuaries are studied in highly urbanized regions. The accumulation of bottom sediments in river mouths is being studied, which usually has a serious impact on the ecological state of the water area. The publications provide a series of hydrographic and bathymetric studies analyzing currents, sediment transport and morphological processes at the river mouth. Simulation results of sediment flow and circulation across seasons are typically studied using time series collected from hydrographic surveys. In addition, many authors use retrospective analysis to analyze trends in changes in hydrological conditions [25–27].

Thus, researchers of hydrodynamic phenomena in estuaries emphasize the importance of retrospective analysis of changes in the structure of currents for making forecasts and calibrating computational models; the task remains relevant. Most researchers use the “shallow water” model when modeling currents in estuaries [28–32]. At the same time, researchers recommend using the finite element method for estuaries that have the same complex configuration of the computational domain as in the Neva Bay [31–33].

In general, we can conclude that there is a gap in research that is focused on creating a methodology for implementing numerical modeling of currents in the Neva Bay for the purpose of conducting a retrospective analysis, and on the other hand, would make it possible to predict the development of the hydrological situation during various catastrophic phenomena.

The purpose of this work is to develop a method for numerical modeling of the shallow water equation in the Neva Bay based on the finite element method. To achieve this goal, the following tasks were solved:

- selection of characteristic periods in the history of the Neva Bay and the formation of numerical modeling options with the determination of boundary conditions;
- determination of geometric characteristics of the computational domain for modeling options;
- generation of a finite element mesh for each option;
- numerical solution of hydrodynamic problems in terms of determining the values of current velocity vectors;
- comparative analysis of the results of solving the hydrodynamic problem of the structure of currents in the Neva Bay in different periods of history.

2. Materials and Methods

When selecting characteristic periods for numerical modeling, the following criteria were used. Firstly, the timing of the construction of hydraulic structures, which significantly influenced the structure of currents in the Neva Bay. Such periods were defined as before and after the construction of the Sea Canal from Kronstadt to St. Petersburg [33], as well as before and after the commissioning of the CFPS [7]. For these periods, it was necessary to determine the availability of nautical charts for the selected periods. These maps can be obtained in scanned form from the Archive of the Navy, a branch of the Central Archive of the Ministry of Defense of the Russian Federation [34]. Also, in the Archive, you can obtain data on currents in the Neva Bay, which allows you to determine the boundary conditions for the direction and speed of the current.

The geometric characteristics of the computational area for modeling options are obtained thanks to map digitization using GIS technologies [35]. In this case, the calculation area was selected along the boundary of the currently existing CFPS dam.

A digital representation of the Neva Bay will allow us to move on to the next stage of constructing a finite element mesh. In this case, at the beginning, the finite element mesh was built automatically, and then it was manually optimized around islands and other inhomogeneities.

2.1. Methodology for numerical modeling of the Neva Bay reservoir

Numerical modeling was based on solving shallow water equations in the ANSYS environment in the following form [29]:

$$\frac{\partial h}{\partial t} + \frac{\partial hu_x}{\partial x} + \frac{\partial hu_y}{\partial y} = 0; \quad (1)$$

$$\frac{\partial (hu_x)}{\partial t} + \frac{\partial}{\partial x} \left(hu_x^2 + \frac{1}{2} gh^2 \right) + \frac{\partial}{\partial y} (hu_x u_y) = h \left(f_x^v - g \frac{\partial b}{\partial x} \right) + f_x^s; \quad (2)$$

$$\frac{\partial (hu_y)}{\partial t} + \frac{\partial}{\partial x} (hu_x u_y) + \frac{\partial}{\partial y} \left(hu_y^2 + \frac{1}{2} gh^2 \right) = h \left(f_y^v - g \frac{\partial b}{\partial y} \right) + f_y^s. \quad (3)$$

In equations (1)–(3) the following notations are used (Fig. 1): $h(x, y, t)$ is the height of the water level, measured from the bottom surface, $b(x, y)$ is the bottom level, which is measured from the deep point, $u_x(x, y, t)$, $u_y(x, y, t)$ are components of the horizontal velocity vector, g is gravitational acceleration, $f_x^v(x, y, t)$, $f_y^v(x, y, t)$ are components of the vector of volumetric external force acting on the entire thickness of the water layer, $f_x^s(x, y, t)$, $f_y^s(x, y, t)$ are components of the surface external force vector, $\xi(x, y, t) = h(x, y, t) + b(x, y)$ is the water surface level, $h_0(x, y, t)$ is the height of the equilibrium water level, then the deviation from equilibrium value $\eta(x, y, t) = h_0(x, y) - h(x, y, t)$.

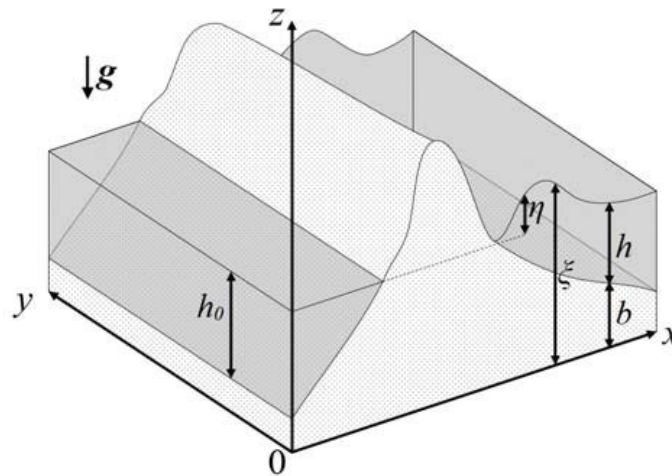


Figure 1. Input data for the shallow water equation.

One of the well-known methods for numerically solving water flow equations for small reservoirs is the finite element method [36]. According to the basic idea of the finite element method, a continuous function is approximated by a set of piecewise continuous functions defined on a finite set of nodes in the domain under consideration. The problem solution area (a reservoir with its geometric characteristics) is divided into a finite number of elements according to the continuity condition. The main advantages of the method are the ease of approximation of boundaries when solving problems in the area of a reservoir of complex shape, since water elements can have a curvilinear shape and heterogeneous physical properties.

Calculation using the ANSYS Fluent package is carried out on a structured mesh containing 1,600,000 to 4,000,000 elements. The 1877 model does not have the Sea Channel, which, due to the small size area relative to the design area and the need to compact the grid, accounts for a significant part of the elements.

To adjust the FEM grid, the automatically generated finite element grid was manually adapted. After refining the grid, the basic size of which is 20 meters to 1 meter in places of sharp changes in depth.

Boundary conditions of the computational domain:

At the boundaries of the computational domain (bottom and shore), the flow rates are equal to 0.

This makes it possible to consider the influence on the structure of the current of the coastline of the Neva Bay, on which traditional no-flow condition (the normal projection of velocity to the solid boundary is zero). For the Neva River, the Chezy coefficient is 55, for deep sections (sea canal and fairways) 75, for the rest of the Neva Bay 45.

At the coastal boundaries, no-slip conditions on a solid surface (zero velocity vector) were used for velocities, and at the mouth of the Neva (in the branches) and along the CFPS boundary, known long-term values were used [10]. at the open border in the area of the Liteiny Bridge, the average annual flow rate (2500 m³/s) in the Neva River was set. In the Neva Bay area, along the CFPS axis:

1. at the open boundary in the CFPS location area, the free water surface elevation was set ($h+b=const$);
2. on the open CFPS at the locations of navigation and culvert structures, the free water surface elevation was set ($h+b=const$) (Fig. 2).



Figure 2. Scheme of the Protective Structures Complex.

Fig. 3–6 show, respectively, the results of calculations in the ANSYS Fluent (CFD) package of a finite element three-dimensional model of the Neva Bay with depth-averaged values of water flow velocities. The graphical image editor shows current velocity vectors and their numerical calculated values in m/sec.

A comparison of the results of numerical calculations and measurements shows that the values calculated on the finite element model are in good agreement with the measurement results, reproducing the maximum and minimum values of the flow parameters.

To model the Neva Bay reservoir, a three-dimensional 8-node fluid isoperimetric element (FLOW3D) was used. General description FLOW3D 8-node element for 3D problems for calculating water flow. Properties of fresh water: Dynamic viscosity $VISC=1.005E^{-3}$ Pa·sec., Density $DENS=1000$ kg/m³. The resulting values are the speed values displayed at each node. Numerical simulation results were obtained for four time periods.

The results present the structure of water flows in the form of velocity vectors.

To verify the results of calculations using the proposed model, data from field observations at the KZS in culverts B2, B6 were used. The average speed is 0.4 m/s. Which corresponds to the calculated data obtained from the model. The deviation of the calculated data and observational data is no more than 5 %, which makes it possible to confidently use this model for calculating flow rates. Fig. 3 shows velocity measurements at culvert B6. Field observations were carried out at a water level in Lake Ladoga (Petrokrepost) of 453 cm, which corresponds to the average flow in the Neva River equal to 2500 m³/s [1].

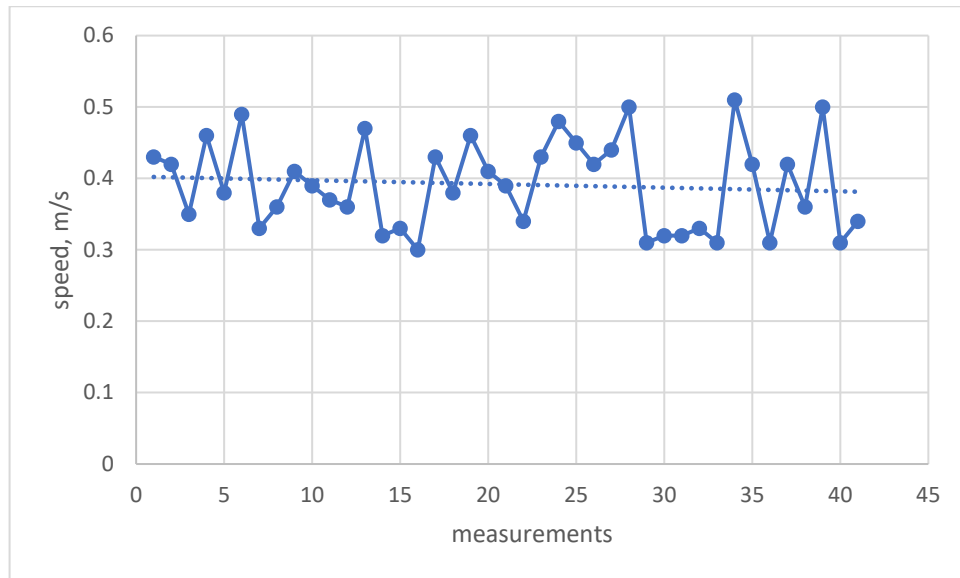


Figure 3. Velocity at culvert B6.

3. Results and Discussion

The solution to the problem is presented in the form of a field of velocities and streamlines of currents. The maximum speed at the water entry into the Neva Bay from the Neva River delta is set to 0.2 m/s. The speed in the Neva River ranges from 0.8 to 1.1 m/s.

Fig. 3 shows the calculated currents for 1877. The main current lines run from the north of Kotlin Island and from the south between Kotlin Island and Fort Kronshlot. The water speed in the Neva River delta is more than 0.6 m/s. Due to the high current speed (more than 0.6 m/s), a ravine formed between Kotlin Island and Fort Kronshlot, along which a historical fairway was formed. Velocities in the northern part of the Neva Bay between Kotlin Island and Lisiy Nos are distributed evenly and amount to 0.1 m/s. In the coastal zone there is practically no water flow.

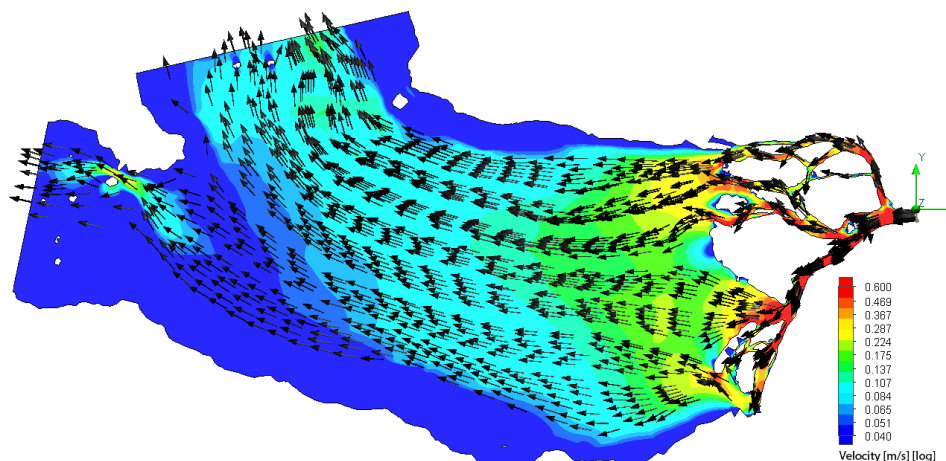


Figure 3. Velocity field and streamlines for the 1877 model.

Since 1877, construction began on the St. Petersburg Sea Canal, connecting the southern part of Kotlin Island and Gutuevsky Island and exiting through an artificial canal into the bed of the Bolshaya Neva. To protect the Sea Canal from silting, a sea canal dam was created, which had a significant impact on the currents, limiting the currents towards the southern part of the Neva Bay. The average values in this part of the Neva Bay have decreased and do not exceed 0.15 m/s. Currents from the northern part have not undergone significant changes and average 0.1 m/s; there is practically no current in the coastal zones. Fig. 4 shows the velocity field and streamline for the 1920 model.

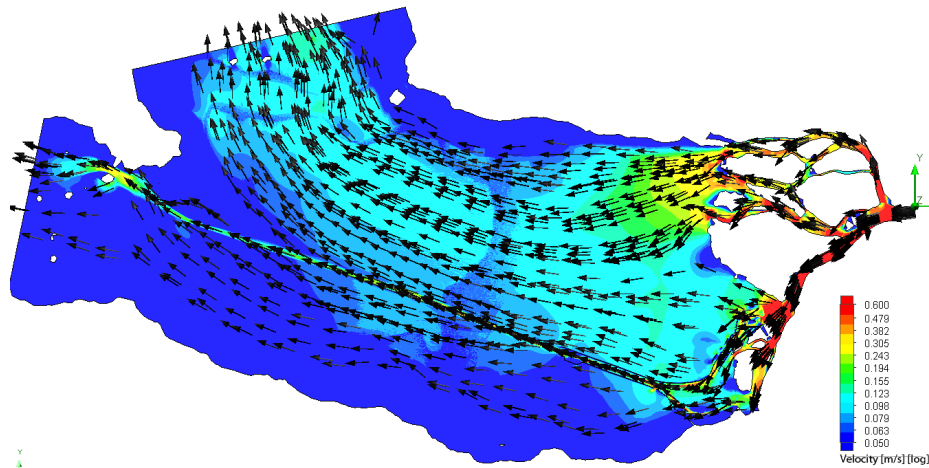


Figure 4. Velocity field and streamlines for the 1920 model.

Figure 5 shows the velocity field and streamline for the 1997 model. By 1997, the main work on filling the CFPS earthen dam was completed. For the passage of water, culverts B1-6 and navigation passages C1, C2 were left, and additional fairways were created, such as the fairway connecting navigation passage C2 with the Sea Canal, as well as the “Petrovsky Canal” connecting the Marine Canal with the Malaya Neva. Due to this, the currents became less uniform, and jets began to form in the flow with a higher speed of 0.11 m/s. Also, due to shallowing, the average current speed north of the Sea Channel increased, amounting to 0.15 m/s.

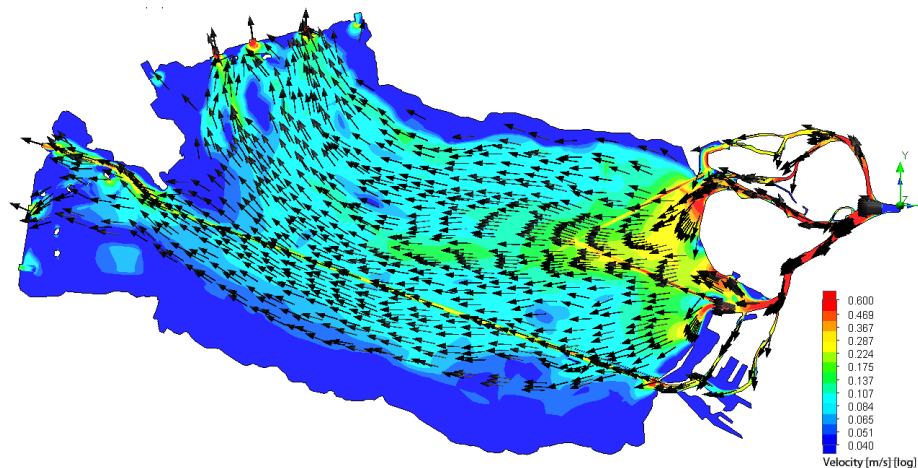


Figure 5. Velocity field and streamlines for the 1997 model.

Figure 6 shows the velocity field and streamline for the 2022 model. The 2022 model is characterized by the completion of the construction of all elements of the CFPS, the construction of the Western High-Speed Diameter (WHSD), and the elevation of ground levels in the western part of the Vasilievsky and Krestovsky Islands, as well as in the Lakhtinsky Razliv area. Due to the reasons described above and the significant shallowing of the Neva Bay, local average speeds increased north of the Sea Canal, and speeds around culverts B4-B6 increased. As a result, gullies began to form around culverts B4-B6 and navigation structures C2. The maximum water speeds through culverts and navigation structures are 0.4–0.6 m/s, which corresponds to field observations, so the average speed in the B-6 culvert is 0.4 m/s. Average speeds north of the Sea Channel increased and amounted to 0.15 m/s.

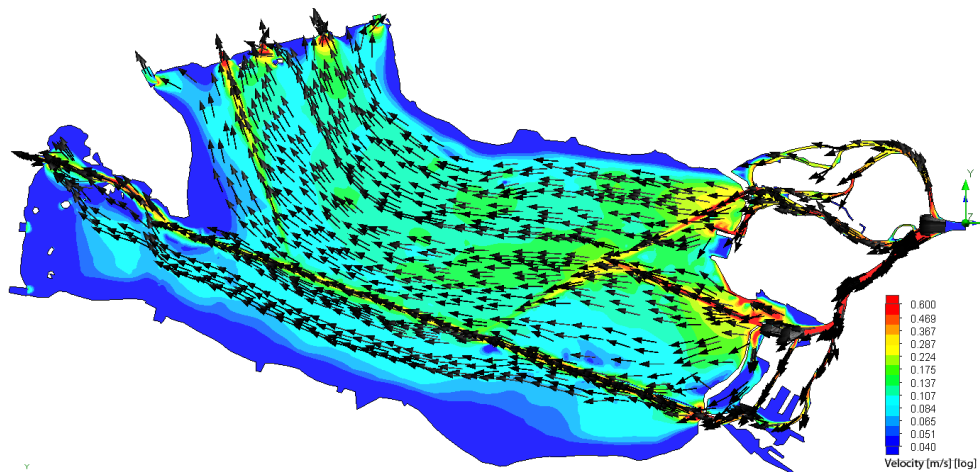


Figure 6. Velocity field and streamlines for the 2022 model.

4. Conclusion

We developed a method for numerical modeling of the shallow water equation in Neva Bay based on which a solution to the hydrodynamic problem was performed for 4 characteristic dates in the history of Neva Bay. As a result of solving hydrodynamic problems, the velocity fields and streamlines of water flows were determined, and an analysis of the results obtained was performed. As a result of solving the problem, the following conclusions were drawn:

1. Changes in the velocity field occurred due to works on the fairway and the construction of dams of the CFPS, which contributed to the shallowing of the Neva Bay water area.
2. Today there is almost no water flow south of the Sea Canal. Water exchange between the Neva Bay and the Gulf of Finland is carried out due to culverts in the northern part of the CFPS and shipping facilities; average speeds are 0.6 m/s.
3. Since the average flow of the Neva River during the calculation period has not changed and is 2500 m³/s, an increase in speeds occurs north of the Sea Canal; the maximum speeds in the center of the Neva Bay are 0.2 m/s.
4. Due to changes in currents, the formation of local high-speed flows towards culverts is observed.

References

1. Nezhikhovskiy, R.A. Reka Neva i Nevskaya guba [The Neva River and Neva Bay]. Leningrad: Gidrometeoizdat, 1981. 112 p. (rus)
2. Ryabchuk, D.V., Nesterova, E.N., Zhamoida V.A., Kotilainen A., Vallius G., Sukhacheva L.L., Spiridonov M.A. Dinamika sedimentatsionnykh protsessov v Nevskoy gube (Finskiy zaliv) pod vozdeystviyem tekhnogennykh faktorov [Dynamics of sedimentation processes in the Neva Bay (Gulf of Finland) under the influence of technogenic factors]. Uchenyye zapiski Rossiyskogo gosudarstvennogo gidrometeorologicheskogo universiteta. 2014. No. 35. Pp. 102–118. (rus)
3. Shilin, M.B., Sychev, V.I., Mikheev, V.L., Istomin, Y.P., Lednova, Yu.A., Luk'yanov, S.V., Abramov, V.M. Results of investigations of the Neva Bay technosphere at RSHU. Gidrometeorologiya i ekologiya. 2020. 60. Pp. 351–370. DOI: 10.33933/2074-2762-2020-60-351-370 (rus)
4. Kovaleva, O.A., Ryabchuk, D.V., Sergeyev, A.Yu., Budanov, L.M. Monitoring razvitiya beregovykh protsessov vostochnoy chasti Finskogo zaliva pod vliyaniyem prirodnykh i tekhnogennykh faktorov [Monitoring the development of coastal processes in the eastern part of the Gulf of Finland under the influence of natural and man-made factors]. Morya Rossii: God nauki i tekhnologii v RF-Desyatiletiiye nauk ob okeane OON [Conference proceedings]. Sevastopol, 2021. Pp. 408–409. (rus)
5. Leontyev, I.O., Ryabchuk, D.V., Spiridonov, M.A., Kurennoi, D.N. The coastal profile in the Eastern Gulf of Finland: the results of a survey and the reconstruction of the evolution in the late Holocene. Okeanologiya. 2010. 50(6). Pp. 1034–1044. (rus)
6. Voltsinger, N.Ye., Zolnikov, A.V., Klevanny, K.A., Preobrazhensky, L.Yu. Calculation of the hydrological regime of the Neva inlet. Meteorologiya i gidrologiya. 1990. 1. Pp. 70–77. (rus)
7. Mikhaylenko, R.R. Saint-Petersburg flood prevention facility complex as a techno-natural system for integrated management of water resources: its social, economical and environmental benefits. Biosfera. 2015. 7(1). Pp. 1–25.
8. Rodionov, V.Z. Kompleks zashchitnykh sooruzheniy Sankt-Peterburga ot navodneniy: istoriya i ekologicheskiye problem [Complex of protective structures of St. Petersburg from floods: history and environmental problems]. Regionalnaya ekologiya. 2016. 4. Pp. 13–23. (rus)
9. Rumyantsev, V., Kondrat'yev, S., Pozdnyakov, Sh., Ryabchenko, V., Basova, S., Shmakova, M. Osnovnyye faktory, opredelyayushchiye funktsionirovaniye vodnoy sistemy Ladozhskoye ozero—reka Neva—Nevskaya guba—vostochnaya chast Finskogo zaliva v sovremennykh usloviyakh [The main factors determining the functioning of the water system Lake Ladoga—Neva River—Neva Bay—eastern part of the Gulf of Finland in modern conditions]. Proceedings of the Russian Geographical Society. 2012. 144(2). Pp. 55–69. (rus)
10. Nezhikhovskiy, R.A. Voprosy gidrologii r. Nevy i Nevskoy guby. [Issues of hydrology of the river. Neva and Neva Bay]. Leningrad: Gidrometizdat, 1988. 108 p.

11. Zakharchuk, Ye.A., Tikhonova, N.A., Sukhachev, V.N. Spatial structure and propagation of the Neva flood waves. *Meteorologiya i gidrologiya* 2020. 4. Pp. 42–53. (rus)
12. Ivanov, S.V., Visheratin, A.A., Nasonov, D.A., Boukhanovsky, A.V. Method of reconstruction of extreme natural phenomena of low frequency for improvement of Saint Petersburg flood-prevention facility. *Izvestiya vysshikh uchebnykh zavedeniy. Priborostroenie*. 2014. 57(12). Pp. 68–70. (rus)
13. Andreyev, P.N., Liberman, Yu.M., Mostamandi, S. Kompleks morskikh gidrodinamicheskikh modeley v Sankt-Peterburgskom TsGMS-R [Complex of marine hydrodynamic models in the St. Petersburg Central Hydrodynamics Center-R]. *SOI Proceedings*. 2011. 213. Pp. 74–79. (rus)
14. Martyanov, S.D., Ryabchenko, V.A. Simulation of the Resuspension and Transport of Bottom Sediments in the Neva Bay Using a 3D Circulation Model. *Fundamental and Applied Hydrophysics*. 2013. 6(4). Pp. 32–43. (rus)
15. Vinogradov, M.V., Tikhonova, N.A., Zakharchuk, Ye.A. Long-term variations of the Baltic sea level in the second half of the 20th - beginning of the 21st century. *Gidrometeorologiya i fizika atmosfery: sovremennyye dostizheniya i tendentsii razvitiya* [Conference Proceedings]. St. Petersburg, 2023. Pp. 91–95. (rus)
16. Klevanny, K.A., Kolesov, A.M., Mostamandi, M.S.V. Predicting the floods in St. Petersburg and the eastern part of the Gulf of Finland under conditions of operation of the flood prevention facility complex. *Meteorologiya i gidrologiya*. 2015. 2. Pp. 61–70. (rus)
17. Sergeev, A.Yu., Ryabchuk, D.V., Nosevich, E.S., Prishchepenko, D.V., Zhamoida, V.A., Piskarev-Vasiliev, A.L., Elkina, D.V., Bashirova, L.D., Ponomarenko, E.P., Budanov, L.M., Grigoriev, A.G. Evolution of sedimentation environment of postglacial basins in the Eastern Gulf of Finland during the holocene under the changing climate. *Okeanologiya*. 2022. 62(3). Pp. 466–484. (rus)
18. Shilin, M.B., Zhigulsky, V.A., Bobylev, N.G., Ahmad, A., Lednova, J.A., Don, S. Development a complex of compensation measures to reduce the negative impact of port Bronka construction on the south coast of Nevskaya lip. *Natural and Technical Sciences*. 2020. 3. Pp. 178–188. DOI: 10.25633/ETN.2020.03.11 (rus)
19. Pavlovskiy, A.A., Menzhulin, G.V. Dynamics of St. Petersburg flooding and its changes during different climatic periods. *Vestnik Sankt-Peterburgskogo Universiteta, Seriya Geologiya i Geografiya*. 2010. 2010(2). Pp. 71–83. (rus)
20. Wu, W., Wang, L., Lei, X., Zheng, Y., Wei, J., Mao, X.-zh. Sustainable estuarine governance based on artificial island scheme for a highly anthropogenic influenced Shenzhen Bay, China. *Journal of Hydrology*. 2023. 616. 128784. DOI: 10.1016/j.jhydrol.2022.128784
21. Zhou, Y., Wang, L., Zhou, Y., Mao, X.-zh. Eutrophication control strategies for highly anthropogenic influenced coastal waters. *Science of the Total Environment*. 2020. 705. 135760. DOI: 10.1016/j.scitotenv.2019.135760
22. Xiao, Y., Wu, Zh., Cai, H., Tang, H. Suspended sediment dynamics in a well-mixed estuary: The role of high suspended sediment concentration (SSC) from the adjacent sea area. *Estuarine, Coastal and Shelf Science*. 2018. 209. Pp. 191–204. DOI: 10.1016/j.ecss.2018.05.018
23. dos Santos, V.H.M., da Silva Dias, F.J., Dottori, M., Torres, A.R., Santos, R.L., Soares, R. de A., Ribeiro, J.C.M., Serejo, J.H.F., Lima, H.P., Azevedo, I.H.R. Investigation of physical properties and suspended particulate matter discharge in a macrotidal estuary at the Amazon-semiarid transition zone. *Regional Studies in Marine Science*. 2023. 67. 103194. DOI: 10.1016/j.rsma.2023.103194
24. Torres-Marchena, C.A., Flores, R.P., Aiken, C.M. Impacts of training wall construction on littoral sedimentation under seasonal flow variability and sea-level rise: A case study of the Magdalena River (Colombia) *Coastal Engineering*. 2023. 183. 104306. DOI: 10.1016/j.coastaleng.2023.104306
25. do Carmo, J.S.A. The changing paradigm of coastal management: The Portuguese case. *Science of the Total Environment*. 2019. 695. 133807. DOI: 10.1016/j.scitotenv.2019.133807
26. Pye, K., Blott, S.J. The geomorphology of UK estuaries: the role of geological controls, antecedent conditions and human activities. *Estuarine, Coastal and Shelf Science*. 2014. 150. Pp. 196–214. DOI: 10.1016/j.ecss.2014.05.014
27. Schrijvershof, R.A., van Maren, D.S., Torfs, P.J.J.F., Hoitink, A.J.F. A Synthetic Spring-Neap Tidal Cycle for Long-Term Morphodynamic Models. *Journal of Geophysical Research: Earth Surface*. 2023. 128(3). e2022JF006799. DOI: 10.1029/2022JF006799
28. Klimovich, V.I., Voronkov, O.K., Davidenko, V.M., Ivanov, S.N. Alkali-activated slag binders from rock-wool production wastes. *Magazine of Civil Engineering*. 2018. 82(6). Pp. 228–242. DOI: 10.18720/MCE.82.21.
29. Bulatov, O.V., Yelizarova, T.G. Regularized shallow water equations for numerical simulation of flows with a moving shoreline. *Computational Mathematics and Mathematical Physics*. 2016. 56(4). Pp. 665–684. (rus)
30. Ivanov, A.V. Computer complex for modelling of sea currents using regularized shallow water equations. *Mathematical Models and Computer Simulations*. 2021. 33(10). Pp. 109–128. DOI: 10.20948/mm-2021-10-08
31. Behzadi, F., Newman III, J.C. An exact source-term balancing scheme on the finite element solution of shallow water equations. *Computer Methods in Applied Mechanics and Engineering*. 2020. 359. 112662. DOI: 10.1016/j.cma.2019.112662
32. Heniche, M., Secretan, Y., Boudreau, P., Leclerc, M. A two-dimensional finite element drying-wetting shallow water model for rivers and estuaries. *Advances in Water Resources*. 2000. 23(4). Pp. 359–372. DOI: 10.1016/S0309-1708(99)00031-7
33. Dikiy, D.I., Sokolov, A.N., Chubarenko, B.V., Artem'yeva, V.D. Metodika opredeleniya optimalnogo podkhoda k chislenному modelirovaniyu techeniy v pribrezhnykh lagunakh dlya ekologicheskikh prilozheniy [Methodology for determining the optimal approach to numerical modeling of currents in coastal lagoons for environmental applications]. *Information and Space*. 2018. 2. Pp. 117–125. (rus)
34. Kurnosova, O.B. 130 years anniversary of opening the seaway channel from Kronshadt to St. Petersburg. *Shipbuilding*. 2015. 3. Pp. 86–89. (rus)
35. Korshunov, E.L., Rupasov, A.I. Archive of the navy - branch of the central archive of the Ministry of defense of the Russian Federation: stages of history. *Herald of an Archivist*. 2018. 3. Pp. 915–925.
36. Nikonorov, A., Badenko, V.L. Flood events dynamics estimation methodology in a GIS environment. *Magazine of Civil Engineering*. 2021. 101(1). Article no. 10110. DOI: 10.34910/MCE.101.10
37. Kozinec, G.L. Generalization of the Methodology of Studying the Durability of Segmental Gates. *Power Technology and Engineering*. 2018. 52(4). Pp. 395–399.

Information about authors

Dmitry Zotov,

E-mail: zotovdk@gmail.com

Galina Kozinets, Doctor of Technical Sciences

E-mail: kozinets_gl@spbstu.ru

Pavel Kozinets,

E-mail: pavelstrenger@gmail.com

Petr Chernov,

ORCID: <https://orcid.org/0000-0003-0267-1505>

E-mail: PchelkaDragpet@mail.ru

Vladimir Badenko, Doctor of Technical Sciences

ORCID: <https://orcid.org/0000-0002-3054-1786>

E-mail: vbadenko@gmail.com

Received 25.08.2023. Approved after reviewing 26.11.2023. Accepted 30.11.2023.



Research article

UDC 66.067.1

DOI: 10.34910/MCE.124.12



Hydrodynamic analysis of an unsteady pressureless filtration flow in earth cofferdams

V.V. Sergeev, E.V. Kotov , S.V. Horobrov, M.M. Sabri , D. Nemova 

Peter the Great St. Petersburg Polytechnic University, St. Petersburg, Russian Federation

 ekotov.cfd@gmail.com

Keywords: soil cofferdam, unsteady fluid motion, numerical analysis, drawdown curve, ANSYS FLUENT, PLAXIS 2D, FEM

Abstract. Non-pressure filtration flows with a free surface, on which the fluid pressure is a constant and equal to the external atmospheric pressure, are essential characteristic of groundwater filtration through such hydraulic structures as, dams, water drawdowns, drains, foundations, and pits during their drain. The problems of fluid filtration in porous media are distinguished by a variety of boundary conditions for the desired complex filtration potential, geometric and physical characteristics of the filtration flow. Solving such problems by analytical methods becomes significantly more complicated due to the nonlinearity of the equation describing the filtration movement, the presence of a free surface and the geometry of the slopes of the structure. An alternative to their solution is the use of numerical methods for estimating unsteady free-flow filtration flows. This research is dedicated to developing a hydrodynamic analysis approach of the process of unsteady filtration by the methods of computational fluid dynamics on the example of a rectangular cofferdam of various configurations to apply the results in the design of hydraulic structures. Numerical modeling of an unsteady free-flow filtration in a rectangular cofferdam using the finite volume URANS method (ANSYS FLUENT) and finite-element method (PLAXIS 2D) was carried out. The depression curve evolution through time was obtained. Also, numerical results have been compared both with the experimental results and classical theoretical assumptions. Was found that the constructed models both for finite-volume and finite-element methods are consistent enough with the experimental data, and on the other hand, theoretical assumptions don't agree with experimental and numerical data. Further, the filtration patterns in rectangular cofferdams with different drain positions were obtained using the developed calculation model, which allows to choose the most effective drain position for different purposes.

Funding: This research was funded by the Ministry of Science and Higher Education of the Russian Federation within the framework of the state assignment No. 075-03-2022-010 dated 14 January 2022 (Additional agreement 075-03-2022-010/10 dated 09 November 2022), FSEG-2022-0010.

Acknowledgments: The authors are grateful to Professor N.I. Vatin for his attentive, critical attitude to the work performed and persistence in the presentation of the results and preparation of the article.

Citation: Sergeev, V.V., Kotov, E.V., Horobrov, S.V., Sabri, M.M., Nemova, D. Hydrodynamic analysis of an unsteady pressureless filtration flow in earth cofferdams. Magazine of Civil Engineering. 2023. Article no. 12412. DOI: 10.34910/MCE.124.12

1. Introduction

Non-pressure filtration flows with a free surface, on which the fluid pressure is a constant and equal to the external atmospheric pressure, are essential characteristic of groundwater filtration through such hydraulic structures as, dams, water drawdowns, drains, foundations, and pits during their drain. These

characteristics occupy more than 80% of all designed and built groundwater hydraulic structures in the world.

The filtration theory for such water management, transport and environmental hydraulic structures was developed by N.N. Pavlovsky [1]. It is noted in [2] that in the exact formulation, the study of non-pressure motion presents significant mathematical difficulties. Therefore, the researches of P.Y. Polubarinova-Kochina, who obtained some exact solutions to the problem of an unpressurized filtration flow through a rectangular cofferdam [3–5].

The existing methods of filtration calculation of dams and barrier dams are based on the use of a model with a linear filtration law (Darcy's law) [4], which establishes a relationship between the filtration velocity vector u and the pressure field p , which causes a filtration flow

$$u = -k \cdot \nabla H; H = y + \frac{p}{\rho g}, \quad (1)$$

where g is the gravity acceleration, ρ is the density of the filtering liquid, k is the filtration coefficient of the porous medium, y is the height (parallel to the direction of gravity).

It should be noted that the analytical solutions to the problems of non-pressure filtration flows are obtained under the assumption of stationarity of fluid motion in a porous medium. The assumption of motion stationarity is fundamentally important [2–6], since the classical methods for calculating seepage flows use the apparatus of the theory of analytic holomorphic functions.

Subsequent studies showed the need to improve Darcy's law. The researches [7–9] indicate the reasons for such a correction. The first is that the application of the macroscopic law of motion when filtering sufficiently fast flows inside a porous medium (Darcy's law) must consider the volume force of viscous resistance acting on the fluid from the side of the porous skeleton. Such conditions are typical for filtration through gravel, pebbles, granular media in industrial process plants. The second is the difference between the rheological relationships of the filtered liquid from the Navier-Stokes law. In [10], a review of the calculation approaches that considers the nonlinear, nonstationary regime of liquid filtration through a porous medium. In [11, 12], a criterion for the nonlinear regime of liquid filtration through a porous medium was proposed. In the papers of [13–15], numerical methods for solving the fluid flow through a porous medium with a nonlinear filtration is proposed.

The application of analytical and numerical methods of filtration for a classical object such as a rectangular cofferdam and objects with a complex hydrogeological structure is considered in [16–19]. The filtration methods for liquids in modern medical and building materials with a regular and random structure are considered in [20–22].

In the context of the current literature on unsteady pressureless filtration flow, it is important to highlight St. Petersburg Polytechnic university contribution to the study of the impact of unsteady flow conditions on filtration processes in porous media. The scientific group of M.R. Petrichenko proceeded both theoretical studies [28–29], in which Crocco equation is employed to describe filtration, and experimental [27, 30–31], where filtration process was modelled with special experimental rig and also some numerical work was proceeded.

In many engineering filtration problems, it is required to determine the instantaneous characteristics of filtration flows [15–18], which leads to the need to study unsteady motion modes. For example, the instantaneous positions of the depression curve and the height of the seepage interval characterize the drain efficiency of the construction pit and the dimensions of the sheet pile wall fixing the slope. The instantaneous positions of the depression curve in the body of the earth cofferdam must be considered when the water level changes in the pools.

The unsteady mode of the filtration flow interaction with a porous medium affects the strength and stability of soil hydraulic structures. Thus, the location of the depression curve determines the boundary of the area occupied by saturated and unsaturated media, thereby determining the area suitable for construction work. The exit of the depression curve to the tailwater slope is accompanied by the formation of a seepage gap. The value of the seepage interval must be considered to prevent frost heaving of the alluvial soil and failure of the slope. At the same time, the problems of fluid filtration in porous media are distinguished by a variety of boundary conditions for the desired complex filtration potential, geometric and physical characteristics of the filtration flow.

Solving such problems by analytical methods becomes significantly more complicated due to the nonlinearity of the equation describing the filtration movement, the presence of a free surface and the geometry of the slopes of the structure.

An alternative to their solution is the use of numerical methods for estimating unsteady free-flow filtration flows.

This research is dedicated to developing a hydrodynamic analysis approach of the process of unsteady filtration by the methods of computational fluid dynamics on the example of a rectangular cofferdam of various configurations to apply the results in the design of hydraulic structures. So, this cofferdam is a research object and the depression curve in this cofferdam that obtained through filtration is the research subject. To achieve the aims of the research, the following tasks were formulated and solved:

- The simulation of the problem of establishing a flow in a rectangular cofferdam was performed using the PLAXIS and ANSYS software packages FLUENT.
- Verification of the obtained numerical solutions by comparing them with experimentally based analytical solutions.
- A study of the efficiency of the cofferdam in the presence of drain was carried out and the characteristic features of the transient process for one of the selected solutions were described.

2. Methods

With non-pressure fluid filtration through the body of a hydraulic structure (dam), caused by the difference in the hydrostatic pressure of the fluid on opposite walls of the dam, the area of fluid movement is limited from above by a free surface, called the depression surface, at each point of which a constant pressure act. The section of the surface of the depression along the movement of fluid through the body of the structure is a depression curve. In the works of [23–26], it is shown that the exit of the free surface to the wall of the structure is carried out not at the level of the tailwater, but above. The resulting gap between the outlet of the depression curve and the tailwater is the seepage surface.

The filtration calculation scheme (Figure 1) assumes a non-stationary nature of filtration in a porous medium. Stationary filtration modes are treated as limiting (for "large" times) states of the filtration flow. The starting identity is the continuity condition for unsteady motion: $\partial h / \partial t + \partial q / \partial x = 0$, moreover, due to the

Dupuis condition $q = -kh \frac{\partial h}{\partial x}$, where k is the filtration coefficient. Then to distribute $h(t, x)$ the Boussinesq equation is achieved:

$$m \frac{\partial h}{\partial t} = \frac{\partial}{\partial x} \left(kh \frac{\partial h}{\partial x} \right), \quad (2)$$

where t is time, x is coordinate, $h = h(t, x)$ is seepage flow depth, $h_e \leq h_0 < h \leq H$, m is porosity coefficient, $0 < m < 1$.

The change of variables $t' := \frac{kt}{mH} > 0$, $x' = \frac{x}{H}$, $0 < x' < \lambda := l/H$, $\lambda \leq \Lambda := L/H$, $u := h/H$, $u_0 < u < 1$, $u_0 = h_0/H$, brings the Boussinesq equation to a dimensionless form:

$$\frac{\partial u}{\partial t'} = \frac{\partial}{\partial x'} \left(u \frac{\partial u}{\partial x'} \right), \quad (3)$$

The solution of the Boussinesq equation for unsteady flows is associated with significant difficulties and requires the search for approaches to its solution, one of which is the use of numerical simulation.

The problem of establishing a filtration flow in a vertical plane in a rectangular cofferdam is considered. For setting the tasks variants, a linear drain is used, located on the lower face of the cofferdam. The distance from the tailwater to the beginning of the drain varies ($l_0 = 0H, 1H, 4.5H, 8H$). The length of the drain is H . The problem is formulated in a dimensionless setting (Figure 1), the height of the cofferdam is H , equal to 1 meter, is chosen as the length scale. The time scale is introduced – $\tau = kt/mH$.

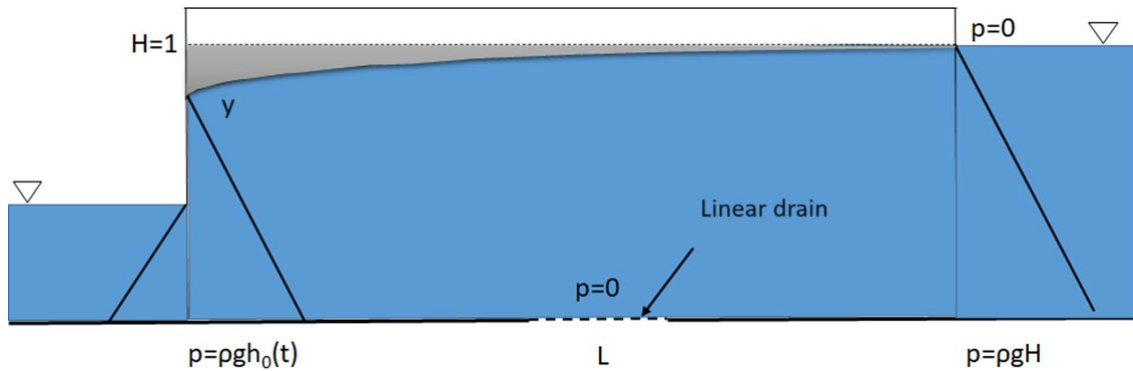


Figure 1 Statement of the problem.

3. Results and Discussions

3.1. Conditions for modeling the non-pressure filtration process

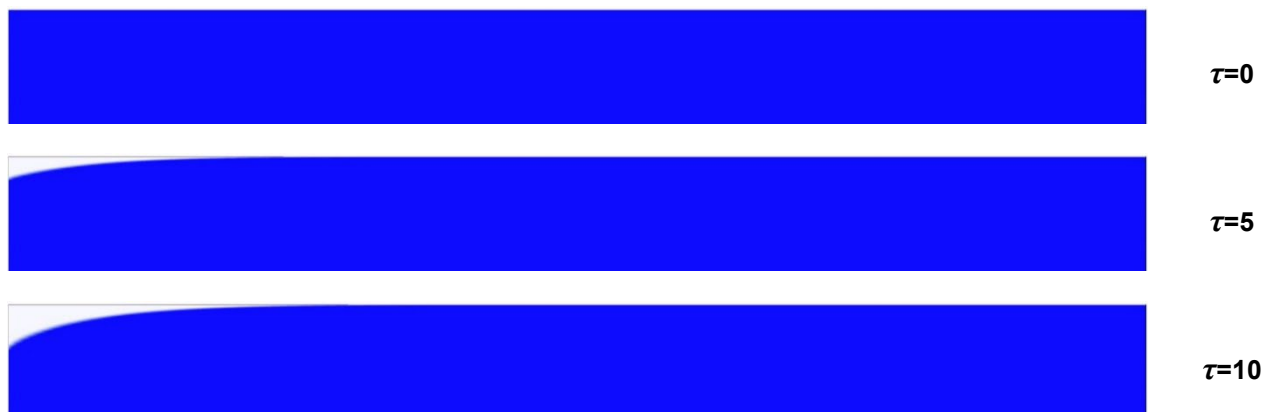
A constant hydrostatic pressure and a free boundary condition is set on the tailpipe, where the pressure is extrapolated from within the computational domain. On the lower boundary of the computational domain, except for the drain area, the no-slip condition is set. At the lower boundary in the drain area and at the upper boundary, a constant overpressure $p = 0$ is set.

The convergence criterion for the class of problems under consideration is the constancy of the flow rate through the tailwater and drain; for a numerical experiment, the problem can be considered converged if, at the next time step, the flow rate has changed by less than 0.5% relative to the previous one, as well as the position of the depression curve, which does not change over time.

To solve the filtration problem, a two-dimensional finite-volume method was used. Non-stationary Navier-Stokes equations are solved numerically together with the Volume of Fluid method for tracking the position of the interface between media. Since the velocity of the liquid during filtration is small, it is considered that filtration is laminar. The cofferdam is modeled by a porous body with constant isotropic resistance (porosity is 0.2, absolute permeability – 10^{-6} m^2). For each geometry of the cofferdam, a structured finite-volume mesh with sizes from 3,000 to 7,000 elements was constructed. The problem was solved with a time step of 0.1 s. Water with a density of 998.2 kg/m^3 and a viscosity of $1.003 \cdot 10^{-3} \text{ Pa}\cdot\text{s}$ and air with a density of 1.22 kg/m^3 and a viscosity of $1.7 \cdot 10^{-5} \text{ Pa}\cdot\text{s}$ were employed as working fluids. At the interface in the VOF model, a surface tension of 0.072 N/m is established.

3.2. Numerical simulation of filtration flow in a rectangular cofferdam in the ANSYS software package FLUENT: Data verification

The calculation of a rectangular cofferdam was performed without drain at a ratio L/H equal to 10. Since the fields of quantities at any time can be obtained as a result of the solution, the field of the liquid volume fraction was reduced during its evolution in time, Figure 2. The position of the interface zone, where the volume fraction is 50%, is essentially the depression curve. The flow pattern changes most actively in the period from $\tau = 0$ to $\tau = 50$, then from $\tau = 50$ to $\tau = 200$, where the flow pattern changes slightly, however the depression curve still changes its shape, Figure 3. The flow after $\tau = 200$ is considered to be steady.



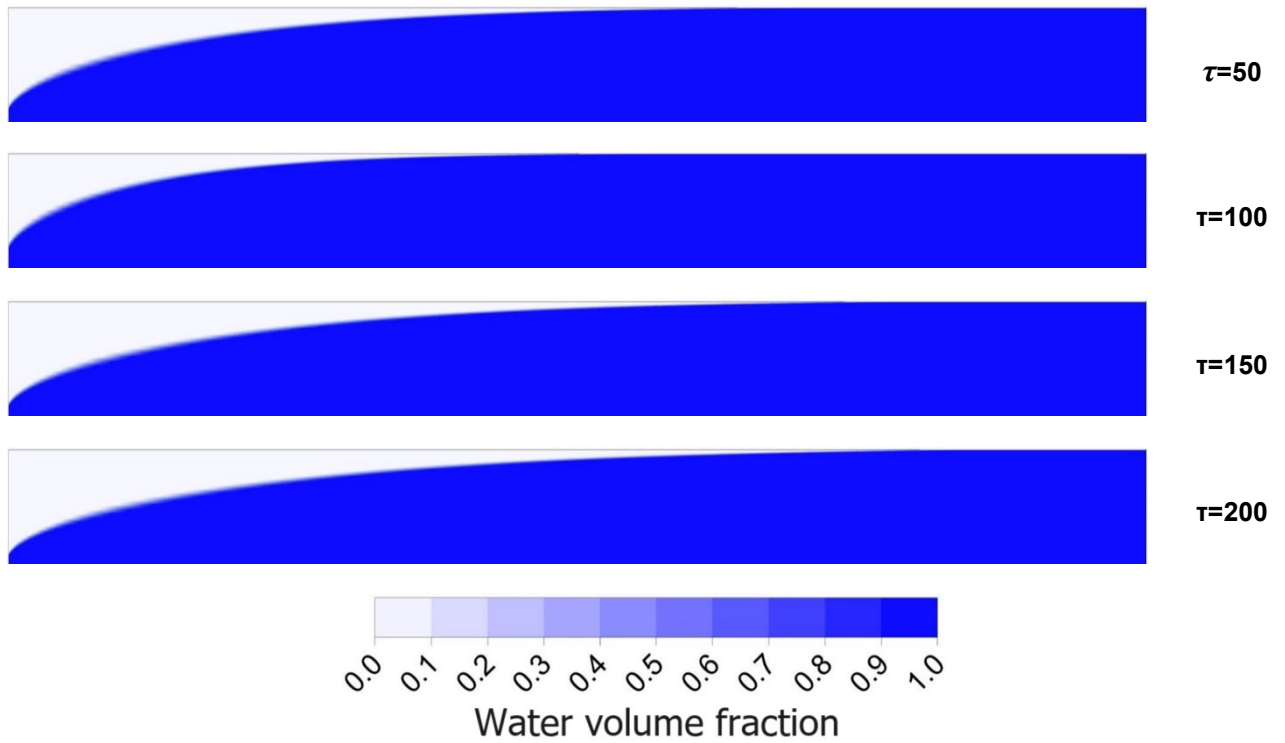


Figure 2. Volumetric concentration of liquid in the calculation area at different moments of the given time for setting without drainage.

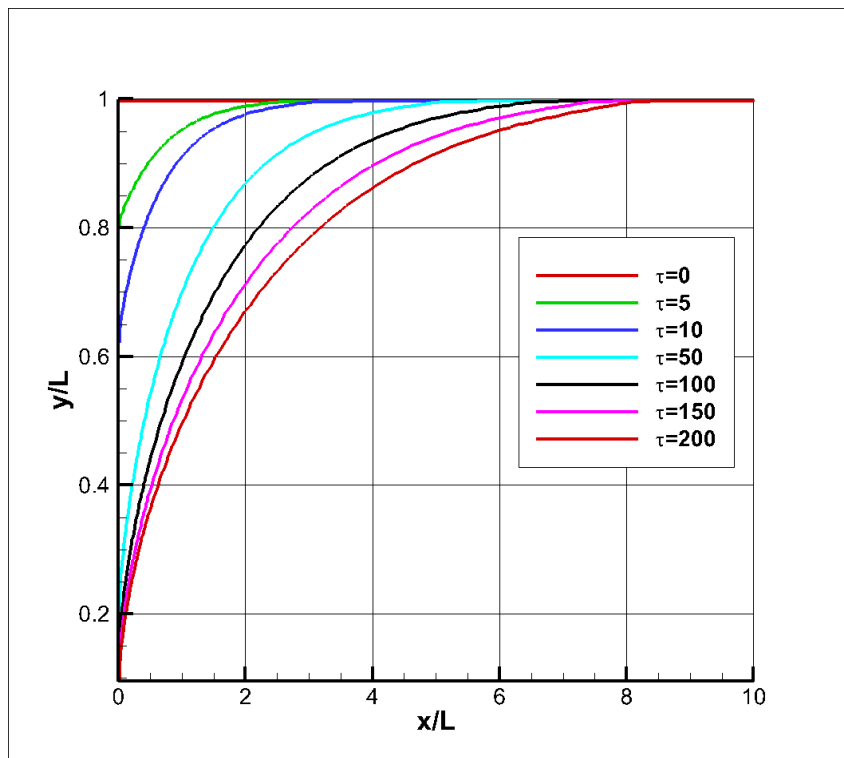


Figure 1 Depression curves at different time points.

An important characteristic of the transient seepage process is the tailwater flow. In the case of calculations in the ANSYS software package, it is possible to compare the results with experimental data and, thus, verify the calculation model. The flow rate is reduced to a dimensional form for ease of comparison with the results of experimental research carried out by D.D. Zaborova [27] as shown in Figure 4. The flow mismatch at the initial moment of time is due to a sharp increase in the flow rate in the calculation, the flow rate increases from 0 to some unsteady level. The observed flow peak is due to the possibility of instantaneous "opening" of the damper in the calculation, which is difficult to achieve on an experimental stand. In general, the consumptions rate at $t/t_{set} > 0.3$ differ by 5% or less, which indicates a

good agreement between the calculation model and experimental results. Based on the gained results, the ANSYS non-stationary computational model has been verified experimentally.

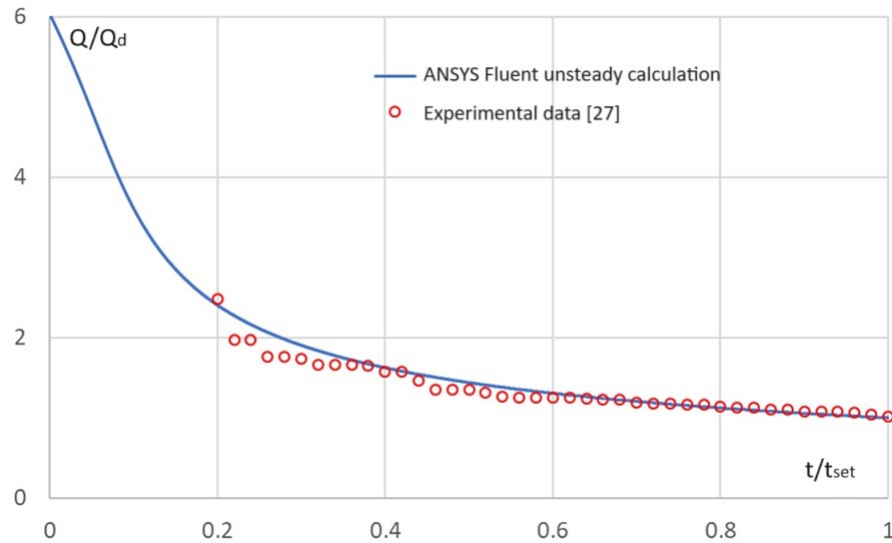


Figure 4. Comparison of reduced discharges across the tailwater.

3.3. Numerical simulation of filtration flow in a rectangular cofferdam in the PLAXIS 2D software package

Similar calculations of rectangular lintels in an identical formulation were performed by the PLAXIS 2D software package.

The calculations were carried out for lintels with linear dimensions $L/H=0.2, 0.4, 0.6, 0.8, 1.5, 2$. The results were obtained on computational grids that ensure the convergence of the solution. Figure 5 shows the volumetric concentration fields of liquid in the cofferdams with a linear size $L/H=0.2, 0.8, 1.5$ after the establishment of the filtration flow.

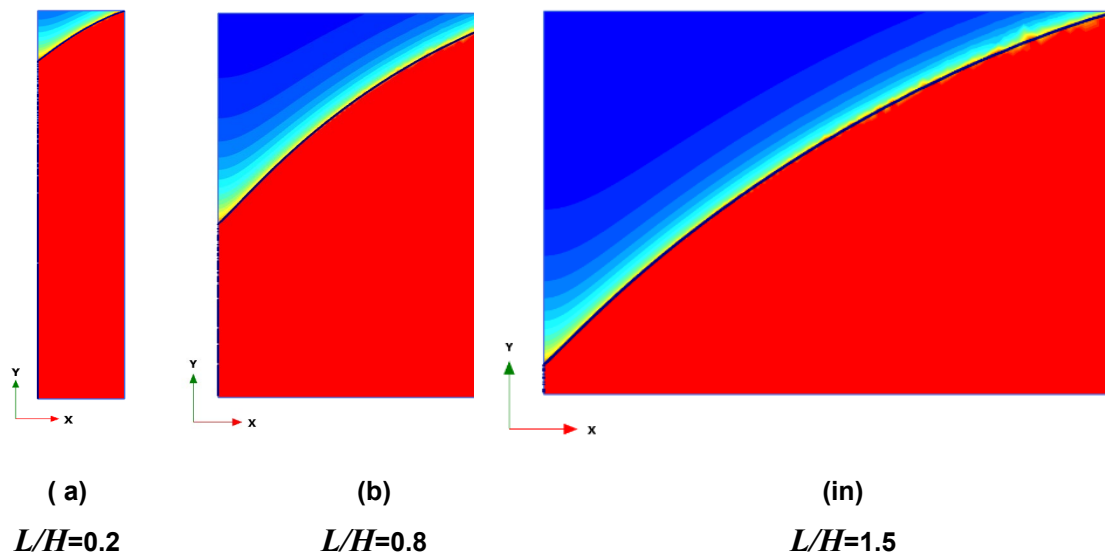


Figure 5. The volumetric concentration field of liquid in the cofferdams of various lengths after the establishment of the filtration flow.

Since it is impossible to compare the instantaneous positions of the drawdown curves due to the difference in the applied approaches to the solution implemented in the considered software packages, the comparison of the drawdown curves was carried out after the establishment of the filtration flow. Figure 6 shows the values of seepage gaps depending on the longitudinal size of the cofferdam, obtained analytically and numerically.

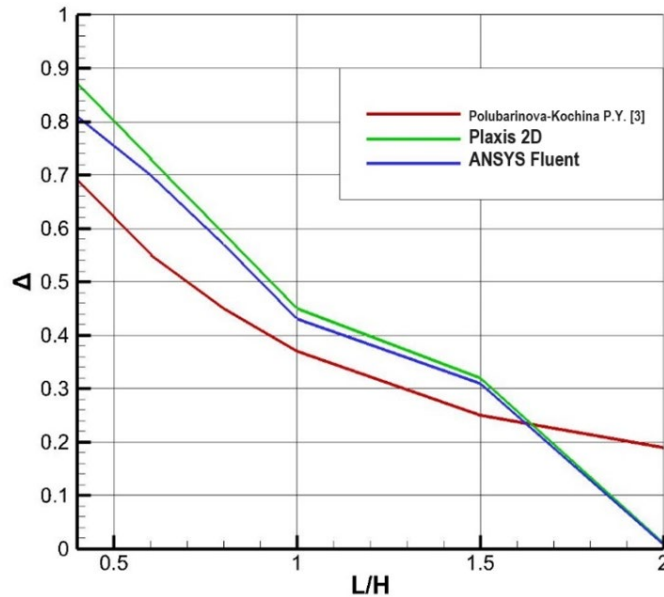


Figure 6. A comparison of the seepage intervals values obtained analytically and numerically.

The seepage intervals obtained using the ANSYS and PLAXIS 2D software packages practically coincide. The mismatch is observed for the cofferdams of $L/H \leq 1$. Seepage gaps obtained according to the theory of P.Y. Polubarinova-Kochina [3] are significantly smaller for lintels with $L/H \leq 1.7$ in relation to the solutions obtained using numerical analysis. For cofferdams with $L/H \geq 1.7$ analytical solution overestimates the value of the seepage interval.

3.4. Time evolution of the depression curve for the problem with drain

A similar problem to the solved task 1, however with the presence of drain, is considered. The problem without drain is referred to by the number "1", while the problem with drain is referred to by " l_0 " and indicated at $l_0 = 0 - 2$, at $l_0 = 1 - 3$, at $l_0 = 4.5 - 4$, and at $l_0 = 8 - 5$. To track the evolution of depression curves, a comparison between the tasks of tasks 1–5 were carried out as shown in Figure 7.

In the absence of drain or its location near the tailwater (tasks 1–3), the shape of the steady depression curves between the drain (if any) and the upstream is identical. However, the depression curves at the initial moments of time (up to $\tau = 10$ inclusive) have the greatest difference in shape and characterize the structure of the filtration flow. For tasks 2 and 3, a soft slope "descent" of the depression curve (than in task 1) is observed in the drain area at this time stage.

For the formulated problems 3–5, after $\tau = 50$ the depression curve is divided into two sections, the gap is located at the site of drain, the maximum of the left part of the depression curves is located exactly between the drain and the tailwater, and the left part of the depression curve itself is symmetrical. At the same time, the liquid remains between the runoff and the tailwater remain even in problem 3.

In the case of tasks 4 and 5, at the initial moments of time (up to $\tau = 10$ inclusive), the depression curve, on the contrary, has a steeper "descent" in the drain area. The position of the lower point of the depression curve for tasks 4 and 5 coincides. It should be noted that in the case of problem 5, due to the extremely small distance between the upstream and the runoff, the depression curve on the right side is established faster than on the left.

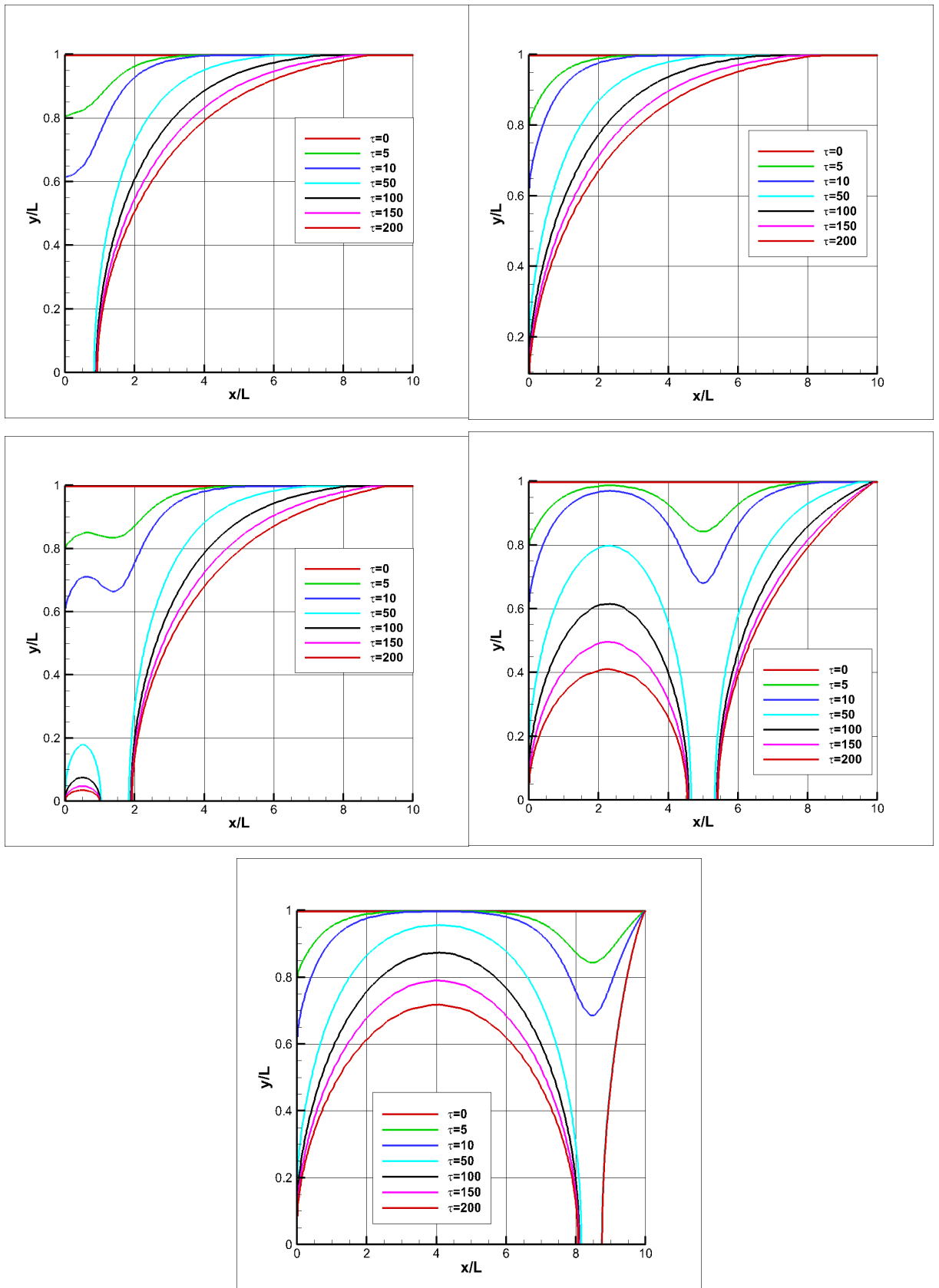


Figure 7. Evolution of depression curves for tasks 1-5 (numbering from left to right, top to bottom).

3.5. Study of the work of a cofferdam with drain depending on its position

For a more visual demonstration of the operation of the drain from its position, a comparison was made of the steady depression curves for tasks 1–5 as shown in Figure 8. The shape of the left side of the curve for tasks 3–5 is identical, the shape of the right side of the curve is also identical for tasks 1–5. The

left parts of the curves are similar to each other and can be obtained from each other by scaling along the X and Y axes, while the right parts of the curves are also similar but can be obtained from each other by scaling along the X axis.

According to the obtained depression curves, it can be concluded that it is rational to place the drain one caliber away to the right of the tailwater to accelerate the drain of saturated masses in a rectangular cofferdam of a fixed height. This approach allows to drain a larger volume of the porous body to the tailwater slope.

The introduction of linear drain at some distance to the right of the tailwater is equivalent to reducing the length of the cofferdam under consideration by the value of this distance, however, the time for the complete establishment of such a problem will be slightly longer, since in the interval from the tailwater to the location of the drain, a hilly area saturated with liquid is formed, the drain of which occurs exclusively due to the forces of gravity.

The result obtained is of significant practical importance, since if linear drain is located close to the upstream, a reservoir with a depth of about $0.3H$ and a width of $9H$ can be drained in a time equal to the time of setting the problem without drain.

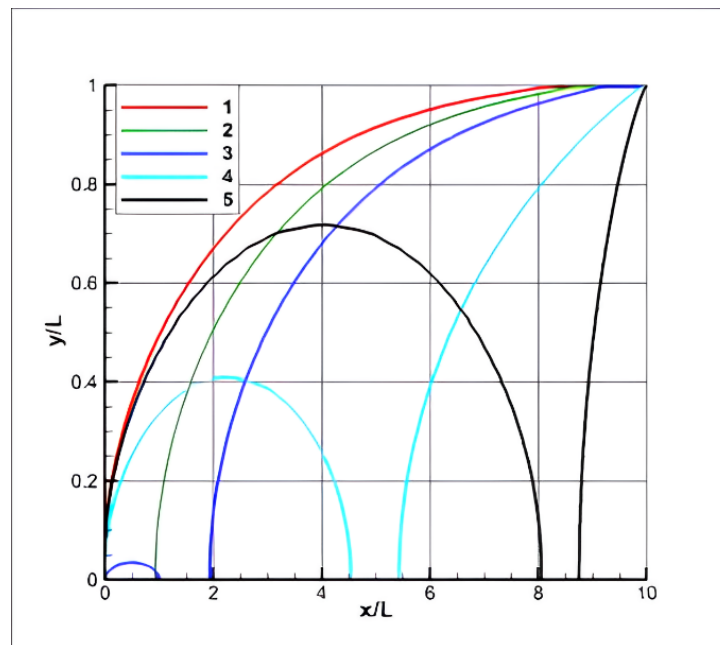


Figure 8. Steady-state depression curves for tasks 1–5.

The efficiency of drain is an essential practical task in the researched area. To evaluate the effectiveness, the given consumptions rates for tasks 2–5 are compared as shown in Figure 9.

The discharge through the drain is significantly higher than the discharge through the tailwater for all considered problems. When the drain is removed from the tailwater, the flow through it increases. This is justified by the fact that the size of the hilly area saturated with liquid increases, the liquid filtration in this area occurs solely due to the action of gravity. At the same time, at the initial stage, the configuration from task 3 is the most effective, in this case, both drain and tailwater show the largest reduced flow rate in the time interval from 0 to $0.2 t/t$ set. For tasks 2 and 3, almost the entire flow rate, when the current is established, goes through the drain; in the case of tasks 4 and 5, a small part of the flow goes through the tailwater.

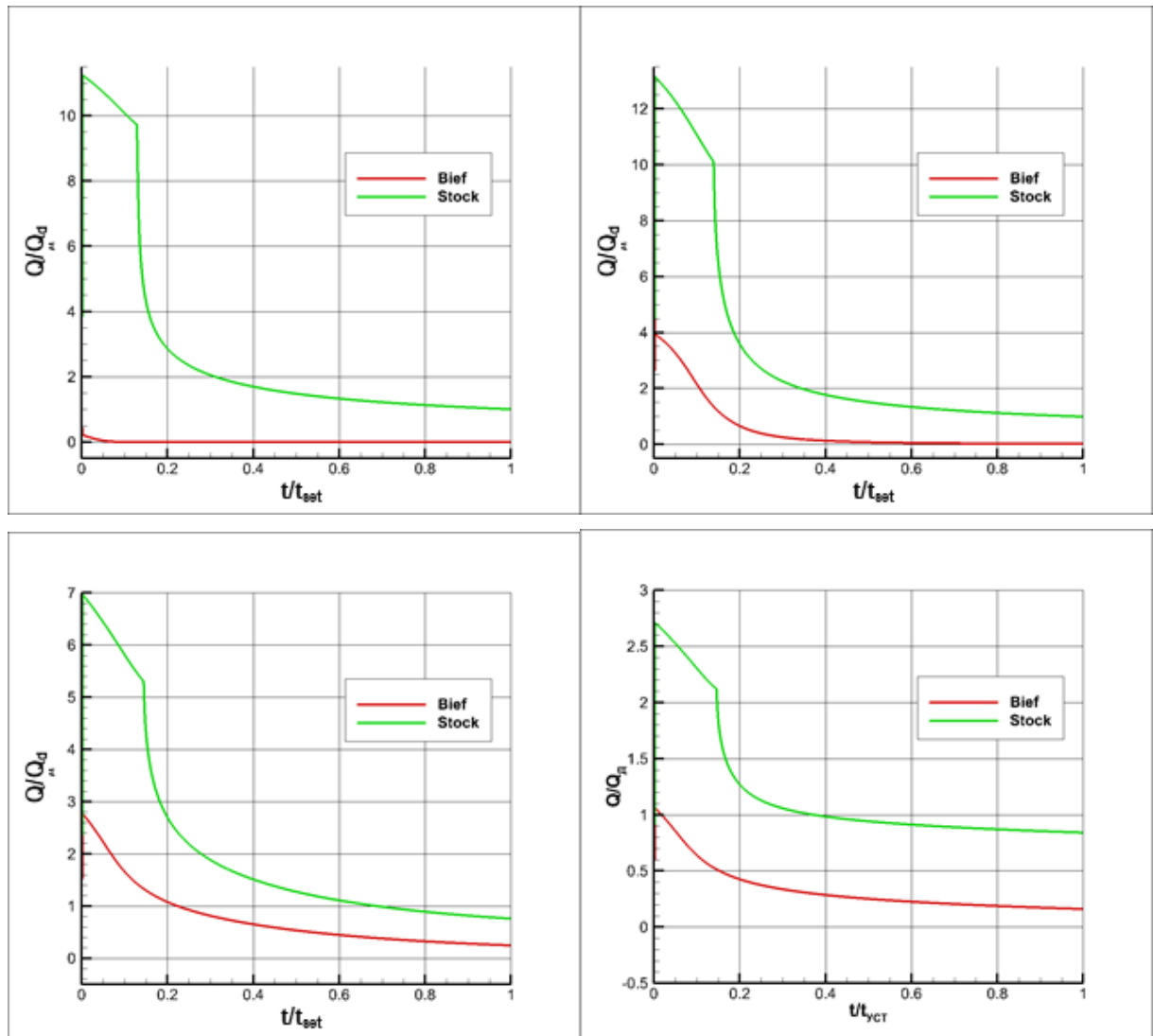


Figure 9. Comparison of the given consumption rates for tasks 2-5 (numbering from left to right, top to bottom).

4. Conclusion

According to the analysis of experimentally verified proposed numerical models of an unsteady free-flow filtration in a rectangular cofferdam using the ANSYS FLUENT and PLAXIS 2D software packages, the following are concluded:

1. Numerical modeling of an unsteady free-flow filtration flow in a rectangular cofferdam using ANSYS software packages FLUENT and PLAXIS 2D allows obtaining instantaneous values of the coordinates of the depression curve and instantaneous values of the seepage interval. The proposed models are consistent with the theoretical solutions.
2. A verification of the proposed models was carried out through a comparison of the gained results using the numerical developed model built in ANSYS FLUENT with the existing experimental data in the literature. It was found that the numerical gained results show a good consistency with the existing in the literature experimental results, thereby, the proposed models were verified.
3. With the help of the verified models, the filtration patterns in rectangular dams with different drain positions were obtained. It was found that, in the case of a sufficient removal of the drain from the tailwater, the established drawdown curve will be divided into two parts by the drain.
4. According to the criterion of the reduced flow rate, the most effective is a cofferdam with drain removed from the tailwater by one height of the cofferdam.

The obtained results can be applied in the design of hydrotechnical construction objects.

References

1. Pavlovskiy, N.N. Sobraniye sochineniy: T.1: Osnovy gidravliki. Otkrytyye rusla i sopryazheniye byefov sooruzheniy [Collected works. Vol. I. Fundamentals of hydraulics. Open channels and connection of tailwaters of structures]. Moscow: Izd-vo AN SSSR, 1955. 547 p.; T.2: Dvizheniye gruntovykh vod. Moscow: Izd-vo AN SSSR, 1956. 771 p. (rus)
2. Barenblatt, G.I., Yentov, V.M., Ryzhik, V.M. Dvizheniye zhidkostey i gazov v prirodnykh plastakh [Movement of liquids and gases in natural formations]. Moscow: Nedra, 1984. 211 p. (rus)
3. Polubarinova-Kochina, P.Y. Teoriya dvizheniya gruntovykh vod [Theory of groundwater movement]. Moscow: Gosudarstvennoye izdatelstvo tekhniko-teoreticheskoy literatury, 1952. 677 p. (rus)
4. Polubarinova-Kochina, P.Y. Razvitiye issledovaniy po teorii filtratsii v SSSR (1917—1967) [Development of research on the theory of filtration in the USSR (1917-1967)]. Moscow: Nauka, 1969. 545 p. (rus)
5. Polubarinova-Kochina, P.Y. Nekotoryye zadachi ploskogo dvizheniya gruntovykh vod [Some problems of plane movement of groundwater]. Moscow - Leningrad: Izd-vo AN SSSR, 1942. 142 p. (rus)
6. Pykhachev, G.B., Isayev, R.G. Podzemnaya gidravlika [Underground hydraulics]. Moscow: Nedra, 1973. 359 p. (rus)
7. Coulaud, O., Morel, P., Caltagirone, J. Effects non-lineaires les ecoulements en milieu poreux. C. R. Acad. Sci. Paris. 1986. Ser. II. 6. Pp. 263–266.
8. Andersen, O.H., Burcharth, H.F. On the One-Dimensional Steady and Unsteady Porous Flow Equation. Coastal Engineering. 1995. 24. Pp. 233–257.
9. Rojas, S., Koplik, J. Nonlinear flow in porous media. Physical review. 1998. 58(4). Pp. 4776–4782.
10. Bakhtiarain, A.H., Shokri, M., Razmara, M. A Review on Non-Linear Unsteady One Dimensional Flow through Coarse Porous Media. 6thSASTech. Malaysia, Kuala Lumpur, 2012. P.10
11. Miyan, M. The Fluid Flow Motion through Porous Media for Slightly Compressible Materials. International Journal of Pure and Applied Researches. 2016. 3(1). Pp. 28–35.
12. Zeng, Z., Grigg, R. A Criterion for Non-Darcy Flow in Porous Media. Transport in Porous Media. 2006. 63. Pp. 57–69.
13. Abutaliyev, F.B., Baklushin, M.B., Yerbekov, Ya.S., Umarov, U.U. Effektivnyye priblizhenno-analiticheskiye metody dlya resheniya zadach teorii filtratsii [Effective approximate analytical methods for solving problems in filtration theory]. Tashkent: Fan, 1978. 244 p. (rus)
14. Gladkiy, A.V., Lyashko, I.I., Mistetskiy, G.Ye. Algoritmizatsiya i chislennyi raschet filtratsionnykh skhem [Algorithmization and numerical calculation of filtration schemes]. Kiyev: Vishcha shkola, 1981. 287 p. (rus)
15. Kurtseva, K.P., Lapin, A.V., Sheshukov, Ye.G. Resheniye setochnymi metodami zadachi filtratsii zhidkosti v plotine pri nelineynom zakone filtratsii [Solution by grid methods of the problem of fluid filtration in a dam with a nonlinear filtration law]. Izv. vuzov. Matematika. 1999. 2. Pp. 47–52. (rus)
16. Bereslavskiy, E.N., Dudina, L.M. Zadacha filtratsii v pryamougolnoy peremychke s chastichno neproniysayemoy vertikalnoy stenкой [Filtration problem in a rectangular lintel with a partially impermeable vertical wall]. Vestnik SPbGU. Matematika. Mekhanika. Astronomiya. 2019. 6(64). 2. Pp. 288–297. DOI: 10.21638/11701/spbu01.2019.211 (rus)
17. Vlasyuk, A.P., Martynyuk, P.N. Kontaktnyy razmyv i filtratsionnaya konsolidatsiya gruntov v usloviyakh teplo-soleperenosy [Contact erosion and filtration consolidation of soils under conditions of heat and salt transfer]. Matem. Modelirovanie. 2012. 24(11). Pp. 97–112. (rus)
18. Kurtseva, K.P., Sheshukov, E.G., Yakimov, N.D. Zadacha beznapornoy filtratsii cherez gruntovuyu plotinu pri nalichii neproniysayemogo vklucheniya [The problem of gravity filtration through a soil dam in the presence of an impermeable inclusion]. Problemy energetiki. 2016. 11–12. Pp. 68–76. (rus)
19. Bereslavskiy, E.N. O primenenii metoda P.Y. Polubarinovoy- Kochinoy v teorii filtratsii [About the application of the method of P.I. Polubarinova-Kochina in the theory of filtration]. Zhurnal vychislitelnoy i prikladnoy matematiki. 2013. 1(111). Pp. 12–18. (rus)
20. Pavlovskaya, G.E., Meersmann, T., Jin, C., Rigby, S.P. Fluid flow in a porous medium with transverse permeability discontinuity. Physical review fluids. 2018. 3. 044102. DOI: 10.1103/PhysRevFluids.3.044102
21. Saeedmonir, S., Khoei, A.R. Multiscale modeling of coupled thermo-hydro-mechanical analysis of heterogeneous porous media. Computer Methods in Applied Mechanics and Engineering. 2022. 391. 114518. DOI: 10.1016/j.cma.2021.114518
22. Termuhlen, R., Fitzmaurice, K., Yu, H.-C. Smoothed boundary method for simulating incompressible flow in complex geometries. Computer Methods in Applied Mechanics and Engineering. 2022. 399. 115312. DOI: 10.1016/j.cma.2022.115312
23. Muskat, M. Seepage of water through dams with vertical Faces. Journal of General and Applied Physics. 1935. 6. Pp. 402–415.
24. Anakhayev, K.N. Raschet filtratsii cherez peremychku na neproniysayemom osnovanii [Calculation of filtration through a jumper on an impermeable base]. Izvestiya vysshikh uchebnykh zavedeniy. Stroitelstvo i arkhitektura. 1990. 7. Pp. 78–82. (rus)
25. Anakhayev, K.N. O filtratsionnom raschete peremychki [About the filtration calculation of the lintel]. Matematicheskoye modelirovaniye. 2011. 23(2). Pp. 148–158. (rus)
26. Anakhayev, K.N. O razvitii analiticheskikh metodov rascheta filtratsii [On the development of analytical methods for calculating filtration]. Prirodoobustroystvo. 2014. 1. Pp. 72–75.
27. Zaborova, D., Musorina, T., Petritchenko, M. Non-stationary filtration through a homogeneous rectangular closing dike. Proceedings of the IOP Conference Series: Materials Science and Engineering. 2020. 883(1). 012043. DOI: 10.1088/1757-899X/883/1/012043
28. Petrichenko, M. R. Typical and atypical boundary problems for the Crocco equation. St. Petersburg Polytechnic University Journal. Physics and Mathematics. 2014. 26(4). Pp. 122–128.
29. Petrichenko, M.R., Kharkov, N.S. Boundary problems for the Crocco equation in the transport theory. St. Petersburg Polytechnic University Journal. Physics and Mathematics. 2014. 25(3). Pp. 47–56.
30. Zaborova, D.D., Petritchenko, M.R., Musorina, T.A. The Dupuis paradox and mathematical simulation of unsteady filtration in a homogeneous closing dike, St. Petersburg Polytechnical State University Journal. Physics and Mathematics. 2018. 11(2). Pp. 50–58.
31. Zaborova, D.D., Loktionova, E.A., Musorina, T.A. Free Surface Boundary Modeling in a Rectangular Homogeneous Earth-Filled Cofferdam. Power Technology and Engineering. 2023. 57. Pp. 85–89. DOI: 10.1007/s10749-023-01626-5

Information about authors:

Vitaly Sergeev, Doctor of Technical Sciences

E-mail: sergeev_vitaly@mail.ru

Evgeny Kotov, PhD

E-mail: ekotov.cfd@gmail.com

Svyatoslav Horobrov, PhD

E-mail: horobrov_sv@spbstu.ru

Mohanad Sabri, PhD

ORCID: <https://orcid.org/0000-0003-3154-8207>

E-mail: mohanad.m.sabri@gmail.com

Darya Nemova, PhD in Technical Sciences

ORCID: <https://orcid.org/0000-0003-2673-4566>

E-mail: nemova_dv@spbstu.ru

Received 01.10.2022. Approved after reviewing 29.12.2022. Accepted 30.12.2022.



Research article

UDC 665.775.4

DOI: 10.34910/MCE.124.13



Increasing the level of aging stability of bitumes modified by kaolinite

P.E. Bulanov , E.A. Vdovin , V.F. Stroganov 

Kazan State University of Architecture and Engineering, Kazan, Russian Federation

✉ pavel.bulanov1991@yandex.ru

Keywords: bitumen, kaolinite, aging, modification, clay mineral

Abstract. During the literature review analysis, the main causes of bitumen binders aging were identified and the kaolinite modifier was proposed that have increased the bitumen aging resistance. The physical and mechanical properties of bitumen modified by kaolinite for the following indicators were studied: penetration at 25 °C, softening point, ductility at 0 °C, Fraas brittle point, dynamic viscosity at 105 °C, 135 °C and 165 °C. The bituminous binder aging was simulated in an RTFOT oven. The aging quality was determined by the softening point change, after aging in the RTFOT oven. The possibility of short-term aging reducing of modified bitumen at a kaolinite content of 2 % to 8 % by 12.5–28.6 % has been established. The characteristic peaks of bituminous binder aging: 1738, 1640, 1654, 1217, 1033 cm^{-1} were revealed by the IR spectroscopy method. It was established that the kaolinite introduction into bitumen has caused a significant decrease of aging processes, which has confirmed by the IR spectroscopy data: the peaks at 1640, 1564 and 1217 cm^{-1} almost completely have disappeared in the difference spectrum, and the intensity of carbonyl absorption band at 1738 cm^{-1} has decreased. The obtained experimental data confirmed the similarity of the processes described in previously published studies of other authors and the continuing research prospects in the direction of increasing the bitumen binders aging resistance at searching for new modifiers types and determining them optimal quantities.

Citation: Bulanov, P.E., Vdovin, E.A., Stroganov, V.F. Increasing the level of aging stability of bitumes modified by kaolinite. Magazine of Civil Engineering. 2023. Article no. 12413. DOI: 10.34910/MCE.124.13

1. Introduction

Asphalt concrete consists of various types of coarse-grained and fine-grained aggregates, connected by bitumen. In asphalt mix the bitumen makes up only 3.5–7 % by weight or approximately 11–18 % by volume. The bitumen makes up only 3.5–7 % by weight or approximately 11–18 % by volume of asphalt concrete mixture and provides the significant effect on the road surfaces durability, exhibiting its elastic properties at negative ambient temperatures and viscous properties at high air temperatures [1, 2].

However, due to the constant increase of traffic intensity and axial loads on asphalt concrete pavements prepared from ordinary bitumen, various types of defects are formed: plastic rut, fatigue cracks, low-temperature cracking, wear, spalling, aging, etc. [3, 4].

Bitumen, being one of the main building materials in road construction, is exposed to air for a long time, solar radiation, wind, rain and vehicles [5, 6]. Road bitumen is the organic binder that constantly changes its properties, group and chemical composition as part of the road surface [7]. One of the main factors affecting the defects formation in asphalt concrete is the bitumen aging [8]. The bitumen aging is a complex process, the consequence of which is the rigidity increase and the fragility increase, both during the asphalt concrete mixtures (short-term aging) preparation and during the asphalt concrete (long-term

aging) operation. The aging process mainly involves material oxidation and manifests itself in physical changes such as volatile fractions loss or bitumen hardening [7, 9].

Bitumen aging results to increase its cohesive strength and softening temperature. In addition, oxygen-containing functional groups are formed (determined by IR spectroscopy) as a result of interaction with oxygen. There are changes in the four main bitumen fractions, namely, saturated and aromatic hydrocarbons, resins and asphaltenes, in the form of components transition from less to more polar fractions. Since the bitumen fractions have different reactivity during oxidation, the result is the decrease of naphthenic aromatic compounds content with a corresponding increase of asphaltenes proportion [10].

One of the main factors is thermal oxidative bitumen aging, which is an irreversible chemical reaction between bitumen and atmospheric oxygen [10]. Bitumen oxidation can occur during mixing with hot aggregates, during transport, laying and compaction of mixture. In addition, bitumen aging is possible when it was modified by polymers due to increased preparation temperature (more than 170 °C) and high shear rate for a long time (2–4 hours) [11, 12]. Slow oxidation processes occur during the entire service life in road pavements [13].

There are number of publications confirming the effectiveness of studies about bitumen modification by nanoparticles of titanium dioxide, copper, zinc, silicon, etc., as well as nanoparticles of clay minerals (kaolinite, montmorillonite, etc.) [14–16]. It has been established that these additives have improved the bitumen quality, including increasing the binder aging resistance [17–19]. It should be noted that the studies performed with these modifiers were considered on residual bitumen, and in Russia, oxidized bitumen was mainly used. These bitumens are obtained by oxidizing oil residues with atmospheric oxygen in various types of oxidizing reactors. Residual bitumen is mainly obtained by two technologies: with a sufficiently high vacuum of the oil distillation residue or by compounding oil residues [20]. There is the fundamental difference in the road bitumen quality produced by domestic oil refineries from bitumen produced abroad, where only oils of a certain group and chemical composition, in which there is practically no solid paraffin, are used as raw materials. The number of oils suitable for the residual bitumen production is limited in Russia. This explains the fact that almost the entire volume of consumed bitumen is produced by the oxidation of various oil residues [21].

In this regard, there are practically no studies on improving the bitumen aging resistance in Russia.

Studies [22, 23] describe the possibility of clay minerals using as modifiers. One of these minerals is kaolinite [19, 24, 25].

In this regard, the purpose of the work is to establish the degree of properties change and the possibility of aging resistance increasing of Russian bitumen modified by kaolinite.

To achieve this goal, the following tasks were solved:

- study the kaolinite influence on basic physical and mechanical properties of modified bitumen;
- study the effect of kaolinite on the change of softening temperature of modified bitumen after aging in the RTFOT furnace;
- study by IR spectroscopy the main absorption bands as a result of bitumen aging in the RTFOT furnace;
- establishment by the method of IR spectroscopy of the kaolinite influence on the modified bitumen aging resistance.

2. Materials and Methods

The study used bitumen grade BND 100/130 produced by Novokuibyshevsk Oil Refinery JSC in accordance with Russian State Standard GOST 33133-2014 (Table 1).

Kaolinite clay is produced in Samara region, LLC NPP Industrial Minerals. In accordance with Russian State Standard GOST 9169-75, according to mineral composition, it refers to kaolinite clay with a kaolinite mineral content up to 95 %.

The preparation of modified bitumens was carried out on a SILVERSON L5M laboratory mixer (Great Britain). The packing used was a standard high shear mixing head with square holes. Mixing of the modified bitumen was carried out in tin cans with a volume of 1 liter. An oil bath Memmert ONE 22 (Germany) was used to heat and maintain the required operating temperature during the preparation and ripening process. Silicone oil PMS-100 (LLC Penta Junior, Russia) was used as a heat carrier. A tin with a measured amount of bitumen was immersed in an oil bath (the coolant liquid did not reach the top of the tin by 2–3 cm).

The modified bitumen preparation was carried out as follows: a pre-weighed amount of bitumen in can was immersed in an oil bath. The bitumen was heated up to operating temperature of preparation –

160 °C. The mixer head was immersed in bitumen and a mixing speed of 2500 rpm was created. Kaolinite clay, previously dried to constant weight, was introduced at a rate of 5 g/min. After the introduction of additives, mixing was carried out for 10 minutes at a temperature of 160 °C and a rotation speed of 2500 rpm. It was previously established [19, 22, 23] that significant changes occurred in the range of 2–6% kaolinite content in bitumen. Taking these data into account, research estimates range from 2 to 8%.

Table 1. Physical and technical properties of bitumen grade BND 100/130.

Indicator name	Unit	Actual values	Requirements Russian State Standard GOST 33133-2014	Test Methods
2	3	4	5	6
Penetration at 25 °C	0.1 mm	107	101–130	Russian State Standard GOST 33136
Softening point	°C	46	not lower than 45	Russian State Standard GOST 33142
Ductility at 0 °C	cm	4.6	not less than 4.0	Russian State Standard GOST 33138
Softening point change after warming up	°C	5,6	No more than 7.0	Russian State Standard GOST 33140
Fraas brittle point	°C	-21	Not higher than -20	Russian State Standard GOST 33143
Flash point, not below	°C	293	230	Russian State Standard GOST 33141
Sample mass change after aging, %, no more	%	0.21	0.6	Russian State Standard GOST 33140

Modified bitumen tests were carried out in accordance to Russian State Standard GOST 33133-2014 requirements for the following indicators:

- Penetration at 25 °C. The test method consists in measuring the depth to which the penetrometer needle is immersed in the test bitumen sample under certain conditions (temperature, load and duration of load application), which is expressed in units corresponding to tenths of a millimeter (0.1 mm). The Lintel PN-20 penetrometer, produced by JSC Bashkir Special Design Bureau Neftekhimavtomatika, was used as a device.
- Softening point. The test method consists in determining the temperature at which bitumen, poured and cooled inside rings of given sizes, softens under test conditions and, moving under the weight of a steel ball, touches the bottom plate. As a device, an automatic apparatus for determining the softening temperature of petroleum bitumen Lintel KISH-20, manufactured by JSC Bashkir Special Design Bureau Neftekhimavtomatika, was used.
- Ductility at 0 °C. The method consists of stretching of bitumen sample at a constant rate, at a given temperature, to determine the maximum tensile force and bitumen extensibility. As a device, an automatic apparatus for determining the extensibility of oil bitumen Lintel DB-20-100, manufactured by JSC Bashkir Special Design Bureau Neftekhimavtomatika, was used.
- Fraas brittle point. The test method consists of cooling at a uniform rate and periodically bending the bitumen sample and determining the temperature at which cracks appear or the bitumen sample breaks. As a device, an automatic apparatus for determining the temperature of oil bitumen Lintel ATX-20, manufactured by JSC Bashkir Special Design Bureau Neftekhimavtomatika, was used.
- Sample weight change and softening point change after aging in the RTFOT oven. The method consists of exposing a moving thin film of bitumen to high temperature (163 °C) and air and determining the effect of this exposure on the bitumen by comparing the physical and chemical parameters of the bitumen obtained before and after exposure. Rolling thin-film B066N1 equipment (Matest, Italy) was used.
- Dynamic viscosity at 105 °C, 135 °C and 165 °C, respectively, according to Russian State Standard GOST 33137-2014. The test method is to measure the relative flow resistance caused by shearing bitumen by rotating configuration elements. Dynamic viscosity is calculated as the ratio between applied shear stress and shear rate. A Brookfield DV2T viscometer (Brookfield, USA) was used.

The IR spectroscopy method was used to identify functional groups, as well as to determine the effect of aging after the RTFOT oven. The registration and processing of IR spectra was carried out using a Miracle ATR for FT-IR Spectrometer ATR attachment (ZnSe crystal) in the region of 4000–650 cm^{-1} on a Perkin Elmer FT-IR Spectrometer model Spectrum 65 spectrophotometer under standard recording conditions and the supplied software.

3. Results and Discussion

It can be seen (Figure 1) that kaolinite introduction in an amount of 2–8% into bitumen, the softening point, Fraas brittle point, dynamic viscosity at 105 °C, 135 °C and 165 °C increased by 1.1–2.6 %, 9.5–28.6 %, 9.2–33.1 %, 6.9–24.1 %, 11.1–55.6 %, respectively. The following indicators decreased: penetration at 25 °C by 8.4–22.4 %; ductility at 0 °C by 4.3–15.2 %; sample weight change and softening point change after aging in the RTFOT oven by 12.5–28.6 %.

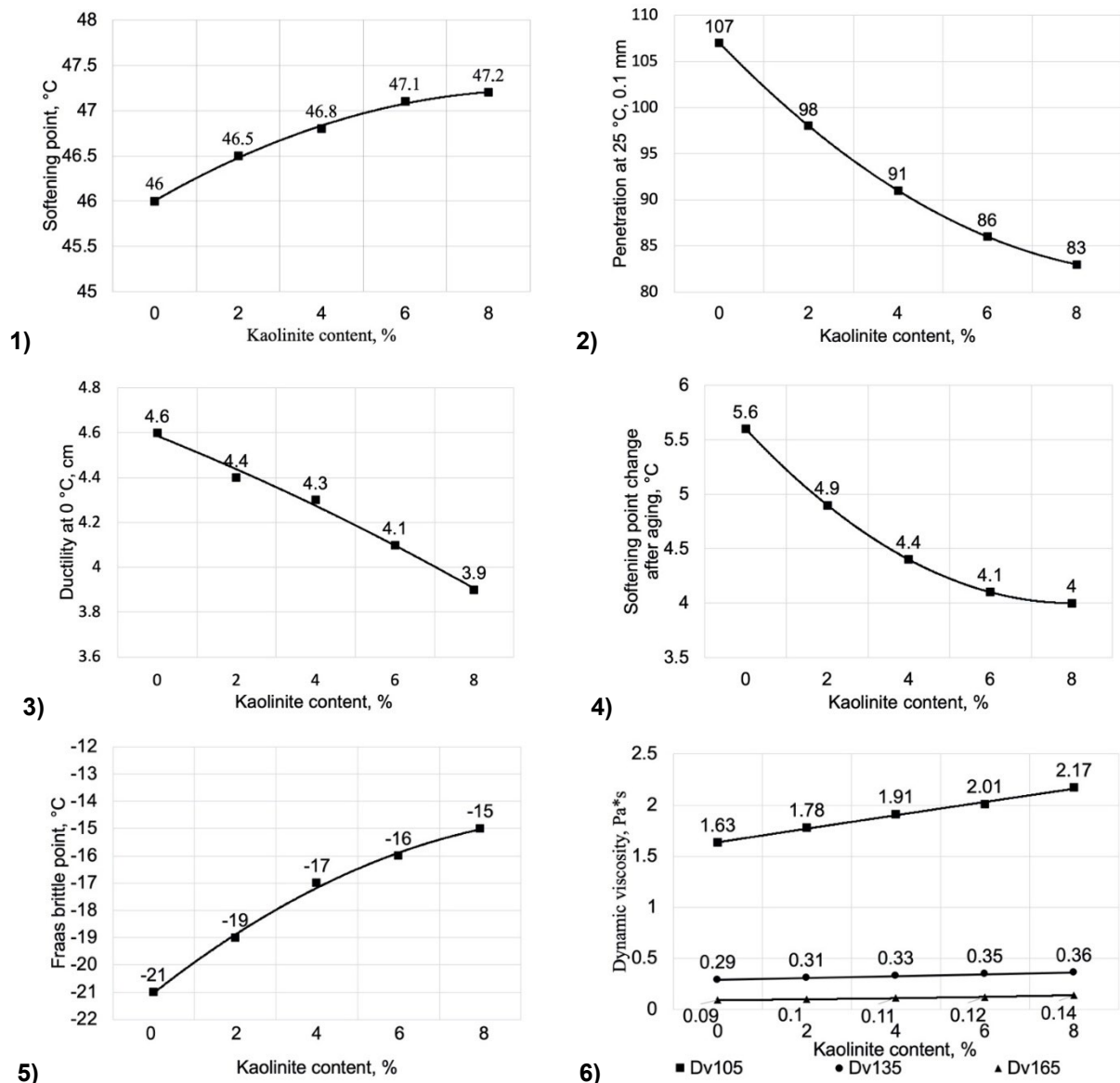


Figure 1. The dependence of bitumen physical and mechanical characteristics from the kaolinite content:

1 – softening point; 2 – penetration at 25 °C; 3 – ductility at 0 °C; 4 – softening point change after aging; 5 – Fraas brittle point; 6 – dynamic viscosity at 105 °C, 135 °C and 165 °C.

It should be noted that the effect increased with the increasing of kaolinite amount and it was observed in seven studied dependencies (Figure 1). The exception is the parameter that determines the softening temperature change after RTFOT oven aging. The effectiveness of the kaolinite influence on bitumen with a content of more than 6 % for the softening temperature change after RTFOT oven aging is sharply reduced.

In our opinion, the increase of dynamic viscosity and softening point, as well as a decrease of penetration at 25 °C and ductility at 0 °C, are possibly associated with the solid clay particles presence in bitumen, which cause less mobility of bitumen matrix and, consequently, higher flow resistance. In addition, the following assumption is interesting [26, 27]: due to the dual nature (polar and nonpolar), clay plates can be located at the interface between asphaltenes and maltenes, and aromatic compounds, due to their lower molecular weight, can intercalate between clay plates. Clay plates, partially exfoliating, can be distributed in aromatic compounds and resins, located mainly at the interface between them. In the intercalation process, the clay mineral plays the surfactant role, which provides and enhances the interaction between the asphaltene and maltenic phases. The consequence of this process is a decrease in asphaltene micelles size. As a result, the amount and mobility of the "free" aromatic fraction decreases. This, obviously, is the reason for the resulting increase of modified bitumen viscosity.

The established dependencies (Figure 1) show that the short-term aging reduction with the kaolinite introduction in amount from 2 % to 8 % into the bitumen composition was 12.5–28.6 %.

The given IR spectra of the original bitumen and bitumen after aging in the RTFOT furnace and their difference spectrum (Figures 2 and 3) allow us to judge the changes that occur after aging in the middle spectrum part with following peaks: 1738, 1640, 1654, 1217, 1033 cm^{-1} absent in the original bitumen. The band at 1738 cm^{-1} corresponds to stretching vibrations of C=O carbonyl groups formed during the thermal-oxidative degradation, and the 1217 cm^{-1} peak corresponds to C-O stretching vibrations, which are part of the ester groups. The 1033 cm^{-1} peak corresponds to S=O bonds of sulfoxide groups, which are also formed during aging. These newly formed groups intensity in the bitumen spectrum (after aging in the RTFOT furnace) is quite high, which indicates intensive processes of bitumen thermal degradation during aging in the RTFOT furnace.

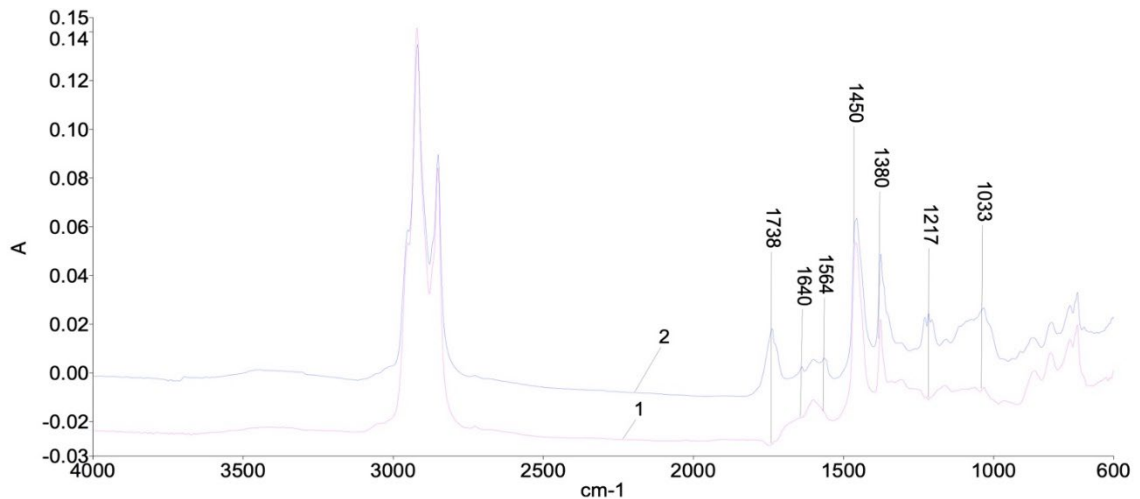


Figure 2. The original bitumen IR spectra and bitumen after aging in the RTFOT furnace: 1 – original bitumen; 2 – bitumen after aging in the RTFOT furnace.

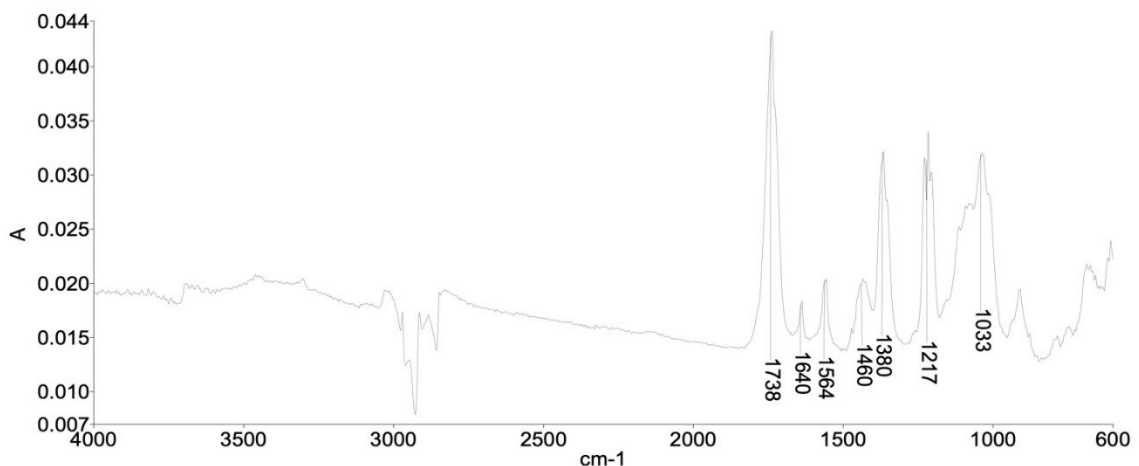


Figure 3. Difference IR spectrum of the original bitumen and bitumen after aging in the RTFOT furnace.

In the middle spectrum part the methylene CH_2 groups bending vibrations correspond to a peak at 1460 cm^{-1} , and to methyl CH_3 groups - a peak at 1380 cm^{-1} (Figure 3). In the middle spectrum part these vibrations are separated, while in the high-frequency part, at $2800\text{-}3000\text{ cm}^{-1}$ stretching vibrations, they are strongly superimposed.

Along with the fact that all the "aging" bands at 1738 , 1217 , 1033 cm^{-1} are clearly manifested in the difference spectrum, it is noteworthy that the 1380 cm^{-1} band becomes noticeably more intense than the 1460 cm^{-1} peak, while in the original spectrum the dependence is inverse. This means that the CH_3 groups concentration increases during aging significantly. Methyl groups are usually the end groups of chain linear or slightly branched organic molecules, and methylene CH_2 groups form the chain backbone. A significant increase of end groups concentration should mean a general significant molecules "shortening" as a result of thermal degradation and, as a result, a decrease of weighted average molecular weight of bitumen macromolecules after aging by the RTFOT method.

Bitumen IR spectra before and after aging in the RTFOT furnace (Figure 4, curves 1 and 2, respectively), the spectrum of bitumen modified by kaolinite after aging in the RTFOT furnace (curve 3), as well as the difference spectrum of bitumen modified by kaolinite after aging in RTFOT furnace and original bitumen (Figure 5) shows a significant increase the bitumen aging resistance level. As can be seen from the spectra, the kaolinite introduction has a very significant effect on the aging processes: the "aging" peaks at 1640 , 1564 and 1217 cm^{-1} almost completely disappear in the difference spectrum, and the carbonyl absorption band at 1738 cm^{-1} intensity significantly decreases. It is difficult to judge the sulfoxide groups behavior in this case, since the 1033 cm^{-1} $\text{S}=\text{O}$ groups absorption peak in this case is superimposed on a very intense 1030 cm^{-1} $\text{Si}-\text{O}$ kaolinite peak, which is the reason of sharp increase of peak intensity in the modified by kaolinite bitumen spectrum, after aging in the RTFOT furnace and the original bitumen. However, it can be assumed that the kaolinite introduction inhibits the sulfoxide groups formation as well as carbonyl ones. We add that the peaks intensities ratio at 1460 cm^{-1} and 1380 cm^{-1} of the CH_2 and CH_3 groups deformation vibrations in the modified by kaolinite bitumen spectrum, after aging in the RTFOT furnace, becomes equally comparable (Figure 5). The above facts quite convincingly testify to the unambiguous kaolinite influence on the thermal and mechanical bitumen degradation processes.

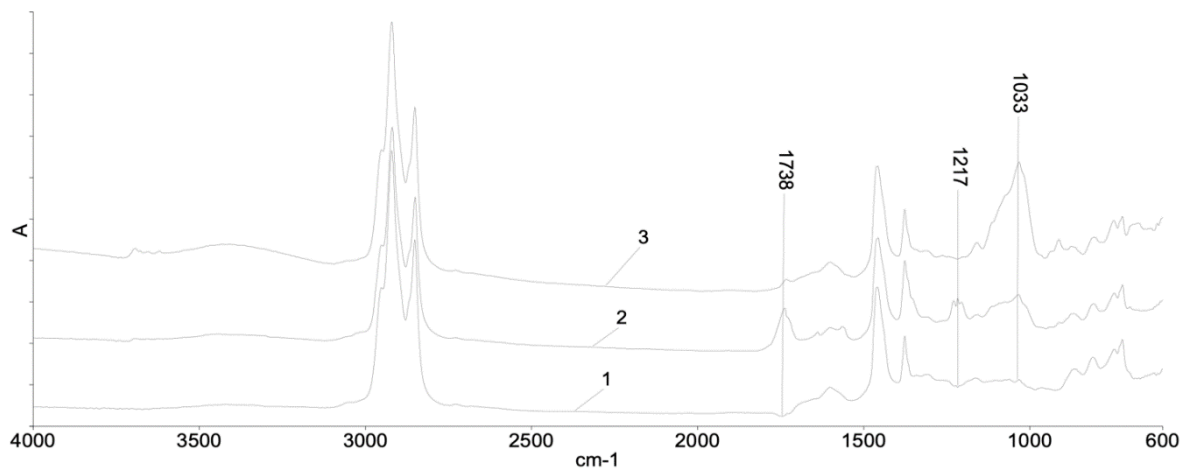


Figure 4. IR spectra:
1 – original bitumen; 2 – bitumen after aging in the RTFOT furnace;
3 – bitumen modified by kaolinite, after aging in the RTFOT furnace.

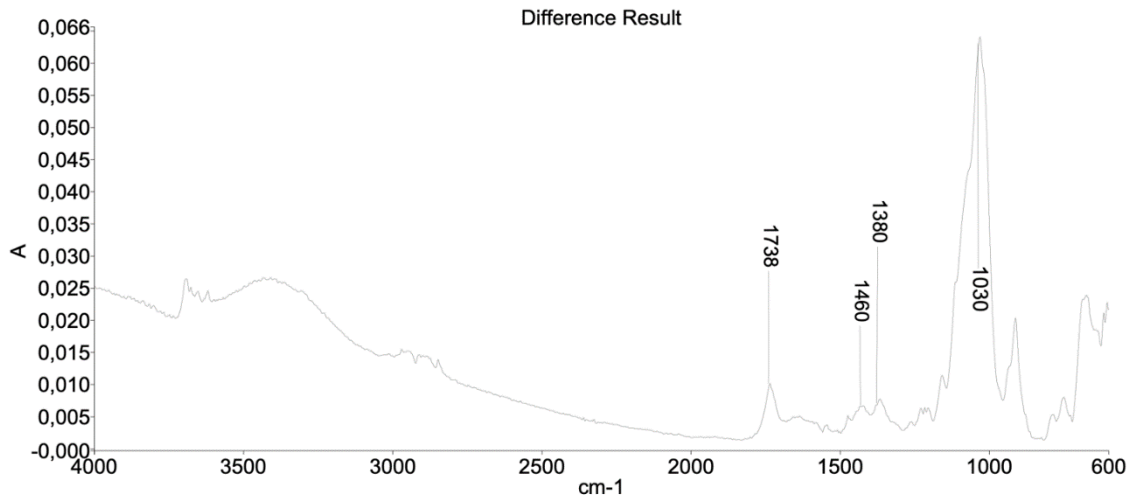


Figure 5. Difference spectrum of bitumen modified by kaolinite after aging in the RTFOT furnace and the original bitumen.

It was noted in [23] that in bitumen, which is in an intermediate state between a sol and a gel, some asphaltenes combine to form open-packed irregular micelles, which are peptized by resins. In our opinion, in a binary mixture of bitumen modified by kaolinite, due to clay plates located mainly at the asphaltene interface, solvation processes with a bitumen structure close to sol proceed more actively. This raises the possibility that these processes result clay plates inhibit the bitumen molecules oxidation and the light fraction from the binder volatilization. As a consequence of these processes, as noted in [26, 27], as a result of the clay plates introduction the paths for the oxygen influx and the light fraction molecules exit from the bitumen matrix become more elongated, which significantly affects the bitumen binder aging mechanism.

The effect of mass change after RTFOT oven aging was studied. When kaolinite is introduced in bitumen from 2 to 8 %, the mass changes were 0.6, 0.32, 0.21, 0.11, 0.09 %, respectively, which confirmed the decrease the light fraction molecules yield as a result of binder thermal oxidation [27, 28].

The experimental data obtained in this work confirm the similarity of the processes described in the studies [19, 22–28].

4. Conclusions

It was found that the kaolinite introduction in amount of 2–8 %, the softening point, Fraas brittle point, dynamic viscosity at 105 °C, 135 °C and 165 °C increased by 1.1–2.6 %, 9.5–28.6 %, 9.2–33.1 %, 6.9–24.1 %, 11.1–55.6 %, respectively. The following indicators decreased: penetration at 25 °C by 8.4–22.4 %; ductility at 0 °C by 4.3–15.2 %. The increase of dynamic viscosity and softening point, as well as the decrease of penetration at 25 °C and ductility at 0 °C are obviously associated with the solid clay particles presence in bitumen, which causes bitumen matrix less mobility and, consequently, higher flow resistance. In addition, the following assumption is interesting: due to the dual nature (polar and nonpolar), clay plates can be located at the interface between asphaltenes and maltenes, and aromatic compounds, due to their lower molecular weight, can intercalate between clay plates. Clay plates, partially exfoliating, can be distributed in aromatic compounds and resins, located mainly at the interface between them. In the intercalation process, the clay mineral plays the surfactant role, which provides and enhances the interaction between the asphaltene and maltenic phases. This process consequence is a decrease the asphaltene micelles size. As a result, the amount and mobility of the "free" aromatic fraction decreases. This, obviously, is the resulting reason of increasing the modified bitumen viscosity.

Based on the analysis of changes the physical and mechanical properties and structure by IR spectroscopy, it was established that the short-term aging reducing on 12.5–28.6 % of modified bitumen with a kaolinite content of 2 % to 8 % have been possible. It was established that the kaolinite introduction into bitumen have caused a significant decrease of aging processes, which has been confirmed by the IR spectroscopy data: the peaks at 1640, 1564 and 1217 cm^{-1} almost completely have disappeared in the difference spectrum, and the intensity of carbonyl absorption band at 1738 cm^{-1} has decreased. In our opinion, in the binary bitumen mixture modified by kaolinite, due to clay plates located mainly at the asphaltene interface, solvation processes with a bitumen structure close to sol proceed more actively. This suggests the possibility that clay plates prevent the oxidation processes of bitumen molecules and volatilization the light fraction from the binder. As a result of clay plates introduction, the oxygen inflow paths and the light fraction molecules exit from the bitumen matrix become more remote, which significantly affects the aging mechanism of bituminous binder.

The obtained experimental data confirmed the similarity of the processes described in previously published studies of other authors and the continuing research prospects in the direction of increasing the bitumen binders aging resistance at searching for new modifiers types and determining their optimal quantities.

References

- Kofteci, S., Gunay, T., Ahmedzade, P. Rheological Analysis of Modified Bitumen by PVC Based Various Recycled Plastics. *Journal of Transportation Engineering Part B Pavements*. 2020. 146(4). 04020063. DOI: 10.1061/JPEODX.0000214
- Geçkil, T., Ahmedzade, P. Effects of Carbon Fibre on Performance Properties of Asphalt Mixtures. *The Baltic Journal of Road and Bridge Engineering*. 2020. 15(2). Pp. 49–65. DOI: 10.7250/bjrbe.2020-15.472
- Somé, S.C., Barthélémy, J.-F., Mouillet, V., Hammoum, F., Liu, G. Effect of thermo-oxidative ageing on the rheological properties of bituminous binders and mixes: Experimental study and multi-scale modeling. *Construction and Building Materials*. 2022. 344(20). 128260. DOI: 10.1016/j.conbuildmat.2022.128260
- Pires, G.M., Presti, D.L., Airey, G.D. A practical approach to estimate the degree of binder activity of reclaimed asphalt materials. *Road Materials and Pavement Design*. 2021. 22(5). Pp. 1093–1116. DOI: 10.1080/14680629.2019.1663244
- Mazzoni, G., Bocci, E., Canestrari, F. Influence of rejuvenators on bitumen ageing in hot recycled asphalt mixtures. *Journal of Traffic and Transportation Engineering (English Edition)*. 2018. 5(3). Pp. 157–168. DOI: 10.1016/j.jtte.2018.01.001
- Bulanov, P., Vdovin, E., Stroganov, V., Mavliev, L., Juravlev, I. Complex Modification of Bituminous Binders by Linear Styrene-Butadiene-Styrene Copolymer and Sulfur. *Proceedings of STCCE 2022. Lecture Notes in Civil Engineering*. 2023. 291. Pp. 204–213. DOI: 10.1007/978-3-031-14623-7_35
- Tang, N., Yang, Y.-L., Yu, M.-L., Wang, W.-L., Cao, S.-Y., Wang, Q., Pan, W.-H. Investigation of Ageing in Bitumen Using Fluorescence Spectrum. *Materials*. 2018. 11(8). 1325. DOI: 10.3390/ma11081325
- Zhang, F., Yu, J., Wu, S. Influence of Ageing on Rheology of SBR/Sulfur-Modified Asphalts. *Polymer Engineering and Science*. 2012. 52. Pp. 71–79. DOI:10.1002/pen.22047.
- Percz-Lcpe, A., Martmez-Boza, F.J., Gallegos, C., Gonzalez, O., González-Bello, O.J., Muñoz, M.E., Santamaria, A. Influence of the processing conditions on the rheological behaviour of polymer-modified bitumen. *Fuel*. 2003. 82. Pp. 1339–1348. DOI: 10.1016/S0016-2361(03)00065-6
- Nivitha, M., Prasad, E., Krishnan, J., Ageing in modified bitumen using FTIR spectroscopy. *International Journal of Pavement Engineering*. 2015. 17(7). Pp. 1–13. DOI: 10.1080/10298436.2015.1007230
- Abdel Bary, E.M., Reem, K.F., Ragab, A.A., Ramy Mohamed, A., Abo-Shanab, Z.L., Saleh, A.M.M. Colloidal stability and dynamic mechanical properties of asphalt modified with unsaturated polyester prepared from waste polyethylene terephthalate. *Egyptian Journal of Chemistry*. 2019. 62(11). Pp. 13–14. DOI: 10.21608/ejchem.2019.7451.1601
- Ahmed, S., Abdelrahman, N., El-Wahab H.A., El-Fattah M.A., Abdelzaher M. Preparation and Characterization of Modified Reclaimed Asphalt by Using Styrene-butyl Acrylate Nanoemulsion Copolymer. *Egyptian Journal of Chemistry*. 2018. 61(2). Pp. 280–290. DOI: 10.21608/ejchem.2018.2956.1245
- Ahmed, S., Mansour, N. F. Ghaly, A.M. Eldidamony, Nessim M.I., Manal, G. Mohamed. Improving the Aging Effect of Bitumen and SBS Modified Bitumen by Using Newly Prepared Antioxidants. *Egyptian Journal of Chemistry*. 2019. 63(6). Pp. 2213–2233. DOI: 10.21608/ejchem.2019.18500.2151
- Karahancer, S., Enieb, M., Saltan, M., Terzi, S. Evaluating mechanical properties of bitumen and hot mix asphalt modified with nano ferric oxide. *Construction and Building Materials*. 2020. 234. 117381. DOI: 10.1016/j.conbuildmat.2019.117381
- Shafabakhsh, G.A., Sadeghnejad, M., Ahoor, B., Taheri, E. Laboratory experiment on the effect of nano SiO₂ and TiO₂ on short and long-term aging behavior of bitumen. *Construction and Building Materials*. 2019. 237(2). 117640. DOI: 10.1016/j.conbuildmat.2019.117640
- Sedaghat, B., Taherian, R., Hosseini, S.A., Mousavi, S.M. Rheological properties of bitumen containing nanoclay and organic warm-mix asphalt additives. *Construction and Building Materials*. 2020. 243. Pp. 118092. DOI: 10.1016/j.conbuildmat.2020.118092
- Pirmohammad, S., Majd Shokorlou, Y., Amani, B. Experimental investigation of fracture properties of asphalt mixtures modified with Nano Fe₂O₃ and carbon nanotubes. *Road Materials and Pavement Design*. 2019. 21(1). Pp. 1–23. DOI: 10.1080/14680629.2019.1608289
- Pirmohammad, S., Shokorlou, Y.M. Fracture Resistance of HMA Mixtures Modified with Nanoclay and Nano-Al₂O₃. *Journal of Testing and Evaluation*. 2019. 47(5). 20180919. DOI: 10.1520/JTE20180919
- Norhidayah, A.H., Ismail, C.R., Al-Saffar, Z.H., Ramadhansyah, P.J., Masri, K.A., Muzamir, H., Wan Azahar, W.N.A. The influence of nano kaolin clay as alternative binder on the penetration properties. *IOP Conference Series: Earth and Environmental Science*. 2021. 682. 012063. DOI: 10.1088/1755-1315/682/1/012063
- Shekhovtsova, S.Yu., Vysotskaya, M.A., Korolev, E.V. Kriteriálnaya otsenka termodestruktivnykh protsessov v asfaltobetone na osnove okisleniya i ostatochnykh bitumov [Criteria estimation of thermal destructive processes in asphalt concrete on the basis of oxidized and residual bitumen]. *Izvestiya vysshikh uchebnykh zavedeniy. Stroitel'stvo*. [News of higher educational institutions. Construction]. 2018. 5(713). Pp. 58–70. DOI: 10.1520/JTE20180919. (rus)
- Dzhumayeva, O., Solodova, N.L., Emelyanycheva, E.A. Osnovnyye napravleniya proizvodstva bitumov v Rossii [The main directions of bitumen production in Russia]. *Vestnik tekhnologicheskogo universiteta [Bulletin of the Technological University]*. 2015. 18(20). Pp. 132–136. (rus)
- Shah, P.M., Mir, M.S. Effect of kaolin clay/SBS on rheological performance of asphalt binder. *Innovative Infrastructure Solutions*. 2020. 5(1). Pp. 5–21. DOI: 10.1007/s41062-020-0270-8
- Hainin, M.R., Ramadhansyah, P.J., Awang, H., Azman, M.K., Suhana, M.R.I., Nordiana, M., Norhidayah, A.H., Haryati, Y., Ros, I.C. Marshall stability properties of asphaltic concrete with kaolin clay under aging. *IOP Conf. Series: Earth and Environmental Science*. 2019. 220. 012040. DOI: 10.1088/1755-1315/220/1/012040
- Merusi, F., Giuliani, F., Filippi, S., Polacco, G. A model combining structure and properties of a 160/220 bituminous binder modified with polymer/clay nanocomposites. A rheological and morphological study. *Materials and Structures*. 2014. 47. Pp. 819–838. DOI: 10.1617/s11527-013-0096-3

25. Mohd Warid, M.N., Al-Saffar, Z.H., Ramadhansyah, P.J., Masri, K.A., Muzamir, H., Mudjanarko, S.W. Performance of nano kaolin clay modified bitumen under aging through the viscosity. IOP Conference Series: Earth and Environmental Science. 2021. 682. 012064. DOI: 10.1088/1755-1315/682/1/012064
26. Huiming, B., Wu, C., Zhang, Y. Study on the adhesion between activated kaolin modified asphalt and mineral materials. Journal of Physics: Conference Series. 2021. 1732. 012109. DOI: 10.1088/1742-6596/1732/1/012109
27. Wang, D. Thermal oxidative and ultraviolet ageing behaviour of nano-montmorillonite modified bitumen. Road Materials and Pavement Design. 2019. 22(3). 1619619. DOI: 10.1080/14680629.2019.1619619
28. Zare-Shahabadi, A., Shokuhfar, A., Ebrahimi-Nejad, S. Preparation and rheological characterization of asphalt binders reinforced with layered silicate nanoparticles. Construction and Building Materials. 2010. 24. Pp. 1239–1244. DOI: 10.1016/j.conbuildmat.2009.12.013

Information about authors:

Pavel Bulanov, PhD in Technical Sciences

ORCID: <https://orcid.org/0000-0002-0149-8854>

E-mail: pavel.bulanov1991@yandex.ru

Evgenii Vdovin, PhD in Technical Sciences

ORCID: <https://orcid.org/0000-0002-0649-4342>

E-mail: vdovin007@mail.ru

Victor Stroganov, Doctor of Chemical Sciences

ORCID: <https://orcid.org/0000-0001-9680-6698>

E-mail: Svf08@mail.ru

Received 13.06.2023. Approved after reviewing 01.12.2023. Accepted 01.12.2023.

